Potential of Lithium Manganese Oxide Sorbent for Direct Lithium Extraction from Geothermal Brine

Zur Erlangung des akademischen Grades eines

DOKTORS DER NATURWISSENSCHAFTEN (Dr. rer. nat.)

von der KIT-Fakultät für

Bauingenieur-, Geo- und Umweltwissenschaften

des Karlsruher Instituts für Technologie (KIT)

genehmigte

DISSERTATION

von

M.Sc. Klemens Slunitschek

Tag der mündlichen Prüfung: 27. Juli 2026

Hauptreferent: Prof. Dr. Jochen Kolb

Korreferentin: Prof. Dr. Simona Regenspurg

Karlsruhe 2026

Abstract

Over the last two decades, global Li demand has increased significantly and is expected to continue rising. The primary driver of this development and largest application is batteries for electric vehicles. To meet this demand, new deposits must be developed, and unconventional resources, such as geothermal brines, are increasingly being considered. However, conventional evaporative Li mining is not feasible for many geothermal brines due to low Li concentrations and climatic restrictions. Consequently, new technologies for Direct Lithium Extraction (DLE) are being developed, including ion exchange, adsorption, and membrane processes, among others.

For Li extraction from geothermal brines, high selectivity and extraction efficiency are required to reduce downstream processing. Furthermore, the technology must exhibit fast extraction kinetics and withstand elevated temperature and pressure, for integration into geothermal power plants. To avoid the formation of scales, alterations to brine chemistry and operating conditions must be minimised, and the technology should operate at native brine pH. Additionally, the technology needs a high resistance to salinity and corrosivity.

The Lithium Manganese Oxide (LMO) sorbent $Li_{1.6}Mn_{1.6}O_4$ has been identified as a promising candidate for geothermal DLE. To investigate the potential of the LMO sorbent under ambient brine conditions and identify challenges for industrial integration, a pilot plant was developed and constructed. The pilot plant was set up in the geothermal power plant in Bruchsal, Germany and connected to the reinjection line through a bypass. In addition, sorption properties of the sorbent were investigated in laboratory experiments.

The sorbent exhibits fast Li sorption kinetics and high Li sorption capacity, making it suitable for high-flow-rate applications. In addition, the high selectivity for Li and low selectivity toward brine-dominating elements supports the suitability for highly saline brines. However, the sorption and accumulation of potentially problematic elements such as As and radionuclides might limit and pose challenges for end-of-life handling. The high stability of the sorption and selectivity processes supports the potential for long-term application.

A key challenge for industrial application is the production of larger, granular particles while maintaining the advantageous sorption properties. Moreover, to exploit the high selectivity of the sorbent and obtain a high-purity desorption solution, cross-contamination from geothermal brine into the desorption solution must be minimised. In addition, high Li concentration in the desorption solution is required to achieve high purity.

In summary, the LMO sorbent $Li_{1.6}Mn_{1.6}O_4$ has high potential for DLE from geothermal brines, provided that the advantageous sorption properties are transferred to industrially relevant particle sizes.

Kurzfassung

Innerhalb der letzten zwei Jahrzehnte ist die globale Lithiumnachfrage signifikant angestiegen und ein weiterer Anstieg wird prognostiziert. Ursache dieser Entwicklung ist der steigende Bedarf an Batterien für Elektrofahrzeuge, die gleichzeitig der wichtigste Anwendungsbereich von Lithium sind. Zur Deckung der Nachfrage werden neue Lagerstätten erschlossen, wobei zunehmend auch bislang ungenutzte, unkonventionelle Ressourcen wie geothermische Wässer in Betracht gezogen werden. Die konventionelle Lithiumgewinnung aus Solen mittels Evaporation ist für geothermische Wässer aufgrund niedriger Lithiumgehalte sowie ungünstiger klimatischer Bedingungen jedoch meist nicht möglich. Daher werden neue Technologien zur Direkten Lithiumextraktion (DLE) entwickelt, unter anderem Ionentauscher-, Adsorptions- und Membranverfahren.

Für die Lithiumextraktion aus geothermischen Wässern sind eine hohe Selektivität sowie eine hohe Extraktionseffizienz erforderlich, um den Umfang nachgeschalteter Verfahrensschritte zu reduzieren. Zusätzlich muss die Technologie für die Integration in Geothermiekraftwerke eine hohe Extraktionskinetik aufweisen und unter erhöhtem Druck und hohen Temperaturen betrieben werden können. Zur Vermeidung mineralischer Ausfällungen aus dem Geothermalwasser sind Veränderungen der Wasserchemie und der Betriebsbedingungen des Kraftwerks auf ein Minimum zu begrenzen. Zudem sollte die Technologie im Bereich des natürlichen pH-Werts des Geothermalwassers betrieben werden können. Darüber hinaus ist eine erhöhte Beständigkeit gegenüber hoher Salinität und Korrosion erforderlich.

Als vielversprechender Kandidat für die geothermale DLE wurde das Lithium-Manganoxid-Sorbens $Li_{1.6}Mn_{1.6}O_4$ identifiziert. Zur Untersuchung des Potenzials des Sorbens unter Realbedingungen sowie zur Identifikation zentraler Herausforderungen der industriellen Umsetzung wurde eine Pilotanlage entwickelt und gebaut. Diese wurde im Geothermiekraftwerk in Bruchsal, Deutschland, installiert und über einen Bypass an die Reinjektionsleitung des Kraftwerks angeschlossen. Ergänzend wurden die Sorptionseigenschaften des Sorbens unter Laborbedingungen bestimmt.

Das Sorbens zeichnet sich durch eine schnelle Sorptionskinetik sowie eine hohe Sorptionskapazität für Lithium aus, was den Einsatz in Prozessen mit hohen Volumenströmen ermöglicht. Zudem weist es eine hohe Selektivität für Lithium bei gleichzeitig geringer Selektivität gegenüber den in der Sole dominierenden Ionen auf, was den Einsatz in hochsalinaren Lösungen begünstigt. Einschränkungen können sich durch die Sorption und Akkumulation potenziell kritischer Elemente wie As und Radionuklide ergeben, die insbesondere im Hinblick auf die Entsorgung am Ende der Lebensdauer relevant sind. Die hohe Stabilität der Sorptions- und Selektivitätsprozesse unterstreicht das Potenzial des Sorbens für einen Langzeitbetrieb.

Eine zentrale Herausforderung für die industrielle Umsetzung ist die Herstellung größerer granularer Partikel bei gleichzeitigem Erhalt der Sorptionseigenschaften. Darüber hinaus ist zur optimalen Nutzung der Selektivität des Sorbens und zum Erreichen einer hohen Reinheit der Desorptionslösung eine Minimierung der Querkontamination durch Geothermalwasser erforderlich. Zusätzlich ist eine hohe Lithiumkonzentration in der Desorptionslösung notwendig.

In der Gesamtbetrachtung weist das Sorbens $Li_{1.6}Mn_{1.6}O_4$ ein hohes Potenzial für die direkte Lithiumextraktion aus geothermischen Wässern auf, jedoch stellt der Erhalt der Sorptionsegenschaften bei industriell relevanten Partikelgrößen eine wesentliche Voraussetzung für die Anwendung dar.

Table of contents

List of Figures

List of Tables

1. Introduction

1.1. Lithium – Resource, demand and mining

Lithium is the lightest metal and possesses a low density and high chemical reactivity. Due to its high specific capacity, low electrochemical potential, and high energy density, it is particularly suitable for battery applications (Choubey et al., 2016; Liu et al., 2016; Ngoy et al., 2025). In 2024, around 87% of global end use of Li was for rechargeable batteries, 5% for ceramics and glasses, 2% for lubricating greases, 1% for pharmaceuticals, and 6% for other applications (USGS, 2025). For battery applications, high purities >99.5 wt.-%, so-called battery grade, are required (Choe et al., 2024). Accordingly, purification accounts for 30–40% of the total production costs. Thus, Li extraction processes requiring lower purification efforts downstream of the production are beneficial and researched.

Since 1995, global Li demand has increased strongly, especially due to the rise in electric vehicles (Martin et al., 2017). In 2024, global Li production, excluding the United States of America, amounted to 240,000 t, increasing by 18% from 2023 (USGS, 2025). Prices for battery-grade lithium carbonate (Li_2CO_3) ranged from 9,400–14,500 US$/t, strongly dependent on global EV sales (USGS, 2025). The global Li demand is projected to increase to 455,000 t Li by 2030 and 928,000 t by 2040 (IEA, 2025).

Lithium is mined from hard rocks and brines and can be recovered from the recycling of Li batteries of EVs and other applications. Lithium recovery from battery recycling is not presented in more detail, as Li recycling is currently very low and EV battery recycling often targets more valuable elements, e.g., cobalt (Swain, 2017; Bae and Kim, 2021).

In 2024, the majority of Li was mined in Australia (~37% of global production, predominantly hard rock), Chile (~20%, brine) and China (~20, hard rock and brine; Meng et al., 2021; USGS, 2025). Currently, Europe plays no role in global Li mining and production, with only one mine in Portugal producing 380 t, or ~0.16% of global production, in 2024 (USGS, 2025). European reserves are estimated at 60,000 t, representing 0.2% of the global reserves. However, Europe has potential for Li mining with resources in, amongst others, Germany (4 Mt), Czechia (1.3 Mt) and Serbia (1.2 Mt, USGS, 2025). Regarding the total global resources, around 6% are contained in Europe, with 7.2 of 150 Mt. Lithium deposits occur globally in the form of brines, hard rock and seawater. Despite the low Li concentration in seawater of 0.1–0.2 mg/L, the oceans contain a huge resource of around 230 Gt, compared to 150 Mt of terrestrial resources (Diallo et al., 2015; Murphy and Haji, 2022; USGS, 2025). Due to the very low concentration, extraction technologies with minimal resource requirements are needed for Li seawater mining. While Li extraction from seawater is researched, e.g. Yoshizuka et al. (2002), currently no commercial project is known.

Hard rock deposits are primarily igneous rocks or clays, of which the former accounts for 14%

of the total resources and 25% of global production (Wu et al., 2025). Granitic pegmatites are the most important hard rock Li deposits occurring globally and being mined, amongst others in Australia and China (Meng et al., 2021). The most relevant minerals in pegmatites are spodumene ($LiAlSi_2O_6$), lepidolite ($KLi_{1.5}Al_{1.5}[Si_3O_{10}][F,OH]_2$, petalite ($LiAlSi_4O_{10}$) and zinnwaldite ($KLiFeAl\ [AlSi_3]O_{10}[OH,F]_2$), with a Li concentration of 1–4 wt.-% in the whole rock (Wu et al., 2025). In the standard spodumene processing, the mined ore is crushed and ground, concentrated through flotation, leached at high temperature and pressure with different chemicals, and crystallised as lithium carbonate (Li_2CO_3) or lithium hydroxide monohydrate ($LiOH \cdot H_2O$; Meng et al., 2021; Wu et al., 2025). Due to the high energy and chemical demand, Li production from hard rocks is comparably expensive, costing 3600–8000 US$/t LCE, and greenhouse gas intensive (Wu et al., 2025).

Lithium-rich brines can be categorised into continental brines, also termed salt lake or salar brines, geothermal brines, and oilfield brines. Continental brines occur globally, with the most important mining areas in Bolivia, Chile, Argentina, and China. The mining of continental brines accounts for 59% of global Li production (Wu et al., 2025). In general, continental brines contain high Li concentrations of 54–1600 mg/L, and some even up to 5000 mg/L (Wu et al., 2025). Conventionally, brines are mined evaporatively, whereby brine is evaporated in large evaporation ponds until a Li concentration of around 6000 mg/L is reached. Thereby, 30–90% of the brine is evaporated, requiring 6–18 months (Murphy and Haji, 2022). Throughout the process, various salts, depending on the brine chemistry and mineral solubility, such as halite (NaCl), sylvite (KCl), sylvinite ($NaCl \cdot KCl$) and various Mg minerals (Wu et al., 2025), are precipitated. Once the target Li concentration is reached, dissolved Mg, Ca and sulphate are precipitated through the addition of calcium hydroxide ($Ca(OH)_2$) and sodium carbonate (Na_2CO_3), followed by precipitation of Li carbonate (Li_2CO_3, Murphy and Haji, 2022). Lithium recovery in evaporative mining can be relatively low, with efficiencies of ~50–80%, due to the entrapment of Li-rich brine in precipitating Mg flocculants (Ventura et al., 2016; Flexer et al., 2018; Wu et al., 2025). Evaporation mining is climatically restricted to areas with high solar radiation, low rainfall and much wind, such as, e.g. in the Salar de Atacama, Chile, Salar de Hombre Muerto, Argentina or Dontai salt lake, China (Vera et al., 2023). Furthermore, the methodology is only feasible for higher Li concentrations, due to the time required to evaporate the brine (Murphy and Haji, 2022). In addition, high Mg/Li ratios of >10 can make evaporative mining economically infeasible due to increased Li losses and high consumption of precipitation agents (Wu et al., 2025). With production costs of 3300–4900 US$/t LCE, evaporative mining is more cost-effective than hard rock mining (Nicolaci et al., 2023). Disadvantages are the long production time and high brine consumption. Thereby, the dominant problem is the inflow of freshwater into the brine aquifer, making it unusable for human and agricultural consumption (Vera et al., 2023).

Oilfield brines are highly saline brines, produced as a waste by-product of oil and gas production. Lithium-rich oilfield brines occur globally, e.g. in the Smackover Formation in Kansas, USA (Dugamin et al., 2021; Gerardo and Song, 2025). Geothermal brines are subsurface brines pumped to the surface for electricity or heat generation. Lithium-rich geothermal brines occur globally, e.g. in the Upper Rhine Graben, Germany and France, or in Salton Sea in the USA (Sanjuan et al., 2016; Sanjuan et al., 2022; Dobson et al., 2023). The extraction of Li from geothermal and oilfield brines represents a secondary use and provides additional valorisation of the already exploited resources. As a result, Li extraction may be economically feasible despite the lower average Li concentrations of 10–500 mg/L, compared with continental brines (Fatoki et al., 2026). Since evaporative mining of these brines is not possible due to, amongst others, the lower Li concentration and potential climatic restrictions, technologies for Direct Lithium Extraction (DLE) are researched. Direct Lithium Extraction encompasses different technologies, e.g. ion exchange, sorption, membrane processes, able to extract Li directly from the brine, with high selectivity and low co-extraction of other elements.

1.2. Geothermal brines of the Upper Rhine Graben

The Upper Rhine Graben (URG) in southwest Germany and southeast France is an in average 35 km wide graben structure, stretching over 300 km north-south from Frankfurt am Main, Germany, to Basel, Switzerland. It is flanked by the Vosges. The crystalline basement consists of gneiss and granite, overlain by sediments, amongst others Buntsandstein and Upper Muschelkalk (Stober and Bucher, 2015). The strata within the Graben and the Graben shoulders are vertically displaced and only partially hydraulically connected (Stober and Bucher, 2015). Within the Graben, elevated thermal gradients of in average 36.3°C/km are present, compared to 27°C/km usually found in Variscan Central Europe (Agemar et al., 2013; Stober and Bucher, 2015) Along the western border of the graben, several thermal anomalies with increased temperature gradients of up to >100°C/km are found (Agemar et al., 2013; Stober and Bucher, 2015). The elevated thermal gradients persist to more than three km of depth and stem from the convective circulation of deep brines (Stober and Bucher, 2015; Sanjuan et al., 2016). The hydrodynamics and brine migration in and between the reservoirs are controlled by a system of fractures (Stober and Bucher, 2015; Vidal and Genter, 2018; Frey et al., 2022). Due to the elevated thermal gradients, the area has an enhanced potential for geothermal energy production of electricity and heat.

In 2026, five geothermal power plants are active in the URG, with Soultz-sous-Forêts and Rittershoffen in France and Bruchsal, Insheim and Landau in Germany, with several more in planning and development (Informationsportal Tiefe Geothermie; Frey et al., 2022; Bundesverband Geothermie, 2024). The geothermal power plant in Soultz-sous-Forêts is of the Enhanced Geothermal System (EGS) type, injecting water into a doublet in the ground, where

it is heated by the surrounding rocks before extraction. The wells are up to 5000 m deep, reaching into the granitic basement (Frey et al., 2022). The borehole bottom temperature is around 200°C, and the production temperature at the wellhead is around 150–165°C at a flow rate of 30 kg/s (Mundhenk et al., 2013; Sanjuan et al., 2014; Baujard et al., 2018). The production pressure of 20–23 bar is kept throughout the processing, and brine is reinjected into the subsurface at ~70°C (Mundhenk et al., 2013; Fries et al. 2022). Gases are dissolved in the brine with a gas-to-liquid ratio of 75–107 vol%, consisting predominantly of carbon dioxide (CO_2, 86.2%), nitrogen (N_2, 9.85%) and methane (CH_4, 2.28%) and with an oxygen content of <0.001% (Nitschke et al., 2014; Sanjuan et al., 2014). The extracted heat is used to produce electricity (Fries et al. 2022).

The geothermal power plant Bruchsal produces subsurface brine from ~2500 m depth from a Buntsandstein reservoir at a borehole bottom temperature of 130°C (Eggeling et al., 2013; Stober and Bucher, 2015; Sanjuan et al., 2016). The wellhead production temperature is ~120°C at a pressure of 22±2 bar and with a flow rate of 24 L/s. Reinjection of the brine occurs at 18±2 bar and 60–80°C (Fechner et al., 2022). Up to 1.9 L of gas are dissolved per litre brine, consisting predominantly of CO_2 (94.5%), N_2 (3.5%), CH_4 (1.9%) and 0.009% O_2 (Sanjuan et al., 2016; Fechner et al., 2022). The geothermal power plant is used to produce electricity and district heating.

To avoid degassing and scaling formation, the brine pressure is kept relatively constant, and the temperature is only decreased to 60–80°C in both plants (Mundhenk et al., 2013; Fechner et al., 2022; Fries et al. 2022). This avoids oversaturation and precipitation of mineral phases, such as sulphates, sulphides and carbonates (Mundhenk et al., 2013; Nitschke et al., 2014; Kölbel et al., 2022). The brines of Soultz-sous-Forêts (Electricité de Strasbourg, France) and Bruchsal (Energie Baden-Württemberg AG, Germany) are relatively similar, with a total dissolved solids concentration of 99 and 121 g/L (Table 1.1; brine data from Sanjuan et al., 2016). Both are dominated by Na, Ca, and K, with concentrations of 28,140–35,127 mg/L, 7,225–7,363 mg/L, and 3,195–3,113 mg/L (Table 1.1). Magnesium is contained in lower concentrations, with 131 mg/L in Soultz-sous-Forêts and 301 mg/L in Bruchsal. Lithium is slightly more concentrated in Soultz-sous-Forêts than in Bruchsal, with 173 to 159 mg/L, respectively (Table 1.1). Manganese and Fe are contained in similar concentrations, with 16.9–25.2 mg/L and 25.5–42.4 mg/L, while Zn is ~7 times and Pb ~24 times more concentrated in the Bruchsal brine (Table 1.1). Additionally, the brines have higher concentrations of various radionuclides, including Ra, Th, U, and Pb (Table 1.1; Eggeling et al., 2013; Sanjuan et al., 2016; Kölbel et al., 2022). The dominant anion is Cl-, at 58,559 mg/L in Soultz-sous-Forêts and 73,566 mg/L in Bruchsal. Sulphate is the second most concentrated anion with comparably lower concentrations of 157 and 267 mg/L (Table 1.1). Both brines have a pH~5 and reducing conditions (Mundhenk et al., 2013; Sanjuan et al., 2016).

The origin of Li in the brines of the URG is the subject of ongoing research and is not yet fully understood. Drüppel et al. (2020) show the leaching of Li from basement rocks as a potential origin of Li. Jungmann et al. (2024) propose that in addition to leaching, Li originates from Li-enriched, seawater-derived connate brines and the dissolution of evaporites.

Table 1.1: Selected major and trace elements of Bruchsal and Soultz-sous-Forêts brine. Data from Sanjuan et al. (2016), except for 1, adapted from Eggeling et al. (2013).

	Li	Na	Mg	K	Ca	Mn	Fe	Zn
	mg/L	mg/L	mg/L	mg/L	mg/L	mg/L	mg/L	mg/L
Soultz-sous-Forêts	173	28140	131	3195	7225	16.9	25.5	2.17
Bruchsal	159	35127	301	3113	7363	25.2	42.4	15.2

	As	Sr	Ba	Pb	^{226}Ra[1]	Cl	SO_4	TDS
	mg/L	mg/L	mg/L	mg/L	Bq/kg	mg/L	mg/L	g/L
Soultz-sous-Forêts	9.31	455	5.1	0.14	29.1 ± 1.3	58559	157	99
Bruchsal	8.82	391	9.3	3.39	28.1 ± 1.3	73566	267	121

1.3. Direct Lithium Extraction

The application of conventional, evaporative brine mining is restricted to areas with high evaporation and to brines with high Li concentrations and lower Mg/Li ratios, amongst others (Murphy and Haji, 2022; Vera et al., 2023; Wu et al., 2025). Through DLE technologies, Li deposits and sources not accessible with evaporation mining shall become exploitable, such as geothermal or oilfield brines or process solutions from hydrometallurgical EV battery recycling. Additionally, these methods may offer lower water consumption, decreasing the environmental impact of Li mining, especially in arid areas. For DLE from geothermal brines, technologies have to be able to handle the complex brine chemistry, high salinity, high temperatures (up to >100°C) and elevated pressure, be highly selective for Li and have fast extraction kinetics (Stringfellow and Dobson, 2021). Furthermore, the produced Li-rich solution needs to be of high purity to achieve battery grade with little additional downstream purification. In the following, a general overview of the most relevant DLE technologies is provided, complementing the review by Reich et al. (2022) in Chapter 4. For clarity, some repetition with Reich et al. (2022) is unavoidable.

Within DLE, solvent extraction, membranes, electrochemical methods, adsorbents and ion exchangers (IX) are currently being intensively researched (Wu et al., 2025). In solvent extraction, also termed liquid–liquid extraction, an organic phase (e.g. D2EHPA, MEHPA) is mixed with the brine, whereby both are immiscible, resulting in Li^+ transfer into the organic phase from the brine (Wu et al., 2025). After mixing, the two liquids are separated, and Li is stripped from the organic phase, typically using an acid. Afterwards, the organic phase can be recycled

and reused. Due to the high solubility of Li in the organic phase, high sorption capacities, e.g. up to 4.4 g/L, and high Li recovery are achieved (Hanada and Goto, 2021; Wu et al., 2025). The affinity for competing monovalent ions is low, but can be high for divalent ions, such as Ca^{2+}, Mg^{2+} or Sr^{2+}, depending on the solvent (Wu et al., 2025). The application of solvent extraction in DLE can benefit from the existing know-how, experience, technology and component availability resulting from the long-lasting application in the refining of other metals, e.g. Mn, Ni or rare earth elements. Disadvantages in addition to the potentially low selectivity are high solvent replenishment costs, the environmental hazard potential of the solvent and the potential generation of large volumes of acidic wastewater (Wu et al., 2025).

The membrane processes reverse osmosis, nanofiltration and electrodialysis are researched for the application in DLE, separating ions based on their ionic radii and charge. Thereby, the ions are driven through semi-permeable membranes with pressure, concentration gradients or electric potential differences (Wu et al., 2025). The selectivity of the membrane relies on the pore diameter and its positive charge. Due to the positive charge, higher-charged cations are more rejected than cations with lower charge (Wu et al., 2025). Membrane processes can run continuously without desorption, stripping or regeneration steps, decreasing downtime (Khalil et al., 2022). Additionally, the chemical consumption is significantly lower due to the absence of these steps, decreasing costs and making membrane processes more environmentally friendly. However, membrane processes often have lower Li recovery rates, below 80%, and the electricity consumption to create the needed pressure or electric field can be substantial (Safari et al., 2020; Wu et al., 2025). Furthermore, the formation and accumulation of organic and mineral phases on and in the membranes, so-called membrane fouling, results in reduced permeability and Li extraction efficiency over time (Wu et al., 2025). This requires regular maintenance, resulting in downtime and costs.

Electrochemical methods utilise electric fields to extract Li from brines by sorption in Li-selective electrodes (Wu et al., 2025). The electrodes are often made of the same materials used in EV batteries, such as Lithium Manganese Oxide (LMO) or Lithium Iron Phosphate (LFP). Through the application of an electric field, Li^+ moves from the brine to the electrode, where it is intercalated and accumulated, based on the selectivity of the electrode material (Wu et al., 2025). By reversing the electric field, the accumulated Li ions are released into a recovery solution. The process has low chemical consumption, reduced water usage and allows for precise control over the extraction process (Wu et al., 2025). Depending on the electrode material, durability can be reduced. Furthermore, the selectivity of the process, especially for Mg, can be low (Wu et al., 2025). Due to high electrode degradation, short lifetime and high costs for electrodes and electricity, electrochemical methods are amongst the most expensive DLE technologies (Kong et al., 2025).

Adsorbents are inorganic, solid materials binding Li reversibly to the outer and inner surface

or intercalating it into the crystal framework through physical or chemical bonds (Wu et al., 2025). Lithium-Aluminium-Layered Double Hydroxide chloride $[LiAl_2(OH)_6]Cl{\cdot}nH_2O$ (LiAl-LDH) are amongst the most extensively researched adsorbents and ion-exchange materials and the only material used at commercial scale and over various decades (Safari et al., 2020). The adsorbent is synthesised from LiCl and $Al(OH)_3$ (gibbsite), resulting in a layered, plated structure of Al hydroxide with Li in octahedral vacancies (Boroumand and Razmjou, 2024; Wu et al., 2025). Intercalation of Li results in a positive charge of the plate, which is compensated by Cl^- and water, occupying the interlayer space. While water is sufficient for the desorption of Li, a LiCl eluate is normally used, preventing the degradation of the sorbent to unreactive gibbsite (Wu et al., 2025). The required LiCl solution is taken as an aliquot of the desorption solution, thus can be produced on-site without the input of additional chemicals. Furthermore, no acids are needed, making the process more economical and environmentally friendly in comparison to IX. The adsorbent can have a high Li selectivity in brines with low Mg/Li, but shows lower selectivity at high ratios (Safari et al., 2020). Furthermore, the sorption capacity is lower (<7 mg/g) and the kinetics slower, in comparison to IX. To improve extraction, pre-concentration can be required at low Li concentrations. To achieve the necessary sorption kinetics, brine preheating to elevated temperatures of 45–95°C is required, resulting in increased operation costs (Saleem et al., 2025). At brine pH < 6, LiAl-LDH can dissolve, limiting its application to brines with corresponding pH levels or requiring pH adjustment (Saleem et al., 2025).

Ion exchangers are inorganic, solid materials, with the most promising for DLE being LMO and Lithium-Titanium Oxide (LTO). Both materials are synthesised, whereby the presence of Li acts as a template, leading to a Lithium Ion Sieve effect (LIS). Thus, only ions with a similar or smaller ionic radius and hydration energy can occupy the Li crystal sites (Wu et al., 2025). Lithium sorption is based predominantly on ion-exchange reactions with H^+ as the exchange ion in most cases. Additionally, Li can sorb through redox reactions, depending on the sorbent chemistry (Wu et al., 2025). In the mineral framework, Li is intercalated and bound strongly through the IX reaction, whereas on the material surface Li can be bound through weak physisorption in addition (Wu et al., 2025). For desorption, the Li-H^+ exchange is reversed, resulting in the uptake of H^+ from the desorption solution and release of Li^+, thus requiring acidic desorption solutions. The IX process is strongly dependent on the pH, with high brine pH facilitating Li sorption and low pH facilitating desorption. Lithium Ion Sieves are highly selective for Li^+ and can exhibit low selectivity towards Mg^{2+} (Wu et al., 2025). Advantages of IX sorbents are fast sorption kinetics and higher sorption capacities in comparison to adsorbents (Wu et al., 2025). Disadvantages are the utilisation of acid for desorption, potential material degradation due to redox processes and potential performance loss due to structural changes over time (Wu et al., 2025). Currently, IX and especially LMO are regarded as the most promising DLE technology. Since a spinel LMO is used in the following studies, they are discussed in

more detail in the following.

Spinel LMO are a group of materials with a spinel tunnel structure framework and various different chemical compositions, e.g. $LiMn_2O_4$ (Hunter, 1981), $Li_{1.33}Mn_{1.67}O_4$ (Ammundsen et al., 1996) or $Li_{1.6}Mn_{1.6}O_4$ (Chitrakar et al., 2000), all derived from the spinel $LiMn_2O_4$ (Wu et al., 2025). The tunnel structure creates a LIS and results from the priming with Li during synthesis. The different chemical compositions are achieved through variations of synthesis type and parameters. The LMO sorbents can be synthesised through hydrothermal, solid-state (mechanochemical, microwave combustion) and soft-chemical methods, such as sol-gel, co-precipitation or spray drying with pyrolysis (see Xu et al. (2016) or Weng et al. (2020) for an overview or e.g. Yang et al., 2000; Jang and Moorehead, 2002; Shi et al., 2011; Sun et al., 2011; Chen et al., 2016; Ryu et al., 2017; Yang et al., 2018). The crystal framework consists of MnO_4 octahedra in a cubic closed-packed oxygen framework (32e) within the Fd3m space group (Figure 1.1, adapted from Berg et al. (2000); Thackeray et al., 1983; Feng et al., 1992; Thackeray, 1997; Wu et al., 2025). Manganese is situated on octahedral sites 16d and Li predominantly on tetrahedral 8a sites. In sorbents with a higher Li:Mn stoichiometric ratio than 1:2, such as $Li_{1.6}Mn_{1.6}O_4$, the amount of trivalent Mn at the octahedral sites is decreased, and nearly all Mn is present as Mn^{4+}. Vacant octahedral sites, formerly occupied by $Mn^{3+,}$ are occupied by Li (Julien, 2006; Safari et al., 2020). Additionally, Li occupies octahedral interstitial 16c sites (Julien, 2006). Lithium diffuses through the material by moving through interstitial sites, in the order of 8a → 16c → 8a → 16c for Li on 8a sites and 16d → 16c → 16d → 16c for Li on 16d sites (Feng et al., 1995; Celestian et al., 2026).

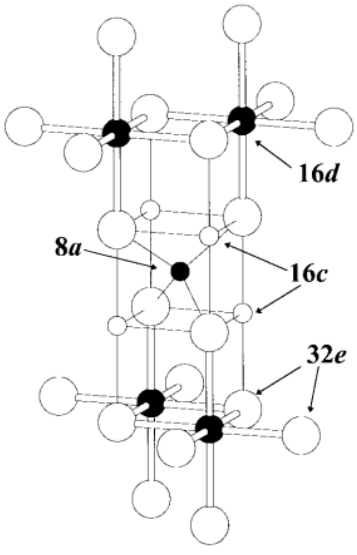

Figure 1.1: Spinel structure of LMO, adapted from Berg et al. (2000)

Li sorption and desorption are based on a Li^+-H^+ ion exchange and a redox mechanism, with the latter being dependent on Mn^{3+} in the framework (Ooi et al., 1989; Wu et al., 2025). During desorption, Mn is dissolved, resulting from the disproportionation of two Mn^{3+} into Mn^{4+} and

Mn^{2+}, with the dissolution of the latter (Ooi et al., 1988; Ooi et al., 1989; Gao et al., 2018). Manganese dissolution results in a continuous degradation of the sorbent with every extraction cycle and a reduction of its lifetime. Thus, sorbents with solely Mn^{4+} in the theoretical structure, such as $Li_{1.6}Mn_{1.6}O_4$, are preferred for industrial application, due to the longer expected lifetime. In order to reduce Mn dissolution, the sorbent structure can be doped with specific elements, such as Al^{3+}, Mg^{2+} or Ti^{4+} (Wu et al., 2025). Thereby, dopants replace Mn^{3+} in the structure, inhibiting Mn reduction and strengthening the crystal framework through stronger metal-oxygen bonds (Wu et al., 2025). Another approach to reduce Mn loss is the application of metal oxide coatings onto the particle surface, acting as a physical barrier and reducing the contact with Mn-reducing agents, e.g. organic compounds or H_2S (Wu et al., 2025).
Through the occupation of additional sites by Li, LMO sorbents possess high sorption capacities, e.g. 68 mg/g for $Li_{1.6}Mn_{1.6}O_4$. However, experimentally only lower values have been achieved, due to, amongst others, sorbent morphology, structural impurities and defects, particle size, particle clustering, sorption of competing elements, brine chemistry and pH (Wu et al., 2025). More information regarding achieved sorption capacity from brines, and sorbent selectivity and industrial integration are given in Reich et al. 2022 (Chapter 4), Slunitschek et al. 2025 (Chapter 5) and in Chapter 8.

1.4. Sorption processes

The determination of the sorption type and process is relevant to understand the interaction between sorbate and sorbent. With regard to the extraction of a target metal, such as Li, it can instruct the optimisation of the extraction process and the sorbent. Furthermore, changes to the sorbent and the extraction process with regard to the sorption and extraction of unwanted, competing elements are instructed by it.
Elements dissolved in water can be present as ions, neutral molecules or complexes (Koretsky, 2000). Due to the electric charge of ions, a hydration sphere of water molecules forms around them, linked through dipole-ion bonds (Koretsky, 2000). Lithium, for example, is tetrahedrally coordinated by four H_2O molecules in general (Persson, 2010). Thereby, the binding strength of the hydration sphere to the ion is related to the charge density of the ion. At high charge densities, several layers of the hydration shell can form, supported by H^+ bonds between the coordinating water molecules (Kiriukhin and Collins, 2002; Persson, 2010). The hydration sphere can also contain cations or anions, depending on the central ion, termed aqueous complex (Koretsky, 2000).
Due to the discontinuity of the crystal framework, crystal surface atoms are coordinatively unsaturated due to missing binding partners (Koretsky, 2000). This can result in the hydroxylation of cations and protonation of anions. The formed hydroxyl groups may form surface complexes with dissolved ions and chemical species or act as dissolution or precipitation sites (Koretsky,

2000). Furthermore, these sites can be amphoteric, protonating and deprotonating in dependence of the pH level. Thereby, they can form $M–OH^0$, $M–OH_2^+$, and $M–O^-$, with M–O being the amphoteric metal oxide (Anderson and Malotky, 1979). The latter two forms lead to a charge of the mineral surface. The point of zero charge (pH_{PZC}) is the pH level at which positive ($M–OH_2^+$) and negative ($M–O^-$) charges on the mineral surface are balanced, resulting in a net zero charge (Koretsky, 2000). The pH_{PZC} is a mineral-specific property, depending on the protonation constants of the amphoteric metal oxide (Anderson and Malotky, 1979). Above the pH_{PZC}, H^+ concentration in the solution is low, favouring deprotonation of hydroxyl groups to MO^-, resulting in a net negative charge. Below the pH_{PZC}, the H^+ concentration is high, favouring protonation to $M–OH_2^+$ and resulting in a net positive charge (Anderson and Malotky, 1979).

Dissolved ions can bind to a surface site through outer- and inner-sphere complexes (Figure 1.2). Outer-sphere complexes are solely based on electrostatic interaction and relatively weak (Koretsky, 2000). Thereby, the hydration shell around the dissolved ion pertains, resulting water molecules between the surface site and dissolved ion (Figure 1.2). In inner-sphere complexes, the ion is directly bound to the surface site, without separating water molecules, through covalent or ionic bonds between the metal and the ligand (Figure 1.2, Koretsky, 2000). This results in a stronger bond compared to outer-sphere complexes.

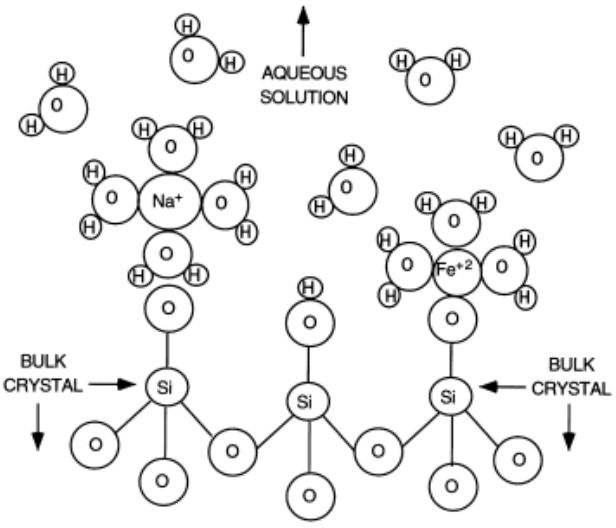

Figure 1.2: Illustration of outer-sphere (Na+) and inner-sphere (Fe2+) complex at Si oxide. Adapted from Koretsky (2000).

The binding of a dissolved ion to a mineral or other solid material is termed sorption in general. Adsorption describes the bonding of a dissolved ion through electrostatic or van der Waals forces or through chemical bonds in a monolayer to the mineral surface (Figure 1.3, Koretsky, 2000; Choi et al., 2001; Ford et al., 2001). Absorption describes the chemical binding of the ion inside the crystal framework of the sorbent (Figure 1.3, Koretsky, 2000). Additionally, ions

and complexes can precipitate or co-precipitate as a new solid phase on mineral surfaces (Limousin et al., 2007). Physisorption describes the binding process through physical forces, weak electrostatic and van der Waals forces, without direct chemical bonds (Choi et al., 2001). It is often the process behind non-specific adsorption and outer-sphere complexes (Koretsky, 2000). Chemisorption describes the sorption through strong ionic or covalent bonds, resulting in direct and specific binding and inner-sphere complexes (Koretsky, 2000). While chemisorption is constricted to a monolayer, physisorption can generate multi-layer sorption, depending on the concentration of the adsorbate (Choi et al., 2001).

In DLE and LMO research literature, the terminology of ‘adsorption’ and ‘absorption’ is not handled strictly. In most cases, the term ‘adsorption’ is used for the binding of Li, despite its intercalation into the crystal framework (Feng et al., 1992; Wu et al., 2025). In this work, the term sorption is used as an umbrella term for all sorption processes. The specified sorption terms are used if applicable.

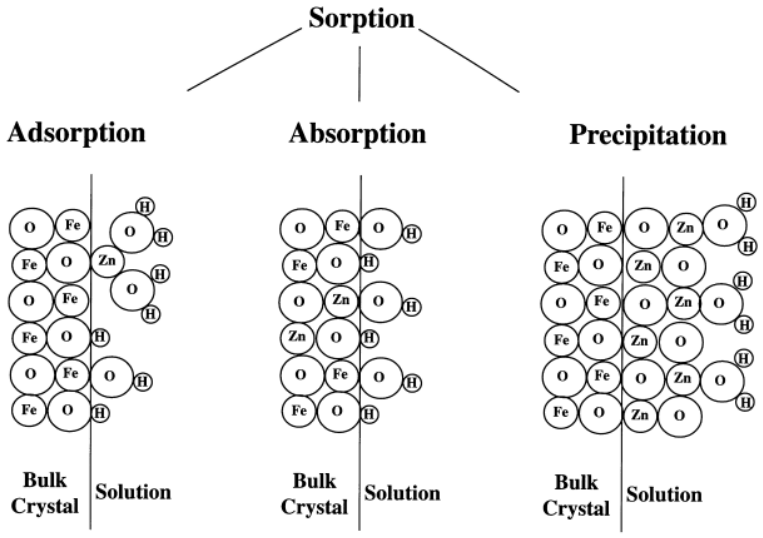

Figure 1.3: Schematic representation of sorption processes of Zn^{2+} to Fe oxide. Adapted from Koretsky (2000).

The transport of dissolved ions from the bulk solution to surface sites and into intra-particle sorption sites can be divided into several steps. In the first step, ions diffuse from the bulk of the solution to the liquid film surrounding the particle, termed bulk diffusion (Hu et al., 2024). In the following film diffusion, ions diffuse into and through the liquid film to the mineral-water interface (Qiu et al., 2009). Thereby, the diffusion rate positively correlates with the particle surface area and the concentration gradient between the film and the bulk (Qiu et al., 2009). If the particle contains fluid-filled pores, intra-particle or pore diffusion occurs, whereby ions diffuse into these from the exterior surface (Hu et al., 2024). This is followed by adsorption of the ion at the binding site through physi- or chemisorption. Once adsorbed at the particle surface, the ion can move into the crystal framework through vacancies, interstitials or atom exchange,

depending on the ion and its size (Choi et al., 2001). This is termed intra-crystalline diffusion. Bulk diffusion and adsorption can be regarded as very fast, while film, intra-particle and intra-crystalline diffusion can be the mass transport limiting processes (Choi et al., 2001; Qiu et al., 2009; Hu et al., 2024). In sorbent and IX research, intra-particle diffusion is often used as an umbrella term for intra-particle and intra-crystalline diffusion, if the exact diffusion process is not distinguished (e.g. Recepoğlu et al., 2017). This terminology is adopted in the present work as well.

2. Research objective

The objective of this research is the identification of a Li selective sorbent and the evaluation of its potential for DLE from geothermal brines. For this, requirements for geothermal DLE are identified from properties of geothermal brines and the operating conditions of geothermal power plants. Based on these, the suitability of state of the art DLE technologies is assessed and a promising sorbent identified. To evaluate the potential for geothermal DLE, detailed laboratory and pilot-scale investigations are conducted under geothermal conditions. Therefore, a pilot plant suitable for integration into a geothermal power plant is developed. For this purpose, a sub-objective is to define the requirements, design criteria, and operational characteristics of the pilot plant. To address the overall objective, the following additional sub-objectives are addressed using laboratory and pilot experiments:

- Assessment of the lithium sorption performance of the sorbent in Upper Rhine Graben brine
- Investigation of the selectivity of the sorbent toward both major and trace elements and to infer the associated binding behaviour
- Evaluation of the stability of sorption selectivity during repeated extraction cycles
- Identification of the origin and transport pathways of elements affecting the purity of the desorption solution

3. List of publications & contributions

This thesis combines published scientific articles (Chapters 4, 5, and 9), a manuscript article (Chapter 7), and two additional chapters (Chapters 6 and 8). The published articles and the manuscript contain a bibliography, while the literature used in the introduction, additional chapters and discussion are summarised in the general Bibliography. Appendices with all data used and further information is given at the end of each chapter. The contributions to each article and chapter are given below.

Chapter 4 - Publication

Reich, Rebekka; **Slunitschek, Klemens**; Danisi, Rosa Micaela; Eiche, Elisabeth; Kolb, Jochen, (2022): Lithium Extraction Techniques and the Application Potential of Different Sorbents for Lithium Recovery from Brines. In *Mineral Processing and Extractive Metallurgy Review*, pp. 1–20. DOI: 10.1080/08827508.2022.2047041.

In this review article about the suitability of current DLE technology for Li extraction from geothermal brines, I contributed to the conceptualisation, analysis and interpretation and drafting of the LMO section. Additionally, I contributed to the review and editing of the complete article.

Chapter 5 - Publication

Slunitschek, Klemens; Eiche, Elisabeth; Kolb, Jochen, (2025): Sorption of lithium and competing ions from geothermal brine to lithium manganese oxide sorbent and implication for industrial use. In *Separation and Purification Technology* 378(3), 134594.
DOI: 10.1016/j.seppur.2025.134594.

For this article about the sorption of Li and competing elements from geothermal brines and the implications for industrial application, I developed the scientific ideas in collaboration with Elisabeth Eiche and Jochen Kolb. I conceptualised the synthesis and the experiments, defined required components and developed these together with Kevin Altinger, head of KIT-AGW workshop. I conducted the experiments and analyses, curated, analysed and interpreted the data, conceptualised, drafted and edited the article. Jochen Kolb und Elisabeth Eiche contributed to data analysis and interpretation, conceptualisation of the article and reviewed it.

Chapter 6 – Selectivity stability during cyclic extraction

In this chapter repeated, consecutive Li extraction cycles in higher number were executed to investigate the sorption of Li and competing elements over time. To conduct this, I conceptualised and developed an automated test bench, identified needed requirements and properties

and suitable materials and designed various components. Ralf Wachter, technician at the KIT-AGW, Chair Geochemistry & Economic Geology, supported the concept development and constructed and programmed the test bench. Kevin Altinger supported the concept development and manufacturing of components. I planned and conducted the experiments, supported by Janine Wagner, Maya Denker, Chantal Kotschenreuther and Nadine Hüll, laboratory technicians at KIT-AGW – Chair Geochemistry & Economic Geology, in the preparation of solutions, filtration of samples and analyses. The XPS analysis and data curation were conducted at the Institute of Applied Materials – Energy Storage Systems, Group Surface & Interface Analysis of the Karlsruhe Institute of Technology by Vanessa Trouillet. In addition, Vanessa Trouillet contributed the XPS section of the methodology. Analysis and interpretation of XPS data were conducted by me with support from Vanessa Trouillet. All other data curation, analysis, interpretation and drafting and editing of the chapter were done by me.

Chapter 7 – Manuscript

Slunitschek, Klemens; Reich, Rebekka; Hettkamp, Thomas; Kaymakci, Elif; Altinger, Kevin; Eiche, Elisabeth; Kluge, Tobias; Kolb, Jochen: Requirements and design of a pilot plant for the on-site investigation of Direct Lithium Extraction (DLE) from pressurised geothermal brines

In this manuscript, the construction and first functioning tests of a pilot plant for DLE research in a geothermal power plant are presented, summarising the development process of the pilot plant from idea to first tests. The manuscript is intended to be published in shared first authorship of myself and Rebekka Reich. The basic concept of the pilot and its functionality and properties was mostly developed by me. Rebekka Reich, Thomas Hettkamp (company Bestec) and Elif Kaymakci (company EnBW) contributed to some extent. Conceptualisation of the programming was done by me and Thomas Hettkamp. For technical planning and procurement of components, me, Thomas Hettkamp and Kevin Altinger were in charge, strongly supported by Rebekka Reich. Manufacturing of components was primarily conducted by Kevin Altinger. On-site construction was led by Kevin Atlinger and Thomas Hettkamp with support by me, Rebekka Reich and Elif Kaymakci. For the production of the sorbent used for the functioning tests and in Chapter 8 and Chapter 9 - Kölbel et al. (2024b), synthesis were conducted by me with support from Janine Wagner and Maya Denker. Functioning experiments were conceptualised, designed and planned by me, reviewed by Elisabeth Eiche and Jochen Kolb. Experiment conduction was led by me with support from Thomas Hettkamp, Elif Kaymakci and Rebekka Reich. Samples were analysed by me with support from Chantal Kotschenreuther. Data curation, analysis and interpretation were done by me. The concept and structure of the article was developed by Rebekka Reich and me and Jochen Kolb to similar extents, with contributions from Tobias Kluge and Elisabeth Eiche. The manuscript was drafted and edited by

Rebekka Reich and me, with Rebekka Reich contributing more extensively. The manuscript was reviewed by all authors.

Chapter 8 – On-site investigation of DLE performance from pressurised geothermal brine

In this chapter, DLE with LMO under natural conditions in the geothermal power plant is investigated. The experiments in the pilot plant were conceptualised, designed and planned by me, reviewed by Elisabeth Eiche and Jochen Kolb. Conduct was led by me, with support from Thomas Hettkamp, Rebekka Reich and Elif Kaymakci. Post-treatment of the sorbent was primarily conducted by Janine Wagner. Analyses were conducted by me, Chantal Kotschenreuther and Maya Denker. Data curation, analyses, interpretation and drafting and editing of the chapter were done by me. Jochen Kolb and Elisabeth Eiche contributed by reviewing data interpretation.

Chapter 9 – Publication

Kölbel, Lena; **Slunitschek, Klemens**; Kaymakci, Elif; Kölbel, Thomas; Reich, Rebekka; Schneider, Jochen, (2024): Lithium recovery from geothermal brines: An investigation into radioactive nuclide uptake on lithium-manganese-oxide (LMO) granules. In *Hydrometallurgy* 224, 106266. DOI: 10.1016/j.hydromet.2024.106266.

In this publication, the extraction of radionuclides by LMO in the geothermal power plant is presented. For this, the experiments from chapters 7 and 8 are used. Aside from leading the experiment conduction, I contributed to data evaluation regarding the sorption and desorption performance. Furthermore, I contributed to drafting and reviewing the article.

Non-scientific publications and science communication

The study “Lithium in Europa”, published by the THINKTANK für Industrielle Ressourcenstrategien, Karlsruhe in 2022 (Steiger et al., 2022), summarises the global Li production and mining technologies. Furthermore, it discusses several mining projects within Europe. I contributed to the chapters 4 (Lithium aus konventionellen Ressourcen in Europa) and chapters 5 (Lithium aus unkonventionellen Ressourcen in Europa).

Lithium production from geothermal and especially german resources gained a wide popularity, resulting in numerous articles, interviews, and radio and television contributions, amongst others in RAI3, Deutschlandfunk Nova, Rheinpfalz, SWR, GIT Laborfachzeitschrift, Verkehrsrundschau, greenpeace magazine.

4. Publication

–

Lithium Extraction Techniques and the Application Potential of Different Sorbents for Lithium Recovery from Brines

Rebekka Reich, Klemens Slunitschek, Rosa Micaela Danisi, Elisabeth Eiche & Jochen Kolb

This work has been published in Mineral Processing and Extractive Metallurgy Review (44, 4)

published online: 08 Mar 2022

available online:

https://www.tandfonline.com/doi/full/10.1080/08827508.2022.2047041

DOI: 10.1080/08827508.2022.2047041

MINERAL PROCESSING AND EXTRACTIVE METALLURGY REVIEW
https://doi.org/10.1080/08827508.2022.2047041

Taylor & Francis
Taylor & Francis Group

Lithium Extraction Techniques and the Application Potential of Different Sorbents for Lithium Recovery from Brines

Rebekka Reich[a], Klemens Slunitschek[a], Rosa Micaela Danisi[b], Elisabeth Eiche[a], and Jochen Kolb[a]

[a]Chair of Geochemistry and Economic Geology, Institute of Applied Geosciences, Karlsruhe Institute of Technology, Karlsruhe, Germany; [b]Chair of Technical Petrophysics, Institute of Applied Geosciences, Karlsruhe Institute of Technology, Karlsruhe, Germany

ABSTRACT

Geothermal power plants produce large amounts of high-temperature fluids from variable depths. These fluids can be enriched in lithium to up to 240 mg/L, rendering them an exploitable resource, not yet processed at industrial scale. The pressure on Li demand is expected to increase in the future, making the technical degradability of new Li resources indispensable. We examine Li-extraction methods from aqueous solutions systematically, dealing with evaporation, direct precipitation, membrane-related processes, solvent extraction, sorption, and ion exchange. Sorption and ion-exchange techniques are regarded to be the most promising methods with a high potential for the feasible lithium extraction. Therefore, Li sorption on different inorganic sorbents, in particular for the implementation into operating geothermal power plants, is evaluated. Inorganic sorbents, such as lithium–manganese oxide, titanium oxide, aluminum hydroxide, iron phosphate, clay minerals, and zeolite group minerals besides other sorbents, e.g. zirconium phosphate, tin antimonate, antimony oxide, tantalum oxide, and niobium oxide, are regarded. Promising inorganic sorbents for an environmentally friendly, efficient, and selective Li extraction are lithium–manganese oxide, iron phosphate, or zeolite. To evaluate the effectiveness of these sorbents to large-scale industrial Li_2CO_3 (or LiOH) production, we highlight their potential advantages and disadvantages in the application under geothermal operating conditions.

KEYWORDS

Sorption; ion-exchange; inorganic sorbents; geothermal; direct lithium extraction (DLE)

Introduction

Lithium is an important component in several industrial applications and is used in lithium–ion batteries (LIBs), ceramics, glass, cement, special alloys, lubricants, air conditioners, polymers, chemicals, and nuclear power plant industry as well as psycho-medical pharmacy (Gruber et al. 2011; Kudryavtsev 2016; Meng et al. 2021; Nie et al. 2017; Peerawattuk and Bobicki 2018; Swain 2017). It is lithophile, the lightest solid alkali earth element and highly mobile in fluidal systems due to its incompatibility in most silicates (Benson et al. 2017; Gruber et al. 2011; Mohr, Mudd and Giurco 2012). It mainly occurs as monovalent cation in solution and is characterized by a small dehydrated and hydrated ionic radius of 0.6 and 3.4 Å, respectively (Helmke and Sparks 1996). Its small ionic radius is similar to that of Mg^{2+} and Na^{+} (0.72 and 1.02 Å, respectively), which makes Li separation from these elements in solution difficult (e.g. Song et al. 2017; Wei et al. 2020). Lithium occurs in several species, e.g. $Li^{+}_{(aq)}$, $LiOH_{(aq,s)}$, $Li_{(s)}$, $LiH_{(s)}$, $LiSO_4^{-}$, $Li_2O_{(s)}$ and $Li_2O_{2(s)}$ (Blanc et al. 2012; Takeno 2005) and the oxygen coordination of Li is mostly tetrahedral or distorted octahedral (Tadesse et al. 2019; Wenger and Armbruster 1991). The dominant Li species in aqueous solutions is Li^{+}, which is assumed to occur in four-fold $[Li(H_2O)_4]^{+}$ clusters at T = 25–100°C, P = 1 bar, pH < 13.5, Eh = −0.8–1.2 V, total dissolved solids (TDS) = 100 g/L (Blanc et al. 2012; Bowell et al. 2020; Sanjuan et al. 2016; Sverjensky, Shock and Helgeson 1997; Takeno 2005; Wunder et al. 2007).

Major Li deposits are igneous rocks, sedimentary rocks, and brines comprising 25–35%, 8–13%, and 52–66% of the world's Li resources in 2019, respectively (Figure 1; Gruber et al. 2011; Mohr, Mudd and Giurco 2012; Sykes 2019). Ambrose and Kendall (2020a) estimate the total global Li resource at 55–99 Mt Li. Bolivia, Argentina, Chile, USA, and Australia have the largest resources world-wide, owning 21 Mt, 19.3 Mt, 9.6 Mt, 7.9 Mt, and 6.4 Mt Li, respectively (Figure 1; Schmidt 2017; US Geological Survey 2021). Currently, the world's major Li producers are Australia, Chile, Argentina, and China (Schmidt 2017; US Geological Survey 2021). An additional theoretical resource is seawater, comprising 230 Gt Li (Fasel and Tran 2005).

The future demand of Li is expected to grow rapidly. The global annual Li demand is estimated to increase by factors of 27–37 from 32,000 t annual production in 2012 to 850,000 – 1,200,000 t Li in 2050 (Xu et al. 2020; Ziemann et al. 2018). Considering 90% recycling rate and an increase in the annual gross domestic product of 2–3%, 12–20 Mt Li would be required globally between 2010 and 2100 (Gruber et al. 2011). However, recycling is not expected to significantly reduce the global Li demand by 2050 since most recycling technologies are currently under investigation only at lab-scale (Ambrose and Kendall 2020a; Asadi Dalini et al. 2021; Moazzam et al. 2021; Xu et al. 2020). It remains uncertain whether recycling can reduce the demand for battery-grade Li since current recycling technologies produce Li with insufficient purity (e.g. Qiao et al. 2021; Ziemann et al. 2018).

CONTACT Rebekka Reich rebekka.reich@kit.edu Chair of Geochemistry and Economic Geology, Institute of Applied Geosciences, Karlsruhe Institute of Technology, Campus Süd, Adenauerring 20b, Gebäude 50.40, Karlsruhe 76131, Germany

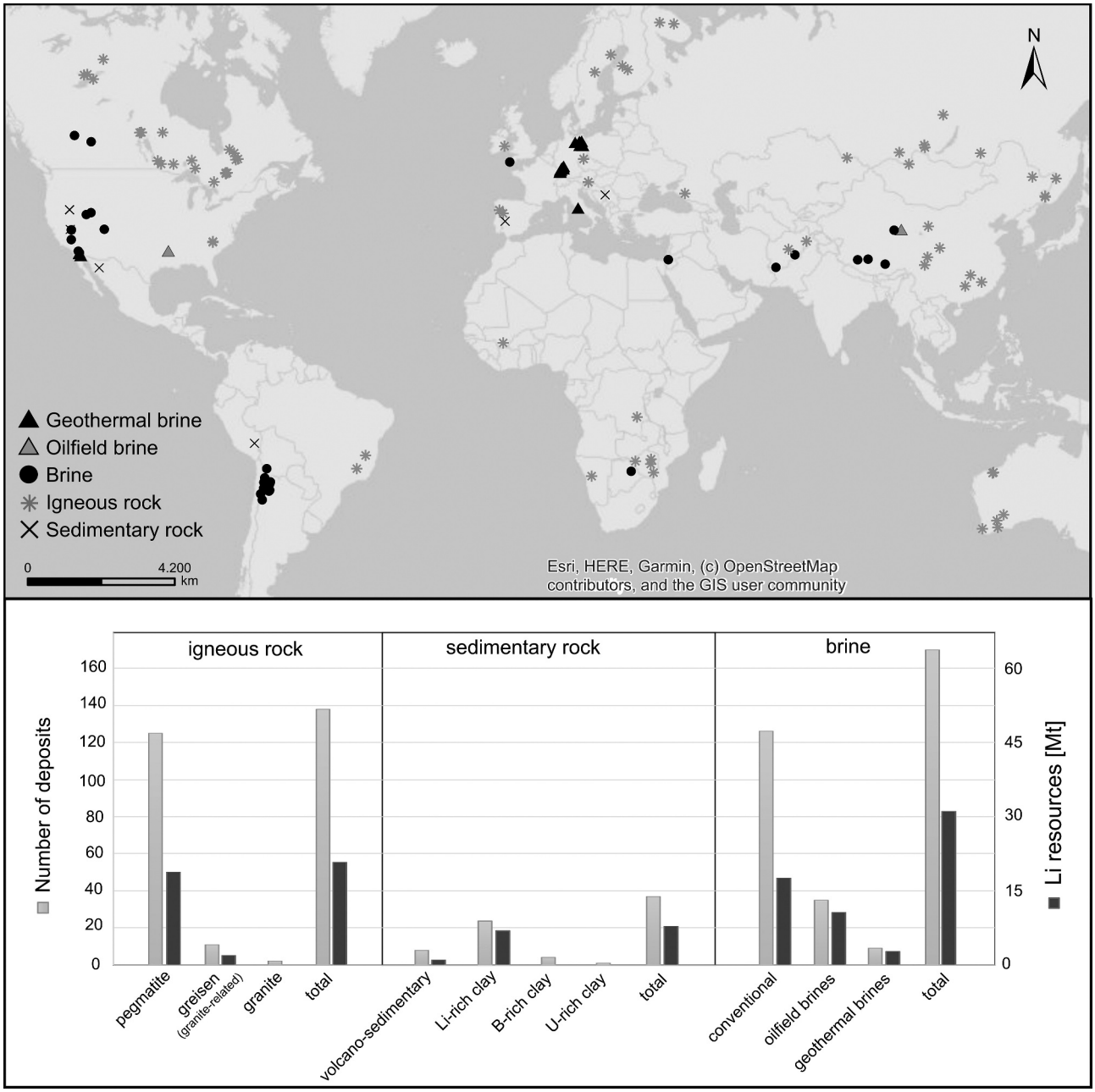

Figure 1. Global Li deposits and resource distribution between different deposit types. Data from Pauwels et al. (1993), Houston (2010), Savannah Resources Plc (2010-2021), Kesler et al. (2012), Schmidt (2017), Sykes (2019), The Mineral Corporation (2019), Bowell et al. (2020), Bundesanstalt für Geowissenschaften and Rohstoffe (2020), Rio Tinto (2020), Mining Data Online (2021). Basemap from ArcGIS (2020).

With the resources currently available, the demand can be met, but new methods for Li extraction from aqueous solutions will become more important in the future (Kawamoto and Tamaki 2011; Liu et al. 2014; Peerawattuk and Bobicki 2018; Yaksic and Tilton 2009). An alternative source may be geothermal brines. The geochemistry of the brines is variable (Table 1) and differs between the various localities, but can also change over time at one location, reflecting water–rock interaction processes. Lithium-bearing, conventionally mined brines and typical geothermal brines are similarly characterized by TDS ~100–330 g/L, slightly acidic to slightly alkaline pH and high concentrations of major cations (e.g. 47–135 g/L Na^+, 2–27 g/L K^+) and anions (e.g. 50–190 g/L Cl^-, 1.5–470 g/L SO_4^{2-}) (Table 1; Pauwels, Brach and Fouillac 1993, Aquilina et al. 1997, Pueyo, Chong and Ayora 2017, Reidel and Ehren 2018, Garcia et al. 2020). Lithium concentrations in most brines vary between 20 and 1750 mg/L (Table 1), which is considerably higher than Li concentrations in Earth's major lakes, oceans (0.17 mg/L Li^+) and freshwater (Ambrose and Kendall 2020a; Dodbiba et al. 2014; Hoyer, Kummer and Merkel 2015; Kudryavtsev 2016; Meng et al. 2021). Besides geothermal brines, oilfield brines, which are similar to geothermal brines regarding temperature, pressure, and flow rate, are reported to comprise Li and can significantly increase the global Li resources (e.g. 750,000 t Li in the Smackover Formation, USA) (Collins and Vine 1976; Evans 2008). However, reliable resource estimations for brine systems are complicated since climatic effects, precipitation of salts with time and fluid flux have to be taken into consideration (Border and Sawyer 2014).

Table 1. Comparison of chemical composition and average pH values in geothermal brines (Germany), conventionally mined brines and common fluids, sediments, soils, and Earth's crust.

	Li^+[mg/L]	Na^+[g/L]	K^+[g/L]	Ca^{2+} [g/L]	Mg^{2+} [g/L]	Cl^- [g/L]	SO_4^{2-} [g/L]	TDS [g/L]	pH
Geothermal brines	150–240	60–135	4–27	1–16	2–17	120–180	1.5–62	100–300	~5
Conventionally mined brines	18–1750	47–110	2–25	0.02–36	0.030–34	50–190	3.5–470	170–330	~8
Earth's major lakes and oceans	0.1–14	30	5	15	30	160	0.5	0.5–30	~8
Freshwater	0.0007–0.04	0.005–0.013	0.0002–0.0008	0.0008–0.009	0.0005–0.002	0.007–0.024	0.003–0.008	<0.5	6–7
Seawater	0.17	10	0.4	0.4	1	20	3	30–40	~8
	Li [mg/kg]	Na [g/kg]	K [g/kg]	Ca [g/kg]	Mg [g/kg]	Cl [g/kg]	S [g/kg]		
Sediment	56	4–12	4–12	7–54	9–18	-	-	-	6–7.5
Soil	3–350	0.001–7	0.0007–10	0.001–10	0.00005–6	0.001–0.1	0.001–0.5	-	4–11
Earth's crust	20–60	12–25	12–30	25–50	15–30	0.3–0.6	9–20	-	-

Data from Banks (1953), Gorham (1956), Morcos (1970), Butterman (1988), Bukowsky and Uhlemann (1993), Condie (1993), Wedepohl (1995), Bohn, Myer and O'Connor (2002), Banks et al. (2004), Zhu et al. (2006), Blackford and Gilbert (2007), Ferreira et al. (2007), Aral and Vecchio-Sadus (2008), McCauley, Jones and Jacobsen (2009), Marion et al. (2011), An et al. (2012), Dodbiba et al. (2014), Hoyer, Kummer and Merkel (2015), Choubey et al. (2017), Flexer, Baspineiro and Galli (2018), Moran (2018), Mimura et al. (2019)

Direct Li extraction (DLE) from geothermal brines is accompanied by major challenges. The process has to be stable in order to resist high pressure (~20 bars), high temperature (~60–80°C), and needs to operate at specific pH due to the danger of scaling at high pH, depending on the solubility of the respective mineral phase (Haklıdır and Balaban 2019). As the flow rate in geothermal power plants is continuously high with up to 90 L/s (Stober and Bucher 2012), fast extraction kinetics are needed. Due to the high TDS of up to 300 g/L (Table 1), the DLE must have a high Li selectivity to prevent extraction of undesired components and thus, reduce purification efforts in previous or following processing steps. Additionally, a high Li recovery rate is needed to minimize Li reinjection into the ground and to increase the efficiency of the DLE process (Warren 2021).

Review articles about different Li extraction methods from minerals (e.g. Cisternas et al. 2021; Gourcerol et al. 2019; Salakjani, Singh and Nikoloski 2021; Tadesse et al. 2019), aqueous solutions (e.g. Meng et al. 2021; Meshram and Pandey 2018; Stringfellow and Dobson 2021; Swain 2016; Zhang et al. 2019) and different sorbents are available (e.g. Choubey et al. 2017, 2016; Safari, Lottermoser and Alessi 2020). However, sparse work has been done in specifically addressing the technical challenges and practicability of Li recovery from geothermal brines. Therefore, this article aims at examining the potential application of different extraction techniques for future implementation into geothermal power plants.

Extraction techniques for brines

Evaporation

Evaporation is one of the most popular techniques for Li recovery from salt lake brines and is also considered for seawater (e.g. An et al. 2012; Epstein et al. 1981). The liquid is pumped into large evaporation ponds where the concentration of Li and other dissolved elements becomes relatively enriched during evaporation (Figure 2)). With increasing concentration, precipitation of less soluble salts, e.g. halite (NaCl), gypsum ($CaSO_4 \cdot 2\ H_2O$), carbonates ($(Ca, Mg, Fe)CO_3$), carnallite ($KCl{\cdot}MgCl_2 \cdot 6H_2O$), or bischofite ($MgCl_2 \cdot 6H_2O$) at ~4.4 wt.% Li proceeds (Figure 2); An et al. 2012; Ventura et al. 2016). Lithium concentration is increased to ~6 wt.% before further processing (Peerawattuk and Bobicki 2018). Ions such as Mg^{2+}, Ca^{2+}, and BO_3^{3-} are removed by addition of precipitants to increase the purity of Li-concentrates (An et al. 2012; Peerawattuk and Bobicki 2018). Finally, the addition of Na_2CO_3 induces precipitation of Li_2CO_3 at high purity (99.5–99.9% Li_2CO_3) (An et al. 2012; Peerawattuk and Bobicki 2018).

Due to Li-carnallite precipitation, Li recovery only reaches ~50–80% (Table 2; An et al. 2012, Ventura et al. 2016). This effect is minimized by attentive control of the evaporated volume, since Li recovery is increased by ~50%, with the Li concentration not exceeding 1500 mg/L and the solution level in the ponds kept above 0.32 m (Valdez, Flores and Orce 2016). Lithium recovery is additionally dependent on the brine chemistry: Li_2SO_4 precipitation occurs after 31 days of evaporation at the Salar de Uyuni, whereas Li is progressively enriched in the Salar de Atacama due to preferred Na and K precipitation (Ogawa et al. 2014).

Evaporation is simple and cheap, with total production costs of 2,000–5,700 US$/t lithium carbonate equivalent (LCE) (Ambrose and Kendall 2020a; Gaikwad, Misal and Gupta 2011). The evaporation process, however, is time consuming (i.e. several months or years) and only works in areas where the ponds are exposed to the sun with high evaporation and low precipitation rates (Gaikwad, Misal and Gupta 2011; Safari, Lottermoser and Alessi 2020; Wiśniewska et al. 2018). Significant amounts of freshwater (5–50 m^3 freshwater/t LCE) are consumed, which is of concern regarding the aridity of most areas with processing facilities (Flexer, Baspineiro and Galli 2018) and large areas for the evaporation ponds (80.53 km^2 in the Salar the Atacama in 2017, Liu, Agusdinata and Myint (2019d)) are needed. Scientific studies concerning the environmental effects of water consumption and land-use change for Li extraction are sparse (Flexer, Baspineiro and Galli 2018; Kaunda 2020; Kelly et al. 2021; Marazuela et al. 2020). Evaporation can be optimized by manual induction of energy, rendering the method more efficient although higher energy consumption increases the environmental impact and the cost (Gaikwad, Misal and Gupta 2011). Although suitable

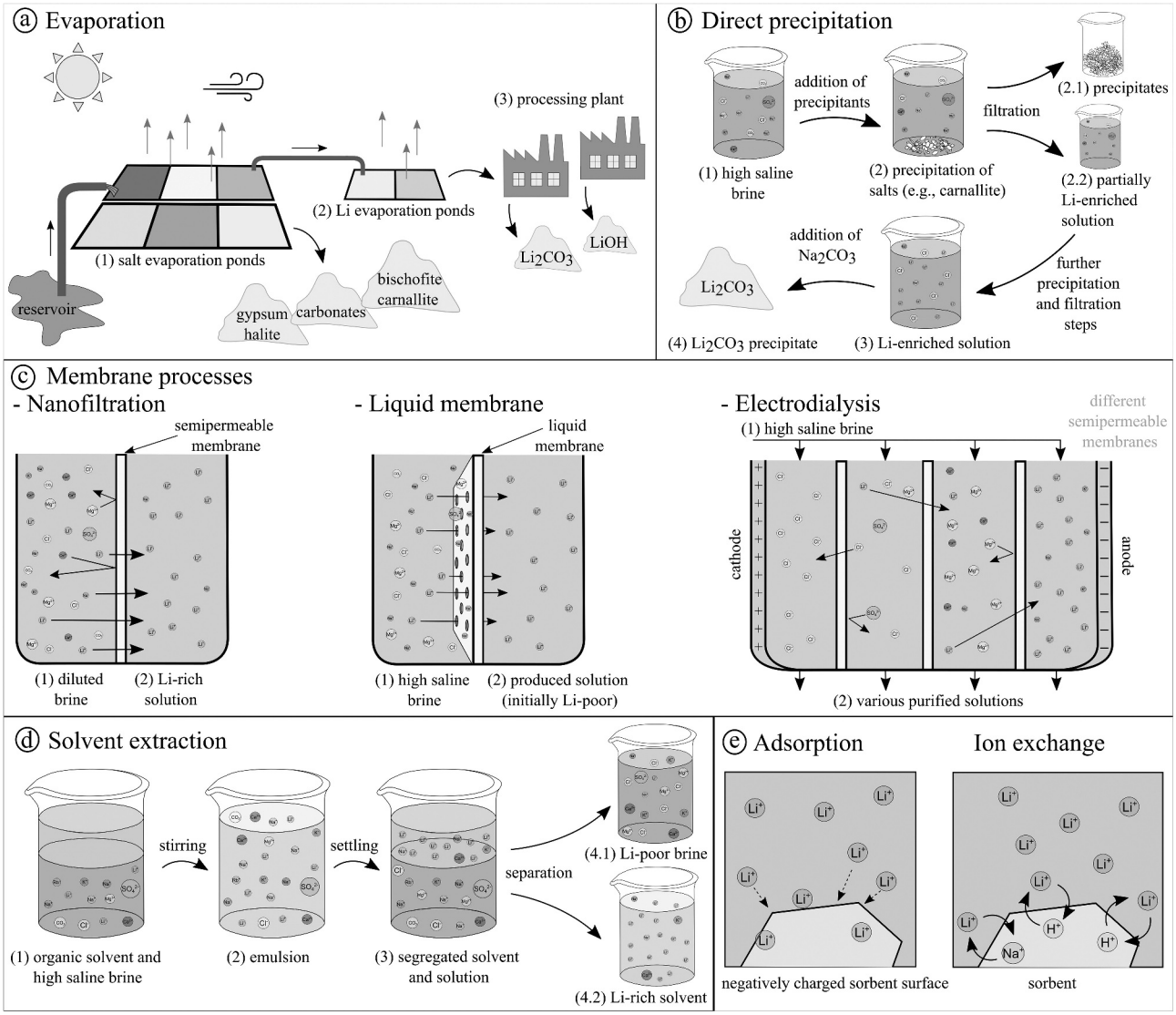

Figure 2. Sketch of different extraction technologies for Li from aqueous solutions. (a) Evaporation process of conventionally mined brines in Bolivia, Chile and Argentina; (b) Direct precipitation from brines including the precipitation of e.g. carnallite and optional further purification steps prior to Li precipitation; (c) Different membrane processes, e.g. nanofiltration (selectivity based on ion charge), liquid membrane (selectivity based on ionic radius and complexation) and electrodialysis (combination of electric current and different semipermeable membranes); (d) Solvent extraction using organic solvents for Li extraction; and (e) Adsorption, where a negatively charged surface causes van der Waals bonding with a positively charged Li ion and Ion exchange, where Li ions substitute monovalent cations in the sorbent.

for Li processing from salars, evaporation for processing geothermal brines is not generally applicable globally because of long evaporation times needed, the land use of evaporation ponds, and the required climatic conditions (Flexer, Baspineiro and Galli 2018; Gaikwad, Misal and Gupta 2011; Liu, Agusdinata and Myint 2019d).

Direct precipitation

Direct extraction by precipitation is based on the formation of chemical compounds by reducing the solubility of dissolved species. Precipitation is influenced by variation in pH, temperature, redox, impurities, and concentration of precipitant (Figure 2); Zhang et al. 2019). For natural brine systems, numerous precipitation methods exist, e.g. carbonate and aluminate precipitation, and borate and phosphate co-precipitation (Zhang et al. 2019). The method used depends on the specific brine composition, especially on the Mg/Li ratio, as Mg and Li have similar ionic properties and are therefore difficult to separate (Table 2; Nie et al. 2017). With increasing Mg/Li ratio, Mg has to be pre-precipitated to recover Li (Figure 2)). Thereby, 20–30% of the Li are lost (Zhang et al. 2019), presumably due to Li-carnallite precipitation (An et al. 2012). By-products and interfering elements (e.g. B, Mg, Fe, Ca) are precipitated by addition of different reagents (e.g. CaO, NaOH, $C_2H_2O_4$, $AlCl_3{\cdot}H_2O$) prior to the extraction of the desired element (Table 2; An et al. 2012, Zhang et al. 2019, Ambrose and Kendall 2020a). At the last stage, Li_2CO_3 precipitation is induced by Na_2CO_3 addition (Figure 2); Zhang et al. 2019). To increase the Li recovery to up to 98–99%, aluminum salts (i.e. $NaAlO_2$ or $AlCl_3$) are the most suitable co-precipitants for Li at pH of 10–13 (Table 2; Yoshinaga, Kawano and Imoto 1986). Precipitation of solutes from geothermal brines is currently investigated in pilot-scale projects (Borrmann, Schweig and Johnston 2019; Goldberg et al.

Table 2. Overview of commonly used and recently studied lithium extraction methods.

Method	Time	Technical effort	Industrial scale	Energy consumption	CO_2	Applicable to (medium)	Resources [Mt Li]*	Chemicals/ hazards	Li recovery [%]	Cost	Source
Evaporation	+	-	Yes	-	o	Brine	31–67	NaOH, $C_2H_2O_4$, $AlCl_3{\cdot}H_2O$, CaO, $NaAlO_2$, Na_2CO_3	~50–80	o	Gaikwad, Misal and Gupta (2011), Ambrose and Kendall (2020a), Kelly et al. (2021)
Precipitation	-	-	Yes	-	o	(Low Mg/Li-) brine	31–38	Seawater evaporation	98–99	o	Yoshinaga, Kawano and Imoto (1986), Liu et al. (2017), Nie et al. (2017), Zhang et al. (2019), Ambrose and Kendall (2020a), Ambrose and Kendall (2020b), Kelly et al. (2021)
Membrane processes	o	-	Pilot	-	-	Seawater, (low-Mg -B/"low"-Na) brine, LIBs	230,000 + 31–38 + ?	Organic membrane	5–22	o	Li et al. (1983), Sakamoto, Kimura and Shono (1987), Fasel and Tran (2005), Wen et al. (2006), Hoshino (2013), Somrani, Hamzaoui and Pontie (2013), Melnikov et al. (2017), Ambrose and Kendall (2020a)
Solvent extraction	o	o	Pilot	-	-	Brine, seawater, LIBs	31–67 + 230,000 + ?	TBP, TOPO, TTA, HDBM, kerosene/ methyl isobutyl ketone, isoamyl alcohol, 2-Ethyl-1,3-hexanediol, diisopropyl ether, diethyl ether, $FeCl_4^-$, ClO_4^-, $B(C_6H_5)_4^-$, acidic wastewater	65–96	-	Epstein et al. (1981), Bukowsky and Uhlemann (1993), Nan, Han and Zuo (2005), Kawamoto and Tamaki (2011), Harvianto, Kim and Ju (2016), Xiang et al. (2016), Liu et al. (2017), Shi et al. (2017), Ambrose and Kendall (2020a), Millennial Lithium Corp (2020), Warren (2021)
Sorption and ion exchange	-	o	Pilot	-	-	Brine, LIBs	31–67 + ?	Desorption/ leaching solution (see Table 3)	95	-	Pauwels, Brach and Fouillac (1990), Tian, Ma and Han (2010), Ambrose and Kendall (2020a)

- Minor/less.
o Neutral/none/average.
+ Yes/high/much.
? No literature data.
* Estimated resource to which the method is applicable.

Table 3. Overview of different mineral sorbents studied for selective Li-extraction from geothermal brines.

Sorbent	t_{Equ}	Ideal pH	Ideal temperature [°C]	Type of sorption	Q_{max} [mg/ g]	Chemicals/ hazards	Industrial scale	Source
Mn-oxides	24 h	Alkaline	>30	$H^+ \leftrightarrow Li^+$ ion exchange	53.5	HCl, HNO_3	Pilot	Wang et al. (2008), Tian, Ma and Han (2010), Xiao et al. (2012), Liu et al. (2015), Bajestani, Moheb and Masigol (2019), Qian et al. (2019), Ventura et al. (2020), Warren (2021)
Ti-oxides	10–192 h	Alkaline	60	$H^+ \leftrightarrow Li^+$ ion exchange	94.5	HCl, HNO_3	Pilot	Chitrakar and Abe (1988), Shi et al. (2013), Moazeni et al. (2015), Lawagon et al. (2016), Wang et al. (2016), Wei et al. (2020), Li et al. (2021), Marthi et al. (2021)
Al-hydroxides	5 min–24 h	7–9	30–80	Physisorption & $H^+ \leftrightarrow Li^+$ ion exchange	123.5	CH_3COONH_4, H_2SO_4, HF	Pilot	Pauwels, Brach and Fouillac (1990), Hawash, Abd El Kader and El Diwani (2010), Prodromou (2016), Heidari and Momeni (2017), Fukuda (2019)
Fe-oxy-hydroxides	?	Alkaline	?	Physisorption & $H^+ \leftrightarrow Li^+$ ion exchange	3.5	?	No	Nielsen et al. (2005), Kim, Nielsen and Grey (2008), Heidary, Khodabakhshi and Kharat (2016)
$FePO_4$	1.5–3 h	7	25–65	$Na^+ \leftrightarrow Li^+$ ion exchange/redox reaction	46.4	$K_2S_2O_8$, NaCl	No	Intaranont et al. (2014), Fukuda (2019), Liu et al. (2019c), Sun et al. (2020)
Clay minerals	?	Alkaline?	<50	Physisorption & $H^+ \leftrightarrow Li^+$ ion exchange	0.9	$Ca(CH_3COO)_2$	No	Greene-Kelly (1955), Eckstein, Yaalon and Yariv (1970), Gaskova and Bukaty (2008), Meroufel et al. (2013)
Zeolites	15–30 min	Alkaline	40– ?	$Na^+ \leftrightarrow Li^+$ ion exchange	25.0	HCl	No	Navarrete-Casas et al. (2007), Lemaire et al. (2014), Wiśniewska et al. (2018)

? No literature data.

2021) and thus needs more research and development for upscaling. The major challenge in applying direct precipitation is related to the complexity of controlling coprecipitation effects to maximize the Li recovery rate.

Membrane processes

Selective extraction using membranes gains increasing interest for Li extraction from brines (Somrani, Hamzaoui and Pontie 2013; Song et al. 2017). Membrane processes, also referred to as reverse osmosis, include the technologies of nanofiltration, liquid-membrane, and electrodialysis (Gaikwad, Misal and Gupta 2011; Wiśniewska et al. 2018). The membranes are selective for Li rather than other ions due to differences in ion charge, ionic radius or diffusive properties (Sun et al. 2015).

Nanofiltration describes ion filtration through membranes with different selectivity for mono- and divalent ions (Figure 2)), which is often also called "near reverse osmosis" or "near ultrafiltration" (Gaikwad, Misal and Gupta 2011; Van der Bruggen 2013). The membranes can be made of polymers, ceramics, or polymeric-ceramic combinations (Van der Bruggen 2013). To reduce the osmotic pressure on the membranes prior to the separation of monovalent Li^+ from divalent ions, such as Mg^{2+} or Ca^{2+}, the brine must be diluted (Figure 2); Somrani, Hamzaoui and Pontie 2013; Song et al. 2017; Sun et al. 2015; Wen et al. 2006). Furthermore, Sun et al. (2015) found that an increase in temperature to >18–20°C negatively affects the selectivity of the membrane due to an increased osmotic pressure, decreasing viscosity of the solution and a change in the membrane pore size. Wen et al. (2006) and Somrani, Hamzaoui and Pontie (2013) show that nanofiltration is not applicable for Li separation of high Mg- and B-brines and it also fails to separate Li^+ from Na^+ (Figure 2)).

Liquid membranes separate a large volume of Li-rich solution from a smaller volume of Li-poor solution. Lithium is thereby efficiently transported against the osmotic gradient from the Li-rich into the Li-poor solution (Figure 2); Sakamoto, Kimura and Shono 1987). Most liquid membranes reported in literature are organic compounds, e.g. nitrophenols, polyether amide derivatives, or crown ether derivatives (Sakamoto, Kimura and Shono 1987; Warnock et al. 2021). High selectivity for Li^+ compared to Na^+ in a chloride matrix was found since Na^+ dehydrates more easily than Li^+ forming complexes with the studied membrane (Figure 2)). Hoshino (2013) coupled an organic liquid membrane with electrodialysis to selectively recover Li^+ over Na^+ from seawater with Li recoveries between only 5–22% (Table 2).

Electrodialysis is based on different diffusion rates for monovalent and divalent cations in an electric current (Figure 2)). For electrodialysis application, a cathode, an anode, and an electrolyte medium are needed (Figure 2); Peerawattuk and Bobicki 2018). The electric current applied induces redox reactions in the electrodes by incorporation of Li^+ where the anode recovers Li from the aqueous solution, which is very similar to electrolysis (Song et al. 2017). However, semipermeable membranes are used in electrodialysis to successively separate the ions and thereby purify the recovered solution (Figure 2); Melnikov et al. 2017). For cathodes and anodes, different materials are used, e.g. $FePO_4/LiFePO_4$, $Ag/Na_2S_2O_3$ and λ-MnO_2/Ag (Peerawattuk and Bobicki 2018; Song et al. 2017). Due to their high salinities, brines or spent LIBs can be used as the electrolyte and the Li source. Also, brines with complex chemical composition, e.g. those with high Mg/Li ratios can be treated, as Li and Mg are separated by the semipermeable membrane (Figure 2); Song et al. 2017). The presence of sulfate ions improves Li recovery (Nie et al. 2017). The voltage has to be carefully controlled, as deposition of contaminants, e.g. Na^+, Mg^{2+}, on the electrodes may be caused (Zhao et al. 2013).

Operational costs for membrane processing of Li from brines are estimated at ~3.000 $/t LCE (Song et al. 2017; Warren 2021). Direct lithium extraction techniques based on membrane processes combined with organic ion-exchange resins are already tested at pilot scale (Melnikov et al. 2017). Reaction times of 8 h were applied for 77 cycles over a total test time of 770 h (Melnikov et al. 2017). This is however much longer compared to ~10 min for >85% extraction of Cu (Li et al. 1983; Melnikov et al. 2017). Membrane processes are easy to control and require little energy because only low electrical currents of 1–18 V are applied (Song et al. 2017). The main problem by applying Li selective membranes is that poorly soluble phases, e.g. $CaSO_4$, become enriched in the brine (Gaikwad, Misal and Gupta 2011). The application of membrane technologies for processing Li from geothermal brines is challenging because cooling of the brine is critical and their efficiency is limited to specific brine compositions and long reaction times in a regime with high flow rates (Melnikov et al. 2017; Somrani, Hamzaoui and Pontie 2013; Sun et al. 2015; Wen et al. 2006).

Solvent extraction (or liquid–liquid extraction)

The solvent extraction method, also called liquid–liquid extraction, is based on the distribution of a solute, e.g. Li, in two immiscible liquid phases of different densities physically separated in a vessel (Figure 2); Rydberg 2004). One phase contains the solute (e.g. Li in the brine or seawater), while the other one acts as solvent (commonly an organic compound) into which the solute diffuses after mixing (Figure 2)). The extraction efficiency is given by the ratio of solute concentration in both phases. It increases with increasing solvent volume and simultaneously decreases with equilibrium extraction time (Harvianto, Kim and Ju 2016; Rydberg 2004). Known solvents for Li extraction are listed in Table 2 (Harvianto, Kim and Ju 2016; Lee et al. 1968; Shi et al. 2017; Xiang et al. 2016). However, there is only a limited selectivity for Li^+ compared to Na^+, K^+, Ca^{2+}, and Mg^{2+} (Figure 2); Harvianto, Kim and Ju 2016). Seawater, for example, needs to be pretreated: Mg is removed by precipitation and the pH must be increased to 10.6–11.0 before Li extraction (Harvianto, Kim and Ju 2016; Warren 2021). In contrast, Bukowsky and Uhlemann (1993) found increasing extraction efficiency for LiCl with decreasing pH (<6) using an isoamyl alcohol and 2-ethyl-1,3-hexanediol solvent. Solvent extraction is also used to recycle spent LIBs (Asadi Dalini et al. 2021; Nan, Han and Zuo 2005). The LIBs have to be dismantled before leaching the metals by alkalis,

dissolution with H_2SO_4 and filtration, before the actual solvent extraction of Co, Cu, as well as Li_2CO_3 precipitation can be performed (Asadi Dalini et al. 2021; Nan, Han and Zuo 2005).

The solvent extraction method has to be used in combination with other extraction techniques due to limited selectivity (Table 2; compare Nan, Han and Zuo 2005, Harvianto, Kim and Ju 2016). A Li recovery between 65% and 96% is reached and it is an inexpensive technology (~2,800 US$/t LCE from the Dead Sea) but produces large amounts of acidic wastewater and toxic organic solvent waste (Table 2; Epstein et al. 1981, Kawamoto and Tamaki 2011, Harvianto, Kim and Ju 2016, Liu et al. 2017, Shi et al. 2017, Joshi and Adhikari 2019, Su et al. 2020). The method is already part of pilot-scale tests, e.g. in Salta, Argentina (Millennial Lithium Corp., 2020). The application of solvent extraction for DLE from geothermal water is regarded to be critical since the fluid's physicochemical properties have to be changed and competitive elements need to be removed (Harvianto, Kim and Ju 2016).

Sorption and ion exchange

Inorganic sorbents are intensively studied regarding their implementation into new technologies for Li recovery from (geothermal) brines (e.g. Guneysu 2020; Taghvaei, Taghvaei and Askari 2020; Weng et al. 2020; Xue et al. 2020). Sorption is defined as a reaction between a solute and an insoluble phase that removes the solute from the solution (Figure 2); Barrow 2008). Sorption of a solute on a sorbent can occur in different ways: (1) hydrated ionic species can form outer-sphere complexes on the sorbent surface, (2) dehydrated ions can form inner-sphere complexes, or (3) the ion can be more strongly bound to the crystal structure of the sorbent (Limousin et al. 2007).

Because sorption is a kinetically, and sometimes also physically, controlled process, adsorption and desorption durations can be extremely variable and thermodynamic equilibrium is often not reached (Limousin et al. 2007). To describe a sorption process, it is crucial to characterize the retention (i.e. adsorption) and release (i.e. desorption) of a solute, by sorption isotherms (Limousin et al. 2007).

In ion-exchange processes, an insoluble solid phase, comprising exchangeable cations or anions, interacts with the compounds in a liquid phase (Helfferich 1995). An equal amount of exchangeable cations from the exchanger can be substituted by cations from the solution (Figure 2); Bruggenwert and Kamphorst 1979; Helfferich 1995). All ion-exchange processes (independent of the selected exchanger) depend on pH, temperature, ion concentration in the solution, the structure and specific kinetics of the exchanger and its cation exchange capacity (CEC), the use of additives, contact time, and the stirring rate (e.g. Bouguerra et al. 2007; Eckstein, Yaalon and Yariv 1970; Hawash, Abd El Kader and El Diwani 2010; Lemaire et al. 2014; Navarrete-Casas et al. 2007; Ooi et al. 2016; Prodromou 2016; Sullivan et al. 2003; Sun et al. 2020; Wiśniewska et al. 2018). The most common ion-exchange process for systems containing Li can be described as: $Li^+_{(aq)} + Cl^-_{(aq)} + (Na,H)X \leftrightarrow (Na,H)^+_{(aq)} + Cl^-_{(aq)} + LiX$ where X denotes the ion exchanger (Figure 2); e.g. Gast and Klobe 1971; Kim and Grey 2010; Marthi et al. 2021; Navarrete-Casas et al. 2007; Ooi et al. 2016).

Inorganic sorbents

Li-Mn-oxides

Lithium manganese oxide sorbents (LMO) are a group of synthetical sorbents with a Mn-O framework and various crystal structures, e.g. orthorhombic ramsdellite-type (e.g. Zhang et al. 2007), tetragonal hollandite-type (e.g. Feng et al. 1995b) or cubic spinel-type (e.g. Chitrakar et al. 2000). Spinel-type sorbents, e.g. $Li_{1+x}Mn_{2-x}O_4$, $Li_{1.6}Mn_{1.6}O_4$ and λ-type MnO_2, are of particular interest as they reach Li sorption capacities of up to 53.5 mg/g (Figure 3, Table 3) after 24 h equilibration time (e.g. Bajestani, Moheb and Masigol 2019; Ohashi and Tai 2019; Slunitschek, Kolb and Eiche 2021; Yoshizuka et al. 2021). Additionally, spinel-type LMO have high Li selectivity (sorption of <5 mg/g competing ions) and stability (Bajestani, Moheb and Masigol 2019; Kawamoto and Tamaki 2011; Ohashi and Tai 2019; Ooi, Miyai and Katoh 1987; Ryu et al. 2015). The sorption capacity increases with increasing temperature during the experiments and T > 30°C increases the Li uptake (Qian et al. 2019; Wang et al. 2008). Lithium is de-/intercalated in LMO by Li^+ $^-$ H^+ -ion exchange and a redox reaction, whereas the share of each process on total Li sorption depends on the LMO chemistry (Feng et al. 1992; Gao et al. 2019; Ooi, Miyai and Sakakihara 1991; Xu et al. 2016; Yoshizuka et al. 2021). While desorption of redox-intercalated Li leads to LMO degradation caused by the disproportionation of $Mn(III)_{(s)}$ to $Mn(IV)_{(s)}$ and $Mn(II)_{(aq)}$, ion-exchange-intercalated Li has no effect on the chemical stability of the material (Feng et al. 1992; Gao et al. 2019; Hunter 1981; Ooi, Miyai and Sakakihara 1991). Commonly used desorption solutions (Table 3) are diluted acids, such as HCl (Xiao et al. 2015b, 2012; Yoshizuka et al. 2021; Zhu et al. 2014) or HNO_3 (Feng et al. 1995a; Ooi et al. 1989; Sato et al. 1997). During Li^+ elution using HCl, Mn dissolution of up to 60% with 3 mol/L HCl occurs but can be reduced significantly by using less concentrated (<2 mol/L) HCl (Yoshizuka et al. 2021). Ventura et al. (2020) tested Li desorption using CO_2 gas without affecting the chemical stability of the sorbent. To increase the chemical stability, transition metals (e.g. Sb, Ce, Cr, Cu, Co, Ni, Fe) can be incorporated into the framework during synthesis (Bajestani, Moheb and Masigol 2019; Cao et al. 2019; Chitrakar et al. 2014; Li et al. 2014; Liu, Sun and Yu 2019a; Zhao et al. 2018).

The high Li selectivity of spinel-type LMO results from tunnels in the Mn-O structure that forms a Li-selective ion-sieve (e.g. Bajestani, Moheb and Masigol 2019; Cao et al. 2019; Chitrakar et al. 2014; Han, Kim and Park 2012; Hong et al. 2018; Li et al. 2014; Liu, Sun and Yu 2019a; Yoshizuka et al. 2021). Lithium is sorbed inside the structure and on the surface while sorption of competing ions is restricted to the sorbent surface (Miyai, Ooi and Katoh 1988; Slunitschek, Kolb and Eiche 2021; Zhang et al. 2010b). To improve the sorption performance and chemical stability of LMO-type sorbents, the parameters during synthesis are modified. The framework

structure of spinel-type Mg-doped LMO is achieved by focusing on the structural properties during synthesis (Chitrakar et al. 2013). The combination with $Al(OH)_3$ or with electrochemical techniques improves the LMO sorption properties as well (Tian, Ma and Han 2010, Han, Kim and Park 2012; Chitrakar et al. 2014; Li et al. 2014; Hong et al. 2018; Bajestani, Moheb and Masigol 2019; Cao et al. 2019; Liu, Sun and Yu 2019a).

The selectivity order is $Na^+ < K^+ < Rb^+ < Cs^+ \sim Mg^{2+} < Ca^{2+} < Li^+$ (Figure 3; Ooi, Miyai and Katoh 1987; Zandvakili and Ranjbar 2018; Zhang et al. 2007), but strongly depends on the chemical composition of the solution (Chitrakar et al. 2000; Miyai, Ooi and Katoh 1988; Zhang et al. 2010b). The Li^+ sorption capacity generally increases with increasing pH (optimum at pH 12) and Li^+ concentration (200 mg/L) up to 37.4 mg/g, reaching recoveries up to 95% after four adsorption/desorption cycles (Tian, Ma and Han 2010). Chitrakar et al. (2014) extracted Li^+ from unbuffered and buffered brines of the Salar de Uyuni (Bolivia) using Fe-doped LMO reaching Li^+ uptake capacities of 18 mg/g at pH = 2 and 28 mg/g at pH = 7.2. Chromium-doped LMO reach sorption capacities of 31.7 mg/g but show Mn loss of 0.35–3.5% within the first 20 adsorption/desorption cycles, resulting in decreasing sorption capacities of 2.5–19.5% (Bajestani, Moheb and Masigol 2019; Cao et al. 2019, and references therein; Ohashi and Tai 2019). The kinetics and chemical stability of λ-MnO_2 are improved by coating with CeO_2 (Li et al. 2014).

Ryu et al. (2013) improve Li selectivity of $Li_xMn_{2-x}O_4$ by 3 times by applying an electric voltage. Moreover, they reduce the use of acids for Li desorption and improve the lifetime of the sorbents. The combination of LMO-type sorbents with electrochemical techniques in a flow-through reactor produces a Li-solution of 94% purity after 9 sorption cycles (Palagonia, Brogioli and La Mantia 2020). The application of 0.5 mA induces the reduction of LMO and simultaneously oxidizes NiHCF in a brine containing 1 mM LiCl and 100 mM NaCl. This represents a coupled process where Li^+ is de-/intercalated to LMO by redox reactions and a $Na^+ \leftrightarrow K^+$ exchange takes place in NiHCF (Palagonia, Brogioli and La Mantia 2020).

With the aim of making DLE from seawater industrially applicable, Han, Kim and Park (2012) synthesized a spherical mm-sized ion-sieve foams (SIFs) from spinel-type LMO. Using the SIFs, Li^+ adsorption capacity reaches 3.4 mg/g, which remains constant over five adsorption/desorption cycles. The desorption rate is 86%. Yoshizuka et al. (2021) synthesized $Li_{1.6}Mn_{1.6}O_4$ hydrothermally and reached sorption capacities of 36 mg Li^+/g from seawater at pH = 8.1. Hong et al. (2018) investigate composites consisting of 75% LMO and 25% Al_2O_3 and find a Li^+ adsorption capacity of 9 mg/g and <1% Mn loss after five adsorption/desorption cycles.

The application of LMO-type sorbents for DLE from geothermal water remains challenging due to high cost of the raw material, the use of acids for desorption (e.g. Ventura et al. 2020; Xiao et al. 2015a), its redox-sensitivity (e.g. Ariza et al. 2006; Park, Singhal and Jho 2015) and possibly time-consuming synthesis of the sorbent (Zhang et al. 2010b). Nevertheless, LMO are already intensively studied and regarded as potentially feasibly applicable and are therefore tested in pilot-scale projects for DLE from geothermal brines and seawater Li extraction (Liu et al. 2015; Ventura et al. 2020; Warren 2021).

Ti-oxides

Titanium nanoribbons, $H_2Ti_3O_7$, $H_4Ti_5O_{12}$, H_2TiO_3 and Ti-Sb-sorbents have been studied for their Li sorption behavior (Safari, Lottermoser and Alessi 2020; Wei et al. 2020; Wiśniewska et al. 2018; Zhang et al. 2010c). These phases can be hydrothermally and/or thermally synthesized from TiO_2 (anatase or rutile) (e.g. Chaban et al. 2019; Gentili et al. 2012; Li et al. 2020; Moazeni et al. 2015; Olson, Nelson and Islam 2006; Taghvaei, Taghvaei and Askari 2020), but the synthesis is complicated and time-consuming (e.g. Zhang et al. 2010c; Safari, Lottermoser and Alessi 2020 and references therein).

Ji et al. (2017) synthesized a H_2TiO_3 Li sorbent from Li_2CO_3 and TiO_2 within 5 h. Sorption capacities for an equilibrium time of 60 min decreased from ~27–24 to ~19–17 mg/g Li^+ after three sorption/desorption cycles. Synthetic porous spinel $H_4Ti_5O_{12}$ nanofibers are highly Li^+ selective ($K_d(Li^+)$ = 232 mL/g, K_d (Na^+, K^+, Mg^{2+}, Ca^{2+}) <1.5 mL/g) and reach a high sorption capacity of ~60 mg/g, which decreases after 6 adsorption/desorption cycles to 86.5% of the initial value (Wei et al. 2020). Molybdenum-doped Ti-oxide is highly selective for Li (i.e. ~93% Li^+, ~7% competing ions of total ions adsorbed) and adsorbs up to 78 mg/g Li^+ (Table 3; Wang et al. 2019).

The sorption kinetics of Ti-oxide sorbents are relatively slow, but increase with increasing temperature (Table 3; Zhang et al. 2010c, Moazeni et al. 2015, Lawagon et al. 2016, Wei et al. 2020, Marthi et al. 2021). Equilibrium times vary between 10 and 192 h (Table 3) for hydrothermal waters and synthetic LiCl and LiOH solutions, with sorption capacities between <1 and 94.5 mg/g Li^+ at alkaline pH, respectively (Figure 3; Zhang et al. 2010c; Shi et al. 2013; Lawagon et al. 2016; Choubey et al. 2017, and references therein). The ad-/desorption process is a Li^+ – H^+-ion exchange (Marthi et al. 2021; Moazeni et al. 2015; Wei et al. 2020). Titanium loss (0.06–2.50% Ti^{4+}) during desorption with HCl or HNO_3 results in a progressive decrease in sorption capacity within five cycles (Gu et al. 2018; Kamran and Park 2020; Lawagon et al. 2016).

Titanium oxides are promising for an industrial-scale application in geothermal power plants regarding implementation possibilities (e.g. as nanoribbons) and high sorption capacities. The long equilibration times needed and limited chemical stability of the sorbent are challenging, but Ti-oxides are already tested regarding Li extraction from geothermal brines and seawater at pilot scale (Li et al. 2021).

Al-hydroxides

Amorphous, polymeric, and crystalline $Al(OH)_3$ as well as hexagonal $LiAl_2(OH)_6$ are used as selective adsorbents for DLE from brines (Bouguerra et al. 2007; Hawash, Abd El Kader and El Diwani 2010; Prodromou 2016). Variable Li^+ sorption capacities of up to 123 mg/g at alkaline pH (Hawash, Abd El Kader and El Diwani 2010) or only ~0.6–22.9 mg/g in flow through and batch sorption experiments are reached (Jiang et al. 2020a; Jiang, Yang and Yu 2020b; Xue et al. 2020). Sorption temperature >30°C has negligible effects on the Li^+ sorption capacity (Figure 3; Hawash, Abd El Kader and El

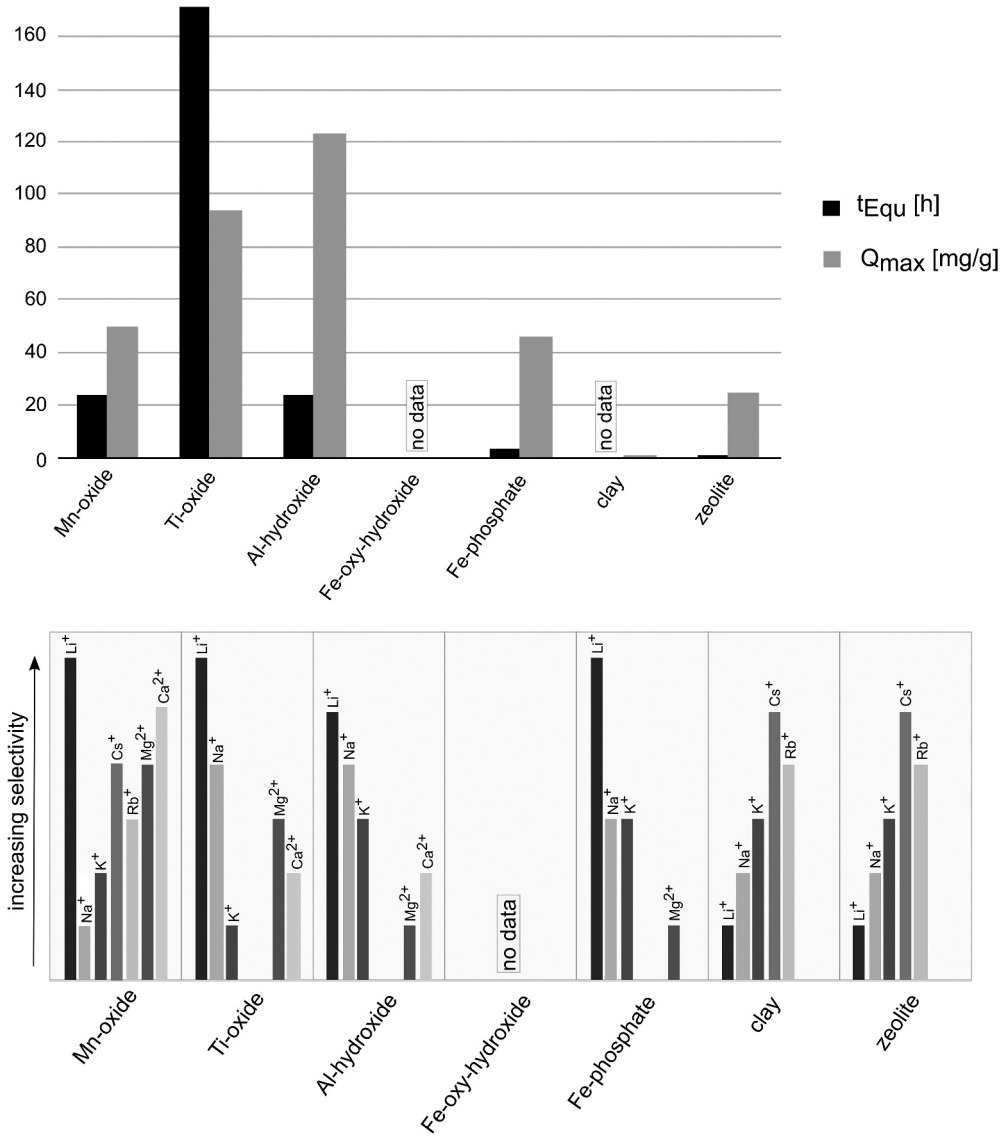

Figure 3. Comparison between sorbents according to equilibrium time (t_{Equ} [h]), maximum sorption capacity (Q_{max} [mg/g]) (top) and relative qualitative selectivity of different ions (bottom) (Bajestani et al. 2019; Chitrakar et al. 2000; Choubey et al. 2017; Colella 1996; Greene-Kelly 1955; Han et al. 2012; Hawash et al. 2010; Heidari and Momeni 2017; Hoyer et al. 2015; Intaranont et al. 2014; Jiang et al. 2020a; Lawagon et al. 2016; Lemaire et al. 2014; Prodromou 2016; Shi et al. 2013; Wisniewska et al. 2018; Zhang et al. 2010a; Zhang et al. 2010b).

Diwani 2010; Heidari and Momeni 2017). Equilibrium times vary significantly between 5 min and >24 h (Pauwels, Brach and Fouillac 1990; Prodromou 2016; Xue et al. 2020).

Pauwels, Brach and Fouillac (1990) investigated Li sorption from natural geothermal waters on amorphous Al-hydroxide. Optimum sorption conditions occur at 80°C, at pH >5 and an Al/Li ratio ~3.5, reaching Li-recovery >90%. Experiments with polymeric $Al(OH)_3$ combined with ion-exchange resins at varying Li concentrations (5.5–1000 mg/L in brines and synthetic solutions, respectively) show that Li-uptake correlates positively with initial Li concentration and increasing pH in 70 experimental runs (Hawash, Abd El Kader and El Diwani 2010). This indicates that $Li^+ - H^+$ substitution is the main Li-uptake process, whereas only ~10% of total amount of Li^+ adsorbed can be attributed to physisorption (Prodromou 2016, compare Heidari and Momeni 2017). In contrast, Heidari and Momeni (2017) concluded that optimal conditions were reached at pH ~7.

To investigate the applicability of Al-hydroxides in geothermal plants, flow tests have been performed. Thereby, the Li uptake is positively influenced by decreasing bed height and increasing flow rate (Jiang, Yang and Yu 2020b). Besides CH_3COONH_4, acids, such as H_2SO_4 or HF, are used for desorption (Hawash, Abd El Kader and El Diwani 2010; Heidari and Momeni 2017; Prodromou 2016). To apply Al-hydroxides for DLE from geothermal brines, further research is needed concerning desorption with non-problematic acids for technical application. However, they are recently tested in pilot-scale projects (Fukuda 2019).

Fe-oxy-hydroxides

Iron-oxy-hydroxides are widespread in soils world-wide and known to adsorb cations (e.g. Li^+, Mg^{2+}, Ni^{2+}, Zn^{2+}, Cu^{2+}, Cd^{2+}) due to their negatively charged surface at alkaline pH (Nielsen et al. 2005). Synthetic akageneite ($FeO_{0.833}(OH)_{1.167}Cl_{0.167}$ or β-FeOOH), for instance, has a large surface area of

up to 280 m^2/g which is generally advantageous for adsorption (Kim and Grey 2010). Natural Fe-oxy-hydroxides, e.g. goethite (α-FeOOH) and lepidocrocite (γ-FeOOH), have similarly large surface areas of up to 260 m^2/g (Kim, Nielsen and Grey 2008). The crystal structure of lepidocrocite is not affected by Li adsorption (Kim, Nielsen and Grey 2008). In goethite, Li^+ occupies octahedral and tetrahedral sites in the tunnels (Nielsen et al. 2005). At pH > 7.1, Li^+ is more strongly attached to the sorbent surface and OH^- groups are deprotonated, indicating that the substitution of H^+ by Li^+ is the main process of Li^+ uptake (Kim, Nielsen and Grey 2008). Sorption experiments with Fe-oxy-hydroxides were run for 24 h–7 days, but no information on equilibrium times, optimal temperatures or eluting solutions are available (Table 3; Nielsen et al. 2005, Kim, Nielsen and Grey 2008, Kim and Grey 2010).

Iron-oxy-hydroxides are cheap but have relatively low adsorption capacities of 0.2–0.5 meq/g corresponding to 3.5 mg/g Li^+ (Table 3; reported for membranes with in-situ formed FeOOH nanoparticles) (Heidary, Khodabakhshi and Kharat 2016; Kim and Grey 2010). Their application for Li extraction from geothermal brines is critical as they are not selective for Li compared to toxic metals and radioactive ions, such as Pb^{2+}, Cd^{2+}, Cr^{6+}, and As^{3+} (Cole et al. 2004; Kim and Grey 2010).

(Li)$FePO_4$

Lithium–iron-phosphates are synthetic sorbents characterized by an iron phosphate framework with the ability to reversibly incorporate monovalent cations, such as Li^+ (Dodd, Fultz and Yazami 2006). Iron–phosphate is used as a sorbent for selective Li^+ recovery from high saline solutions (Intaranont et al. 2014). $LiFePO_4$ (triphylite) and $FePO_4$ (heterosite) are commonly used as electrodes in LIBs (Arnold et al. 2003; Liu et al. 2014).

In batch experiments, 0.3 and 0.7 M sodium thiosulfate ($Na_2S_2O_3$) is added to the Li-bearing solution and $FePO_4$ sorbent at Na^+/Li^+ ratios of 10/1 to 100/1. After 24 h, Li is eluted from $LiFePO_4$ by oxidation with potassium persulfate ($K_2S_2O_8$) and thereby a Li-sulfate ($Li_2SO_{4(aq)}$) – K-sulfate ($K_2SO_{4(aq)}$) solution and the delithiated sorbent are recovered (Intaranont et al. 2014). The use of an oxidizing agent is needed since the sorption process is mainly controlled by the redox-reaction $Fe^{+III}PO_4 + e^- + Li^+ \rightarrow LiFe^{+II}PO_4$ (Fukuda 2019; Intaranont et al. 2014). Sorption capacity increases with temperature between 25°C and 65°C and it is optimal at pH = 7 (Fukuda 2019). Up to 46 mg Li^+/g are incorporated at 65°C when reaching equilibrium (Table 3; Intaranont et al. 2014, Fukuda 2019), exceeding the theoretically possible maximum adsorption capacity of 44 mg/g reported by Zhao et al. (2013) within analytical error.

The sorption of competing ions, such as Na^+, K^+ and Mg^{2+}, is <3 mg/g, indicating high Li selectivity (i.e. $Li^+/Na^+_{(s)}$ of 390–4000 at $Li^+/Na^+_{(aq)}$ of 10–100, respectively, Figure 3) (Intaranont et al. 2014). Equilibrium times vary between 1.5 and 3 h (Figure 3; Intaranont et al. 2014; Sun et al. 2020). For high Mg/Li brines, Li^+ can be successively separated from Mg^{2+} by controlling the applied voltage precisely (Zhao et al. 2013). Up to 41.3 mg/g Li^+ can be incorporated during the electrochemically induced redox reaction at an applied current of less than 1 V (Zhao et al. 2013). Geothermal water with a composition of 2.5 g/L TDS and a Li^+ concentration of 25.8 mg/L at pH 8.8 is processed by a $LiFePO_4$-$FePO_4$-Ag/AgCl electrode combined with a semipermeable, Cl^-–selective membrane (Sun et al. 2020). By applying 1 V, 97.8% (~10 mg/g) Li^+ are recovered from the initial solution. The adsorption capacity is increased by ~27–36% when using additives, such as NH_4HCO_3 or PEG-6000 (i.e. a water-soluble polymer), in the electrode (Sun et al. 2020). To avoid redox-reactions, NaCl is an ideal reagent to recover LiCl and $NaFePO_4$ and finally to precipitate Li_2CO_3 in an acid-free procedure (Liu et al. 2019c). Thereby, the isomorphic substitution of Li^+ by Na^+ in $LiFePO_4$ yields a Li-recovery of 27%. Another approach for the recovery of Li^+ from $LiFePO_4$ by leaching, using a mixture of H_2O_2 and CH_3COOH that only reacts with Li^+ rather than with $FePO_4$ (Yang et al. 2018). Thereby, less acid is consumed to extract 95.0% of Li^+ with high purity (i.e. 99.95 wt.%). Further research concerning technical implementation is needed to evaluate the applicability of $FePO_4$ for DLE from geothermal water at industrial scale, although the available data on chemical stability, selectivity, and sorption capacity are promising.

Clay minerals

Clay minerals are phyllosilicates comprising alternating layers of $(Si,Al,Fe)O_4$ tetrahedra (T) and $(Al,Mg,Fe)(OOH)_6$ octahedra (O) (Kloprogge, Komarneni and Amonette 1999; Zhang et al. 2010a). Lithium can adsorb onto negatively charged surfaces of clay minerals or substitute octahedrally bound elements in the clay mineral lattice (Gaskova and Bukaty 2008; Odom 1984; Williams and Hervig 2005). Most likely, Li forms hydrated inner-sphere and outer-sphere complexes onto the clay mineral surface or in the interlayers but can also be octahedrally or tetrahedrally coordinated by exchange with H^+ (Eckstein, Yaalon and Yariv 1970; Greene-Kelly 1955; Li and Liu 2020; Odom 1984). This indicates pH reduction during adsorption and better performance at higher pH, which has been proven for Zn^{2+} sorption on kaolinite (Meroufel et al. 2013). Chemisorption is the dominating process at high pH, whereas both physisorption and chemisorption are of importance at lower pH (Li and Liu 2020). Lithium is preferentially strongly bound in hectorite ($Na_{0.33}(Mg,Li)_3Si_4O_{10}(OH,F)_2$) and Li-bearing montmorillonite ($Li_x(Al_{4-x}Mg_x)Si_8O_{20}(OH)_4{\cdot}nH_2O$) among Li-free montmorillonite, kaolinite ($Al_4Si_4O_{10}(OH)_8$) and vermiculite ($(Mg,Ca)_{x/2}^{2+}(Al_{4-x}Mg_x)Si_8O_{20}(OH)_4 \cdot 8H_2O$), where it can only be adsorbed (Amer 2008; Chang, Skipper and Sposito 1997; Eckstein, Yaalon and Yariv 1970; Greene-Kelly 1955; Kloprogge, Komarneni and Amonette 1999; Nir et al. 1986).

The maximum adsorption capacity for Li on clay minerals varies between 0.02 and 0.90 mg/g Li^+ and 0.5–0.6 mg/g Li^+ for kaolinite and montmorillonite, respectively (Figure 3; Eckstein, Yaalon and Yariv 1970; Greene-Kelly 1955). Increasing temperature leads to decreasing adsorption capacity as well as decreasing selectivity for Li (Gast and Klobe 1971). Vermiculite, opposed to montmorillonite, preferentially adsorbs Na^+ over Li^+ (Gast and Klobe 1971). The few studies that report sorption data from an experimental approach used stirring times of 24 h and desorbed afterward using calcium

acetate (Table 3; Eckstein, Yaalon and Yariv 1970, Hoyer, Kummer and Merkel 2015). No data on equilibration times and kinetics are available (Figure 3; Table 3), revealing the necessity for further research on Li sorption to clay minerals. The technical applicability of clay minerals for the DLE is critical due to limited temperature stability, low Li sorption capacity, as well as their coagulation and decomposition behavior.

Zeolites

Zeolite group minerals are hydrous framework aluminosilicates that consist of interconnected SiO_4 – AlO_4 tetrahedra resulting in a network of micropores and channel systems (e.g. Navarrete-Casas et al. 2007; Obaid et al. 2018; Rao et al. 2006; Zhou et al. 2013). Due to the substitution of Si^{4+} by Al^{3+}, a negatively charged surface develops, which enables cation sorption (Belova 2019; Erdem, Karapinar and Donat 2004; Gaikwad, Misal and Gupta 2011; Obaid et al. 2018; Rao et al. 2006).

Zeolites possess a large and well-developed surface area (up to 726 m^2/g, Zhou et al. (2013)), high ion exchange and adsorption capacity, as well as fast kinetics enabling it to perform as ion-sieve (Figure 3; Corma 2003; Danisi and Schilling 2021; Wiśniewska et al. 2018). They are nontoxic, cheap, widely available in different grain size, shape, and composition and are reusable over several adsorption–desorption cycles that renders them rather environmentally friendly (Akgül et al. 2006; Belova 2010; Wiśniewska et al. 2018; Zhou et al. 2013).

Zeolites can be easily modified to tune their physicochemical properties (Beyaz Kayiran and Lamari Darkrim 2002). Pretreatment and post-synthetic modifications increase the sorption capacity and allow desorption with NaCl instead of acids (Athanasiadis and Helmreich 2005; Carland and Aplan 1995; Navarrete-Casas et al. 2007; Zamzow et al. 1990; Zamzow and Murphy 1992). The chemical stability of zeolite is limited to moderate pH values (Hoyer, Kummer and Merkel 2015), although some authors state that zeolitic materials would be alkali and acid resistant (Belova 2019; Zhou et al. 2013).

Lithium sorption on zeolite depends on pH, temperature, Li concentration, and competing ions, channel diameter and surface area (Colella 1996; Hoyer, Kummer and Merkel 2015; Inglezakis et al. 2005; Lemaire et al. 2014; Navarrete-Casas et al. 2007; Sullivan et al. 2003; Wiśniewska et al. 2018). Lithium is extracted from geothermal brines and synthetic LiCl solution by natural clinoptilolite and synthetic zeolite Na-X using polyacrylic acid (PAA) as additive to prevent precipitation of hydroxides and improve Li selectivity (Wiśniewska et al. 2018). The amount of 50% Li was recovered with clinoptilolite at naturally relevant pH of 5.5. Under laboratory conditions, 100% Li was extracted from synthetic LiCl solutions at pH = 9 with zeolite Na-X and PAA. In contrast, Belova (2010) and Belova (2017) improve zeolite selectivity for Li by modifying the precursor zeolite Si/Al ratio with $Al(OH)_3$ without the use of additives. A sorption capacity for Li^+ of 1.6 mg/g is reached at an initial Li-concentration of 40 mg/L at pH = 8.5 (Belova 2017). Approximately 83% Li^+ is recovered from a synthetic solution with a Li-concentration of 3 mg/L after 2 h (Belova 2017).

Zeolites are promising sorbents for DLE from geothermal brines concerning kinetics and sorption capacity. They are thermally stable within the temperature ranges of thermal waters, which is beneficial for their application in geothermal brines (Zhou et al. 2013), but data on sorption characteristics at T > 40°C are lacking and need further research.

Other sorbents

Other sorbents, such as Zr-phosphate, Sn-antimonates, Sb-oxides, Ta-oxides, and $H_8Nb_{22}O_{59} \cdot 8H_2O$ have been studied for their selective Li uptake behavior. Zirconium phosphate reaches 48.9 mg/g adsorption capacity at equilibration times of 48 h and its selectivity is dependent on the total amount of ions that are adsorbed and is represented by $Cs^+ \sim Na^+ < Li^+$ for high and $Li^+ < Na^+ < Cs^+$ for low loadings (Clearfield and Troup 1970; Clearfield and Tuhtar 1976). Lithium substitutes H^+ sites during adsorption, resulting in a $Zr(LiPO_4)_2 \cdot 4H_2O$ phase after 80% exchange. By acid treatment with HCl, only 5% of the exchanged Li is recovered (Clearfield and Troup 1970). The incorporation of H^+ during desorption, however, is accompanied by a structural change indicated by the resulting gel-like structure of Zr-phosphate sorbent (Clearfield and Troup 1970).

Synthetic Sn-antimonates are highly Li-selective sorbents represented by the sequences $Na^+ < K^+ < Rb^+ < Cs^+ \ll Li^+$ and $Cs^+ < Rb^+ < K^+ < Na^+ < Li^+$ for Li^+/H^+ equivalent fractions in the sorbent between 0–0.04 and >0.14, respectively (Abe and Furuki 1986; Abe and Tsuji 1983). Isotherm batch experiments have been performed in the temperature range between 30°C and 60°C. The ion-exchange reaction is represented by $Li^+ – H^+$ substitution (Abe and Furuki 1986). Information on the maximum adsorption capacity is lacking, but slow kinetics for Li^+ (~10 days) compared to the other alkali ions (~24 h) have been reported (Abe and Furuki 1986).

For Sb-oxides, the maximum sorption capacity for Li^+ reaches ~22 mg/g (Chitrakar and Abe 1988). The selectivity sequences are determined to be Li < Na < K < Rb < Cs and Li ≪ K < Cs < Rb ≪ Na for amorphous and crystalline sorbents in acid media, respectively (Chitrakar and Abe 1988, 1989). Monoclinic $LiSbO_3$ sorbs up to 39.8 mg Li^+/g from a buffered LiOH solution at 90°C and pH = 9.2 (Oi et al. 2000). The Li uptake is almost twice as much for LiOH compared to LiCl solutions at 90°C. The sorbent undergoes an irreversible phase transition from monoclinic to cubic during incorporation of Na rather than reversibly from monoclinic to orthorhombic by exchange of Li^+ with H^+. For desorption of Li^+, the loaded sorbent $LiSbO_3$ is treated with concentrated HNO_3 (Chitrakar and Abe 1988).

Lithium sorption on cubic $LiTaO_3$ reaches maximum sorption capacities of 16.7 mg/g at 60°C representing 56% of theoretically possible 29.9 mg/g exchangeable sites and increased

to 9.7 mg/g and 14.6 mg/g at 30°C and 45°C, respectively (Inoue and Abe 1996). The main sorption process is the exchange of H^+ and Li^+ (Inoue and Abe 1996).

Another Li-selective sorbent is hexagonal $H_8Nb_{22}O_{59} \cdot 8H_2O$. Its selective behavior is related to the ionic radii of different ions, i.e. $Cs^+ \ll Rb^+ < K^+, Na^+ < Li^+$ (Yang et al. 2005). Optimum pH values for selective Li adsorption are >11 as the ion-exchange process is the substitution of H^+ and Li^+ reaching up to 17.0–20.8 mg/g Li sorption capacities (Yang et al. 2005). Besides Li, Na and K are efficiently removed from the solution as well, reaching removal rates of up to 98–99.9% (Yang et al. 2005).

Discussion

The application of Li extraction from geothermal brines without disturbing the running operation of a power plant is a challenging task (Slunitschek, Kolb and Eiche 2021). The geochemistry of geothermal brines is similar to that from conventionally mined brines (Table 1), but the selected DLE technique implementable to geothermal power plants has to operate efficiently at 60–80°C and resist pressures and flow velocities of 20–50 bars and 30–90 L/s, respectively (Haklıdır and Balaban 2019; Stober and Bucher 2012).

Brine and seawater evaporation can be economically used for Li recovery, e.g. in the Salar de Atacama in Chile, the Salar de Hombre Muerto in Argentina or the Dead Sea in Israel (Bowell et al. 2020; Epstein et al. 1981). However, this technique is not applicable with respect to geothermal power plants as water flows continuously and is mostly reinjected into the deep reservoir, with few exceptions in Iceland, China, and Thailand, where the thermal water is discharged via surface waters (Kaya, Zarrouk and O'Sullivan 2011). The large areas and evaporation times of several months needed (Gaikwad, Misal and Gupta 2011) are not available in urban regions, limiting its feasibility. Additionally, arid climate conditions are not given in many places where geothermal plants are located.

High salinities and SiO_2 concentrations in brines (Table 1) circulating through geothermal power plants are critical. With decreasing temperature during processing, the formation of scales within the rods becomes more likely since SiO_2 solubility decreases with decreasing temperature and pH (Bouguerra et al. 2007; Palmer and Palmer 2003). Other phases, such as $(Ba,Sr,Ca)SO_4$, Pb-As-Sb-sulfides and carbonates, may precipitate depending on brine chemistry, which should always be prevented as they can cause corrosion or clogging and the accumulation of radionuclides (Goldberg et al. 2021; Haas-Nüesch et al. 2018; Haklıdır and Balaban 2019). In many geothermal power plants, therefore inhibiting chemicals, such as phosphate salts, phosphonic acid and polymers, are used (Haas-Nüesch et al. 2018; Haklıdır and Balaban 2019).

Direct precipitation is a cheap method for Li recovery, which is feasibly applicable and easy to set up (Zhang et al. 2019). Due to the complex chemical composition of many brines and their sensitivity on changes in geochemical conditions (i.e. changes in pH, major element chemistry, temperature, etc.), direct precipitation is regarded to be economically applicable but technically inappropriate for DLE in a running geothermal power plant as the risk of undesired scaling is too high.

The high flow rates in geothermal plants limit the feasibility of most membrane-related technologies since long reaction times of several hours for the Li extraction were needed in pilot tests with synthetic Li-solutions (Melnikov et al. 2017). The application of membranes is limited to low Na-Mg-B-brines, since they generally have a modest selectivity for Li compared to these ions (Somrani, Hamzaoui and Pontie 2013; Wen et al. 2006). By processing Ca^{2+}- and SO_4^{2-} -rich brines, $CaSO_4$ becomes progressively enriched in the residual brine and might precipitate, causing clogging of the pumping equipment (Gaikwad, Misal and Gupta 2011). Furthermore, Li recovery is <80% from brines with high Li concentrations when using membrane technologies (Safari, Lottermoser and Alessi 2020). The recovery decreases at temperatures >18–20°C, which contradicts the requirements of efficient and economic geothermal power plants (Sun et al. 2015). DLE using membranes is expensive and produces acidic wastewater, which is a main problem for its applicability in geothermal plants.

Solvent extraction is limited to specific hydrochemical compositions and is not applicable for high Mg/Li (mass ratio >6; Liu, Zhao and He 2020) fluids. Magnesium needs to be removed from the solution prior to increasing its pH to 10.6–11.0 necessary for the solvent extraction process (Harvianto, Kim and Ju 2016). The increase in pH toward more alkaline conditions could cause scaling (Harvianto, Kim and Ju 2016; Warren 2021) and the resulting precipitates must be extracted by membrane filtration (Harvianto, Kim and Ju 2016; Warren 2021).

In contrast, ion exchange and adsorption techniques can be highly efficient for fluids with different chemical compositions, reliable and environmentally friendly, depending on the type of exchanger, its selectivity and CEC for the solute, its commercial availability and its reusability and chemical stability concerning repeating loading/unloading cycles (Tables 2 and 3; Ambrose and Kendall 2020a; Liu et al. 2017; Tian, Ma and Han 2010). Compared to all the other extraction techniques described here, sorption and ion exchange in general are not restricted to specific brine composition (Table 2) and the different types of sorbents allow the applicability of one universal technique at several different locations for fluids differing in composition, temperature, pressure, and flow rate world-wide. For most studied sorbents except Mn-oxide and Al-hydroxide, lacking information on Li sorption at high temperature and pressure or on their stability over many sorption/desorption cycles make a reliable evaluation difficult.

Manganese-oxides are characterized by fast kinetics, high selectivity for Li (i.e. sorption of <5 mg/g competing ions) reaching high sorption capacity (up to 53.5 mg/g), which qualifies them for a potentially feasible DLE in geothermal power plants and the production of high-purity Li-products (Ariza et al. 2006; Bajestani, Moheb and Masigol 2019; Kawamoto and Tamaki 2011; Ohashi and Tai 2019; Ooi, Miyai and Katoh 1987; Ryu et al. 2015). However, the development of a large-scale synthesis process would be essential to supply sufficient amounts of LMO sorbent needed for industrial application. The redox sensitivity and pH treatment are challenging, since all sorbents that operate ideally at alkaline pH conditions require pH adjustment, whereas most natural brines are neutral or slightly acidic (Pirajno 2012).

Sorption of Li from geothermal brines on Al-hydroxides has been studied at temperatures up to 70°C and in 70 cycles (Hawash, Abd El Kader and El Diwani 2010). The sorbent proved a good stability, but (technically) problematic acids (e.g. HF or H_2SO_4, Table 3) are used for desorption, which cannot be implemented into a geothermal power plant (Hawash, Abd El Kader and El Diwani 2010; Heidari and Momeni 2017; Prodromou 2016). Data coverage on the chemical stability of Al-hydroxide-based sorbents against acids is low and needs further investigation.

Titanium-oxide-based sorbents reach rather high adsorption capacities and are highly selective for Li, but they also have to equilibrate up to 10–192 h, which is not viable in geothermal power plants (Lawagon et al. 2016; Shi et al. 2013; Taghvaei, Taghvaei and Askari 2020; Wei et al. 2020). Furthermore, the loss of Ti (e.g. 0.06–2.5% Ti^{4+} after five cycles) in repeating sorption/desorption cycles is significant causing a proceeding decrease in their sorption capacity (e.g. 13.5% after 6 cycles) over time and limits their feasibility (Gu et al. 2018; Kamran and Park 2020; Lawagon et al. 2016). The adsorption of toxic metals, radioactive ions and hazardous oxyanions are a criterion for exclusion of Fe-oxy-hydroxide as sorbents since these substances must not be accumulated at the surface and must not contaminate the Li-concentrate (Cole et al. 2004; Kim and Grey 2010).

Less investigated sorbents are $FePO_4$, clay minerals, and zeolite group minerals (Liu, Zhao and Ghahreman 2019b; Meng et al. 2021; Safari, Lottermoser and Alessi 2020; Stringfellow and Dobson 2021). High Li adsorption capacities (up to 46 mg Li^+/g, Figure 3) on $FePO_4$ are reached after equilibration for 24 h, which may be too long for an efficient implementation in a geothermal power plant with high flow rates. However, optimal adsorption conditions and equilibrium time for upscaling have to be determined. Intaranont et al. (2014), for example, identify a complete Li uptake in <3 h if Li^+ and $S_2O_3^{2-}$ concentrations exceed 0.7 M, which, however, exceed natural brine values by a factor of 3 to 48 (Table 1). Analogous to Mn-oxide ion sieves, redox-sensitivity of $LiFePO_4/FePO_4$ may limit its application in Li extraction from geothermal brines.

Clay minerals may be disadvantageous for applications in flow systems as the platy habitus could negatively influence the flow properties or clog the sorption unit. Coagulation of the particles due to sorbed cations (Lagaly and Ziesmer 2003) can lead to clumping and clogging and may reduce the adsorption capacity in terms of limited fluid-sorbent contact. Furthermore, clay minerals might partially or completely decompose at higher temperature or pH, lowering their adsorption capacities and selectivity for Li^+. So far, many studies focused on natural Li^+ adsorption on clay minerals in soil systems and alluvial plains rather than investigating their economic application potential in mineral processing (Figure 3; e.g. Chang, Skipper and Sposito 1997; Greene-Kelly 1955; Hoyer, Kummer and Merkel 2015; Li and Liu 2020; Odom 1984).

Zeolites successfully adsorb Li from synthetic solutions and geothermal waters (e.g. Navarrete-Casas et al. 2007; Wiśniewska et al. 2018). It was shown that the more negatively charged the zeolite surface, the higher the theoretical sorption capacity (Accardi and Lobo 2000; Barrer, Davies and Rees 1969). Therefore, zeolites with low Si/Al ratio are most suitable. Due to generally low Li selectivity (Figure 3), the use of additives may be necessary (Wiśniewska et al. 2018). However, sorption capacity and stability data for T > 40°C are lacking, which needs to be studied before their applicability for geothermal processes can be evaluated.

For all sorbents discussed in this article, the process of Li^+ intercalation and consequently, the change of the fluid hydrochemistry is a major issue that needs to be considered carefully. Redox-sensitive sorbents often have limited chemical stability since the redox-reactions during every sorption/desorption cycle lead to changes of crystal lattice parameters. This is in particular the case for LMO and $FePO_4$ although minor focus has been spent on $FePO_4$ stability without combination with electrochemical techniques (Cao et al. 2019; Gao et al. 2019; Hunter 1981; Intaranont et al. 2014; Kuss et al. 2014). If the underlying sorption process is an ion exchange, however, H^+ or alkalis (e.g. Na^+) are released to the brine, changing the pH (and requiring pH adjustment) or major fluid chemistry. However, Na^+-exchanged sorbents have never been sufficiently tested in high saline environments due to excess Na^+ in these fluids (Table 1). In this case, desorption by acid exchanges Li^+ by H^+ and not Na^+. This results in a different composition of the sorbent, which may have a negative effect on sorption capacity in the next cycle.

To improve the performance of sorbents, they can either be synthesized to target pure chemical compositions with controlled crystal structure or be combined with other sorbents. Composite materials have been suggested by Zandvakili and Ranjbar (2018) who mixed organic N-methyl-2-pyrrolidone and LMO in a 1:1 ratio. In contrast, Sullivan et al. (2003) show that the amount of clinoptilolite and smectite, as well as the bulk negatively charged surface area of a mixture correlate positively with Li^+ sorption proposing a mixture of clinoptilolite and smectite with a ratio of 1:0.5.

Conclusion

Increasing demand and pressure on the Li market is expected in the future. Widening the portfolio from primary Li deposits to geothermal brines may generate an alternative Li resource. The implementation of DLE into a geothermal power plant at industrial scale is subject of current research, due to the chemical variability of the brines and operating conditions (T = 60–80°C, P = 20–50 bars, flow-rates of 30–90 L/s).

Direct precipitation and evaporation are unlikely to be implemented into geothermal power plants due to the risk of scaling, land consumption, concurrent precipitation of undesired components and/or long evaporation times. Solvent extraction and membrane processes are only suitable for specific brine compositions and can thus only be applied to such brines or the necessity of further purification steps is indispensable. DLE by sorption and ion-exchange processes cannot be performed in a single-step procedure because sorption and desorption have to be temporally separated to prevent mixing of the geothermal brine with the desorption solution. Furthermore, depending on the selected sorbent/ion exchanger, the use of acids for desorption is indispensable. However, membrane-based techniques, sorption and ion exchange as

DLE are regarded most promising for implementation. Since the general DLE technology will be similar for all different materials for sorption and ion exchange, they have the potential to be universally applicable for different fluid compositions by choosing the most appropriate material for the local requirements at the lowest investment.

Sorbent-specific disadvantages are redox-sensitivity, pH adjustment, and the use of acids for desorption. Since operating conditions in geothermal power plants and brine composition vary largely between different sites, the Li-extraction process likely needs to be adjusted to the local context. Sorption using Fe-oxy-hydroxides is not applicable in the geothermal power plant due to adsorption of undesired ions. The phyllosilicate habitus of clay minerals that might cause clogging of the technical equipment are limiting their application. Titanium-oxide- and Al-hydroxide-based sorbents have been implemented in pilot plants, but long equilibration times, limited chemical stability, and problematic acids used for desorption are not appropriate for their application in a regime with high flow rates. Lithium–manganese oxides, in contrast, appear promising, due to fast kinetics and high selectivity for Li reaching high adsorption capacities although these sorbents are redox-sensitive. Other sorbents like $FePO_4$ and zeolite show fast kinetics, variably high sorption capacities, and excellent chemical stability under geothermal conditions, making them promising alternatives. Challenges for lithium–manganese oxide, $FePO_4$, and zeolite are the high flow-rates, high salinities of the brines and high pressures in the power plants, which need to be studied in detailed laboratory and pilot plant experiments to conclusively evaluate their potential for a feasible implementation into operating geothermal power plants for commercial Li-extraction.

Acknowledgments

Michèle Jungmann is acknowledged for many helpful discussions concerning lithium in hydrothermal systems. We especially thank Editor-in-Chief Dr. Kawatra as well as four anonymous reviewers for their comments and revisions that significantly improved the quality of this article. This research is part of the project “UnLimited” which is funded by the German Federal Ministry for Economic Affairs and Energy under Grant O3EE4023D.

Disclosure statement

No potential conflict of interest was reported by the author(s).

Funding

This work was supported by the German Federal Ministry for Economic Affairs and Energy [O3EE4023D].

References

Abe, M., and N. Furuki. 1986. Synthetic inorganic ion-exchange materials. XXXXI. Ion exchange equilibria of alkali metal ions/hydrogen ions on tin (IV) antimonate. *Solvent Extraction and Ion Exchange* 4:547–65.

Abe, M., and M. Tsuji. 1983. Synthesis of quadrivalent metal antimonates as ion exchangers and their selectivities for alkali metal ions. *Chemistry Letters* 12:1561–64.

Accardi, R. J., and R. F. Lobo. 2000. Accessibility of lithium cations in high-silica zeolites investigated using the NMR paramagnetic shift effect of adsorbed oxygen. *Microporous and Mesoporous Materials* 40:25–34.

Akgül, M., A. Karabakan, O. Acar, and Y. Yürüm. 2006. Removal of silver (I) from aqueous solutions with clinoptilolite. *Microporous and Mesoporous Materials* 94:99–104.

Ambrose, H., and A. Kendall. 2020a. Understanding the future of lithium: Part 1, resource model. *Journal of Industrial Ecology* 24:80–89.

Ambrose, H., and A. Kendall. 2020b. Understanding the future of lithium: Part 2, temporally and spatially resolved life-cycle assessment modeling. *Journal of Industrial Ecology* 24:90–100.

Amer, A. M. 2008. The hydrometallurgical extraction of lithium from Egyptian montmorillonite-type clay. *JOM* 60:55–57.

An, J. W., D. J. Kang, K. T. Tran, M. J. Kim, T. Lim, and T. Tran. 2012. Recovery of lithium from Uyuni salar brine. *Hydrometallurgy* 117:64–70.

Aquilina, L., H. Pauwels, A. Genter, and C. Fouillac. 1997. Water-rock interaction processes in the Triassic sandstone and the granitic basement of the Rhine Graben: Geochemical investigation of a geothermal reservoir. *Geochimica et cosmochimica acta* 61:4281–95.

Aral, H., and Vecchio-Sadus, A. 2008. Toxicity of lithium to humans and the environment - a literature review. *Ecotoxicology and Environmental Safety* 70:349–356.

ArcGIS. 2020. Hellgraue Hintergrundkarte. arcgis.com .

Ariza, M. J., D. J. Jones, J. Rozière, R. Chitrakar, and K. Ooi. 2006. Probing the local structure and the role of protons in lithium sorption processes of a new lithium-rich manganese oxide. *Chemistry of Materials* 18:1885–90.

Arnold, G., J. Garche, R. Hemmer, S. Ströbele, C. Vogler, and M. Wohlfahrt-Mehrens. 2003. Fine-particle lithium iron phosphate LiFePO4 synthesized by a new low-cost aqueous precipitation technique. *Journal of Power Sources* 119:247–51.

Asadi Dalini, E., G. Karimi, S. Zandevakili, and M. Goodarzi. 2021. A review on environmental, economic and hydrometallurgical processes of recycling spent lithium-ion batteries. *Mineral Processing and Extractive Metallurgy Review* 42:451–72.

Athanasiadis, K., and B. Helmreich. 2005. Influence of chemical conditioning on the ion exchange capacity and on kinetic of zinc uptake by clinoptilolite. *Water Research* 39:1527–32.

Bajestani, M. B., A. Moheb, and M. Masigol. 2019. Simultaneous optimization of adsorption capacity and stability of hydrothermally synthesized spinel ion sieve composite adsorbents for selective removal of lithium from aqueous solutions. *Industrial & Engineering Chemistry Research* 58:12207–15.

Banks, M. K. 1953. A Method For Concentration oi North Carolina Spodumene Ores.

Banks, D., Markland, H., Smith, P. V., Mendez, C., Rodriguez, J., Huerta, A., and Sæther, O. M. 2004. Distribution, salinity and pH dependence of elements in surface waters of the catchment areas of the Salars of Coipasa and Uyuni, Bolivian Altiplano. *Journal of Geochemical Exploration* 84:141–166.

Barrer, R. M., J. A. Davies, and L. V. C. Rees. 1969. Comparison of the ion exchange properties of zeolites X and Y. *Journal of Inorganic and Nuclear Chemistry* 31:2599–609.

Barrow, N. J. 2008. The description of sorption curves. *European Journal of Soil Science* 59:900–10.

Belova, T. P. 2010. The analysis of sorption extraction of boron and lithium from the geothermal heat-carriers. Proceedings of the World Geothermal Congress, Bali, Indonesia.

Belova, T. P. 2017. Experimental studies in the sorptive extraction of boron and lithium from thermal waters. *Journal of Volcanology and Seismology* 11:136–42.

Belova, T. P. 2019. Adsorption of heavy metal ions (Cu2+, Ni2+, Co2+ and Fe2+) from aqueous solutions by natural zeolite. *Heliyon* 5: e02320.

Benson, T. R., M. A. Coble, J. J. Rytuba, and G. A. Mahood. 2017. Lithium enrichment in intracontinental rhyolite magmas leads to Li deposits in caldera basins. *Nature Communications* 8:1–9.

Beyaz Kayiran, S., and F. Lamari Darkrim. 2002. Synthesis and ionic exchanges of zeolites for gas adsorption. *Surface and Interface Analysis: An International Journal Devoted to the Development and Application of Techniques for the Analysis of Surfaces, Interfaces and Thin Films* 34:100–04.

Blackford, J. C., and F. J. Gilbert. 2007. pH variability and CO2 induced acidification in the North Sea. *Journal of Marine Systems* 64:229–41.

Blanc, P., A. Lassin, P. Piantone, M. Azaroual, N. Jacquemet, A. Fabbri, and E. C. Gaucher. 2012. Thermoddem: A geochemical database focused on low temperature water/rock interactions and waste materials. *Applied Geochemistry* 27:2107–16.

Bohn, H. L., R. A. Myer, and G. A. O'Connor. 2002. *Soil chemistry*. New York, USA: John Wiley & Sons.

Border, S., and L. Sawyer. 2014. Evaporites and brines–geological, hydrological and chemical aspects of resource estimation. *Applied Earth Science* 123:95–106.

Borrmann, T., M. Schweig, and J. H. Johnston. 2019. Transforming silica into silicate–pilot scale removal of problematic silica from geothermal brine. *Chem NZ* 83:63–70 .

Bouguerra, W., M. B. S. Ali, B. Hamrouni, and M. Dhahbi. 2007. Equilibrium and kinetic studies of adsorption of silica onto activated alumina. *Desalination* 206:141–46.

Bowell, R. J., L. Lagos, C. R. de Los Hoyos, and J. Declercq. 2020. Classification and characteristics of natural lithium resources. *Elements: An International Magazine of Mineralogy, Geochemistry, and Petrology* 16:259–64.

Bruggenwert, M. G. M., and A. Kamphorst. 1979. Survey of experimental information on cation exchange in soil systems. In *Developments in Soil Science* 5 G.H. Bolt , 141–203. Amsterdam: Elsevier.

Bukowsky, H., and E. Uhlemann. 1993. Selective extraction of lithium chloride from brines. *Separation Science and Technology* 28:1357–60.

Bundesanstalt für Geowissenschaften und Rohstoffe. 2020. Lithium: Rohstoffwirtschaftliche Steckbriefe. 6.

Butterman, W. C.1988. Current status of the specialty metals. *Mineral Processing and Extractive Metallurgy Review* 3:69–86.

Cao, G., X. Yang, Z. Yin, Y. Lei, H. Wang, and J. Li. 2019. Synthesis, adsorption properties and stability of Cr-doped lithium ion sieve in salt lake brine. *Bulletin of the Chemical Society of Japan* 92:1205–10.

Carland, R. M., and F. F. Aplan. 1995. Improving the ion-exchange capacity and elution of Cu+ 2 from natural sedimentary zeolites. *Mining, Metallurgy & Exploration* 12:210–18.

Chaban, M. O., L. M. Rozhdestvenska, O. V. Palchyk, Y. S. Dzyazko, and O. G. Dzyazko. 2019. Structural characteristics and sorption properties of lithium-selective composite materials based on TiO 2 and MnO 2. *Applied Nanoscience* 9:1037–45.

Chang, F.-R. C., N. T. Skipper, and G. Sposito. 1997. Monte Carlo and molecular dynamics simulations of interfacial structure in lithium-montmorillonite hydrates. *Langmuir* 13:2074–82.

Chitrakar, R., and M. Abe. 1988. Synthetic inorganic ion exchange materials XLVII. Preparation of a new crystalline antimonic acid HSbO3. O. 12H2O. *Materials Research Bulletin* 23:1231–40.

Chitrakar, R., and M. Abe. 1989. Synthetic inorganic ion-exchange materials. XLVIII. ion-exchange reaction of alkali metal Ions/H+ on monoclinic antimonic acid. *Solvent Extraction and Ion Exchange* 7:721–33.

Chitrakar, R., H. Kanoh, Y. Miyai, and K. Ooi. 2000. A new type of manganese oxide (MnO2⊙ 0.5 H2O) derived from Li1. 6Mn1. 6O4 and its lithium ion-sieve properties. *Chemistry of Materials* 12:3151–57.

Chitrakar, R., Y. Makita, K. Ooi, and A. Sonoda. 2013. Magnesium-doped manganese oxide with lithium ion-sieve property: Lithium adsorption from salt lake brine. *Bulletin of the Chemical Society of Japan* 86:850–55.

Chitrakar, R., Y. Makita, K. Ooi, and A. Sonoda. 2014. Synthesis of iron-doped manganese oxides with an ion-sieve property: Lithium adsorption from Bolivian brine. *Industrial & Engineering Chemistry Research* 53:3682–88.

Choubey, P. K., K.-S. Chung, M.-S. Kim, J.-C. Lee, and R. R. Srivastava. 2017. Advance review on the exploitation of the prominent energy-storage element Lithium. Part II: From sea water and spent lithium ion batteries (LIBs). *Minerals Engineering* 110:104–21.

Choubey, P. K., M.-S. Kim, R. R. Srivastava, J.-C. Lee, and J.-Y. Lee. 2016. Advance review on the exploitation of the prominent energy-storage element: Lithium. Part I: From mineral and brine resources. *Minerals Engineering* 89:119–37.

Cisternas, L. A., J. I. Ordóñez, R. I. Jeldres, and R. Serna-Guerrero. 2021. Toward the implementation of circular economy strategies: An overview of the current situation in mineral processing. *Mineral Processing and Extractive Metallurgy Review* 1–23.

Clearfield, A., and J. Troup. 1970. Mechanism of ion exchange in crystalline zirconium phosphate. II. Lithium ion exchange of. alpha.-zirconium phosphate. *The Journal of Physical Chemistry* 74:314–17.

Clearfield, A., and D. A. Tuhtar. 1976. The mechanism of ion exchange in zirconium phosphates. 15. The effect of crystallinity of the exchange on lithium (1+)/hydrogen (1+) exchange of. alpha.-zirconium phosphate. *The Journal of Physical Chemistry* 80:1296–301.

Cole, K. E., Y. Paik, R. J. Reeder, M. Schoonen, and C. P. Grey. 2004. 2H MAS NMR studies of deuterated goethite (α-FeOOD). *The Journal of Physical Chemistry. B* 108:6938–40.

Colella, C. 1996. Ion exchange equilibria in zeolite minerals. *Mineralium Deposita* 31:554–62.

Collins, A. G. E. N. E., and J. D. Vine. 1976. Lithium abundance in oilfield waters. *Lithium Resources and Requirements by the Year 2000* 1005:116–23.

Condie, K. C. 1993. Chemical composition and evolution of the upper continental crust: Contrasting results from surface samples and shales. *Chemical Geology* 104:1–37.

Corma, A. 2003. State of the art and future challenges of zeolites as catalysts. *Journal of Catalysis* 216:298–312.

Danisi, R. M., and F. R. Schilling. 2021. Dehydration and lithium ion-exchange of the open framework vanadium silicate VSH-16Na. *Microporous and Mesoporous Materials* 319:111064.

Dodbiba, G., P. Keeratithakul, Y. Kanemitsu, and T. Fujita. 2014. Optimization of lithium electrosorption from brine deposit. *Geosystem Engineering* 17:157–62.

Dodd, J. L., B. Fultz, and R. Yazami. 2006. Determining the phase diagram of LixFePO4. *ECS Transactions* 1:27.

Eckstein, Y., D. H. Yaalon, and S. Yariv. 1970. The effect of lithium on the cation exchange behaviour of crystalline and amorphous clays. *Israel Journal of Chemistry* 8:335–42.

Epstein, J. A., E. M. Feist, J. Zmora, and Y. Marcus. 1981. Extraction of lithium from the dead sea. *Hydrometallurgy* 6:269–75.

Erdem, E., N. Karapinar, and R. Donat. 2004. The removal of heavy metal cations by natural zeolites. *Journal of Colloid and Interface Science* 280:309–14.

Evans, R. K. 2008. *An abundance of lithium*. Santiago: World Lithium.

Fasel, D., and M. Q. Tran. 2005. Availability of lithium in the context of future D–T fusion reactors. *Fusion Engineering and Design* 75:1163–68.

Feng, Q., H. Kanoh, Y. Miyai, and K. Ooi. 1995a. Alkali metal ions insertion/extraction reactions with hollandite-type manganese oxide in the aqueous phase. *Chemistry of Materials* 7:148–53.

Feng, Q., H. Kanoh, Y. Miyai, and K. Ooi. 1995b. Hydrothermal synthesis of lithium and sodium manganese oxides and their metal ion extraction/insertion reactions. *Chemistry of Materials* 7:1226–32.

Feng, Q., Y. Miyai, H. Kanoh, and K. Ooi. 1992. Lithium (1+) extraction/insertion with spinel-type lithium manganese oxides. Characterization of redox-type and ion-exchange-type sites. *Langmuir* 8:1861–67.

Ferreira, C. A. M., J. A. C. Ponciano, D. S. Vaitsman, and D. V. Pérez. 2007. Evaluation of the corrosivity of the soil through its chemical composition. *Science of the Total Environment* 388:250–55.

Flexer, V., C. F. Baspineiro, and C. I. Galli. 2018. Lithium recovery from brines: A vital raw material for green energies with a potential environmental impact in its mining and processing. *Science of the Total Environment* 639:1188–204.

Fukuda, H. 2019. Lithium extraction from brine with ion exchange resin and ferric phosphate. Vancouver: University of British Columbia.

Gaikwad, R. W., S. A. Misal, and D. V. Gupta. 2011. Removal of metal from acid mine drainage (AMD) by using natural zeolite of Nizarneshwar Hills of Western India. *Arabian Journal of Geosciences* 4:85–89.

Gao, A., X. Hou, Z. Sun, S. Li, H. Li, and J. Zhang. 2019. Lithium-desorption mechanism in LiMn 2 O 4, Li 1.33 Mn 1.67 O 4, and Li 1.6 Mn 1.6 O 4 according to precisely controlled acid treatment and density functional theory calculations. *Journal of Materials Chemistry A* 7:20878–90.

Garcia, M. G., L. G. Borda, L. V. Godfrey, R. L. L. Steinmetz, and A. Losada-Calderon. 2020. Characterization of lithium cycling in the Salar De Olaroz, Central Andes, using a geochemical and isotopic approach. *Chemical Geology* 531:119340.

Gaskova, O. L., and M. B. Bukaty. 2008. Sorption of different cations onto clay minerals: Modelling approach with ion exchange and surface complexation. *Physics and Chemistry of the Earth, Parts A/B/C* 33:1050–55.

Gast, R. G., and W. D. Klobe. 1971. Sodium-lithium exchange equilibria on vermiculite at 25 and 50 C. *Clays and Clay Minerals* 19:311–19.

Gentili, V., S. Brutti, L. J. Hardwick, A. R. Armstrong, S. Panero, and P. G. Bruce. 2012. Lithium insertion into anatase nanotubes. *Chemistry of Materials* 24:4468–76.

Goldberg, V., D. Winter, F. Nitschke, M. Rath, S. Held, L. Spitzmüller, I. Budach, M. Pavez, D. Morata, and J. Koschikowski. 2021. The potential of raw material extraction from thermal brines–successful milestones of the BrineMine project. *Oil Gas-European Magazine* 47:26–33 .

Gorham, E. 1956. The chemical composition of some western Irish fresh waters. *Proceedings of the Royal Irish Academy. Section B: Biological, Geological and Chemical Science* 58:237–243.

Gourcerol, B., E. Gloaguen, J. Melleton, J. Tuduri, and X. Galiegue. 2019. Re-assessing the European lithium resource potential–A review of hard-rock resources and metallogeny. *Ore Geology Reviews* 109:494–519.

Greene-Kelly, R. 1955. Lithium absorption by kaolin minerals. *The Journal of Physical Chemistry* 59:1151–52.

Gruber, P. W., P. A. Medina, G. A. Keoleian, S. E. Kesler, M. P. Everson, and T. J. Wallington. 2011. Global lithium availability: A constraint for electric vehicles? *Journal of Industrial Ecology* 15:760–75.

Gu, D., W. Sun, G. Han, Q. Cui, and H. Wang. 2018. Lithium ion sieve synthesized via an improved solid state method and adsorption performance for West Taijinar Salt Lake brine. *Chemical Engineering Journal* 350:474–83.

Guneysu, S. 2020. Lithium sorption from aqueous solution with cationic resins. *Desalination and Water Treatment* 177:102–08.

Haas-Nüesch, R., F. Heberling, D. Schild, J. Rothe, K. Dardenne, S. Jähnichen, E. Eiche, C. Marquardt, V. Metz, and T. Schäfer. 2018. Mineralogical characterization of scalings formed in geothermal sites in the Upper Rhine Graben before and after the application of sulfate inhibitors. *Geothermics* 71:264–73.

Haklıdır, F. S. T., and T. Ö. Balaban. 2019. A review of mineral precipitation and effective scale inhibition methods at geothermal power plants in West Anatolia (Turkey). *Geothermics* 80:103–18.

Han, Y., H. Kim, and J. Park. 2012. Millimeter-sized spherical ion-sieve foams with hierarchical pore structure for recovery of lithium from seawater. *Chemical Engineering Journal* 210:482–89.

Harvianto, G. R., S.-H. Kim, and C.-S. Ju. 2016. Solvent extraction and stripping of lithium ion from aqueous solution and its application to seawater. *Rare Metals* 35:948–53.

Hawash, S., E. Abd El Kader, and G. El Diwani. 2010. Methodology for selective adsorption of lithium ions onto polymeric aluminium (III) hydroxide. *Journal of American Science* 6:301–09.

Heidari, N., and P. Momeni. 2017. Selective adsorption of lithium ions from Urmia Lake onto aluminum hydroxide. *Environmental Earth Sciences* 76:1–8.

Heidary, F., A. R. Khodabakhshi, and A. N. Kharat. 2016. Novel ion-exchange nanocomposite membrane containing in-situ formed FeOOH nanoparticles: Synthesis, characterization and transport properties. *Korean Journal of Chemical Engineering* 33:1380–90.

Helfferich, F. G. 1995. *Ion exchange*. New York, USA: Dover Publications, Inc.

Helmke, P. A., and D. L. Sparks. 1996. Lithium, sodium, potassium, rubidium, and cesium. *Methods of Soil Analysis: Part 3 Chemical Methods* 5:551–74.

Hong, H.-J., T. Ryu, I.-S. Park, M. Kim, J. Shin, B.-G. Kim, and K.-S. Chung. 2018. Highly porous and surface-expanded spinel hydrogen manganese oxide (HMO)/Al2O3 composite for effective lithium (Li) recovery from seawater. *Chemical Engineering Journal* 337:455–61.

Hoshino, T. 2013. Preliminary studies of lithium recovery technology from seawater by electrodialysis using ionic liquid membrane. *Desalination* 317:11–16.

Houston, J. 2010. Technical report on the Cauchari Project, Jujuy Province, Argentina. ed. Orocobre Ltd. Queensland: FloSolutions.

Hoyer, M., N.-A. Kummer, and B. Merkel. 2015. Sorption of lithium on bentonite, kaolin and zeolite. *Geosciences* 5:127–40.

Hunter, J. C. 1981. Preparation of a new crystal form of manganese dioxide: λ-MnO2. *Journal of Solid State Chemistry* 39:142–47.

Inglezakis, V. J., A. A. Zorpas, M. D. Loizidou, and H. P. Grigoropoulou. 2005. The effect of competitive cations and anions on ion exchange of heavy metals. *Separation and Purification Technology* 46:202–07.

Inoue, Y., and M. Abe. 1996. Synthetic inorganic ion exchange materials. XLIII. Ion exchange mechanism of lithium ions on cubic tantalic acid. *Solvent Extraction and Ion Exchange* 14:507–18.

Intaranont, N., N. Garcia-Araez, A. L. Hector, J. A. Milton, and J. R. Owen. 2014. Selective lithium extraction from brines by chemical reaction with battery materials. *Journal of Materials Chemistry A* 2:6374–77.

Ji, Z.-Y., F.-J. Yang, -Y.-Y. Zhao, J. Liu, N. Wang, and J.-S. Yuan. 2017. Preparation of titanium-base lithium ionic sieve with sodium persulfate as eluent and its performance. *Chemical Engineering Journal* 328:768–75.

Jiang, H., Y. Yang, S. Sun, and J. Yu. 2020a. Adsorption of lithium ions on lithium-aluminum hydroxides: Equilibrium and kinetics. *The Canadian Journal of Chemical Engineering* 98:544–55.

Jiang, H., Y. Yang, and J. Yu. 2020b. Application of concentration-dependent HSDM to the lithium adsorption from brine in fixed bed columns. *Separation and Purification Technology* 241:116682.

Joshi, D. R., and N. Adhikari. 2019. An overview on common organic solvents and their toxicity. *Journal of Pharmaceutical Research International* 28:1–18.

Kamran, U., and S.-J. Park. 2020. Functionalized titanate nanotubes for efficient lithium adsorption and recovery from aqueous media. *Journal of Solid State Chemistry* 283:121157.

Kaunda, R. B. 2020. Potential environmental impacts of lithium mining. *Journal of Energy & Natural Resources Law* 38:237–44.

Kawamoto, H., and W. Tamaki. 2011. *Trends in supply of lithium resources and demand of the resources for automobiles*.Tokyo, Japan: NISTEP Science & Technology Foresight Center.

Kaya, E., S. J. Zarrouk, and M. J. O'Sullivan. 2011. Reinjection in geothermal fields: A review of worldwide experience. *Renewable and Sustainable Energy Reviews* 15:47–68.

Kelly, J. C., M. Wang, Q. Dai, and O. Winjobi. 2021. Energy, greenhouse gas, and water life cycle analysis of lithium carbonate and lithium hydroxide monohydrate from brine and ore resources and their use in lithium ion battery cathodes and lithium ion batteries. *Resources, Conservation and Recycling* 174:105762.

Kesler, S. E., P. W. Gruber, P. A. Medina, G. A. Keoleian, M. P. Everson, and T. J. Wallington. 2012. Global lithium resources: Relative importance of pegmatite, brine and other deposits. *Ore Geology Reviews* 48:55–69.

Kim, J., and C. P. Grey. 2010. 2H and 7Li solid-state MAS NMR study of local environments and lithium adsorption on the iron (III) oxyhydroxide, akaganeite (β-FeOOH). *Chemistry of Materials* 22:5453–62.

Kim, J., U. G. Nielsen, and C. P. Grey. 2008. Local environments and lithium adsorption on the iron oxyhydroxides lepidocrocite (γ-FeOOH) and goethite (α-FeOOH): A 2H and 7Li solid-state MAS NMR study. *Journal of the American Chemical Society* 130:1285–95.

Kloprogge, J. T., S. Komarneni, and J. E. Amonette. 1999. Synthesis of smectite clay minerals: A critical review. *Clays and Clay Minerals* 47:529–54.

Kudryavtsev, P. G. 2016. Lithium in nature, application, methods of extraction. *Journal" Scientific Israel-Technological Advantages* 18:63–83.

Kuss, C., M. Carmant-Dérival, N. D. Trinh, G. Liang, and S. B. Schougaard. 2014. Kinetics of heterosite iron phosphate lithiation by chemical reduction. *The Journal of Physical Chemistry C* 118:19524–28.

Lagaly, G., and S. Ziesmer. 2003. Colloid chemistry of clay minerals: The coagulation of montmorillonite dispersions. *Advances in Colloid and Interface Science* 100:105–28.

Lawagon, C. P., G. M. Nisola, J. Mun, A. Tron, R. E. C. Torrejos, J. G. Seo, H. Kim, and W.-J. Chung. 2016. Adsorptive Li+ mining from liquid resources by H2TiO3: Equilibrium, kinetics, thermodynamics, and mechanisms. *Journal of Industrial and Engineering Chemistry* 35:347–56.

Lee, D. A., W. L. Taylor, W. J. McDowell, and J. S. Drury. 1968. Solvent extraction of lithium. *Journal of Inorganic and Nuclear Chemistry* 30:2807–21.

Lemaire, J., L. Svecova, F. Lagallarde, R. Laucournet, and P.-X. Thivel. 2014. Lithium recovery from aqueous solution by sorption/desorption. *Hydrometallurgy* 143:1–11.

Li, N. N., R. P. Cahn, D. Naden, and R. W. M. Lai. 1983. Liquid membrane processes for copper extraction. *Hydrometallurgy* 9:277–305.

Li, X., Y. Chao, L. Chen, W. Chen, J. Luo, C. Wang, P. Wu, H. Li, and W. Zhu. 2020. Taming wettability of lithium ion sieve via different TiO2 precursors for effective Li recovery from aqueous lithium resources. *Chemical Engineering Journal* 392:123731.

Li, Z., C. Li, X. Liu, L. Cao, P. Li, R. Wei, X. Li, D. Guo, K.-W. Huang, and Z. Lai. 2021. Continuous electrical pumping membrane process for seawater lithium mining. *Energy & Environmental Science* 14:3152–59.

Li, W., and X.-M. Liu. 2020. Experimental investigation of lithium isotope fractionation during kaolinite adsorption: Implications for chemical weathering. *Geochimica et cosmochimica acta* 284:156–72.

Li, L., W. Qu, F. Liu, T. Zhao, X. Zhang, R. Chen, and F. Wu. 2014. Surface modification of spinel λ-MnO2 and its lithium adsorption properties from spent lithium ion batteries. *Applied Surface Science* 315:59–65.

Limousin, G., J.-P. Gaudet, L. Charlet, S. Szenknect, V. Barthes, and M. Krimissa. 2007. Sorption isotherms: A review on physical bases, modeling and measurement. *Applied Geochemistry* 22:249–75.

Liu, W., D. B. Agusdinata, and S. W. Myint. 2019d. Spatiotemporal patterns of lithium mining and environmental degradation in the Atacama Salt Flat, Chile. *International Journal of Applied Earth Observation and Geoinformation* 80:145–56.

Liu, X., X. Chen, Z. Zhao, and X. Liang. 2014. Effect of Na+ on Li extraction from brine using LiFePO4/FePO4 electrodes. *Hydrometallurgy* 146:24–28.

Liu, D.-F., S.-Y. Sun, and J.-G. Yu. 2019a. A new high-efficiency process for Li+ recovery from solutions based on LiMn2O4/λ-MnO2 materials. *Chemical Engineering Journal* 377:119825.

Liu, K., Q. Tan, L. Liu, and J. Li. 2019c. Acid-free and selective extraction of lithium from spent lithium iron phosphate batteries via a mechanochemically induced isomorphic substitution. *Environmental Science & Technology* 53:9781–88.

Liu, W., H. Xu, X. Shi, and X. Yang. 2017. Fractional crystallization for extracting lithium from Cha'erhan tail brine. *Hydrometallurgy* 167:124–28.

Liu, L., H. Zhang, Y. Zhang, D. Cao, and X. Zhao. 2015. Lithium extraction from seawater by manganese oxide ion sieve MnO2· 0.5 H2O. *Colloids and Surfaces. A, Physicochemical and Engineering Aspects* 468:280–84.

Liu, G., Z. Zhao, and A. Ghahreman. 2019b. Novel approaches for lithium extraction from salt-lake brines: A review. *Hydrometallurgy* 187:81–100.

Liu, G., Z. Zhao, and L. He. 2020. Highly selective lithium recovery from high Mg/Li ratio brines. *Desalination* 474:114185.

Marazuela, M. A., E. Vázquez-Suñé, C. Ayora, and A. García-Gil. 2020. Towards more sustainable brine extraction in salt flats: Learning from the Salar de Atacama. *Science of the Total Environment* 703:135605.

Marion, G. M., F. J. Millero, M. F. Camões, P. Spitzer, R. Feistel, and C.-T. A. Chen. 2011. pH of seawater. *Marine Chemistry* 126:89–96.

Marthi, R., H. Asgar, G. Gadikota, and Y. R. Smith. 2021. On the structure and lithium adsorption mechanism of layered H2TiO3. *ACS Applied Materials & Interfaces* 13:8361–69.

McCauley, A., C. Jones, and J. Jacobsen. 2009. Soil pH and organic matter. *Nutrient Management Module* 8:1–12.

Melnikov, S., N. Sheldeshov, V. Zabolotsky, S. Loza, and A. Achoh. 2017. Pilot scale complex electrodialysis technology for processing a solution of lithium chloride containing organic solvents. *Separation and Purification Technology* 189:74–81.

Meng, F., J. McNeice, S. S. Zadeh, and A. Ghahreman. 2021. Review of lithium production and recovery from minerals, brines, and lithium-ion batteries. *Mineral Processing and Extractive Metallurgy Review* 42:123–41.

Meroufel, B., O. Benali, M. Benyahia, M. Zenasni, A. Merlin, and B. George. 2013. Removal of Zn (II) from aqueous solution onto kaolin by batch design. *Journal of Water Resource and Protection* 5:669–80.

Meshram, P., and B. D. Pandey. 2018. Advanced review on extraction of nickel from primary and secondary sources. *Mineral Processing and Extractive Metallurgy Review* 40:157–193.

Millennial Lithium Corp. 2020. *Millennial Lithium Corp. Announces commissioning of lithium carbonate pilot plant at its pastos grandes project in Salta, Argentina.*West Vancouver, BC: Millennial Lithium.

Mimura, K., K. Nakamura, K. Yasukawa, S. Machida, J. Ohta, K. Fujinaga, and Y. Kato. 2019. Significant impacts of pelagic clay on average chemical composition of subducting sediments: New insights from discovery of extremely rare-earth elements and yttrium-rich mud at Ocean Drilling Program Site 1149 in the western North Pacific Ocean. *Journal of Asian Earth Sciences* 186:104059.

The Mineral Corporation. 2019. Mineral Resource estimates for the Falchani Lithium Project in the Puno District of Peru. 76.

Mining Data Online. 2021. Sal de vida project. https://miningdataonline.com/property/3228/Sal-de-Vida-Project.aspx

Miyai, Y., K. Ooi, and S. Katoh. 1988. Recovery of lithium from seawater using a new type of ion-sieve adsorbent based on MgMn2O4. *Separation Science and Technology* 23:179–91.

Moazeni, M., H. Hajipour, M. Askari, and M. Nusheh. 2015. Hydrothermal synthesis and characterization of titanium dioxide nanotubes as novel lithium adsorbents. *Materials Research Bulletin* 61:70–75.

Moazzam, P., Y. Boroumand, P. Rabiei, S. S. Baghbaderani, P. Mokarian, F. Mohagheghian, L. J. Mohammed, and A. Razmjou. 2021. Lithium bioleaching: An emerging approach for the recovery of Li from spent lithium ion batteries. *Chemosphere* 277:1–20.

Mohr, S. H., G. M. Mudd, and D. Giurco. 2012. Lithium resources and production: Critical assessment and global projections. *Minerals* 2:65–84.

Moran, S. 2018. Clean water characterization and treatment objectives. An applied guide to water effluent treatment plant design. United States of American. Elsevier BV Inc., 978-0-12-811309-7 Chap 6, 61–67.

Morcos, S. A. 1970. Chemical composition of seawater and the variation of calcium and alkalinity. *ICES Journal of Marine Science* 33:126–33.

Nan, J., D. Han, and X. Zuo. 2005. Recovery of metal values from spent lithium-ion batteries with chemical deposition and solvent extraction. *Journal of Power Sources* 152:278–84.

Navarrete-Casas, R., A. Navarrete-Guijosa, C. Valenzuela-Calahorro, J. D. López-González, and A. García-Rodríguez. 2007. Study of lithium ion exchange by two synthetic zeolites: Kinetics and equilibrium. *Journal of Colloid and Interface Science* 306:345–53.

Nie, X.-Y., S.-Y. Sun, X. Song, and J.-G. Yu. 2017. Further investigation into lithium recovery from salt lake brines with different feed characteristics by electrodialysis. *Journal of Membrane Science* 530:185–91.

Nielsen, U. G., Y. Paik, K. Julmis, M. A. A. Schoonen, R. J. Reeder, and C. P. Grey. 2005. Investigating sorption on iron– oxyhydroxide soil minerals by solid-state NMR spectroscopy: A 6Li MAS NMR Study of Adsorption and Absorption on Goethite. *The Journal of Physical Chemistry. B* 109:18310–15.

Nir, S., D. Hirsch, J. Navrot, and A. Banin. 1986. Specific adsorption of lithium, sodium, potassium, and strontium to montmorillonite: Observations and predictions. *Soil Science Society of America Journal* 50:40–45.

Obaid, S. S., D. K. Gaikwad, M. I. Sayyed, A. L.-R. Khader, and P. P. Pawar. 2018. Heavy metal ions removal from waste water by the natural zeolites. *Materials Today: Proceedings* 5:17930–34.

Odom, I. E. 1984. Smectite clay minerals: Properties and uses. *Philosophical Transactions of the Royal Society of London. Series A: Mathematical and Physical Sciences* 311:391–409.

Ogawa, Y., H. Koibuchi, K. Suto, and C. Inoue. 2014. Effects of the chemical compositions of S alars de U yuni and A tacama Brines on lithium concentration during evaporation. *Resource Geology* 64:91–101.

Ohashi, F., and Y. Tai. 2019. Lithium adsorption from natural brine using surface-modified manganese oxide adsorbents. *Materials Letters* 251:214–17.

Oi, T., M. Endoh, M. Narimoto, and M. Hosoe. 2000. Ion and lithium isotope selectivity of monoclinic antimonic acid. *Journal of Materials Science* 35:509–13.

Olson, C. L., J. Nelson, and M. S. Islam. 2006. Defect chemistry, surface structures, and lithium insertion in anatase TiO2. *The Journal of Physical Chemistry. B* 110:9995–10001.

Ooi, K., Y. Makita, A. Sonoda, R. Chitrakar, Y. Tasaki-Handa, and T. Nakazato. 2016. Modelling of column lithium adsorption from pH-buffered brine using surface Li+/H+ ion exchange reaction. *Chemical Engineering Journal* 288:137–45.

Ooi, K., Y. Miyai, and S. Katoh. 1987. Lithium-ion sieve property of λ;-type manganese oxide. *Solvent Extraction and Ion Exchange* 5:561–72.

Ooi, K., Y. Miyai, S. Katoh, H. Maeda, and M. Abe. 1989. Topotactic lithium (1+) insertion to. lambda.-manganese dioxide in the aqueous phase. *Langmuir* 5:150–57.

Ooi, K., Y. Miyai, and J. Sakakihara. 1991. Mechanism of lithium (1+) insertion in spinel-type manganese oxide. Redox and ion-exchange reactions. *Langmuir* 7:1167–71.

Palagonia, M. S., D. Brogioli, and F. La Mantia. 2020. Lithium recovery from diluted brine by means of electrochemical ion exchange in a flow-through-electrodes cell. *Desalination* 475:114192.

Palmer, A. N., and M. V. Palmer. 2003. Geochemistry of capillary seepage in Mammoth Cave. *Speleogenesis and Evolution of Karst Aquifers* 1:1–8.

Park, H., N. Singhal, and E. H. Jho. 2015. Lithium sorption properties of HMnO in seawater and wastewater. *Water Research* 87:320–27.

Pauwels, H., M. Brach, and C. Fouillac. 1990. Lithium recovery from geothermal waters of Cesano (Italy) and Cronenbourg (Alsace, France). *Geochimica et Cosmochimica Acta* 57 :2737–2749.

Pauwels, H., M. Brach, and C. Fouillac. 1993. Chemistry and isotopes of deep geothermal saline fluids in the Upper Rhine Graben: Origin of compounds and water-rock interactions. *Geochimica et cosmochimica acta* 57:2737–49.

Peerawattuk, I., and E. R. Bobicki. 2018. Lithium Extraction and Utilization: A Historical Perspective. In *Extraction 2018. The Minerals, Metals & Materials Series. Springer, Cham* 2209–2224.

Pirajno, F. 2012. *Hydrothermal mineral deposits: Principles and fundamental concepts for the exploration geologist*. Berlin Heidelberg: Springer Science & Business Media.

Prodromou, K. P. 2016. Lithium adsorption on amorphous aluminum hydroxides and gibbsite. *Eurasian Journal of Soil Science* 5:13–16.

Pueyo, J. J., G. Chong, and C. Ayora. 2017. Lithium saltworks of the Salar de Atacama: A model for MgSO4-free ancient potash deposits. *Chemical Geology* 466:173–86.

Qian, F., M. Guo, Z. Qian, Q. Li, Z. Wu, and Z. Liu. 2019. Highly lithium adsorption capacities of H1. 6Mn1. 6O4 ion-sieve by ordered array structure. *ChemistrySelect* 4:10157–63.

Qiao, D., G. Wang, T. Gao, B. Wen, and T. Dai. 2021. Potential impact of the end-of-life batteries recycling of electric vehicles on lithium demand in China: 2010–2050. *Science of the Total Environment* 764:142835.

Rao, G. P. C., S. Satyaveni, A. Ramesh, K. Seshaiah, K. S. N. Murthy, and N. V. Choudary. 2006. Sorption of cadmium and zinc from aqueous solutions by zeolite 4A, zeolite 13X and bentonite. *Journal of Environmental Management* 81:265–72.

Reidel, F., and P. Ehren. 2018. Technical report: Lithium and potassium resources. Cauchari Project, Jujuy Province, Argentina.

Rio Tinto. 2020. *Rio Tinto declares maiden Ore Reserve at Jadar*. Melbourne, Australia: Rio Tinto Limited. https://www.riotinto.com/news/releases/2020/Rio-Tinto-declares-maiden-Ore-Reserve-at-Jadar

Rydberg, J. 2004. *Solvent extraction principles and practice, revised and expanded*. New York, USA: CRC press.

Ryu, T., J. C. Ryu, J. Shin, D. H. Lee, Y. H. Kim, and K.-S. Chung. 2013. Recovery of lithium by an electrostatic field-assisted desorption process. *Industrial & Engineering Chemistry Research* 52:13738–42.

Ryu, T., J. Shin, D.-H. Lee, J. Ryu, I. Park, H. Hong, Y. S. Huh, B.-G. Kim, and K.-S. Chung. 2015. Development of multi-stage column for lithium recovery from an aqueous solution. *Hydrometallurgy* 157:39–43.

Safari, S., B. G. Lottermoser, and D. S. Alessi. 2020. Metal oxide sorbents for the sustainable recovery of lithium from unconventional resources. *Applied Materials Today* 19:100638.

Sakamoto, H., K. Kimura, and T. Shono. 1987. Lithium separation and enrichment by proton-driven cation transport through liquid membranes of lipophilic crown nitrophenols. *Analytical Chemistry* 59:1513–17.

Salakjani, N. K., P. Singh, and A. N. Nikoloski. 2021. Production of lithium–A literature review. Part 2. Extraction from spodumene. *Mineral Processing and Extractive Metallurgy Review* 42:268–83.

Sanjuan, B., R. Millot, C. Innocent, C. Dezayes, J. Scheiber, and M. Brach. 2016. Major geochemical characteristics of geothermal brines from the Upper Rhine Graben granitic basement with constraints on temperature and circulation. *Chemical Geology* 428:27–47.

Sato, K., D. M. Poojary, A. Clearfield, M. Kohno, and Y. Inoue 1997. The surface structure of the proton-exchanged lithium manganese oxide spinels and their lithium-ion sieve properties. *Journal of Solid State Chemistry* 131:84–93.

Savannah Resources Plc. 2010-2021. Press release: Mina do Barroso Project, Portugal. https://www.savannahresources.com/assets/mina-do-barroso

Schmidt, M. 2017. *Rohstoffrisikobewertung - Lithium* . Berlin: DERA Rohstoffinformationen 33.

Shi, C., Y. Jing, J. Xiao, X. Wang, Y. Yao, and Y. Jia 2017. Solvent extraction of lithium from aqueous solution using non-fluorinated functionalized ionic liquids as extraction agents. *Separation and Purification Technology* 172:473–79.

Shi, X.-C., Z.-B. Zhang, D.-F. Zhou, L.-F. Zhang, B.-Z. Chen, and L.-L. Yu. 2013. Synthesis of Li+ adsorbent (H2TiO3) and its adsorption properties. *Transactions of Nonferrous Metals Society of China* 23:253–59.

Slunitschek, K., J. Kolb, and E. Eiche. 2021. Lithium extraction from geothermal brines. *GIT Laborfachzeitschrift* 7-8: 14–16.

Somrani, A. A. H. H., A. H. Hamzaoui, and M. Pontie 2013. Study on lithium separation from salt lake brines by nanofiltration (NF) and low pressure reverse osmosis (LPRO). *Desalination* 317:184–92.

Song, J. F., L. D. Nghiem, X.-M. Li, and T. He 2017. Lithium extraction from Chinese salt-lake brines: Opportunities, challenges, and future outlook. *Environmental Science: Water Research & Technology* 3:593–97.

Stober, I., and K. Bucher. 2012. *Geothermie*. Berlin: Springer.

Stringfellow, W. T., and P. F. Dobson 2021. Technology for the Recovery of Lithium from Geothermal Brines. *Energies* 14:6805.

Su, H., Z. Li, J. Zhang, Z. Zhu, L. Wang, and T. Qi. 2020. Recovery of lithium from salt lake brine using a mixed ternary solvent extraction system consisting of TBP, FeCl3 and P507. *Hydrometallurgy* 197:105487.

Sullivan, E. J., P. W. Reimus, S. J. Chipera, and D. Counce 2003. Effects of mineralogy, exchange capacity, surface area and grain size on lithium sorption to zeolitic alluvium near Yucca Mountain, Nevada. *Clays and Clay Minerals* 51:634–43.

Sun, S.-Y., L.-J. Cai, X.-Y. Nie, X. Song, and J.-G. Yu. 2015. Separation of magnesium and lithium from brine using a Desal nanofiltration membrane. *Journal of Water Process Engineering* 7:210–17.

Sun, S., X. Yu, M. Li, J. Duo, Y. Guo, and T. Deng 2020. Green recovery of lithium from geothermal water based on a novel lithium iron phosphate electrochemical technique. *Journal of Cleaner Production* 247:119178.

Sverjensky, D. A., E. L. Shock, and H. C. Helgeson 1997. Prediction of the thermodynamic properties of aqueous metal complexes to 1000 C and 5 kb. *Geochimica et cosmochimica acta* 61:1359–412.

Swain, B. 2016. Separation and purification of lithium by solvent extraction and supported liquid membrane, analysis of their mechanism: A review. *Journal of Chemical Technology and Biotechnology* 91:2549–62.

Swain, B. 2017. Recovery and recycling of lithium: A review. *Separation and Purification Technology* 172:388–403.

Sykes, J. 2019. A global overview of the geology and economics of lithium production.

Tadesse, B., F. Makuei, B. Albijanic, and L. Dyer 2019. The beneficiation of lithium minerals from hard rock ores: A review. *Minerals Engineering* 131:170–84.

Taghvaei, N., E. Taghvaei, and M. Askari 2020. Synthesis of anodized TiO2 nanotube arrays as ion sieve for lithium extraction. *ChemistrySelect* 5:10339–45.

Takeno, N. 2005. Atlas of Eh-pH diagrams. *Geological Survey of Japan Open File Report* 419:102.

Tian, L., W. Ma, and M. Han 2010. Adsorption behavior of Li+ onto nano-lithium ion sieve from hybrid magnesium/lithium manganese oxide. *Chemical Engineering Journal* 156:134–40.

US Geological Survey. 2021. *Mineral commodity summaries 2021: Lithium*. (Reston, VA: U.S. Geological Survey)

Valdez, S. K., H. R. Flores, and A. Orce. 2016. Influence of the evaporation rate over lithium recovery from brines. *World Journal of Research and Review* 3:66–70 .

Hoek, E.M., Tarabara, V.V. and Van der Bruggen, B. 2013. Nanofiltration. In *Encyclopedia of Membrane Science and Technology* (eds E.M. Hoek and V.V. Tarabara). https://doi.org/10.1002/9781118522318.emst077)

Ventura, S., S. Bhamidi, M. Hornbostel, and A. Nagar, International, SRI. 2020. *Selective Recovery of Lithium from Geothermal Brines: Final Project Report.*California, USA: California Energy Commission.

Ventura, S., S. Bhamidi, M. Hornbostel, A. Nagar, and E. Perea 2016. *Selective recovery of metals from geothermal brines*. Menlo Park, CA (United States): SRI International.

Wang, S., Li, P., Cui, W., Zhang, H., Wang, H., Zheng, S., and Zhang, Y. 2016. Hydrothermal synthesis of lithium-enriched β-Li2TiO3 with an ion-sieve application: excellent lithium adsorption. *RSC advances* 6:102608–102616.

Wang, L., C. G. Meng, M. Han, and W. Ma 2008. Lithium uptake in fixed-pH solution by ion sieves. *Journal of Colloid and Interface Science* 325:31–40.

Wang, S., M. Zhang, Y. Zhang, Y. Zhang, S. Qiao, and S. Zheng 2019. High adsorption performance of the Mo-doped titanium oxide sieve for lithium ions. *Hydrometallurgy* 187:30–37.

Warnock, S. J., R. Sujanani, E. S. Zofchak, S. Zhao, T. J. Dilenschneider, K. G. Hanson, S. Mukherjee, V. Ganesan, B. D. Freeman, and M. M. Abu-Omar 2021. Engineering Li/Na selectivity in 12-Crown -4–functionalized polymer membranes. *Proceedings of the National Academy of Sciences* 118:1–8 .

Warren, I. 2021. Techno-economic analysis of lithium extraction from geothermal brines. National Renewable Energy Lab.(NREL), Golden, CO (United States).

Wedepohl K. H. (1995). The composition of the continental crust. *Geochimica et Cosmochimica Acta*, 59:1217–1232.

Wei, S., Y. Wei, T. Chen, C. Liu, and Y. Tang 2020. Porous lithium ion sieves nanofibers: General synthesis strategy and highly selective recovery of lithium from brine water. *Chemical Engineering Journal* 379:122407.

Wen, X., P. Ma, C. Zhu, Q. He, and X. Deng 2006. Preliminary study on recovering lithium chloride from lithium-containing waters by nanofiltration. *Separation and Purification Technology* 49:230–36.

Weng, D., H. Duan, Y. Hou, J. Huo, L. Chen, F. Zhang, and J. Wang 2020. Introduction of manganese based lithium-ion Sieve-A review. *Progress in Natural Science: Materials International* 30:139–52.

Wenger, M., and T. Armbruster 1991. Crystal chemistry of lithium: Oxygen coordination and bonding. *European Journal of Mineralogy* 3:387–400.

Williams, L. B., and R. L. Hervig 2005. Lithium and boron isotopes in illite-smectite: The importance of crystal size. *Geochimica et cosmochimica acta* 69:5705–16.

Wiśniewska, M., G. Fijałkowska, I. Ostolska, W. Franus, A. Nosal-Wiercińska, B. Tomaszewska, J. Goscianska, and G. Wójcik 2018. Investigations of the possibility of lithium acquisition from geothermal water using natural and synthetic zeolites applying poly (acrylic acid). *Journal of Cleaner Production* 195:821–30.

Wunder, B., A. Meixner, R. L. Romer, A. Feenstra, G. Schettler, and W. Heinrich 2007. Lithium isotope fractionation between Li-bearing staurolite, Li-mica and aqueous fluids: An experimental study. *Chemical Geology* 238:277–90.

Xiang, W., S. Liang, Z. Zhou, W. Qin, and W. Fei 2016. Extraction of lithium from salt lake brine containing borate anion and high concentration of magnesium. *Hydrometallurgy* 166:9–15.

Xiao, J., X. Nie, S. Sun, X. Song, P. Li, and J. Yu 2015b. Lithium ion adsorption–desorption properties on spinel Li4Mn5O12 and pH-dependent ion-exchange model. *Advanced Powder Technology* 26:589–94.

Xiao, J.-L., S.-Y. Sun, X. Song, P. Li, and Y. J-g. 2015a. Lithium ion recovery from brine using granulated polyacrylamide–MnO2 ion-sieve. *Chemical Engineering Journal* 279:659–66.

Xiao, G., K. Tong, L. Zhou, J. Xiao, S. Sun, P. Li, and J. Yu 2012. Adsorption and desorption behavior of lithium ion in spherical PVC–MnO2 ion sieve. *Industrial & Engineering Chemistry Research* 51:10921–29.

Xu, X., Y. Chen, P. Wan, K. Gasem, K. Wang, T. He, H. Adidharma, and M. Fan 2016. Extraction of lithium with functionalized lithium ion-sieves. *Progress in Materials Science* 84:276–313.

Xu, C., Q. Dai, L. Gaines, M. Hu, A. Tukker, and B. Steubing 2020. Future material demand for automotive lithium-based batteries. *Communications Materials* 1:1–10.

Xue, F., X. Zhang, Y. Niu, C. Yi, S. Ju, and W. Xing 2020. Preparation and evaluation of α-Al2O3 supported lithium ion sieve membranes for Li+ extraction. *Chinese Journal of Chemical Engineering* 28:2312–18.

Yaksic, A., and J. E. Tilton 2009. Using the cumulative availability curve to assess the threat of mineral depletion: The case of lithium. *Resources Policy* 34:185–94.

Yang, X., Y. Makita, J. Hosokawa, K. Sakane, and K. Ooi 2005. Preparation and alkali metal ion exchange properties of protonated Rb8Nb22O59 compound. *Chemistry of Materials* 17:5420–27.

Yang, Y., X. Meng, H. Cao, X. Lin, C. Liu, Y. Sun, Y. Zhang, and Z. Sun 2018. Selective recovery of lithium from spent lithium iron phosphate batteries: A sustainable process. *Green Chemistry* 20:3121–33.

Yoshinaga, T., K. Kawano, and H. Imoto 1986. Basic study on lithium recovery from lithium containing solution. *Bulletin of the Chemical Society of Japan* 59:1207–13.

Yoshizuka, K., S. Nishihama, M. Takano, and S. Asano. 2021. Lithium recovery from brines with Novel λ-MnO2 adsorbent synthesized by hydrometallurgical method. *Solvent Extraction and Ion Exchange* 39:604–621.

Zamzow, M. J., B. R. Eichbaum, K. R. Sandgren, and D. E. Shanks 1990. Removal of heavy metals and other cations from wastewater using zeolites. *Separation Science and Technology* 25:1555–69.

Zamzow, M. J., and J. E. Murphy 1992. Removal of metal cations from water using zeolites. *Separation Science and Technology* 27:1969–84.

Zandvakili, S., and M. Ranjbar 2018. Preparation and characterisation of lithium ion exchange composite for the recovery of lithium from brine. *Mineral Processing and Extractive Metallurgy* 127:176–81.

Zhang, Y., Y. Hu, L. Wang, and W. Sun 2019. Systematic review of lithium extraction from salt-lake brines via precipitation approaches. *Minerals Engineering* 139:105868.

Zhang, Q.-H., S.-P. Li, S.-Y. Sun, X.-S. Yin, and J.-G. Yu. 2010b. LiMn2O4 spinel direct synthesis and lithium ion selective adsorption. *Chemical Engineering Science* 65:169–73.

Zhang, Q.-H., S.-P. Li, S.-Y. Sun, X.-S. Yin, and J.-G. Yu. 2010c. Lithium selective adsorption on low-dimensional titania nanoribbons. *Chemical Engineering Science* 65:165–68.

Zhang, Q.-H., S. Sun, S. Li, H. Jiang, and J.-G. Yu. 2007. Adsorption of lithium ions on novel nanocrystal MnO2. *Chemical Engineering Science* 62:4869–74.

Zhang, D., C.-H. Zhou, C.-X. Lin, D.-S. Tong, and Y. W-h. 2010a. Synthesis of clay minerals. *Applied Clay Science* 50:1–11.

Zhao, Q., J.-M. Gao, Y. Guo, and F. Cheng 2018. Facile synthesis of magnetically recyclable Fe-doped lithium ion sieve and its Li adsorption performance. *Chemistry Letters* 47:1308–10.

Zhao, Z., X. Si, X. Liu, L. He, and X. Liang 2013. Li extraction from high Mg/Li ratio brine with LiFePO4/FePO4 as electrode materials. *Hydrometallurgy* 133:75–83.

Zhou, C., A. Alshameri, C. Yan, X. Qiu, H. Wang, and Y. Ma 2013. Characteristics and evaluation of synthetic 13X zeolite from Yunnan's natural halloysite. *Journal of Porous Materials* 20:587–94.

Zhu, Q., Aller, R. C., and Fan, Y. 2006. Two-dimensional pH distributions and dynamics in bioturbated marine sediments. *Geochimica et Cosmochimica Acta* 70:4933–4949.

Zhu, G., P. Wang, P. Qi, and C. Gao 2014. Adsorption and desorption properties of Li+ on PVC-H1. 6Mn1. 6O4 lithium ion-sieve membrane. *Chemical Engineering Journal* 235:340–48.

Ziemann, S., D. B. Müller, L. Schebek, and M. Weil 2018. Modeling the potential impact of lithium recycling from EV batteries on lithium demand: A dynamic MFA approach. *Resources, Conservation and Recycling* 133:76–85.

5. Publication

–

Sorption of lithium and competing ions from geothermal brine to lithium manganese oxide sorbent and implication for industrial use

Klemens Slunitschek, Elisabeth Eiche & Jochen Kolb

This work has been published in Separation and Purification Technology (378, 3, 134594) published online: 22 Dec 2025

available online:

https://www.sciencedirect.com/science/article/pii/S1383586625031910?via%3Dihub

DOI: 10.1016/j.seppur.2025.134594

Separation and Purification Technology 378 (2025) 134594

Contents lists available at ScienceDirect

Separation and Purification Technology

journal homepage: www.elsevier.com/locate/seppur

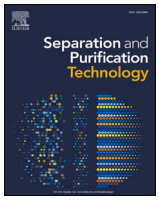

Sorption of lithium and competing ions from geothermal brine to lithium manganese oxide sorbent and implication for industrial use

Klemens Slunitschek [a,b,c,*], Elisabeth Eiche [a,b], Jochen Kolb [a,b]

[a] Chair of Geochemistry and Economic Geology, Institute of Applied Geosciences, Karlsruhe Institute of Technology, Karlsruhe, Germany
[b] Laboratory for Environmental and Raw Materials Analysis (LERA), Institute of Applied Geosciences, Karlsruhe Institute of Technology, Adenauerring 20b, 76131 Karlsruhe, Germany
[c] Magmatic Bio GmbH, Breitenfelder Gasse 14/4., 1080 Vienna, Austria

ARTICLE INFO

Editor: Raquel Aires Barros

Keywords:
Manganese oxide
Selectivity
Geothermal
Brine
direct lithium extraction (DLE)

ABSTRACT

One of the biggest challenges for direct lithium extraction (DLE) from brines, such as geothermal or salar fluids, is the selective extraction of Li with only minor co-extraction of other elements. Due to their high selectivity, spinel-structured lithium manganese oxide (LMO) sorbents are promising for application in DLE. We synthesized the LMO $Li_{1.6}Mn_{1.6}O_4$ and investigated the sorption of Li and competing elements from a geothermal brine of the Upper Rhine Valley. From the brine isotherm experiments, a maximum Li sorption capacity of 30.6 mg/g is achieved. The Li isotherm is best described through the BET isotherm, indicating that apart from the expected Li^+-H^+ ion exchange, additional sorption processes take place. The sorption selectivity follows the order Mn > Zn > As > Ba > **Li** > Sr > Ca > K, Mg > Na. A near-complete extraction is achieved for Li, Ba, As, Mn and Zn. Despite their high concentration in the brine (g/L range), only 0.2–4.7 % of Na, Ca and K are extracted. Within both, the alkaline and alkaline earth metals, increasing charge density and thus stronger binding to the hydration sphere correlates with decreased selectivity. The selectivity variation between alkaline earth and alkaline metals is explained by the higher valence of the former. For both groups of the periodic table, the negative correlation between charge density and selectivity and the independence of the sorption capacity from the sorbent to brine ratio indicates electrostatic sorption. The higher selectivity of the LMO for Mn, Zn and As over Li results primarily from chemical binding and complex formation. Regarding an industrial DLE application, the additional sorption processes enable high Li sorption capacities even at low brine pH, potentially avoiding the addition of base to increase Li extraction. The fast sorption kinetics enable the application of the sorbent in high-discharge industrial DLE applications, such as geothermal power plants. The higher selectivity for Ba, As and Zn than Li and their desorption into the stripping solution may be disadvantageous as it may lead to impure products (LiCl solutions) that require further purification or removal prior to the extraction. Since the desorption of these elements is incomplete, this may result in the accumulation at the sorbent, potentially decreasing Li sorption capacity and resulting in expensive disposal of the sorbent as hazardous waste. Despite this, the low selectivity for Na, Ca and K make the sorbent suitable for brines enriched in these elements.

1. Introduction

The transformation of mobility to electric drives involves increasing demand for designated metals for batteries, especially for Li (e.g. [1]). In order to satisfy the current and future demand, the feasibility of extracting Li from conventional (hard rock, salt lake brines) and unconventional resources (geothermal, oilfield and mine brines, seawater) is currently being under investigation [2–6]. Especially geothermal brines are regarded as promising new resources since they can reach Li concentrations of several hundred mg/L [5,7] and are already pumped to the surface for the generation of electricity or heat [8–10]. Various technologies, e.g. sorbents and ion-exchangers, membranes, liquid–liquid extraction, are investigated for direct Li extraction (DLE) from fluids [5]. Thereby, one of the biggest challenges for DLE especially from hydrochemically complex fluids is the selectivity for Li of the DLE method, often bearing the risk for co-extraction of other elements. Co-extraction can result in the need for brine pre-treatment to avoid co-extraction and/or the purification of the produced Li solution in the

* Corresponding author at: Magmatic Bio GmbH, Am Kanal 27, 1110 Vienna, Austria.
E-mail address: klemens.slunitschek@kit.edu (K. Slunitschek).

https://doi.org/10.1016/j.seppur.2025.134594
Received 30 June 2025; Received in revised form 30 July 2025; Accepted 31 July 2025
Available online 6 August 2025

subsequent processing. Furthermore, co-extracted elements might have to be disposed of, leading to additional costs. Therefore, extraction technologies with a high selectivity are a necessity for successful application of DLE from brines.

Amongst DLE technologies, adsorbents and ion-exchangers receive high attention from research and industry and are already applied in industrial scale, e.g. former Livent Li mine, now Rio Tinto, in the Salar de Hombre Muerto, Argentina. Sorbents and ion-exchangers are regarded as promising due to their properties, especially sorption capacity and kinetics, selectivity and their chemical resistance and lifetime [5]. Currently, the most regarded materials are the ion-exchangers lithium manganese oxide (LMO) and lithium titanium oxide (LTO) and the adsorbent lithium aluminium layered double hydroxides (Li-Al-LDH) [5,11]. The LMO and LTO sorbents have a high Li sorption capacity with reported values of 53.5 mg/g and 94.5 mg/g, respectively [5], in comparison to typical sorption capacities < 10 mg/g for Li-Al-LDH [11]. The higher sorption capacity potentially allows to achieve higher Li concentrations in the desorption solution, reducing the effort of concentration prior to crystallization. For desorption, for LMO and LTO acids are needed, which increases the OPEX in comparison to Li-Al-LDH, which can be desorbed with water [11]. Due to the redox-sensitivity of the LMO, Mn dissolution occurs during desorption, decreasing the lifetime of the sorbent and giving it a lower stability, in comparison to LTO and Li-Al-LDH [5]. While LMO and Li-Al-LDH have comparable sorption kinetics, LTO show lower kinetics [5]. But, to achieve fast sorption kinetics, brine pre-heating to 45–95 °C is required for Li-Al-LDH [11], increasing the OPEX especially for brines with a low Li concentration. In a geothermal DLE plant this might be of low concern, due to the elevated temperature of the brine. In general, Li-Al-LDH sorbents dissolved below pH < 6 [11], requiring pH-adjustment of brines with lower pH prior to extraction, whereas LMO and LTO are applicable at pH < 6. While LMO and LTO show many advantages over Li-Al-LDH, Li-Al-LDH are the only material with proven large-scale readiness and application over many years, in the former Livent mine.

The spinel-structured LMO sorbents contain tunnels inside the crystal lattice, adapted to Li during synthesis [12]. The crystal lattice consists of MnO_6 octahedra with $Mn^{3+/4+}$ on the octahedral position with Li^+ mainly on the tetrahedral site, but as well on octahedral defect sites [13,14]. The sorption sites are classified as (I) Li^+-specific ion-exchange, (ii) redox-type and (iii) non-specific ion-exchange, with the portion of each site depending on the synthesis conditions [15]. The nonspecific ion-exchange sites may result from the formation of pores due to Mn^{2+} dissolution during desorption and the formation of hydroxyl groups in those pores [15]. The main Li sorption process is a Li^+-H^+ ion exchange, resulting in the formation of lattice hydroxyl groups at the ion-exchange sites upon Li^+ desorption [12–14,16–18]. Depending on the synthesis, redox-type exchange sites can exist to a varying degree due to the presence of Mn^{3+} in the crystal lattice [13,19]. During redox-induced Li^+ desorption, two Mn^{3+} disproportionate to Mn^{4+} and Mn^{2+} with the dissolution of the latter [13,18–20].

Spinel-type LMO achieve high Li sorption capacities from natural fluids, with maximum Li sorption capacities of e.g., 10.6 mg/g (seawater, [21]), 27.2 mg/g (salt lake brine, [22]), ~ 28 mg/g (Salar de Uyuni brine, [23]), 40.9 mg/g (seawater, [24]) or 62 mg/g (Urmia salt lake brine, [25]). The Li sorption capacity positively correlates with pH, Li concentration and temperature [22,23,26]. In addition, the priming of the lattice tunnels to Li during synthesis results in an ion-sieve effect and a high Li selectivity [12,22]. While, Li^+–H^+-exchange mainly takes place at the inner surface, other cations with a larger ionic radius can only sorb on the particle surface, as they cannot enter the tunnels due to steric hindrance [22–24]. The selective sorption of Li by LMO over alkaline and alkaline earth metals, especially Na, K, Mg and Ca, has been shown in various studies using artificial or natural solutions and brines (e.g. [12,22,24,25,27,28]. However, previous studies mainly focussed on major elements and less on trace elements in the investigated brines and solutions. In order to understand the co-sorption of elements other than Li, we investigate the sorption and desorption of Li and other elements in a geothermal brine of the Upper Rhine Valley (URV, Germany, France) to the LMO $Li_{1.6}Mn_{1.6}O_4$. Thereby, we evaluate the sorbent properties and the significance and possible effects of competing elements for industrial DLE processes.

2. Materials and methods

2.1. Brine

An Fe-depleted geothermal brine of the geothermal power plant of Soultz-sous-Forêts, France, was used for the experiments. The fluid is produced from the well GPK-2 from a depth of around 5 km at a bottom temperature of 200 °C [29]. The brine has a natural pH of 5.0 and a total dissolved solid concentration of ~ 100 g/L [30]. The fluid chemistry is dominated by Na and Cl with 27.5 g/L and 55.8 g/L, respectively (Table 1). The Li concentration is 181 mg/L (Table 1). Under ambient conditions, the brine has a gas–liquid ratio of 0.75–1.05, consisting mainly of CO_2 (85 vol-%) and N_2 (10.5 vol-%, [30]). Precipitates that form during sampling and storage due to cooling, pressure loss, degassing of dissolved CO_2 and oxidation [31,32] were removed through filtration prior to the experiments. Precipitation results in the complete loss of dissolved Fe and a decrease of Ba (5.1 to 4.2 mg/L) and As (9.3 to 3.1 mg/L, [30], Table 1).

2.2. Sorbent synthesis

The precursor $Li_{1.6}Mn_{1.6}O_4$ was synthesized through an adapted hydrothermal synthesis based on [24] and [22]. MnO_2 (> 90 % purity, Merck) is heated to 680 °C at a heating rate of 7.3 °C/min and calcined at the given temperature for 6 h under ambient conditions. $LiMnO_2$ is produced from the resulting Mn_2O_3 by cooking with 4 M LiOH solution (LiOH: 98 % purity, Merck) with a mass-volume ratio of 1 g to 20 mL in a Teflon-lined steel autoclave for 12 h at 210 °C (heating rate 6.3 °C/min). After cooling of the autoclave to room temperature, the suspension is filtered with a 0.45 μm cellulose-acetate filter. The resulting $LiMnO_2$ is washed with 0.3 L/g ultrapure water and dried at 60 °C for 12 h. To obtain the precursor $Li_{1.6}Mn_{1.6}O_4$, $LiMnO_2$ is calcined at 400 °C for 8 h (heating rate 8.4 °C/min). To obtain the sorbent, the initial delithiation of the precursor $Li_{1.6}Mn_{1.6}O_4$ is conducted with 0.5 M HCl for one hour at 70 °C and an acid-precursor ratio of 0.1 L/g. The delithiation is repeated for a total of three times, using fresh 0.5 M HCl for every repetition.

The phase identification and characterization of the crystal structure are carried out with a D8 Discover diffractometer (Bruker) with CuKα radiation (Kα1 λ = 1.54060 Å and Kα2 λ = 1.5444 Å). The measurement is conducted from 2 to 82° 2θ at 0.02° increments and a measurement time of 0.6 s/step. The software Bruker Diffrac.eva 4.1.1 and the database PDF-2, version 2002 [33] are used for evaluation.

2.3. Sorption experiments

To simulate realistic conditions for the application in a geothermal power plant, the sorption experiments are conducted at 60 °C, corresponding to the reinjection temperature at the Soultz-sous-Forêts plant. Sorption kinetics from brine are determined by stirring 0.5 g sorbent in 0.2 L brine for designated times (1 min – 24 h). The brine isotherm experiment is conducted for one hour with sorbent mass to brine volume (m/V) ratios of 0.2–80.0 g/L. To prevent a pH decrease due to Li^+-H^+ ion exchange, all fluids are buffered to the brine's natural pH = 5 with a Na-acetate buffer. In total, 16.44 g Na-acetate (pro analysis, Merck) and 6.6 mL acetic acid (pro analysis, Merck) are added per litre brine. The pH is finally adjusted to 5 with HCl or NaOH. To determine the desorption of previously sorbed elements, the sorbents from the kinetic and isotherm experiments are treated with 0.5 M HCl at a ratio of 0.1 L/g at 60 °C for one hour. In all sorption and desorption experiments, the solutions are

Table 1
Selected major and minor elements of the buffered Fe-depleted brine used in the sorption isotherm and kinetic experiments.

Cl	Li	Na	K	Mg	Ca	Sr	Ba	As	Mn	Fe	Zn
[g/L]	[mg/L]	[g/L]	[g/L]	[mg/L]	[g/L]	[mg/L]					
55.8	181	32.1	3.46	133	7.31	434	4.19	3.14	16.7	<0.001	2.32

filtered and the sorbent is washed with ultrapure water and dried at 60 °C overnight after the designated duration.

Cation concentrations in liquid samples are determined with the ICP-OES (iCap 7000, radial mode, Thermo Fisher Scientific) through triplicate measurement and calculation of the average as the final value. Analytical uncertainty is calculated with Eq. (1)) using the relative precision (Eq. (2)) and relative accuracy (Eq. (3)) of a certified reference material (MISA Standard 6, LGC Standards) and calibration solutions of different elemental composition and concentration, measured at least three times in triplicate. Anions are analysed by ion chromatography (Methrom, Compact IC 930; Metrosep A Supp 5–150). A certified river water standard (LGC6027, LGC Standards) is used for quality control. For determination of solid chemistry via acid digestion, 0.1 g of sample material is dissolved in 1 mL 30 % HCl (suprapur, Merck) and 1 mL 30 % H_2O_2 (pro analysis, Carl Roth) in a Teflon beaker. After complete digestion, the digest is transferred into a volumetric flask and filled up to a total volume of 50 mL with ultrapure water. The digest is analysed for the same element spectrum as the experiment solutions by ICP-OES.

For all analyses, the analytical uncertainties are good. For the sorption isotherm experiments, analytical uncertainties are 3.1–7.1 % (Table 3). For the sorption kinetic analyses, the uncertainties are 3.8–11.0 % (Table A6), with only Mg exceeding 10 %. For the eluate of desorption of isotherm and kinetic experiments, analytical uncertainties of 2.6–4.8 % (Table A5) are determined.

$$\text{uncertainty} = \sqrt[2]{(precision^2 + accuracy^2)} \quad (1)$$

$$\text{precision}\,[\%] = \frac{\sigma(x)}{\bar{x}} \quad (2)$$

$$\text{accuracy}\,[\%] = \frac{\bar{x} - X}{X} \quad (3)$$

σ = standard deviation of concentration of element x [mg/L] $\bar{x}$ = mean of concentration of element X [mg/L]

X = reference material concentration [mg/L].

2.4. Calculation of sorption capacity

The sorption capacity (Q) based on the concentration in the brine filtrate is calculated after Eq. (4) [22]. For desorption experiments and solid chemistry data, Eq. (5) is used for the calculation of sorption capacity.

$$Q = \frac{(C_0 - C)*V}{m} \quad (4)$$

$$Q = \frac{C_{des,dig}*V}{m} \quad (5)$$

Q = sorption capacity [mg/g], C_0 = initial concentration [mg/L], C = filtrate concentration [mg/L], $C_{des,\ dig}$ = concentration of desorption solution or digest [mg/L], m = sorbent mass [g], V = volume [L]

2.5. Isotherms

The Freundlich isotherm [34] is calculated after Eq. (7) and the Langmuir isotherm [35] is calculated after Eq. (8) [36]. The BET isotherm [37], after the revised form of [36] (Eq. (9)), is used to calculate multi-layer sorption. All isotherm models are fitted to the experimental data through nonlinear fitting, conducted with the software OriginPro 2019 (OriginLab). The sorption-induced concentration changes of Na, K, Mg, Ca and Sr in the brine are smaller than the analytical uncertainties (Table 3). Therefore, a fit of the brine isotherm models is not possible.

$$Q = F*C^n \quad (7)$$

F = Freundlich constant [L/mg], n = constant [-]

$$Q = Q_{max,mono}\frac{K_S*C}{1 + K_S*C} \quad (8)$$

$$Q = Q_{max,mono}\frac{K_S*C}{(1 - K_L*C)(1 - K_L*C + K_S*C)} \quad (9)$$

$Q_{max,mono}$ = maximum sorption capacity of monolayer [mg/g]

K_S = equilibrium constant of sorption for monolayer (1st layer) [L/mg].

K_L = equilibrium constant of sorption for upper layers [L/mg] [36].

2.6. Distribution and separation coefficient

The average distribution coefficient K_d [mL/g] is calculated with Eq. (10) based on the brine isotherm. For each element, all data points are used where complete extraction is not achieved. For Na, K, Mg, Ca and Sr, where the utilisation of filtrate data is not possible, theoretical residual concentrations based on the solid chemistry are calculated. The separation coefficient α was calculated after Eq. (11).

$$K_d = \frac{Q}{C} \quad (10)$$

$$\alpha(Li/Me) = \frac{K_d(Li)}{K_d(Me)} \quad (11)$$

Me = metal

2.7. Desorption efficiency

The average desorption efficiency is determined by interpolating a linear function (Pearson's correlation) between the element concentration at the sorbent before desorption (sorption capacity Q) and after desorption (Q_{des}). At high correlation coefficient (≥0.8), the slope of the linear function yields the percentage of the element remaining at the sorbent after desorption. For the elements As, Ba, Li and Zn, filtrate and solid chemistry data are used, whereas for Na, Ca, K, Mg, and Sr, only solid chemistry data are used (see results). Due to too low sorbent mass after the isotherm experiment, the determination was only possible for samples with m/V ≥ 4 g/L.

3. Results

3.1. Sorbent characteristics & initial delithiation

The precursor dominantly consists of cubic $Li_{1.6}Mn_{1.6}O_4$ with minor amounts of cubic Mn_2O_3 as intermediate product and monoclinic Li_2MnO_3 as by-product (Fig. A1a in electronic supplement). The precursor consists of 67.0 mg/g Li and 551 mg/g Mn, deviating from the ideal composition of $Li_{1.6}Mn_{1.6}O_4$ by 1.6 wt-% and 2.2 wt-%, respectively. After initial delithiation, the sorbents main phase is a cubic spinel Mn-oxide with Mn_2O_3 and Li_2MnO_3 impurities persisting and hexagonal

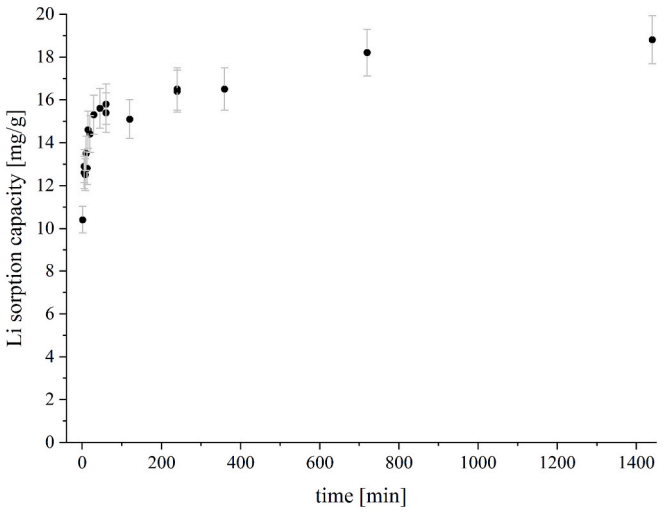

Fig. 1. Lithium sorption kinetics.

akhtenskite (MnO_2) in addition (Fig. A1b). For the sorbent, the peaks slightly shift to higher 2θ-values in comparison to the precursor, showing the topotactic Li^+ exchange by H^+ [12,38]. During the initial delithiation, 65.1 mg/g Li are desorbed and 102 mg/g Mn dissolved, accounting for 97.2 % of the contained Li and 14 wt-% of Mn.

3.2. Sorption kinetics

Lithium, Sr, Ba, As and Zn show similar kinetic behaviour with a fast initial increase in sorption, followed by an asymptotic approximation to equilibrium sorption capacity (Fig. 1, Fig. 2 d-f, h). Within the first minute, 56 % of the maximum Li sorption capacity is reached (Fig. 1), increasing to a maximum of 83 % after one hour. The brine and sorbent are equilibrated after 12 h, with a maximum Li sorption capacity of 18.8 mg/g (Fig. 1). Arsenic, Ba, Zn, and Sr reach 46–73 % of the maximum sorption capacity within the first minute. Equilibrium is reached after 1 h for As (1.1 mg/g), 4 h for Ba (1.2 mg/g) and 12 h for Sr (2.1 mg/g) and Zn (0.9 mg/g, Fig. 2 f, e, d, h). For Mn, equilibrium is reached within the first minute (Fig. 2 g) at a sorption capacity of 6.6 mg/g. The sorption kinetics of Na, K and Ca are characterised by fluctuating sorption capacities throughout the complete duration of the experiment (Fig. 2 a–c). Especially within the first 60 min, the kinetics show fluctuating sorption capacities and no visible trend. At longer durations, the sorption capacities seem to stabilize at ~ 1.4 +/- 0.11 mg/g for Na, ~1.7 +/- 0.11 mg/g for K and ~ 7.2 +/- 0.27 mg/g for Ca (Fig. 2 a–c). A time delay in the sorption of Li and the other elements is not given. Sorption of Li is confirmed through XRD analysis, whereas impurity phases are not found in the diffractogram, potentially due to too low concentration (Fig. A8).

3.3. Sorption isotherm

The brine Li isotherm shows a steep increase of the sorption capacity at low and high residual concentrations and a plateau in between (Fig. 3), with a maximum sorption capacity of 30.6 mg/g (Fig. 3). The brine Li isotherm is best described through the BET model, with $R^2 = 0.97$, and a calculated maximum Li sorption capacity of the first layer of 5.45 mg/g (Fig. 3, Table 2). A satisfactory fit of the data using Langmuir and Freundlich isotherms is not possible.

The highest sorption capacity of the competing elements is reached for Mn with a maximum of 56.8 mg/g (Fig. 4). The sorption behaviour of Mn is best described through the Langmuir isotherm with $R^2 = 0.79$, whereas the Freundlich isotherm reaches only $R^2 = 0.66$ and shows less consistency with the data (Fig. 4 c, Table 2). The BET isotherm is not applicable. The other considered elements have maximum sorption capacities between 0.07 mg/g (Mg) and 5.96 mg/g (Ca, Table 3). Barium, Zn and As cannot be clearly assigned to BET, Langmuir or Freundlich isotherms, because they do not reach equilibrium during our experiments (Fig. 4 a, b, d, Table 2). For Na, K, Mg, Ca and Sr, no isotherms can be calculated since solid chemistry data was used to determine the sorption capacity. Sodium sorption capacities vary inconsistently over the regarded m/V range (Fig. 5 a). Potassium and Mg show constant sorption capacities of 1.98 mg/g and 0.05 mg/g for m/V $\geq$ 30 g/L and m/V $\geq$ 20 g/L, respectively, but inconsistent values below those ratios (Fig. 5 b, c). For m/V < 20 g/L, sorption capacities of Ca and Sr decrease with increasing m/V ratio, while for m/V $\geq$ 20 g/L, sorption capacities are constant with 4.39 mg/g and 1.29 mg/g, respectively (Fig. 5 d, e). X-ray diffractometry analysis shows relithiation of the sorbent, but no impurity phases are detected, probably due to too low concentrations (Fig. A8).

Barium, As, Mn and Zn are effectively sorbed from the brine by LMO with maximum extraction between 98 % (Ba) and 100 % (Zn, Fig. 6 a, Table 3). All four elements, as well as Li, show a positive, logarithm-like relation between m/V ratio and extraction efficiency (Fig. 6 a). Complete extraction is reached at m/V ratios for Mn of 0.2 g/L, As of 2 g/L, Zn of 8 g/L, Ba of 20 g/L and Li of 40 g/L (Fig. 6 a). For Na, K, Mg, Ca and Sr, the extraction efficiency is much lower with < 1 % for Na and a maximum of 23 % for Sr. These elements show a near-linear relation between m/V ratio and extraction efficiency (Table 3, Fig. 6 b).

The total molar sorption capacity of all considered elements lies between 0.54 mmol/g and 5.74 mmol/g, with Li being the dominant element (60–87 %; Fig. 7 a). Regarding only the competing elements, the molar sorption capacity ranges between 0.22 mmol/g and 1.33 mmol/g, with Mn being the dominant element for m/V $\leq$ 2 g/L and Ca for m/V > 2 g/L (Fig. 7 b). Complete extraction of Mn is reached at m/V $\geq$ 0.4 g/L, thus, with increasing m/V ratio the Mn sorption capacity decreases linearly. The same applies to Ba, As and Zn, once they reached complete extraction, explaining the decreasing sorption capacity and their contribution to the total sorption capacity. Although the sorption capacities of Na, K, Mg, Ca and Sr fluctuate over parts of the m/V range (Fig. 5), the fluctuations are relatively little in comparison to the total molar sorption capacity (Fig. 7 b). and the sorption capacity of these elements can be regarded as independent of the m/V ratio (Fig. 7 b). The relative contribution of these elements to the total molar sorption capacity increases with increasing m/V ratio due to the relative decrease of molar sorption capacities of Li, Ba, Mn, Zn and As.

The sorbent shows a high affinity for Li, with a K_d of 216 mL/g, a low affinity for Na, K, Mg and Ca, with K_d values of 0.03 – 0.70 mL/g and separation coefficients α of 6428 – 196 (Table 3). The significant sorption of Ba, As, Zn and Mn is reflected by K_d values of 677 – 13850 mL/g (Table 3), exceeding that of Li. This, and the separation coefficients of 0.002 – 0.270 (Table 3) show the higher affinity of the sorbent towards these elements. The selectivity follows the order Mn > Zn > As > Ba > **Li** > Sr > Ca > K, Mg > Na.

3.4. Desorption efficiency

Based on the filtrate data of the kinetic and isotherm experiments, 74 – 90 % of sorbed Li is desorbed, with one desorption ratio of 120 %, indicating the delithiation from the initially present Li remaining from synthesis. The comparison of Li sorption capacity Q to the remaining Li sorption capacity after desorption Q_{des} shows, that Li desorption can be subdivided into three groups (Fig. 8a; Table A1 in electronic supplement). Two groups (isotherm and kinetic filtrate) indicate a constant Li concentration at the sorbent after desorption, in the ranges of 0.9–3.0 mg/g and 2.6–3.9 mg/g. However, based on the solid chemistry of the kinetic experiment, the remaining Li after desorption decreases with increasing sorption capacity and thus with increasing sorption duration (lower subset in Fig. 8 a). Thus, no distinct Li desorption behaviour can be defined.

Barium, As and Zn show a positive linear correlation of Q and Q_{des}

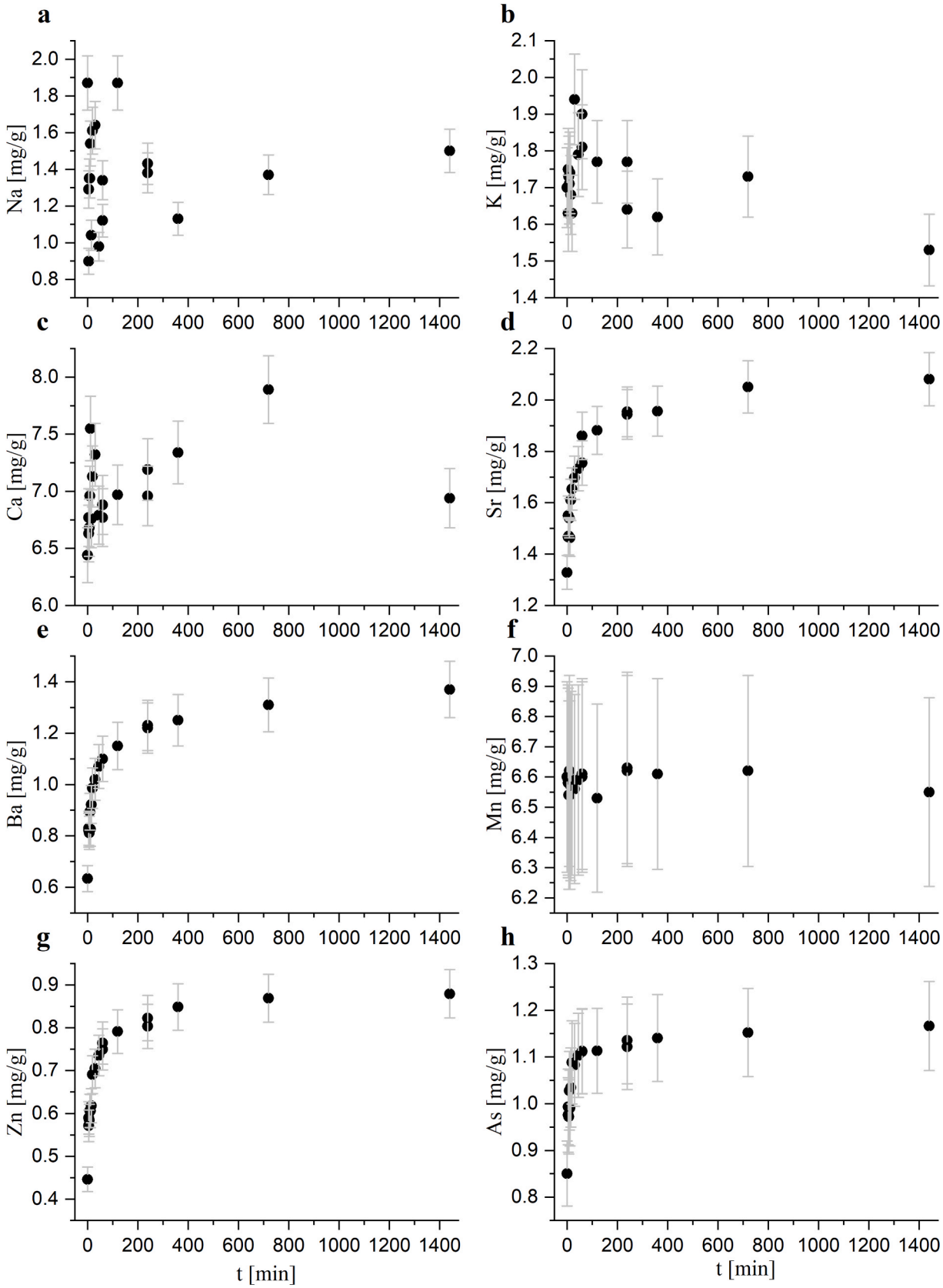

Fig. 2. Sorption kinetics of Na (a), K (b), Ca (c), Sr (d), Ba (e), As (f), Mn (g), Zn (h). For Mg, all concentrations are below detection limit (<0.02 mg/L).

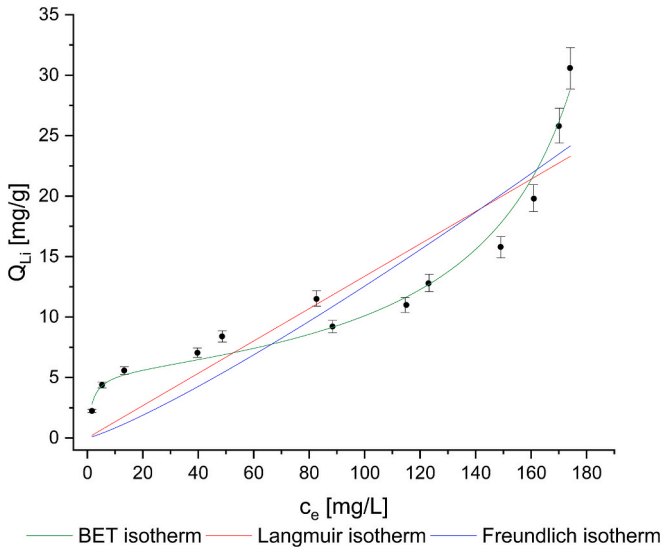

Fig. 3. Lithium isotherm with isotherm models. R^2 of BET isotherm model: 0.97.

(Fig. 8 b, c, d). For Ba, two subgroups of filtrate and solid chemistry data are formed, with the solid chemistry data indicating higher remaining sorption capacities at the same Q. This may be explained by the Ba content of 0.5 mg/g in the sorbent after synthesis (Fig. 8 b). Both subgroups show a linear correlation with R^2 coefficients of 0.99 and 0.95 and desorption efficiencies of 56 % and 73 %, respectively (Table A1). For As, all data are consistent and show a linear relation, with $R^2 = 0.99$ (Fig. 8 c). The desorption efficiency is 9 %, whereas 91 % remain at the sorbent (Table A1). For Zn, an average desorption efficiency of 42 % with a linear correlation coefficient of $R^2 = 0.98$ is determined (Fig. 8 d, Table A1). Sodium, K, Mg, Ca and Sr show average desorption efficiencies of 34 – 88 % and a constant sorption capacity after desorption, independent of Q, is indicated, but the correlation factors are low, with $R^2 = 0.30 – 0.66$ (Table A1, Fig. A4).

Manganese dissolution for the sorption isotherm samples ranges between 0.4 – 3.3 % of the sorbent weight. At the kinetic experiment, 1.5 – 2.4 wt-% of the sorbents were dissolved.

4. Discussion

4.1. Li sorption behaviour

The description of the isotherm through the BET model in this study is in contrast to many studies so far using $Li_{1.6}Mn_{1.6}O_4$ and other spinel-type manganese oxide sorbents of different compositions and application forms (powder, powder bound to carrier material), in which Li sorption is best described through the Langmuir isotherm [12,22,27,39–48]. These two different isotherm models are not necessarily contradictory, since the BET isotherm incorporates the Langmuir isotherm and assumes limited sorption sites on the particle surface as well [37]. Thus, the experimentally determined isotherm (Fig. 3) can be divided into two parts: 1) for equilibrium concentrations < 100 mg/L, the Li sorption is of Langmuir mono-layer type, indicating chemical sorption; and 2) for equilibrium concentrations > 100 mg/L, the steep increase in sorption capacity is characteristic for BET-type and indicates additional sorption processes, e.g. electrostatic multi-layer sorption or the formation of surface complexes or surface precipitates. Additional experiments with brine and LiOH solutions with Li concentrations of 44 mg/L, 137 mg/L, 160 mg/L (Table A3-A4, Fig. A5-A6) confirm the BET sorption behaviour. Since the second increase in the BET isotherm occurs at low m/V ratios, it indicates that the additional sorption process is related to the dissolved Li to sorbent ratio. According to [15], the sorbent contains hydroxyl groups in unspecific sorption sites on the particle surface. At high enough Li to sorbent ratio, Li^+ can exchange with the H^+ in the hydroxyl group, leading to an increase in Li sorption. Furthermore, the sorption of Mn from the brine (Fig. 4c) can generate additional sorption sites, leading to increased Li sorption. Since Mn is completely extracted from the brine for m/V > 0.2 g/L, this process will have a stronger impact at low m/V ratios. Thus, with increasing m/V ratio, the relative contribution of this process to the overall Li sorption will decrease continuously while the relative share of Li^+-H^+-ion exchange will increase. However, the BET sorption behaviour is observed in pure LiOH solutions as well (Table A3-A4, Fig. A5-A6), therefore the Mn-related sorption would be an additional process and cannot be solely responsible for the observed sorption behaviour. So far, no other study observed the BET isotherm with spinel-type LMO to our knowledge and we assume that this is due to differences in the experimental setup, especially m/V ratio, and the brine. Based on the isotherm data alone, a clear discrimination between the potential additional sorption processes

Table 2
Parameters of fitted brine isotherm models. No fitting possible for Ca, K, Mg, Na, Sr, because sorption-induced concentration changes in the brine are smaller than the analytical uncertainties (Table 3). F = Freundlich constant, n = constant, K_S = equilibrium constant of sorption for monolayer (1st layer), Q_{max} = maximum sorption capacity, $Q_{max,\ mono}$ = maximum sorption capacity of monolayer, K_L = equilibrium constant of sorption for upper layers, R^2 = Pearson's correlation coefficient.

Isotherm	Freundlich			Langmuir			BET			
Parameter	F [L/mg]	n	R^2	K_S [L/mg]	Q_{max} [mg/g]	R^2	$Q_{max,m}$ [mg/g]	K_s [L/mg]	K_L [L/mg]	R^2
Li	No fit			No fit			5.45	0.62	0.0047	0.97
Ba	0.68	0.84	0.99	0.11	7.11	0.99	1.54	1.34	0.13	0.99
As	1.76	0.69	0.98	0.58	5.33	0.99	2.81	1.26	0.118	0.77
Mn	35.2	0.38	0.66	1.19	70.2	0.79	No fit			
Zn	1.22	1.34	0.81	No fit			No fit			

Table 3
Maximum measured sorption capacity, relative extraction and average distribution (K_d) and Li separation coefficient (α) of the brine isotherm. X = element.

	Li	Na	K	Mg	Ca	Sr	Ba	As	Mn	Zn
$Q_{max,\ meas}$ [mg/g]	30.6	1.14	2.02	0.07	5.96	1.81	2.09	3.21	56.8	2.40
$extraction_{max}$ [%]	99.1	0.22	4.68	3.29	4.70	22.9	98.4	99.8	99.9	100
K_d [mL/g]	216	0.03	0.5	0.4	0.7	4.0	677	1724	13,850	1783
α(Li/X)	1	6428	367	377	196	40	0.27	0.13	0.002	0.09
analytical uncertainty [%]	5.6	3.8	3.1	6.8	4.2	5.7	4.3	7.1	4.5	3.2

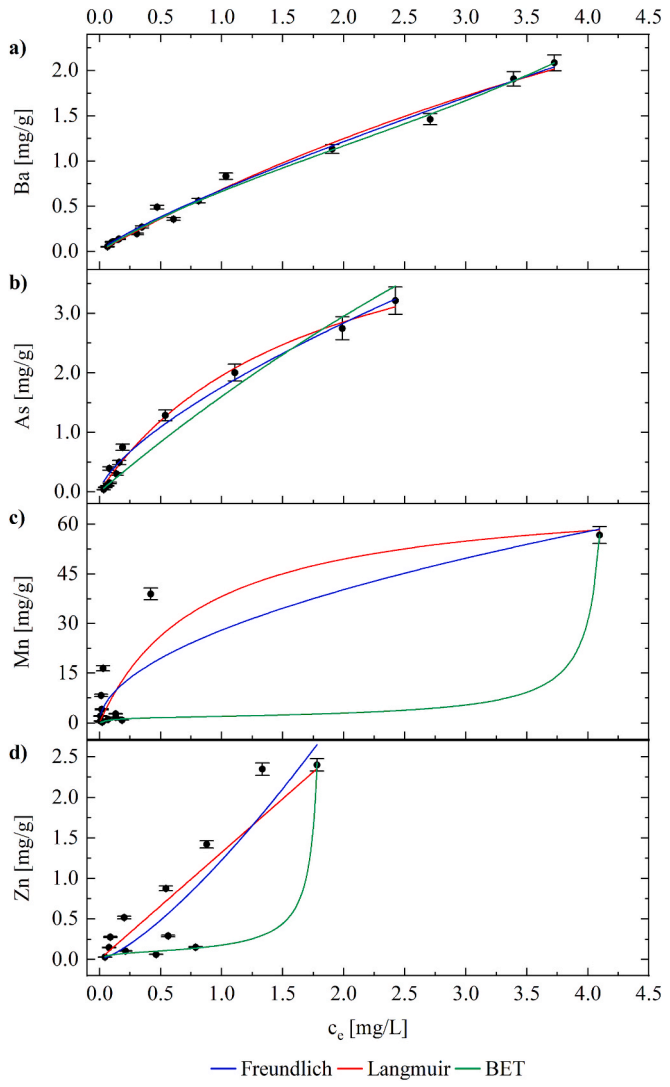

Fig. 4. Isotherms and applied isotherm models of Ba, Zn, Mn and As.

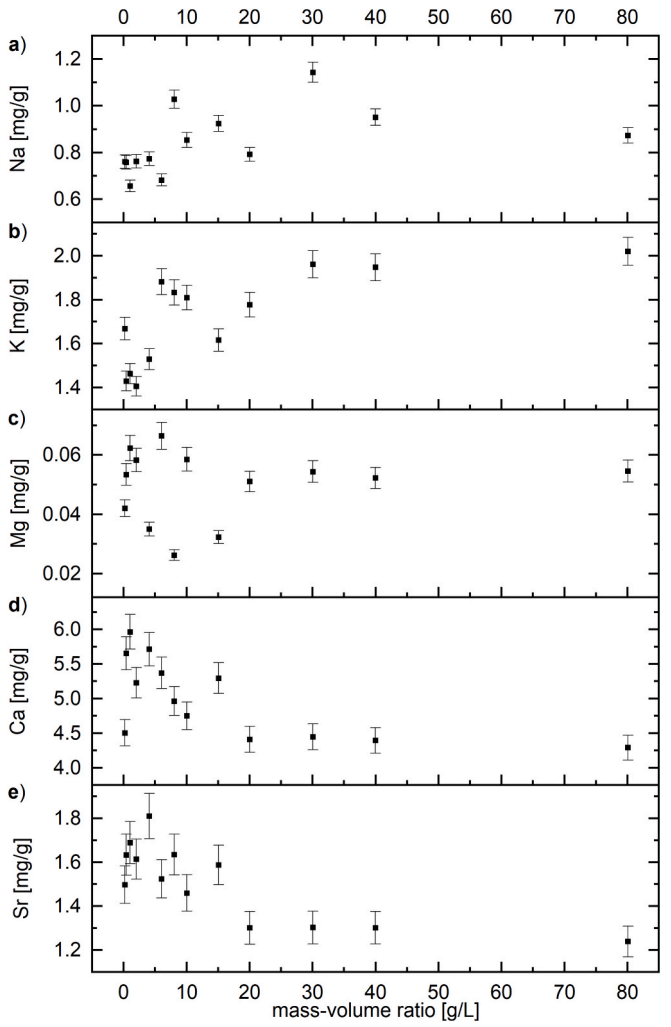

Fig. 5. Sorption capacity of Na, Mg, K, Ca and Sr in relation to mass-volume ratio based on solid chemistry data.

is not possible. Due to these additional processes however, the sorbent may reach a higher total Li sorption capacity than Langmuir-type LMOs.

While the calculated Li monolayer sorption capacity is comparably low with 5.45 mg/g (Table 2), the total maximum sorption capacity of 30.6 mg/g is within the range of other studies with salt lake brines and seawater of 10.6 – 62 mg/g [21,22,24,25]. The low Li monolayer sorption capacity results from the low pH = 5 of the brine, being unfavourable for the Li^+-H^+ ion exchange. The difference in maximum sorption capacity results from variations in sorption-influencing factors like pH, sorption time, Li concentration, sorbent – brine ratio.

Since the Li^+-H^+ ion-exchange is favoured with increasing pH [22], higher sorption capacities are achieved in brines with naturally higher pH, resulting in lower required sorbent mass and smaller industrial DLE plant size. This effect can be achieved for low pH brines through the addition of base as well. However, the additional costs for base have to be balanced by the savings through lower plant size and sorbent mass. In addition, the potential formation of mineral precipitates with pH increase and their subsequent disposal have to be regarded. With the additional sorption processes, that were identified for our sorbent, high sorption capacities are achievable even for brines that have relatively low pH-values. Furthermore, the additional sorption processes and higher sorption capacity results in a lower demand of sorbent, in comparison to other LMO.

In geothermal power plants and conventional evaporation mines, flow reactors will be the preferred processing technology because less brine needs to be stored at the surface compared to batch reactors. While the experiments were conducted in batch reactors in the laboratory, the BET sorption behaviour of Li can be assumed in flow columns as well. This assumption is based on the migration of the initial concentration front through the column over time, resulting in the increase in sorption capacity at high concentrations (Fig. 3). This means, that sorbents further downstream come in contact with high Li concentrations once the sorbent further upstream is saturated, enabling the additional sorption processes. The fast Li sorption kinetic (Fig. 1) makes the sorbent ideal for application in a flow reactor setup and high flow rate systems, such as e.g. in the geothermal power plants of the URV with brine flow rates of 28–80 L/s [49]. Additionally, the fast kinetics enable short durations per extraction cycle and thus a minimization of the DLE columns, post-processing units and brine storage tanks. In a simplified assessment of the sorbent demand for an industrial DLE plant, we assume a Li sorption capacity of 30 mg/g, an extraction cycle duration of 1 h and an annual runtime of 7884 h/a. The assumed annual production capacity is 10,000 t LCE, resulting in a required extraction of 0.24 t/h of Li and a sorbent demand of 7.9 t assuming no sorbent loss. It has to be considered that the assumed 30 mg/g Li sorption capacity are achieved with fine powder and for application in an industrial plant, the sorbent has to immobilised on carrier structures, like e.g. bigger particles. Through the immobilisation, the volume and mass of the final sorbent will increase, resulting in a decrease of the effective sorption capacity and an overall

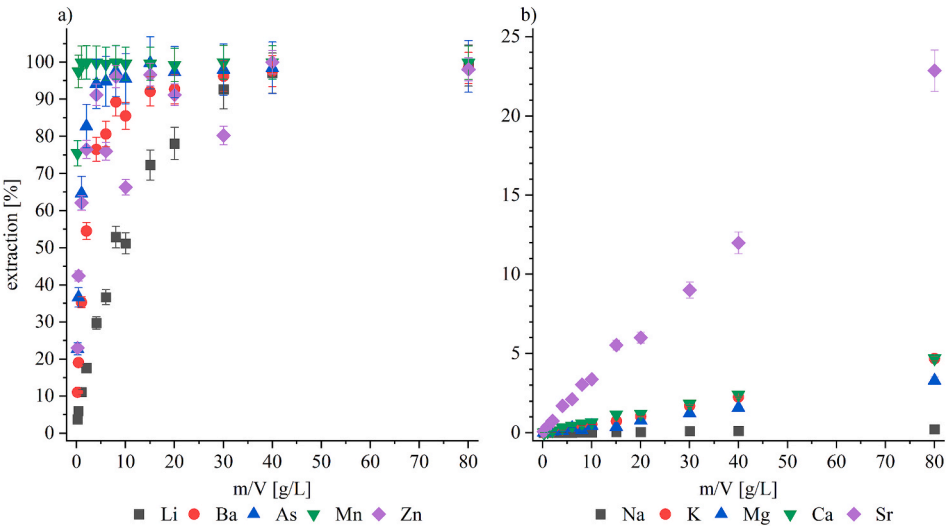

Fig. 6. Extraction of a) Li and selected minor elements and b) major elements.

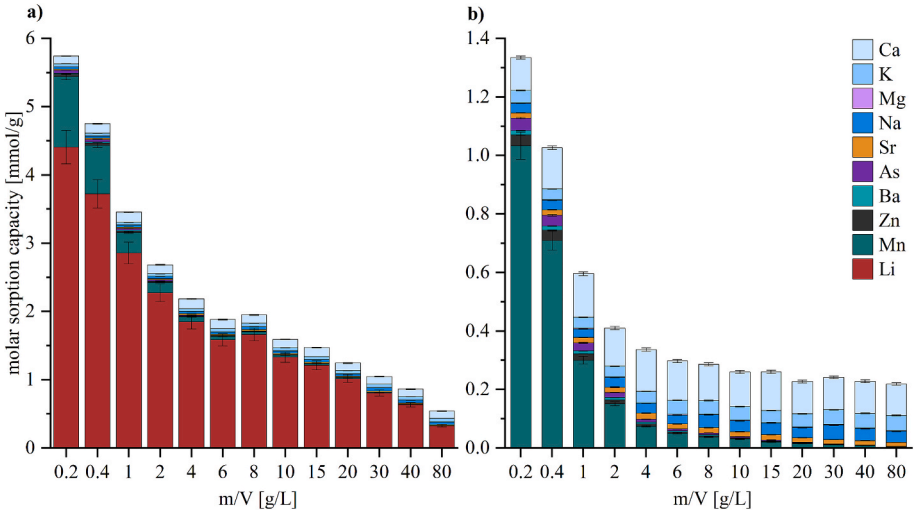

Fig. 7. Composition of total molar-based sorption capacity of a) all elements and b) without Li.

increase of sorbent material needed.

4.2. Selectivity

Lithium contributes 60–87 % to the molar sorption capacity (Fig. 7a) and has high distribution and separation coefficients (Table 3), proving a high Li selectivity of the sorbent. The high Li selectivity over most of the alkaline and alkaline earth elements, with $40 < \alpha < 6428$ (Table 3), results from the ability to specifically sorb Li in tunnels within the crystal lattice which are unavailable for the other cations due to the ion-sieve effect [12,24]. The alkaline and alkaline earth elements can sorb electrostatically [27] or sorb at the hydroxyl groups of nonspecific ion-exchange sites at the particle outer surface [15]. The optimal ratio of Li sorption capacity to accumulated competing element sorption capacity, is achieved at m/V ratios of 2–10 g/L, with a share of Li of the total molar sorption capacity of 85–87 % (Fig. 7 a). At other m/V ratios, the selectivity is lower due to the high Mn sorption capacity (m/V < 2 g/L) or low Li sorption capacities (m/V > 10 g/L), respectively (Fig. 7 a). Within the alkaline and alkaline earth metal groups, the selectivity of the sorbent decreases with increasing hydration energy/enthalpy and charge density (Table A2, values from [50,51]). With increasing charge density, stronger bonds between the metal ions and the water molecules and potentially anions in the first hydration sphere are formed, as shown by the increasing hydration energy (Table A2). While the decrease in selectivity with increasing hydration energy within a periodic group is supported by experiments of [12,27] reports the same behaviour for Na^+ and K^+, but not for Mg^{2+} and Ca^{2+}, using a similar sorbent-PAN nanofiber composite. However, the different selectivity order of Mg^{2+} and Ca^{2+} at [27] may result from sorption at the binder material or is influenced by the high Mg/Ca-ratio of 9:1 or is an artefact because the α-values only differ slightly (99 vs 141). The higher selectivity of the sorbent for alkaline earth over alkaline metals results from the higher valence of the former [52]. This behaviour is shown by [27] as well, but no such relation was observed by [53], using $Li_{1.6}Mn_{1.6}O_4$ powder and achieving $Li^+ > Mg^{2+} > Na^+ > Ca^{2+} > K^+$. The contradictory behaviour in the different studies can be explained by the fact that selectivity not only depends on sorbent properties, but also on the fluid composition, concentration and speciation of elements and physicochemical brine properties. The solution of [53] for example, has a much higher concentration of Na (321.22 mmol/L, 7384.75 mg/L) than Mg (0.69 mmol/L, 16.65 mg/L), Ca (0.06 mmol/L, 2.60 mg/L) and K (9.69 mmol/L, 378.9 mg/L), making Na sorption more likely. Furthermore, the molar ratios of Mg/Ca and Na/K at [53] are smaller than here, potentially explaining the differences in the order of selectivity. Thus, while the

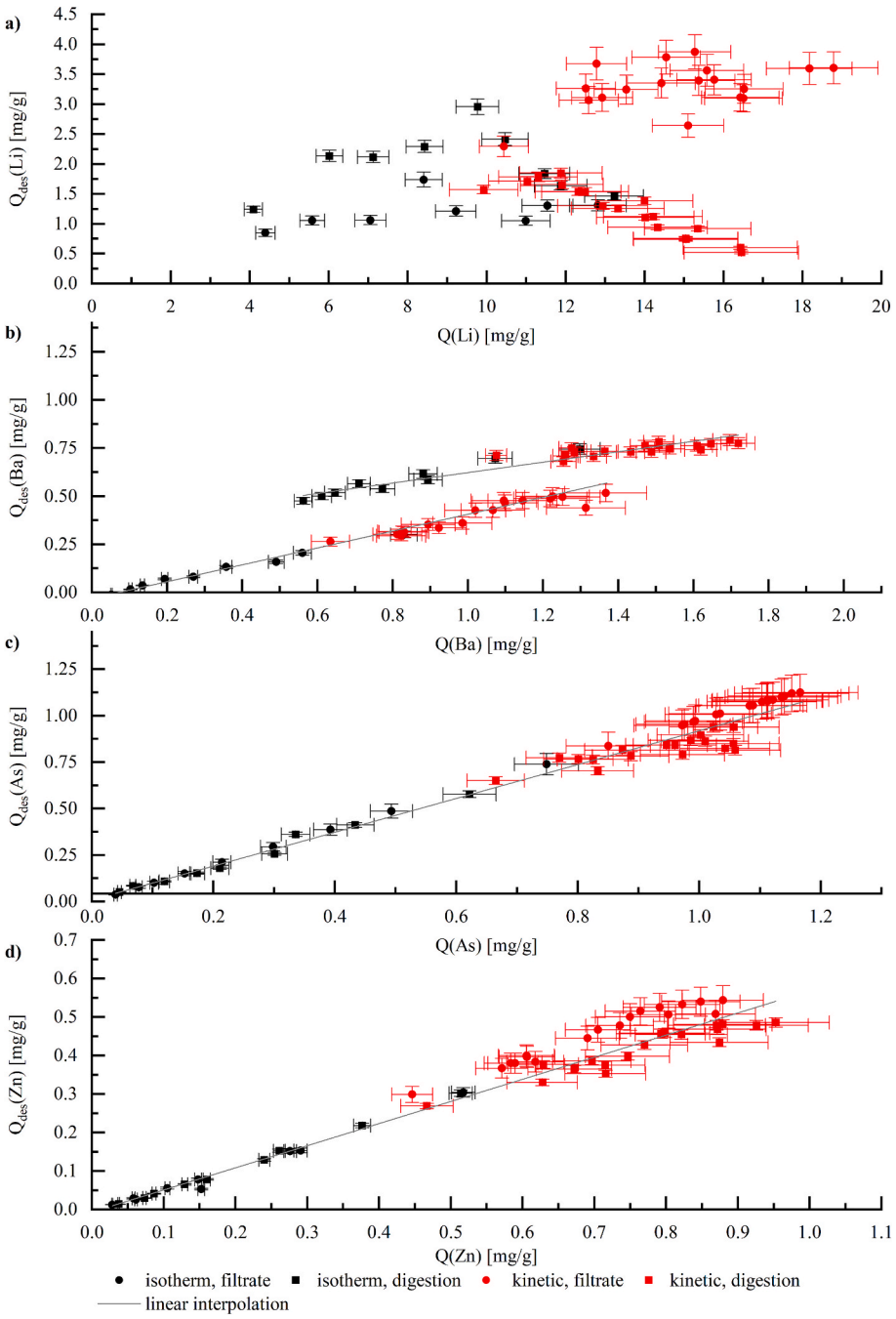

Fig. 8. Relation of element concentration at sorbent after sorption (Q) and desorption (Q_{des}) in isotherm experiment (black) and kinetic experiment (red). The average desorption efficiency is derived from the linear function. R^2: Li no fit; Ba 0.95 (solid) & 0.99 (filtrate); As 0.99; Zn 0.98.

sorption of ions inside the tunnel structure is material-dependent, the sorption selectivity on the outside of the sorbent will largely be influenced by the brine composition and its physicochemical parameters. This means, that DLE technology providers have to compare their sorbent, whether ion-exchange or adsorption, against many different brines to determine the sorption of competing elements and the suitable brine compositions and conditions. Mining companies developing a DLE project should test different sorbents in order to find the most suitable one for their brine, similar to conventional ore processing technologies. Thereby, sorbent performance, including Li sorption capacity and kinetics, stability and sorption of competing elements, should be investigated under natural and changed physicochemical brine conditions, e.g. pH, over an extended number of cycles.

4.3. Sorption and desorption of competing elements

The sorbent shows the highest affinity and selectivity for Mn in our experiments (Table 3), resulting from incorporation of Mn into crystal framework vacancies [54]. Additionally, Mn can sorb through a variety of processes, e.g. by ion-exchange on surface hydroxyl sites [55,56] or sorption on the particle surface or on adsorbed $H_2AsO_4^-$ (see below, [57–61]). The fluid used in our experiments differs in composition from real geothermal brine since it was oxidized during sampling and sample transport, leading to precipitation of Fe phases and Fe-depletion ([30], Table 1). Due to the geochemically similar behaviour of Fe and Mn [62,63], Fe sorption in similar scale to Mn is expected under natural brine conditions. The impact of Mn sorption, whether through incorporation and direct sorption to the sorbent or as co-sorption with As (see

below), on Li sorption capacity and sorbent life-time is not known.

Similarly to Mn^{2+}, Zn^{2+} sorbs through binding to crystal framework oxygen forming multinuclear hydroxo-complexes [55,64–66], Zn hydroxide phases [64] or through physisorption in outer-sphere complexes [67]. Arsenic oxyanions like arsenate sorb onto manganese oxide surfaces (e.g. [68]) and a similar behaviour is expected for LMO. Arsenic speciation in solution depends mainly on the redox potential and pH. Under the experimental conditions (pH = 5; oxic), $H_2AsO_4^-$ will be the dominant species [69,70]. The dissolved $H_2AsO_4^-$ adsorbs through inner-sphere monodentate-mononuclear or bidentate-binuclear complexes [57–59]. The point of zero charge for the similar sorbents $Li_{1.51}Mn_{1.63}O_4$ and $Li_{1.57}Mn_{1.65}O_4$ was determined by [16] at pH ~ 2.5. Thus, at the brine pH = 5, the LMO sorbent synthesised in our study is expected to have a negative surface charge. The negative surface charge results in a partial repulsion of the negatively charged $H_2AsO_4^-$, decreasing its sorption [71]. However, the pentavalent As oxyanion still adsorbs to the sorbent surface due to the stronger binding force of the monodentate-mononuclear or bidentate-binuclear complexes over the comparatively weak electrostatic forces. This occurs preferentially at crystalline edges due to lower negative electrostatic charge [58,71]. However, in the reduced conditions of the geothermal brine [30], $H_3As^{3+}O_3^0$ will be the dominant As-species instead [69,70,72]. Arsenic sorption is also expected under these reduced conditions, through a combined redox reaction, in which $H_3As^{3+}O_3^0$ is oxidized to $HAsO_4^{2-}$ while Mn^{4+} in the sorbent is reduced to Mn^{2+} and subsequently released into the solution [57–61]. The resulting $HAsO_4^{2-}$ adsorbs through the above mentioned complex formation or precipitates on the particle surface as Mn arsenate [57,58]. This process, as well as the above mentioned sorption processes of the other competing elements, requires experimental characterization.

Although Mn^{2+} may be released to the brine during the redox sorption process, re-sorption of Mn^{2+} is expected. However, if the re-sorbed Mn preservers the crystal structure and thus the ion-sieve effect is unknown. Therefore, As sorption and related Mn dissolution may result in accelerated sorbent degradation. Furthermore, sorption from As can decrease the Li sorption capacity, as shown by [73] with spinel-type LMO and a geothermal brine, but the authors give no explanation as to why. Both processes will increase the sorbent amount required for effective Li extraction. To prevent As sorption coupled to redox reactions with the sorbent, it can be removed from the brine through pre-treatment, e.g. through membranes, coagulation, anion exchange, disposable iron media or softening [74].

The only partial desorption of As, Zn, Ba and all other elements (Fig. 8, Table A1), may lead to accumulation of the elements at the sorbent over time [75,76] Especially the accumulation of As can be problematic due to its poisonous nature. For deposition, the necessary landfill category, from municipal solid waste to hazardous waste, depends on the local law. Thereby, the threshold values might be based on the absolute As concentration in the solid or the concentration in eluate after a standardized elution test. For Germany, the landfill category is determined based on the As elution, with thresholds in the range of 0.05 – 2.5 mg/L [77]. The As concentrations in the desorption eluates of the isotherm experiment (0.01 – 0.09 mg/L, Table A5) are not comparable with the thresholds, because these elutions are conducted at pH = 4 and pH = 11 and here at pH = 0.3 [78]. In addition, radionuclides contained in the brine of the URV are expected to accumulate at the sorbent surface [76]. The sorption and potential accumulation of elements potentially problematic and/or expensive at disposal has to be investigated for each brine, even when contained in only low concentrations. Furthermore, in general, LMO may not be applicable in industrial-scale processing of As- or radionuclide-rich brines, but long-term experiments are needed to assess the LMO potential for such brines.

The relative extraction of alkaline and alkaline earth metals increases linearly with the amount of sorbent (Figs. 6–10). This behaviour indicates electrostatic sorption, forming sorption layers around the sorbent particles. The expected negative surface charge of the sorbent enables electrostatic sorption, as reported by [27] for a similar LMO. Electrostatic sorption is additionally positively influenced by the high concentration of the elements in the brine (Table 1). The transfer of electrostatically sorbed elements into the desorption solution can be omitted e.g. through an intermediate washing step using ultrapure water in the laboratory and industrial water at the industrial scale. This leads to decreased purification needed in order to reach a battery-grade product. To minimize the water consumption, the water can be recycled, e.g. through reverse osmosis, and the ion-rich solution can be mixed with the Li-depleted geothermal brine and reinjected. However, the wash step takes time and prolongs the extraction cycle. This means, that in order to extract a designated amount of Li per time, the number of DLE columns has to be increased, in comparison to a flow scheme without a wash step. Thus, the integration of a wash step can potentially reduce costs in the post-processing but those savings have to offset the costs for the additional DLE columns including sorbent, water treatment and consumables of the wash step.

Partial desorption of Na, K, Mg and Ca has been reported for a similar sorbent by [24], but with higher desorption efficiencies of 92 – 99 % in comparison to 34–88 % in this study (Table A1, Fig. A4). The difference is explained by the higher desorption solution – sorbent mass ratio (V/m, 1.3 L/g vs. 0.1 L/g) and longer desorption time (24 vs. 1 h) in the former study, or crystallographic differences in the sorbent, amongst others. The desorption of competing elements (Fig. 8, Fig. A4) results in a decrease of the purity of the final LiCl solution. We achieve 67–79 mol-% (24–35 wt-%) Li in the desorption solutions (Fig. 7a). The LiCl solution purity can be influenced by achieving the optimal Li to competing element sorption ratio (Fig. 7 a) through the optimum sorbent – brine ratio of 2–10 g/L. So far, however, this value is only applicable to batch reactors. While the achieved purity of the LiCl solution is not of battery grade (≥ 99.5 wt-%), it can be increased through intensive washing and further polishing by ion-exchange columns and precipitation of competing ions.

The Mn dissolution values of 0.4 – 3.3 wt-% achieved here are high in comparison to other studies, e.g. 0.06 % after 20 cycles in [79]. The Mn dissolutions stems from the disproportionation of 2 Mn^{3+} to Mn^{4+} and Mn^{2+} and the dissolution of the latter [13,18–20] and from temperature induced dissolution of the sorbent [80]. Low sorbent dissolution is required for industrial application, determining the sorbent lifetime, total sorbent costs and annual sorbent replacement, which is accompanied with plant down-time. For the hypothetical 10kt DLE plant discussed above, 7.9 t of sorbent are needed at one hour. Assuming exponential decay of the sorbent with the lower decay constant of 0.06 % per cycle by [79], 902 t of sorbent are needed annually. At a decay rate of an order of magnitude lower, 0.006 % per cycle, only 12.7 t are needed annually, showing the huge importance sorbent stability has on the industrial application. The Mn dissolution can be decreased amongst others through doping of the sorbent with other elements like e.g. Mg, Cr, Fe or Al [81–84], optimization of type and concentration of the desorption solution [75] or coating of the sorbent [79].

5. Conclusion

We prove that the synthesized spinel-type LMO sorbent of this study allows selective and efficient Li extraction from Soultz-sous-Forêts geothermal brine. Due to the fast Li sorption kinetics combined with the high Li sorption capacity, the sorbent is highly promising for industrial-scale DLE in a flow through or short-term batch setup. Due to the additional sorption processes taking place at high equilibrium concentrations, the sorbent can achieve high sorption capacities even at low pH values of the brine. The sorbent shows a low selectivity towards the highly concentrated elements Na, K and Ca and extracts only low amounts of these elements, making it suitable for highly saline brine. The LMO has a high Li selectivity, but an even higher selectivity for Mn, Zn, As and Ba and sorbs these elements in considerable amounts, even though they are less concentrated in the brine. If the sorption of those

elements has negative impacts on Li sorption performance or sorbent stability, the sorbent is not be suitable for brines rich in Mn, Zn, As, Ba or Fe. Alternatively, measures have to be implemented to prevent the sorption, e.g. through removal of those elements in brine pre-treatment, through sorbent modification or purification of the Li bearing desorption solution. Our study shows, that elements sorbed with high affinity and potentially problematic elements should always be regarded in DLE application research, independent of their concentration in the brine. In order to determine the suitability of a sorbent, the optimal extraction conditions and the usage after end-of-life, experiments with every brine are necessary, similar to processing technologies in conventional ore deposits. Further research should be directed to the sorption behaviour of Li and competing elements over many extraction cycles, the accumulation of the latter at the sorbent and the sorbent stability. In order to gain more insights for the industrial application, this research should be conducted in an upscaled pilot plant in-situ at geothermal power plants.

CRediT authorship contribution statement

Klemens Slunitschek: Writing – review & editing, Writing – original draft, Visualization, Validation, Methodology, Investigation, Funding acquisition, Formal analysis, Data curation, Conceptualization. **Elisabeth Eiche:** Writing – review & editing, Validation, Supervision, Methodology, Conceptualization. **Jochen Kolb:** Writing – review & editing, Supervision, Funding acquisition, Conceptualization.

Funding

This work was supported by German Federal Ministry for Economic Affairs and Climate Action [O3EE4023D] and the Friedrich and Elisabeth Boysen foundation.

Declaration of competing interest

The authors declare that they have no known competing financial interests or personal relationships that could have appeared to influence the work reported in this paper.

Acknowledgements

We are very grateful to Dr. Genter from ÉS-Géothermie for the supply of brine and the permission of publication. We thank Chantal Kotschenreuther, Maya Denker and Janine Wagner for their support at experiments and analysis. Rebekka Reich and Michèle Jungmann are acknowledged for helpful discussions regarding sorption processes. We especially thank Editor-in-Chief Dr. Van der Bruggen as well as the anonymous reviewers for their comments and revisions that significantly improved the quality of this article.

Appendix A. Supplementary material

Supplementary data to this article can be found online at https://doi.org/10.1016/j.seppur.2025.134594.

Data availability

Data will be made available on request.

References

[1] K. Habib, S.T. Hansdóttir, H. Habib, Critical metals for electromobility: Global demand scenarios for passenger vehicles, 2015–2050, Resour. Conserv. Recycl. 154 (2020) 104603, https://doi.org/10.1016/j.resconrec.2019.104603.
[2] S. Safari, B.G. Lottermoser, D.S. Alessi, Metal oxide sorbents for the sustainable recovery of lithium from unconventional resources, Appl. Mater. Today 19 (2020) 100638, https://doi.org/10.1016/j.apmt.2020.100638.
[3] W.T. Stringfellow, P.F. Dobson, Technology for the recovery of lithium from geothermal brines, Energies 14 (2021) 6805, https://doi.org/10.3390/en14206805.
[4] A. Khalil, S. Mohammed, R. Hashaikeh, N. Hilal, Lithium recovery from brine: recent developments and challenges, Desalination 528 (2022) 115611, https://doi.org/10.1016/j.desal.2022.115611.
[5] R. Reich, K. Slunitschek, R.M. Danisi, E. Eiche, J. Kolb, Lithium extraction techniques and the application potential of different sorbents for lithium recovery from brines, Miner. Process. Extr. Metall. Rev. (2022) 1–20, https://doi.org/10.1080/08827508.2022.2047041.
[6] R. Reich, R.M. Danisi, T. Kluge, E. Eiche, J. Kolb, Structural and compositional variation of zeolite 13X in lithium sorption experiments using synthetic solutions and geothermal brine, Microporous Mesoporous Mater. 359 (2023) 112623, https://doi.org/10.1016/j.micromeso.2023.112623.
[7] B. Sanjuan, B. Gourcerol, R. Millot, D. Rettenmaier, E. Jeandel, A. Rombaut, Lithium-rich geothermal brines in Europe: an up-date about geochemical characteristics and implications for potential Li resources, Geothermics 101 (2022) 102385, https://doi.org/10.1016/j.geothermics.2022.102385.
[8] A. Genter, C. Baujard, N. Cuenot, C. Dezayes, T. Kohl, F. Masson, B. Sanjuan, J. Scheiber, E. Schill, J. Schmittbuhl, J. Vidal, Geology, Geophysics and Geochemistry in the Upper Rhine Graben: the frame for geothermal energy use, Proceedings of the European Geothermal Congress 2016, Strasbourg, France, 19-24 Sept 2016 (2016).
[9] J. Vidal, A. Genter, Overview of naturally permeable fractured reservoirs in the central and southern Upper Rhine Graben: insights from geothermal wells, Geothermics 74 (2018) 57–73, https://doi.org/10.1016/j.geothermics.2018.02.003.
[10] M. Frey, K. Bär, I. Stober, J. Reinecker, J. van der Vaart, I. Sass, Assessment of deep geothermal research and development in the Upper Rhine Graben, Geotherm Energy 10 (2022) 1–67, https://doi.org/10.1186/s40517-022-00226-2.
[11] U. Saleem, A. Wilhelms, J. Sottmann, H.K. Knuutila, S. Bandyopadhyay, Direct lithium extraction (DLE) methods and their potential in Li-ion battery recycling, Sep. Purif. Technol. 361 (2025) 131315, https://doi.org/10.1016/j.seppur.2024.131315.
[12] R. Chitrakar, H. Kanoh, Y. Miyai, K. Ooi, A New Type of Manganese Oxide (MnO 2 ·0.5H 2 O) Derived from Li 1.6 Mn 1.6 O 4 and its Lithium Ion-Sieve Properties, Chem. Mater. 12 (2000) 3151–3157, https://doi.org/10.1021/cm0000191.
[13] Q. Feng, Y. Miyai, H. Kanoh, K. Ooi, Lithium+ extraction/insertion with spinel-type lithium manganese oxides. Characterization of redox-type and ion-exchange-type sites, Langmuir (1992) 1861–1867.
[14] B. Ammundsen, P.B. Aitchison, G.R. Burns, D.J. Jones, J. Rozière, Proton insertion and lithium-proton exchange in spinel lithium manganates, Solid State Ion. 97 (1997) 269–276, https://doi.org/10.1016/S0167-2738(97)00065-9.
[15] K. Ooi, Y. Miyai, J. Sakakihara, Mechanism of lithium(1+) insertion in spinel-type manganese oxide. Redox and ion-exchange reactions, Langmuir 7 (1991) 1167–1171, https://doi.org/10.1021/la00054a025.
[16] L. Wang, C.G. Meng, W. Ma, Study on Li+ uptake by lithium ion-sieve via the pH technique, Colloids Surf. A Physicochem. Eng. Asp. 334 (2009) 34–39, https://doi.org/10.1016/j.colsurfa.2008.09.050.
[17] M.J. Ariza, D.J. Jones, J. Rozière, R. Chitrakar, K. Ooi, Probing the local structure and the role of protons in lithium sorption processes of a new lithium-rich manganese oxide, Chem. Mater. 18 (2006) 1885–1890, https://doi.org/10.1021/cm052214r.
[18] A. Gao, Z. Sun, S. Li, X. Hou, H. Li, Q. Wu, X. Xi, The mechanism of manganese dissolution on Li1.6Mn1.6O4 ion sieves with HCl, Dalton Trans. 47 (2018) 3864–3871, https://doi.org/10.1039/c8dt00033f.
[19] J.C. Hunter, Preparation of a new crystal form of manganese dioxide: λ-MnO2, J. Solid State Chem. 39 (1981) 142–147, https://doi.org/10.1016/0022-4596(81)90323-6.
[20] K. Ooi, Y. Miyai, S. Katoh, H. Maeda, M. Abe, Lithium-ion insertion/extraction reaction with λ-MnO 2 in the aqueous phase, Chem. Lett. 17 (1988) 989–992, https://doi.org/10.1246/cl.1988.989.
[21] K. Yoshizuka, A. Kitajou, M. Holba, Selective recovery of lithium from seawater using a novel MnO_2 type adsorbent III-benchmark evaluation, Ars Separatoria Acta 4 (2006) 78–85.
[22] X. Shi, D. Zhou, Z. Zhang, L. Yu, H. Xu, B. Chen, X. Yang, Synthesis and properties of Li1.6Mn1.6O4 and its adsorption application, Hydrometallurgy 110 (2011) 99–106, https://doi.org/10.1016/j.hydromet.2011.09.004.
[23] K. Yoshizuka, S. Nishihama, M. Takano, S. Asano, Lithium recovery from brines with novel λ-MnO_2 adsorbent synthesized by hydrometallurgical method, Solvent Extr. Ion Exch. 39 (2021) 604–621, https://doi.org/10.1080/07366299.2021.1876443.
[24] R. Chitrakar, H. Kanoh, Y. Miyai, K. Ooi, Recovery of lithium from seawater using manganese oxide adsorbent (H1.6Mn1.6O4) derived from Li1.6Mn1.6O4, Ind. Eng. Chem. Res. 40 (2001) 2054–2058, https://doi.org/10.1021/ie000911h.
[25] S. Zandevakili, M. Ranjbar, M. Ehteshamzadeh, Recovery of lithium from Urmia Lake by a nanostructure MnO 2 ion sieve, Hydrometall. 149 (2014) 148–152, https://doi.org/10.1016/j.hydromet.2014.08.004.
[26] H. Park, N. Singhal, E.H. Jho, Lithium sorption properties of HMnO in seawater and wastewater, Water Res. 87 (2015) 320–327, https://doi.org/10.1016/j.watres.2015.09.032.
[27] M.J. Park, G.M. Nisola, A.B. Beltran, R.E.C. Torrejos, J.G. Seo, S.-P. Lee, H. Kim, W.-J. Chung, Recyclable composite nanofiber adsorbent for Li+ recovery from seawater desalination retentate, Chem. Eng. J. 254 (2014) 73–81, https://doi.org/10.1016/j.cej.2014.05.095.

[28] T. Ryu, Y. Haldorai, A. Rengaraj, J. Shin, H.-J. Hong, G.-W. Lee, Y.-K. Han, Y. S. Huh, K.-S. Chung, Recovery of lithium ions from seawater using a continuous flow adsorption column packed with granulated chitosan–lithium manganese oxide, Ind. Eng. Chem. Res. 55 (2016) 7218–7225, https://doi.org/10.1021/acs.iecr.6b01632.
[29] B. Sanjuan, R. Millot, C. Dezayes, M. Brach, Main characteristics of the deep geothermal brine (5km) at Soultz-sous-Forêts (France) determined using geochemical and tracer test data, C. R. Geosci. 342 (2010) 546–559, https://doi.org/10.1016/j.crte.2009.10.009.
[30] B. Sanjuan, R. Millot, C. Innocent, C. Dezayes, J. Scheiber, M. Brach, Major geochemical characteristics of geothermal brines from the Upper Rhine Graben granitic basement with constraints on temperature and circulation, Chem. Geol. 428 (2016) 27–47, https://doi.org/10.1016/j.chemgeo.2016.02.021.
[31] F. Nitschke, J. Scheiber, U. Kramar, T. Neumann, Formation of alternating layered Ba-Sr-sulfate and Pb-sulfide scaling in the geothermal plant of Soultz-sous-Forêts, N. Jb. Miner. Abh. 191 (2014) 145–156, https://doi.org/10.1127/0077-7757/2014/0253.
[32] R. Boch, A. Leis, E. Haslinger, J.E. Goldbrunner, F. Mittermayr, H. Fröschl, D. Hippler, M. Dietzel, Scale-fragment formation impairing geothermal energy production: interacting H2S corrosion and CaCO3 crystal growth, Geotherm Energy 5 (2017) 1–19, https://doi.org/10.1186/s40517-017-0062-3.
[33] JCPDS-ICDD, PDF-2 Release 2002, Newton Square, Pennsylvania, USA, 2002.
[34] H. Freundlich, Kapillarchemie, eine Darstellung der Chemie der Kolloide und verwandter Gebiete, Akademische Verlagsgesellschaft, Leipzig, 1909.
[35] I. Langmuir, The adsorption of gases on plane surfaces of glass, mica and platinum, J. Am. Chem. Soc. 40 (1918) 1361–1403, https://doi.org/10.1021/ja02242a004.
[36] A. Ebadi, J.S. Soltan Mohammadzadeh, A. Khudiev, What is the correct form of BET isotherm for modeling liquid phase adsorption? Adsorption 15 (2009) 65–73, https://doi.org/10.1007/s10450-009-9151-3.
[37] S. Brunauer, P.H. Emmett, E. Teller, Adsorption of gases in Multimolecular Layers, J. Am. Chem. Soc. 60 (1938) 309–319, https://doi.org/10.1021/ja01269a023.
[38] C. Wang, Y. Zhai, X. Wang, M. Zeng, Preparation and characterization of lithium λ-MnO2 ion-sieves, Front. Chem. Sci. Eng. 8 (2014) 471–477, https://doi.org/10.1007/s11705-014-1449-3.
[39] Q.-H. Zhang, S. Sun, S. Li, H. Jiang, J.-G. Yu, Adsorption of lithium ions on novel nanocrystal MnO2, Chem. Eng. Sci. 62 (2007) 4869–4874, https://doi.org/10.1016/j.ces.2007.01.016.
[40] J.-L. Xiao, S.-Y. Sun, J. Wang, P. Li, J.-G. Yu, Synthesis and Adsorption Properties of Li1.6Mn1.6O4 Spinel, Ind. Eng. Chem. Res. 52 (2013) 11967–11973, https://doi.org/10.1021/ie400691d.
[41] G. Zhu, P. Wang, P. Qi, C. Gao, Adsorption and desorption properties of Li+ on PVC-H1.6Mn1.6O4 lithium ion-sieve membrane, Chem. Eng. J. 235 (2014) 340–348, https://doi.org/10.1016/j.cej.2013.09.068.
[42] F. Özmal, Y. Erdoğan, Li + adsorption/desorption properties of lithium ion-sieves in aqueous solution and recovery of lithium from borogypsum, J. Environ. Chem. Eng. 3 (2015) 2670–2683, https://doi.org/10.1016/j.jece.2015.09.024.
[43] Y.K. Recepoğlu, N. Kabay, İ. Yılmaz-Ipek, M. Arda, K. Yoshizuka, S. Nishihama, M. Yüksel, Equilibrium and kinetic studies on lithium adsorption from geothermal water by λ-MnO 2, Solvent Extr. Ion Exch. 35 (2017) 221–231, https://doi.org/10.1080/07366299.2017.1319235.
[44] F. Qian, M. Guo, Z. Qian, Q. Li, Z. Wu, Z. Liu, Highly lithium adsorption capacities of H 1.6 Mn 1.6 O 4 ion-sieve by ordered array structure, ChemistrySelect 4 (2019) 10157–10163, https://doi.org/10.1002/slct.201902173.
[45] F. Qian, B. Zhao, M. Guo, Z. Qian, N. Xu, Z. Wu, Z. Liu, Enhancing the Li+ adsorption and anti-dissolution properties of Li1.6Mn1.6O4 with Fe, Co doped, Hydrometallurgy 193 (2020) 105291, https://doi.org/10.1016/j.hydromet.2020.105291.
[46] F. Qian, B. Zhao, M. Guo, Z. Qian, Z. Wu, Z. Liu, Trace doping by fluoride and sulfur to enhance adsorption capacity of manganese oxides for lithium recovery, Mater. Des. 194 (2020) 108867, https://doi.org/10.1016/j.matdes.2020.108867.
[47] F. Qian, B. Zhao, M. Guo, J. Li, Z. Liu, Z. Wu, K-gradient doping to stabilize the spinel structure of Li1.6Mn1.6O4 for Li+ recovery, Dalton Trans. 49 (2020) 10939–10948, https://doi.org/10.1039/D0DT02405H.
[48] F. Qian, B. Zhao, M. Guo, Z. Wu, W. Zhou, Z. Liu, Surface trace doping of Na enhancing structure stability and adsorption properties of Li1.6Mn1.6O4 for Li+ recovery, Sep. Purif. Tech. 256 (2021) 117583, https://doi.org/10.1016/j.seppur.2020.117583.
[49] V. Goldberg, F. Nitschke, T. Kluge, Herausforderungen und Chancen für die Lithiumgewinnung aus geothermalen Systemen in Deutschland – Teil 2: Potenziale und Produktionsszenarien in Deutschland, Grundwasser - Zeitschrift Der Fachsektion Hydrogeologie (2022) 1–15, https://doi.org/10.1007/s00767-022-00523-4.
[50] Y. Marcus, A simple empirical model describing the thermodynamics of hydration of ions of widely varying charges, sizes, and shapes, Biophys. Chem. 51 (1994) 111–127, https://doi.org/10.1016/0301-4622(94)00051-4.
[51] I. Persson, Hydrated metal ions in aqueous solution: how regular are their structures? Pure Appl. Chem. 82 (2010) 1901–1917, https://doi.org/10.1351/PAC-CON-09-10-22.
[52] S. Adapa, A. Malani, Role of hydration energy and co-ions association on monovalent and divalent cations adsorption at mica-aqueous interface, Sci. Rep. 8 (2018) 12198, https://doi.org/10.1038/s41598-018-30549-9.
[53] G.M. Nisola, L.A. Limjuco, E.L. Vivas, C.P. Lawagon, M.J. Park, H.K. Shon, N. Mittal, I.W. Nah, H. Kim, W.-J. Chung, Macroporous flexible polyvinyl alcohol lithium adsorbent foam composite prepared via surfactant blending and cryo-desiccation, Chem. Eng. J. 280 (2015) 536–548, https://doi.org/10.1016/j.cej.2015.05.107.
[54] P. Yang, J.E. Post, Q. Wang, W. Xu, R. Geiss, P.R. McCurdy, M. Zhu, Metal adsorption controls stability of layered manganese oxides, Environ. Sci. Technol. 53 (2019) 7453–7462, https://doi.org/10.1021/acs.est.9b01242.
[55] P. Loganathan, R.G. Burau, Sorption of heavy metal ions by a hydrous manganese oxide, Geochim. Cosmochim. Acta 37 (1973) 1277–1293, https://doi.org/10.1016/0016-7037(73)90061-6.
[56] H. Tamura, R. Furuichi, Adsorption affinity of divalent heavy metal ions for metal oxides evaluated by modeling with the frumkin isotherm, J. Colloid Interface Sci. 195 (1997) 241–249, https://doi.org/10.1006/jcis.1997.5169.
[57] B.A. Manning, S.E. Fendorf, B. Bostick, D.L. Suarez, Arsenic(III) oxidation and arsenic(V) adsorption reactions on synthetic birnessite, Environ. Sci. Technol. 36 (2002) 976–981, https://doi.org/10.1021/es0110170.
[58] C. Tournassat, L. Charlet, D. Bosbach, A. Manceau, Arsenic(III) oxidation by birnessite and precipitation of manganese(II) arsenate, Environ. Sci. Technol. 36 (2002) 493–500, https://doi.org/10.1021/es0109500.
[59] B.J. Lafferty, M. Ginder-Vogel, M. Zhu, K.J.T. Livi, D.L. Sparks, Arsenite oxidation by a poorly crystalline manganese-oxide. 2. Results from X-ray absorption spectroscopy and X-ray diffraction, Environ. Sci. Technol. 44 (2010) 8467–8472, https://doi.org/10.1021/es102016c.
[60] A.A. Dalvi, N. Ajith, K.K. Swain, R. Verma, Sorption of arsenic on manganese dioxide synthesized by solid state reaction, J. Environ. Sci. Health A Tox. Hazard. Subst Environ. Eng. 50 (2015) 866–873, https://doi.org/10.1080/10934529.2015.1019808.
[61] N. Ajith, K. Bhattacharyya, P.R. Ipte, A.K. Satpati, A.K. Tripathi, R. Verma, K. K. Swain, Interaction of arsenic(III) and arsenic(V) on manganese dioxide: XPS and electrochemical investigations, J. Environ. Sci. Health A Tox. Hazard. Subst Environ. Eng. 54 (2019) 277–285, https://doi.org/10.1080/10934529.2018.1544478.
[62] P. Alexandre, Practical geochemistry, Springer, Cham, 2021.
[63] J. Liu, Q. Chen, Y. Yang, H. Wei, M. Laipan, R. Zhu, H. He, M.F. Hochella, Coupled redox cycling of Fe and Mn in the environment: the complex interplay of solution species with Fe- and Mn-(oxyhydr)oxide crystallization and transformation, Earth Sci. Rev. 232 (2022) 104105, https://doi.org/10.1016/j.earscirev.2022.104105.
[64] L. Bochatay, P. Persson, Metal Ion Coordination at the water-manganite (gamma-MnOOH) interface, J. Colloid Interface Sci. 229 (2000) 593–599, https://doi.org/10.1006/jcis.2000.7014.
[65] X. Li, G. Pan, Y. Qin, T. Hu, Z. Wu, Y. Xie, EXAFS studies on adsorption-desorption reversibility at manganese oxide-water interfaces. II. Reversible adsorption of zinc on delta-MnO2, J. Colloid Interface Sci. 271 (2004) 35–40, https://doi.org/10.1016/j.jcis.2003.11.029.
[66] G. Pan, Y. Qin, X. Li, T. Hu, Z. Wu, Y. Xie, EXAFS studies on adsorption-desorption reversibility at manganese oxides-water interfaces. I. Irreversible adsorption of zinc onto manganite (gamma-MnOOH), J. Colloid Interface Sci. 271 (2004) 28–34, https://doi.org/10.1016/j.jcis.2003.11.028.
[67] P. Trivedi, L. Axe, T.A. Tyson, XAS studies of Ni and Zn sorbed to hydrous manganese oxide, Environ. Sci. Technol. 35 (2001) 4515–4521, https://doi.org/10.1021/es0109848.
[68] M. Younas, A.U.R. Bacha, K. Khan, I. Nabi, Z. Ullah, M. Humayun, J. Hou, Application of manganese oxide-based materials for arsenic removal: a review, Sci. Total Environ. 918 (2024) 170269, https://doi.org/10.1016/j.scitotenv.2024.170269.
[69] D.G. Brookins, Eh-pH diagrams for geochemistry: with 98 figures and 61 tables, Springer, 1988.
[70] P. Smedley, D. Kinniburgh, A review of the source, behaviour and distribution of arsenic in natural waters, Appl. Geochem. 17 (2002) 517–568, https://doi.org/10.1016/S0883-2927(02)00018-5.
[71] L. Schacht, M. Ginder-Vogel, Arsenite depletion by manganese oxides: a case study on the limitations of observed first order rate constants, Soil Syst. 2 (2018) 39, https://doi.org/10.3390/soilsystems2030039.
[72] A. Criaud, C. Fouillac, The distribution of arsenic (III) and arsenic (V) in geothermal waters: examples from the Massif Central of France, the Island of Dominica in the Leeward Islands of the Caribbean, the Valles Caldera of New Mexico, U.S.A., and southwest Bulgaria, Chem. Geol. 76 (1989) 259–269, https://doi.org/10.1016/0009-2541(89)90095-8.
[73] J. Park, H. Sato, S. Nishihama, K. Yoshizuka, Lithium recovery from geothermal water by combined adsorption methods, Solvent Extr. Ion Exch. 30 (2012) 398–404, https://doi.org/10.1080/07366299.2012.687165.
[74] T.S. Choong, T.G. Chuah, Y. Robiah, F.L. Gregory Koay, I. Azni, Arsenic toxicity, health hazards and removal techniques from water: an overview, Desalination 217 (2007) 139–166, https://doi.org/10.1016/j.desal.2007.01.015.
[75] L. Herrmann, H. Ehrenberg, M. Graczyk-Zajac, E. Kaymakci, T. Kölbel, L. Kölbel, J. Tübke, Lithium recovery from geothermal brine – an investigation into the desorption of lithium ions using manganese oxide adsorbents, Energy Adv. (2022), https://doi.org/10.1039/D2YA00099G.
[76] L. Kölbel, K. Slunitschek, E. Kaymakci, T. Kölbel, R. Reich, J. Schneider, Lithium recovery from geothermal brines: an investigation into radioactive nuclide uptake on lithium-manganese-oxide (LMO) granules, Hydrometall. 224 (2024) 106266, https://doi.org/10.1016/j.hydromet.2024.106266.
[77] BMJ, Bundesministeirum der Justiz und Verbraucherschutz - Verordnung über Deponien und Langzeitlager (Deponieverordnung - DepV), Anhang 3: DepV, 2009.
[78] LAGA, LAGA EW 98: Richtlinie für das Vorgehen bei physikalischen und chemischen Untersuchungen von Abfällen, verunreinigten Böden und Materialien aus dem Altlastenbereich. Herstellung und Untersuchung von wässrigen Eluaten: EW 98, 2017.

[79] L.-R. Bao, J.-Z. Zhang, W.-P. Tang, S.-Y. Sun, Synthesis and adsorption properties of metal oxide-coated lithium ion-sieve from salt lake brine, Desalination 546 (2023) 116196, https://doi.org/10.1016/j.desal.2022.116196.
[80] C.-H. Lu, S.-W. Lin, Dissolution kinetics of spinel lithium manganate and its relation to capacity fading in lithium ion batteries, J. Mater. Res. 17 (2002) 1476–1481, https://doi.org/10.1557/JMR.2002.0219.
[81] L. Bao, J. Zhang, J. Wu, G. Zhang, Y. Yang, W. Tang, M. Xue, Preparation of Mg-doped Li1.6Mn1.6O4 with enhanced Li+ adsorption performance and anti-dissolution properties of Mn, Hydrometall. 209 (2022) 105772, https://doi.org/10.1016/j.hydromet.2021.105772.
[82] G. Cao, X. Yang, Z. Yin, Y. Lei, H. Wang, J. Li, Synthesis, adsorption properties and stability of Cr-Doped lithium Ion Sieve in Salt Lake Brine, BCSJ 92 (2019) 1205–1210, https://doi.org/10.1246/bcsj.20190061.
[83] M. Chen, R. Wu, S. Ju, X. Zhang, F. Xue, W. Xing, Improved performance of Al-doped $LiMn_2O_4$ ion-sieves for Li+ adsorption, Microporous Mesoporous Mater. 261 (2018) 29–34, https://doi.org/10.1016/j.micromeso.2017.10.058.
[84] R. Chitrakar, Y. Makita, K. Ooi, A. Sonoda, Lithium recovery from salt lake brine by H2TiO3, Dalton Trans. 43 (2014) 8933–8939, https://doi.org/10.1039/c4dt00467a.

Sorption of lithium and competing ions from geothermal brine to lithium manganese oxide – Electronic Supplement

Slunitschek, Klemens[a,b,*]; Eiche, Elisabeth[a,b]; Kolb, Jochen[a,b]

[a]*Chair of Geochemistry and Economic Geology, Institute of Applied Geosciences, Karlsruhe Institute of Technology, Karlsruhe, Germany*

[b]*Laboratory for Environmental and Raw Materials Analysis (LERA), Institute of Applied Geosciences, Karlsruhe Institute of Technology, Adenauerring 20b, 76131 Karlsruhe, Germany;*

**corresponding author: Klemens Slunitschek; e-mail: klemens.slunitschek@kit.edu; postal address: Adenauerring 20b, 76131 Karlsruhe, Germany; phone: +49 721 608-43322*

a)

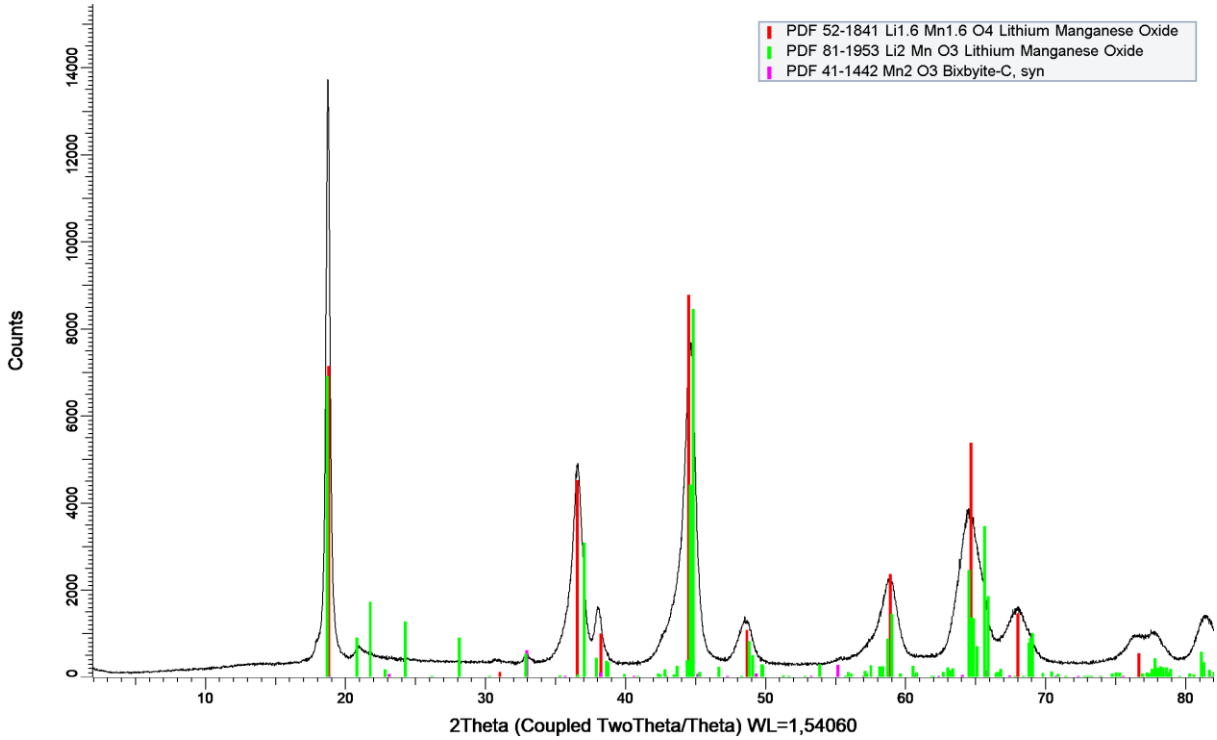

b)

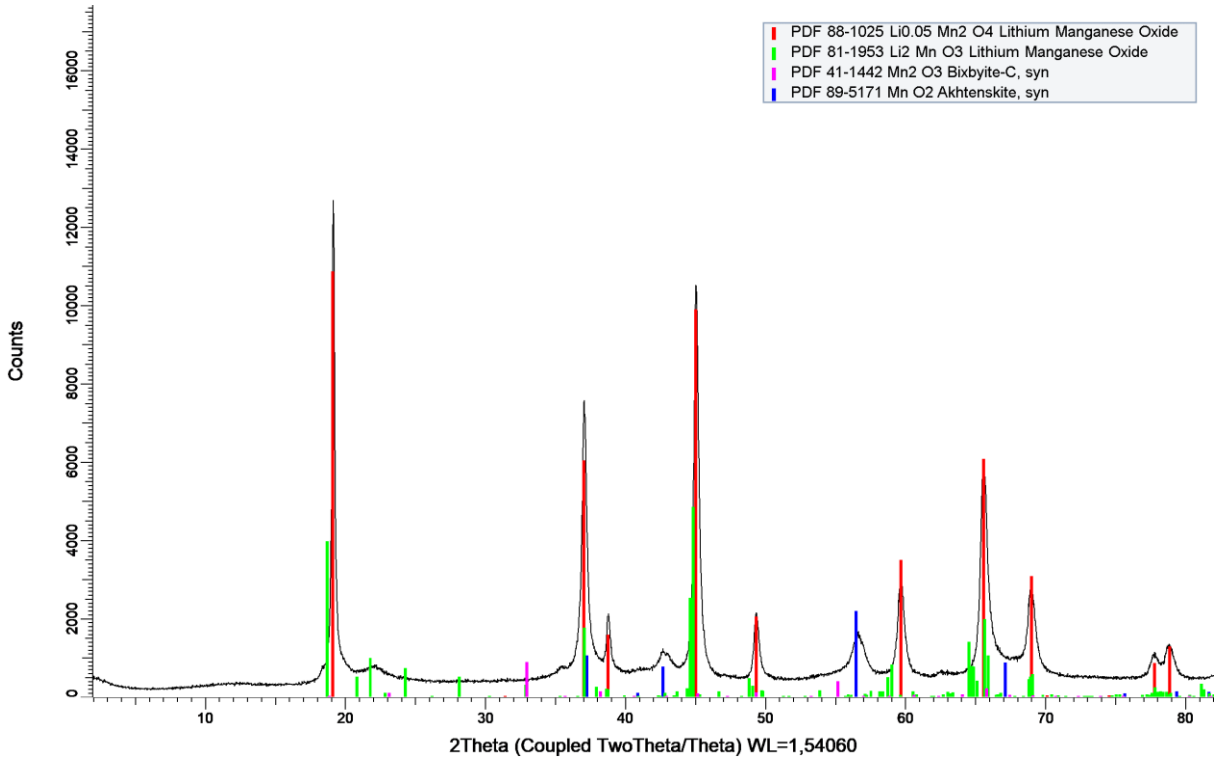

Figure A1: Evaluated diffractograms of precursor (a) and sorbent (b).

Table A1: Average desorption efficiency based on the linear interpolation between sorption capacity and element concentration at the sorbent after desorption of kinetic and isotherm of S4. R = Pearson's R; efficiency = desorption efficiency; remaining = percentage of element remaining at sorbent after desorption. Calculation of efficiency and remaining only for correlation coefficient R > 0.8.

	Li	**Na**	**K**	**Mg**	**Ca**
intercept	-1.04±0.24	0.19±0.034	-0.72±0.21	0.047±0.003	0.86±0.04
slope	-0.3±0.03	0.14±0.032	0.6±0.12	0.12±0.039	-0.019±0.007
R	0.43	0.52	0.60	0.66	-0.53
efficiency [%]					
remaining [%]					
	Sr	**$Ba_{filtrate}$**	**Ba_{solid}**	**Zn**	**As**
intercept	0.51±0.062	-0.03±0.002	0.35±0.02	-0.006±0.001	0.009±0.002
slope	-0.12±0.038	0.44±0.01	0.27±0.02	-0.58±0.01	0.91±0.014
R	-0.30	0.99	0.95	0.98	0.99
efficiency [%]		56.0	73.0	42.0	9.0
remaining [%]		44.0	27.0	58.0	91.0

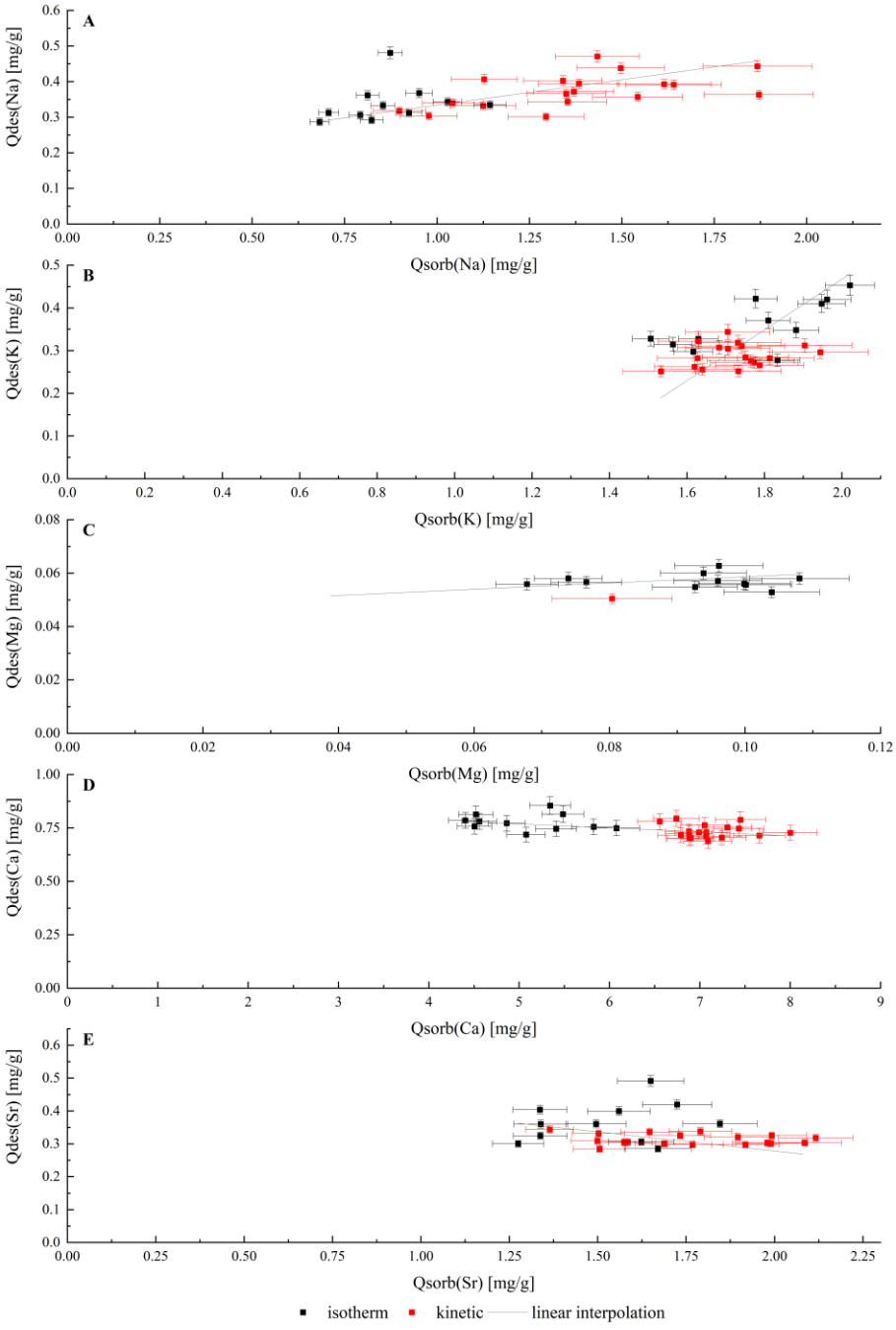

Figure A4: Element concentration at sorbent after sorption (Q_{sorb}) and desorption (Q_{des}) of isotherm (black) and kinetic experiment (red).

Table A2: Ionic radius, charge density, hydration energy and enthalpy, sorted after the determined order of selectivity. Ionic radius after Persson (2010), * Marcus (1994). Hydration energy and enthalpy after Marcus (1994)

Ion	Ionic radius	Charge density	hydration energy	hydration enthalpy
	[Å]	[e/Å]	[kJ/mol]	[kJ/mol]
Mn2+	0.86	2.3	-1760	-1870
Zn2+	0.74	2.7	-1955	-2070
Ba2+	1.48	1.4	-1250	-1330
Li+	0.76	1.3	-475	-530
Sr2+	1.28	1.6	-1380	-1470
Ca2+	1.12	1.8	-1505	-1600
K+	1.38*	0.7	-295	-330
Mg2+	0.76	2.6	-1830	-1945
Na+	1.09	0.9	-365	-415

Additional experiments with brine and LiOH solution

Synthesis of sorbent after same procedure, with slight differences in the initial delithiation, as listed in Table A3 and results in Table A4.

Table A3: Conditions of the initial delithiation of the additional experiments. S4 is the sorbent used in the article.

	S1	S2	S3	S4
temperature [°C]	60	60	60	70
acid/sorbent [L/g]	0.03	0.05	0.05	0.1
cycles	3	3	4	3

Table A4: Composition and initial desorption of the four precursor batches and final composition of the sorbent. S4 is used in the article.

	Li [mg/g]				Mn [mg/g]			
synthesis	S1	S2	S3	S4	S1	S2	S3	S4
precursor [mg/g]	67.1	68.0	69.0	67.0	551	584	537	551
desorbed (solid chemistry) [%]	80.2	85.0	88.0	97.0				
sorbent [mg/g]	13.3	9.9	8.1	1.9	579	589	608	601

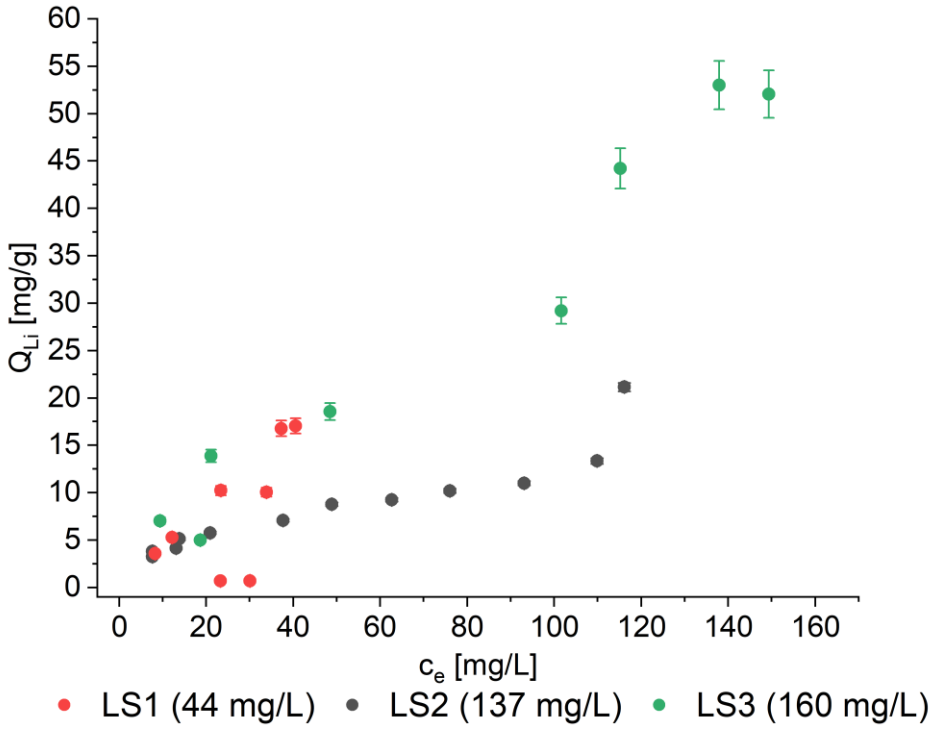

Figure A5: Isotherms from pure LiOH solution experiments with different initial Li concentrations (in parentheses). All solutions are buffered to a pH=5 with the same buffer as described in the article. BET isotherm is indicated at all three isotherms.

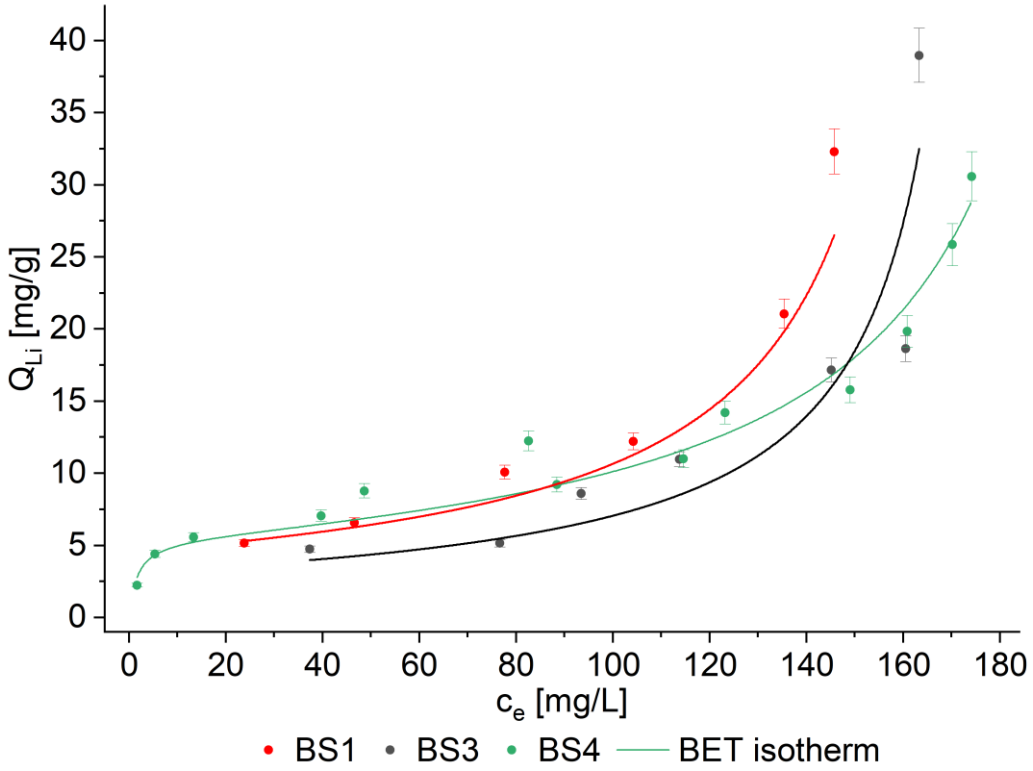

Figure A6: Lithium isotherms from brine experiments with BET isotherm models. BS4 is used in the paper. For BS1 and BS3, data points at low equilibrium concentration are missing for successful application of the BET isotherm, but BET isotherm is indicated.

Table A5: Element concentration in desorption eluate of sorption isotherm samples.

sorption sample with m/V	Aqueous concentration [mg/L]									
g/L	As	Ba	Ca	K	Li	Mg	Mn	Na	Sr	Zn
4	0.09	5.31	43.3	12.1	116	0.37	273	3.97	13.7	2.14
6	0.06	3.56	40.5	12.6	100	0.33	216	2.77	11.2	1.38
8	0.05	3.32	40.5	13.5	103	0.30	110	6.04	14.1	1.24
10	0.04	2.24	34.5	13.3	80.0	0.26	133	4.24	10.5	0.99
15	0.02	1.88	37.5	12.0	66.6	0.27	108	4.58	12.2	0.69
20	0.01	1.24	31.0	12.6	60.0	0.21	107	3.74	8.75	0.49
30	0.01	0.98	31.9	13.0	45.2	0.20	72.7	3.80	9.14	0.35
40	0.01	0.86	32.1	13.7	35.4	0.19	53.8	4.73	9.83	0.29
80	<0.003	0.63	31.3	14.8	26.9	0.18	42.0	3.49	9.42	0.16
analytical uncertainty [%]	3.2	3.7	4.8	5.2	4.4	3.8	3.5	3.5	3.3	2.6

Analytical Quality

Each ICP-OES measurement was conducted in triplicate and the mean value is used as the final result for the sample. The level of detection (LOD) and level of quantification (LOQ) were determined through the repeated measurement of blank samples, that is ultrapure water (MilliQ water). The LOD was calculated as three times the standard deviation of the blank measurement and the LOQ as nine times the standard deviation. The certified reference standard MISA Standard 6 (LGC Standards) was measured several times and used for quality control and for the calculation of the analytical accuracy and precision. Additionally, calibration standards were measured several times for quality control.

For the adaptation of the isotherm models, conducted in OriginPro 2019 (OriginLab), the Levenberg-Marquardt algorithm, based on the method of least squares, was used. Thereby, the isotherm model parameters were fitted to the data and the quality of fit calculated and expressed as R^2 value. For the calculation of the average desorption efficiency, a linear function was interpolated to the element concentration at the sorbent before desorption (sorption capacity Q) and after desorption (Figure 8). For this, Pearson's correlation was calculated, with the R2 value as the indicator for statistical robustness and quality of fit. The interpolation was conducted in OriginPro 2019 (OriginLab), as well.

Table A6: Analytical uncertainty of the analysed samples of the sorption kinetic experiment. Analytical uncertainty of the isotherm experiments is given in the article.

	As	Ba	Ca	K	Li	Mg	Mn	Na	Sr	Zn
Analytical uncertainty %	8.2	8.0	3.8	6.4	6.0	11.0	4.8	7.9	5.0	6,4

Figure A7: Diffractograms of sorbent (dark green) and relithiated sorbents of the sorption kinetic experiment. Red vertical line with diamond: PDF 85-1841 - $Li_{1.6}Mn_{1.6}O_4$; Blue vertical line: PDF 88-1025 - $Li_{0.05}Mn_2O_4$; Magenta: PDF 81-1953 – Li_2MnO_3; Red vertical line: PDF 89-5171 – MnO_2.

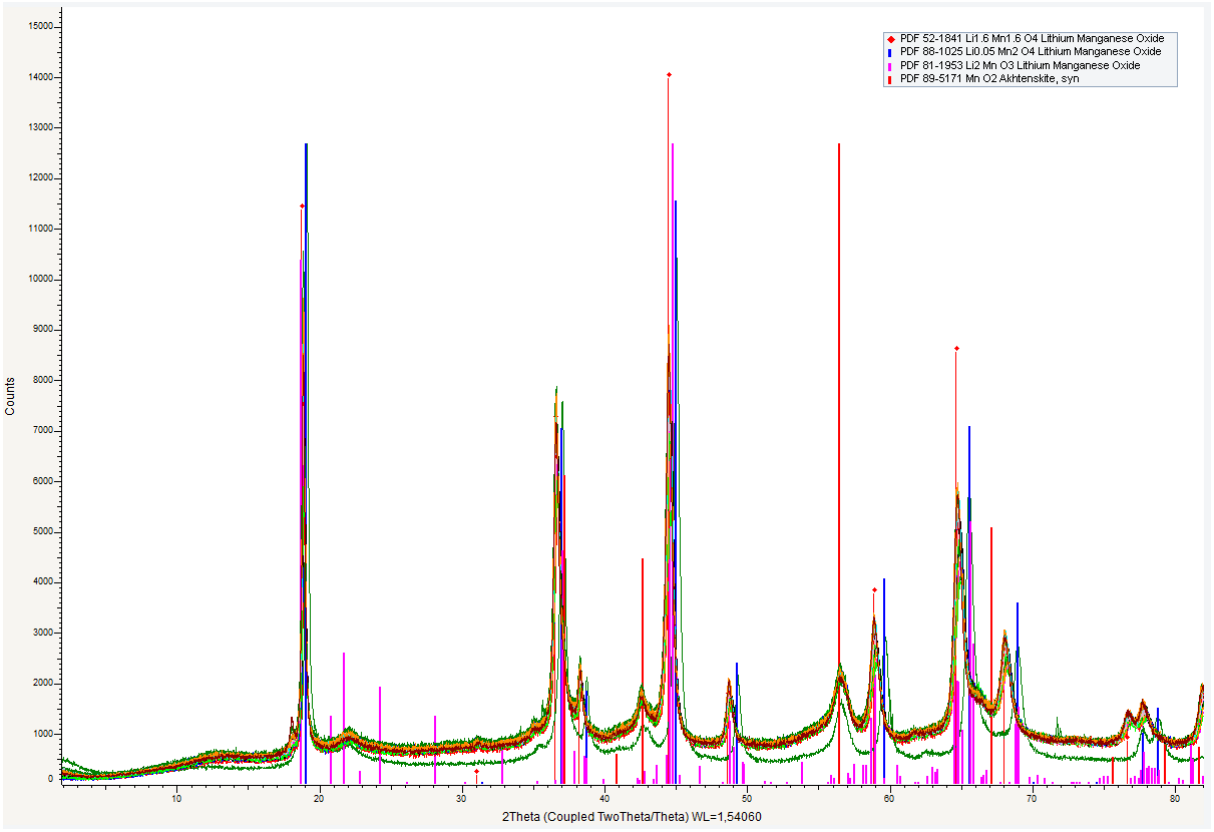

Figure A8: Diffractograms of sorbent (black) and relithiated sorbents of the sorption isotherm experiment. Blue vertical line: PDF 88-1025 – $Li_{0.05}Mn_2O_4$; Magenta: PDF 81-1953 – Li_2MnO_3; Red: PDF 89-5171 – MnO_2.

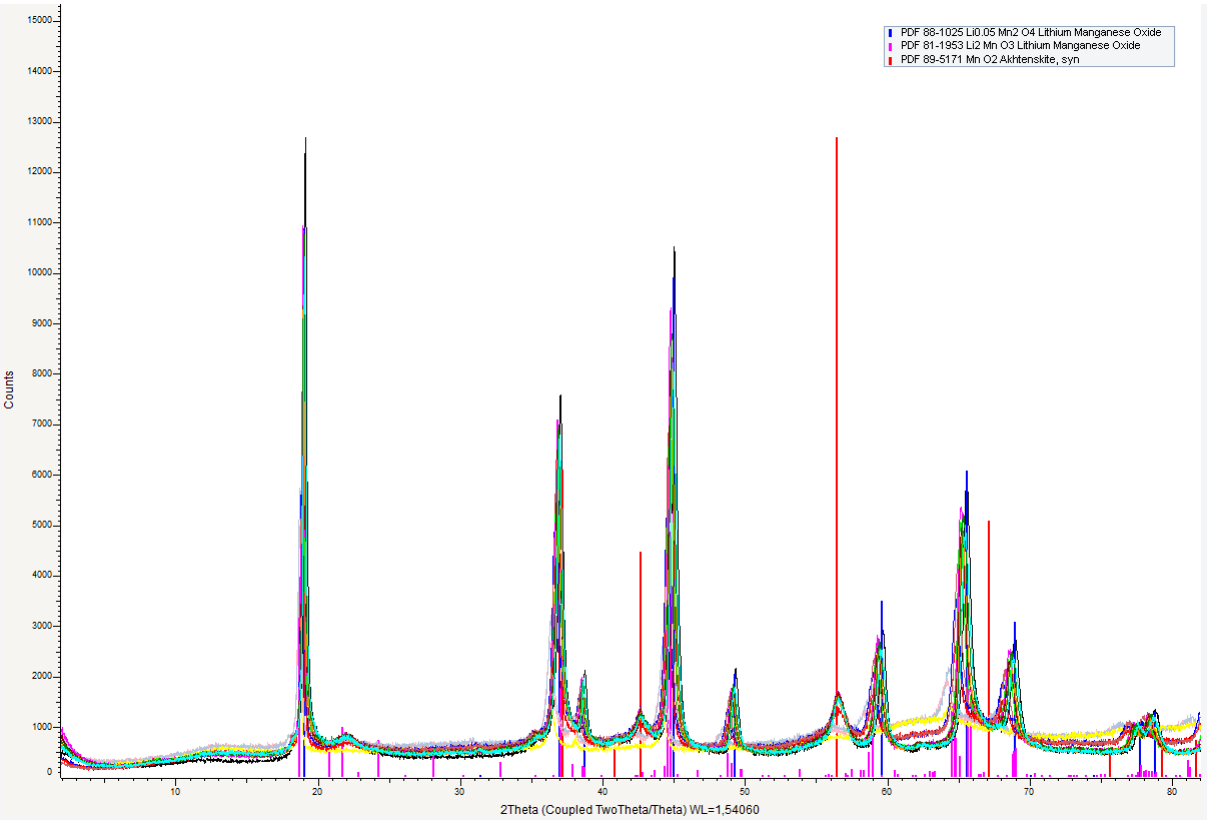

Sorption of lithium and competing ions from geothermal brine to lithium manganese oxide – Electronic Supplement

—

Addendum

Slunitschek. Klemens[a.b.]*; Eiche. Elisabeth[a.b]; Kolb. Jochen[a.b]

[a]*Chair of Geochemistry and Economic Geology. Institute of Applied Geosciences. Karlsruhe Institute of Technology. Karlsruhe. Germany*

[b]*Laboratory for Environmental and Raw Materials Analysis (LERA). Institute of Applied Geosciences. Karlsruhe Institute of Technology. Adenauerring 20b. 76131 Karlsruhe. Germany;*

**corresponding author: Klemens Slunitschek; e-mail: klemens.slunitschek@kit.edu; postal address: Adenauerring 20b. 76131 Karlsruhe. Germany; phone: +49 721 608-43322*

Table AA1: Chemical composition of sorption and desorption eluates of brine isotherm experiment of corresponding sorbents.

Sorption												
sample	mass	volume	As	Ba	Ca	K	Li	Mg	Mn	Na	Sr	Zn
	g	L	mg/L									
brine, buffered		0.1	3.14	4.19	7310	3457	181	133	16.7	32072	434	2.32
brine, buffered		0.1	3.23	4.41	7013	3337	175	131	16.6	32422	432	2.31
20	0.02	0.1	2.42	3.73	7148	3377	174	130	4.1	31426	423	1.78
40	0.04	0.1	1.99	3.39	7143	3376	170	130	0.4	31639	424	1.33
100	0.10	0.1	1.11	2.71	7073	3353	161	129	0.0	30894	423	0.88
200	0.20	0.1	0.54	1.91	7118	3359	149	129	0.01	31828	415	0.54
400	0.41	0.1	0.19	1.04	7048	3188	123	129	0.02	33078	426	0.20
600	0.60	0.1	0.16	0.81	7218	3363	115	132	0.13	31641	420	0.56
800	0.80	0.1	0.08	0.47	6956	3146	82.6	129	0.01	32249	416	0.09
1000	1.00	0.1	0.14	0.61	7103	3318	88.4	132	0.13	31360	413	0.79
1500	1.51	0.1	<0.01	0.35	6814	3111	48.6	128	0.07	31836	397	0.08
2000	2.00	0.1	0.08	0.31	7132	3284	39.7	132	0.19	31693	405	0.21
3000	3.00	0.1	0.06	0.16	6992	3217	13.32	130	0.01	31255	386	0.46
4000	4.00	0.1	0.05	0.10	7044	3270	5.32	127	0.02	31913	386	<0.001
8000	8.01	0.1	0.04	0.07	6778	3105	1.66	127	0.02	31254	333	0.04
m.u. %			7.05	4.25	4.21	3.13	5.60	6.79	4.52	3.78	5.69	3.18
Desorption												
100	0.04	0.01	0.84	5.54	35.9	7.27	91.6	0.67	201	3.90	7.87	3.35
200	0.08	0.01	0.27	6.03	38.2	8.59	102	0.40	394	3.42	9.69	2.62
400	0.20	0.02	0.09	5.31	43.3	12.1	116	0.37	273	3.97	13.7	2.14
600	0.40	0.04	0.06	3.56	40.5	12.6	100	0.33	216	2.77	11.2	1.38
800	0.60	0.06	0.05	3.32	40.5	13.5	103	0.30	110	6.04	14.1	1.24
1000	0.80	0.08	0.04	2.24	34.5	13.3	80.0	0.26	133	4.24	10.5	0.99
1500	1.00	0.1	0.02	1.88	37.5	12.0	66.6	0.27	108	4.58	12.2	0.69
2000	1.00	0.1	0.01	1.24	31.0	12.6	60.0	0.21	107	3.74	8.75	0.49
3000	1.00	0.1	0.01	0.98	31.9	13.0	45.2	0.20	72.7	3.80	9.14	0.35
4000	1.00	0.1	0.01	0.86	32.1	13.7	35.4	0.19	53.8	4.73	9.83	0.29
8000	1.00	0.1	<0.003	0.63	31.3	14.8	26.9	0.18	42.0	3.49	9.42	0.16
m.u.%			3.15	3.66	4.80	5.21	4.40	3.82	3.48	3.46	3.34	2.59

Table AA2: Chemical composition of sorption and desorption eluates of brine kinetic experiment of corresponding sorbents. rep = replicate. m.u.% = measurement uncertainty in %

Sorption

sample	mass	volume	As	Ba	Ca	K	Li	Mg	Mn	Na	Sr	Zn
	g	L						mg/L				
brine, buffered		0.2	3.23	4.41	7013	3337	175	131	16,63	32422	432	2.31
1	0.50	0.2	1.10	2.82	6792	3131	149	134	0.06	30243	416	1.19
5	0.51	0.2	0.77	2.33	6960	3220	144	133	<0.004	31277	423	0.87
5-rep	0.51	0.2	0.72	2.31	6780	3131	143	133	<0.004	30284	414	0.82
8	0.51	0.2	0.76	2.34	6941	3223	144	132	<0.004	31045	421	0.82
10	0.50	0.2	0.65	2.16	6912	3196	141	133	<0.004	31081	421	0.79
13	0.51	0.2	0.72	2.31	6831	3163	143	132	<0.004	30643	410	0.77
15	0.51	0.2	0.61	2.07	6855	3185	138	132	<0.004	30798	420	0.74
20	0.51	0.2	0.49	1.92	6905	3221	139	132	<0.004	31136	416	0.56
30	0.51	0.2	0.49	1.83	6939	3212	137	130	<0.004	31295	420	0.52
45	0.51	0.2	0.45	1.72	6832	3268	136	131	<0.004	30701	416	0.45
60	0.50	0.2	0.43	1.65	6948	3226	136	130	<0.004	31144	413	0.42
60-rep	0.50	0.2	0.44	1.64	6884	3193	137	131	<0.004	30861	420	0.38
120	0.51	0.2	0.40	1.49	6910	3129	137	131	<0.004	31765	422	0.29
240	0.50	0.2	0.38	1.33	6793	3202	134	130	<0.004	30800	418	0.29
240-rep	0.50	0.2	0.41	1.34	6521	3034	134	130	<0.004	29875	403	0.24
360	0.50	0.2	0.36	1.26	6878	3226	134	130	<0.004	31037	416	0.17
720	0.50	0.2	0.34	1.11	6936	3182	130	129	<0.004	31303	422	0.12
1440	0.50	0.2	0.29	0.96	7130	3156	128	130	0.12	32718	431	0.09
m.u. %			8.17	7.99	1.71	0.97	5.97	7.30	4.77	4.54	4.70	6.42
						desorption						
1	0.3	0.03	0.12	3.73	41.12	13.56	82.13	0.26	182	13.63	10.54	1.48
5	0.31	0.03	0.23	5.40	44.77	13.83	97.56	0.29	163	8.32	12.77	2.09
5-rep	0.3	0.03	0.21	5.24	42.85	13.20	99.75	0.28	186	5.44	11.77	2.12
8	0.3	0.03	0.24	5.16	42.40	13.63	93.63	0.27	152	8.09	12.00	2.06
10	0.3	0.03	0.21	5.44	45.02	12.84	103	0.31	168	8.72	12.42	2.11
13	0.3	0.03	0.24	5.09	42.39	12.71	91.11	0.30	165	9.56	11.72	2.06
15	0.3	0.03	0.24	5.89	43.43	12.82	108	0.30	204	5.77	12.96	2.35
20	0.3	0.03	0.33	6.29	46.46	13.65	112	0.34	194	11.81	13.29	2.47
30	0.3	0.03	0.29	5.92	45.21	13.51	114	0.35	199	10.47	13.41	2.38
45	0.29	0.03	0.27	6.24	47.39	12.05	117	0.39	213	4.96	13.64	2.51
60	0.3	0.03	0.27	6.21	46.16	13.77	124	0.37	226	5.28	14.15	2.50
60-rep	0.3	0.03	0.32	6.38	46.07	12.90	121	0.36	188	7.70	14.81	2.51
120	0.3	0.03	0.34	6.72	49.20	13.69	125	0.44	206	12.39	15.12	2.67
240	0.3	0.03	0.36	7.37	51.59	13.10	136	0.52	187	7.50	15.98	3.01
240-rep	0.3	0.03	0.35	7.29	49.76	12.68	133	0.49	200	8.43	15.72	2.89
360	0.3	0.03	0.34	7.59	54.05	12.87	133	0.52	243	5.77	16.14	3.10
720	0.3	0.03	0.32	8.77	55.94	12.42	146	0.62	232	6.39	17.12	3.62
1440	0.3	0.03	0.42	8.54	54.04	12.15	153	0.63	195	9.19	17.78	3.37
m.u. %			3.15	3.66	4.80	5.21	4.40	3.82	3.48	3.46	3.34	2.59

Table AA 3: Chemical analysis of acid digested sorbents after sorption and desorption step of brine isotherm and kinetic experiment. m.u.% = measurement uncertainty in %

Sample	mass	volume	Aqueous concentration [mg/L]									
	g	L	As	Ba	Ca	K	Li	Mg	Mn	Na	Sr	Zn
Isotherm – Sorbent after sorption												
Sorbent	0.1	0.05	<0.005	2.25	0.74	<0.2	142	0.12	1160	<0.1	0.41	0.01
sorbent	0.1	0.05	0.05	1.08	0.24	<0.2	3.89	0.09	1260	<0.1	0.07	0.02
20	0.1	0.01	1.95	2.38	4.80	1.84	20.9	0.09	675	0.84	1.59	2.56
40	0.1	0.01	3.34	4.53	12.9	3.43	41.3	0.21	1319	1.81	3.74	4.84
100	0.1	0.01	6.30	9.28	29.8	7.66	76.9	0.51	2841	3.46	8.45	6.70
200	0.1	0.05	1.58	2.86	9.86	2.78	26.3	0.18	1118	1.50	3.05	1.56
400	0.1	0.05	1.26	2.63	11.8	3.31	26.9	0.16	1212	1.67	3.75	1.04
600	0.1	0.05	0.88	2.18	11.2	3.83	24.2	0.22	1198	1.39	3.18	0.77
800	0.1	0.05	0.87	2.33	13.2	4.78	29.9	0.18	1414	2.68	4.35	0.68
1000	0.1	0.05	0.64	1.88	10.4	3.86	22.3	0.21	1258	1.82	3.19	0.51
1500	0.1	0.05	0.58	2.11	14.8	4.42	26.7	0.20	1624	2.53	4.44	0.44
2000	0.1	0.05	0.40	1.65	10.5	4.12	19.5	0.21	1342	1.84	3.10	0.30
3000	0.1	0.05	0.24	1.33	9.35	4.03	14.6	0.20	1206	2.35	2.75	0.18
4000	0.2	0.1	0.11	1.02	7.51	3.25	10.0	0.16	992	1.59	2.23	0.12
8000	0.1	0.05	0.09	1.15	8.99	4.13	8.35	0.20	1201	1.78	2.60	0.08
Kinetic – Sorbent after sorption												
1	0.1	0.05	1.44	2.34	14.2	3.70	21.6	0.17	1300	4.06	2.96	1.01
2	0.1	0.05	1.60	2.45	13.7	3.94	20.6	<0.05	1417	3.12	2.80	1.08
5	0.1	0.05	1.73	2.69	14.4	3.67	24.9	<0.05	1239	2.71	3.32	1.50
5-rep	0.1	0.05	1.65	2.73	14.4	3.49	25.5	<0.05	1257	1.92	3.22	1.35
8	0.1	0.05	1.65	2.48	13.4	3.43	22.4	<0.05	1179	2.68	2.98	1.24
10	0.1	0.05	1.85	2.78	14.7	3.55	25.7	<0.05	1221	2.81	3.28	1.40
13	0.1	0.05	1.67	2.62	15.9	3.62	22.9	<0.05	1238	3.21	3.12	1.49
15	0.1	0.05	1.86	2.90	14.6	3.58	26.6	<0.05	1244	2.22	3.50	1.48
20	0.1	0.05	2.24	3.30	16.7	3.75	29.8	<0.05	1344	3.72	3.89	1.72
30	0.1	0.05	1.90	2.95	14.9	3.90	26.7	<0.05	1189	3.29	3.48	1.75
45	0.1	0.05	2.32	3.59	16.7	4.32	33.8	<0.05	1425	2.36	4.27	1.86
60	0.1	0.05	2.34	3.58	16.6	4.52	33.8	<0.05	1403	2.67	4.25	1.88
60-rep	0.1	0.05	2.10	3.17	14.5	3.81	29.4	<0.05	1251	2.81	3.98	1.68
90	0.1	0.05	2.10	3.08	14.9	3.88	29.3	<0.05	1288	3.15	3.94	1.63
120	0.1	0.05	2.29	3.33	15.4	3.84	31.0	<0.05	1268	4.04	4.15	1.78
240	0.1	0.05	2.15	3.32	15.1	3.64	31.0	<0.05	1218	2.96	4.08	1.79
240-rep	0.1	0.05	2.16	3.31	14.5	3.35	30.7	<0.05	1209	2.83	4.07	1.78
360	0.1	0.05	2.14	3.44	15.6	3.38	32.1	<0.05	1229	2.36	4.16	1.84
720	0.1	0.1	1.10	1.79	8.34	1.81	17.1	<0.05	638	1.43	2.17	0.96
1440	0.1	0.05	2.32	3.90	16.2	3.52	37.8	0.33	1359	3.44	4.86	2.19
Isotherm – Sorbent after desorption												
100	0.1	0.05	0.73	0.62	0.45	0.19	0.44	0.03	359	0.19	0.25	0.56
200	0.1	0.05	1.14	1.13	1.05	0.40	1.63	0.07	717	0.44	0.61	0.69
400	0.1	0.05	1.17	1.51	1.53	0.66	2.96	0.11	1162	0.59	0.73	0.61
600	0.1	0.05	0.84	1.41	1.65	0.71	3.32	0.12	1175	0.58	0.81	0.44
800	0.1	0.05	0.75	1.22	1.49	0.58	3.82	0.12	1166	0.71	0.59	0.32
1000	0.1	0.05	0.55	1.30	1.64	0.79	5.12	0.12	1200	0.71	0.77	0.27
1500	0.1	0.05	0.37	1.12	1.54	0.62	6.11	0.12	1168	0.65	0.63	0.16
2000	0.1	0.05	0.33	1.23	1.77	0.92	4.98	0.12	1242	0.67	0.88	0.14
3000	0.1	0.05	0.24	1.14	1.72	0.92	4.66	0.13	1246	0.74	0.79	0.09
4000	0.1	0.05	0.18	1.03	1.56	0.85	4.41	0.12	1161	0.76	0.67	0.06
8000	0.1	0.05	0.11	1.03	1.70	0.98	2.69	0.14	1232	1.04	0.65	0.03

Table AA 3 continued: Chemical analysis of acid digested sorbents after sorption and desorption step of brine isotherm and kinetic experiment. m.u.% = measurement uncertainty in %

Sample	mass	volume	Aqueous concentration [mg/L]									
	g	L	As	Ba	Ca	K	Li	Mg	Mn	Na	Sr	Zn
Kinetic – Sorbent after desorption												
1	0.1	0.05	1.36	1.49	1.63	0.72	3.29	0.11	1188	0.76	0.72	0.56
2	0.1	0.05	1.26	1.47	1.64	0.75	2.39	0.10	1167	0.77	0.73	0.56
5	0.1	0.05	1.57	1.50	1.48	0.58	3.78	0.10	1154	0.62	0.63	0.72
5-rep	0.1	0.05	1.69	1.63	1.73	0.70	3.61	0.11	1246	0.69	0.72	0.82
8	0.1	0.05	1.44	1.39	1.47	0.65	3.65	0.10	1180	0.70	0.58	0.68
10	0.1	0.05	1.63	1.47	1.52	0.64	3.21	0.11	1165	0.76	0.64	0.76
13	0.1	0.05	1.77	1.64	1.65	0.72	3.95	0.12	1314	0.82	0.71	0.87
15	0.1	0.05	1.81	1.63	1.63	0.68	3.41	0.11	1253	0.76	0.75	0.86
20	0.1	0.05	1.68	1.55	1.50	0.60	2.76	0.11	1205	0.83	0.64	0.85
30	0.1	0.05	1.71	1.55	1.52	0.60	2.56	0.11	1157	0.79	0.66	0.88
45	0.1	0.05	1.75	1.52	1.46	0.55	2.87	0.11	1191	0.63	0.62	0.89
60	0.1	0.05	1.85	1.67	1.55	0.66	2.38	0.12	1216	0.71	0.72	0.97
60-rep	0.1	0.05	1.79	1.53	1.40	0.56	2.21	0.11	1132	0.80	0.64	0.92
90	0.1	0.05	1.76	1.67	1.70	0.67	2.83	0.14	1289	0.89	0.74	0.96
120	0.1	0.05	1.70	1.56	1.44	0.57	1.97	0.12	1147	0.93	0.62	0.95
240	0.1	0.05	1.73	1.60	1.58	0.58	1.55	0.14	1192	0.99	0.64	1.01
240-rep	0.1	0.05	1.72	1.50	1.44	0.52	1.53	0.13	1069	0.80	0.61	0.95
360	0.1	0.05	1.89	1.55	1.59	0.53	1.85	0.13	1146	0.82	0.65	0.97
720	0.1	0.05	1.95	1.61	1.51	0.52	1.24	0.14	1178	0.77	0.63	0.99
1440	0.1	0.05	1.78	1.63	1.57	0.52	1.08	0.15	1149	0.90	0.66	1.00

6. Selectivity stability during cyclic extraction

6.1. Introduction

Lithium sorption studies over many consecutive extraction cycles (>10) are valuable from scientific and industrial standpoints. In comparison to single cycle experiments, they provide an extended and improved database of the development of Li sorption capacity, sorption of competing elements, Mn dissolution and sorbent stability. This enables more detailed and precise investigation of sorption and selectivity processes, sorbent performance and lifetime. Furthermore, long-term experiments are needed as “proof-of-concept” studies to demonstrate the sorbent ability for DLE for a given brine. However, long-term studies are scarce in the scientific literature, due to the intensive requirements of time, personnel, consumables and analyses. Xiao et al. (2015) observe a slightly decreasing Li sorption capacity over 30 extraction cycles in a flow column with a spinel LMO granulated with polyacrylamide. Chitrakar et al. (2012) conducted experiments with the sorbents $H_{1.33}Mn_{1.67}O_4$ and $H_{1.6}Mn_{1.6}O_4$ for ten consecutive cycles with Bolivian brine and show relatively constant Li sorption capacity. Li et al. (2023) show a decreasing Li sorption capacity over seven cycles, and Herrmann et al. (2022) observed a reduction of the Li capacity over eight consecutive extraction cycles with $Li_{1.6}Mn_{1.6}O_4$ and brine from the geothermal powerplant Bruchsal, Germany. With the same brine and sorbent, Herrmann et al. (2025) show constant Li capacity over five cycles. Several studies show that the spinel structure of the sorbent is preserved over all cycles (Chitrakar et al., 2012; Herrmann et al., 2022; 2025). Based on the literature, the long-term stability of Li sorption is unclear. Regarding the sorption of competing elements, no studies showing the long-term development have been found.

In order to investigate the long-term selectivity stability of $Li_{1.6}Mn_{1.6}O_4$, an automated test bench was developed to conduct batch extraction experiments. The experiments were conducted with geothermal brine from the geothermal power plant Bruchsal, Germany.

6.2. Methodology

Extraction test bench

For the long-term extraction experiments, an automated, cycle-based batch test bench was developed, constructed and programmed. The test bench consisted of a reactor optimised for minimal inside surface area to minimise brine-surface interaction. The inflow of brine, ultrapure water for washing steps and diluted HCl for the desorption step was realised through three peristaltic pumps (Figure 6.1a). Fluids in the reaction chamber were discharged through a peristaltic pump at the outflow and either sampled with an autosampler or discarded (Figure 6.1b). All relevant process and component parameters (e.g. volumes, durations) were programmed

and controlled by a PC and an Arduino Mega 2560 microcontroller (Arduino, Figure 6.1c). To ensure efficient mixing of fluid and sorbent, a stirrer coupled to an electric motor was placed into the PVC-C extraction chamber. To prevent sorbent discharge, a polyester sieve with 1 µm pore size covered the outlet.

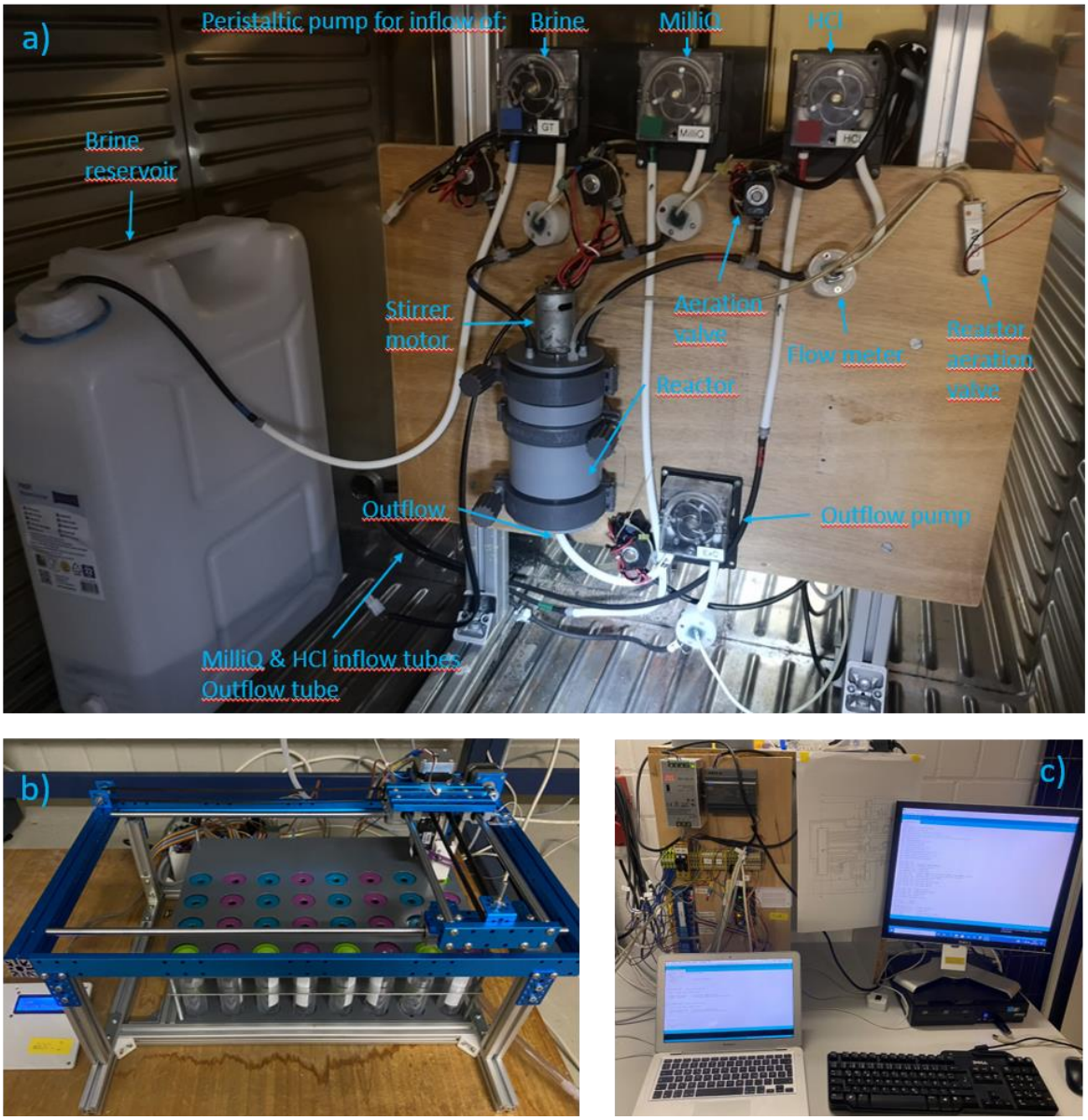

Figure 6.1: a) Test bench inside a laboratory oven at 60°C. Storage containers for ultrapure water, desorption solution and waste are placed outside the oven. b) Autosampler with a capacity of 32 standard 50 mL centrifuge tubes outside the oven. c) Switchboard and computer (black) for test bench programming and control.

As feed solution, the geothermal brine of the geothermal powerplant of Bruchsal was used. Precipitates formed during storage due to cooling, pressure loss, degassing of dissolved CO2 and oxidation (Nitschke et al., 2014; Boch et al., 2017) were removed through filtration prior to the experiments. Each extraction cycle consisted of (I) the sorption, (II) the sorption wash, (III) the desorption, and (IV) the desorption wash step. The brine was buffered to pH = 5 with a

0.2M Na acetate buffer solution (pro analysis, Supelco). For desorption, a 0.5M HCl solution (pro analysis, Supelco) and for the intermediate washing steps, ultrapure water were used.
As sorbent, $Li_{1.6}Mn_{1.6}O_4$ of the batch synthesised in Slunitschek et al. (2025) was used, but sieved to a particle size of 10–40 µm to remove finer particles and prevent sorbent loss and filter clogging. For each step, the fluid was pumped automatically into the sorbent-containing reactor and was stirred for a designated time before an aliquot was discharged into the autosampler (sample volume 0.04–0.05 L) or waste reservoir. The first millilitres of each sample were discarded into the waste reservoir, as they potentially mixed with residues in the tubes from the previous step. To prevent filter clogging, a small aliquot of the fluid (< 0.005 L) was filled into the reactor, sucked through the outlet filter with the discharge pump and used to backwash the outlet filter, at the beginning of each step. Prior to the experiment, four consecutive blank cycles without sorbent were conducted with the same setup and sampling as cycles one, two and four. Thereafter, the inlet tubes were disconnected, the sorbent filled in, and the tubes reconnected (Figure 6.1a).
The experiment was conducted at 60°C, similar to the brine discharge temperature of the Bruchsal geothermal power plant (Fechner et al., 2022), with the test bench and brine container being placed in an oven (Figure 6.1). The 0.5M HCl and ultrapure water were stored at room temperature, as they would not necessarily be heated to brine temperature in an industrial setting. Sorption and desorption were conducted for 15 min each, and a fluid volume of 0.2 L and 0.08 L was used, respectively. Both wash steps were conducted with a stirring time of 1 min and 0.2 L. A total amount of 0.8 g of the sieved sorbent was used for the experiment.

The experiment was conducted for 80 cycles, and for cycles 1–15 each cycle was sampled and then every fifth cycle. At sampling, filtrate from all four steps was collected. Samples containing sorbent were filtered with a 0.45 µm cellulose acetate filter, dried at 60°C overnight, and weighed for sorbent mass determination. Element concentration in all fluids was determined through ICP-OES (iCap 7000, radial mode, Thermo Fisher Scientific), and measurement uncertainty was calculated according to Slunitschek et al. (2025). Measurement uncertainty is depicted in the following graphs as error bars.
Continuous sorbent loss at nearly every cycle and process step occurred throughout the experiment. The total sorbent loss per sample was approximated by scaling the ratio of the amount of sorbent in the sample and sample volume to the total volume of the corresponding step (Table A6.2). Since cycles 16–19 were not sampled, no approximation could be carried out, and the approximated total sorbent loss reflects the minimum loss.
In order to assess the stability of the sorption process, sorption capacities were calculated after Slunitschek et al. (2025). Thereby, loss-corrected sorbent masses were utilised for each cycle (Table A6.2). Since the sorbent loss is unknown for the cycles 16–19, sorption capacities were

only calculated for the first 15 cycles.

For the evaluation of element extraction from brine, the total amount of extracted element was calculated based on the sorption and desorption data. For the sorption step, the total amount of element extracted m_s [mg] (total sorption) was determined through the concentration difference of pristine brine (c_0) and brine eluate (c_e) after passing through the reactor (Eq. 6.1). In case the eluate concentration was below the detection limit, said value was used. For the desorption step, the total extraction m_d [mg] (total desorption) was based on the concentration in the enriched desorption solution (c_d, Eq. 6.2).

$$m_s=(c_0-c_e)*V_s \qquad \text{Eq. 6.1}$$

$$m_d=(c_d)*V_d \qquad \text{Eq. 6.2}$$

V_s/V_d: sorption/desorption volume

Due to the uncertainty of the sorbent mass approximation, evaluation of selectivity was based on the total extraction. For this, distribution and separation coefficients were calculated using molar concentrations. Based on the sorption data, a distribution coefficient PK_d [L] similar to the distribution coefficient K_d [mL/g] (Slunitschek et al., 2025) was calculated for each element in each cycle (Eq. 6.3). The separation coefficient α [-] for Li over other elements E (Slunitschek et al., 2025) was calculated despite the missing K_d values, as it is independent of the sorbent mass m, as deduced in Eq. 6.4.

$$PK_d= \frac{m_s}{c_{e,s}} \qquad \text{Eq. 6.3}$$

$$\alpha(Li/E)= \frac{K_d(Li)}{K_d(E)} = \frac{Q_{Li}}{c_{e,Li}} * \left(\frac{Q_E}{c_{e,E}}\right)^{-1} = \frac{(c_{0,Li}-c_{e,Li})*V_s}{m*c_{e,Li}} * \left(\frac{(c_{0,E}-c_{e,E})*V_s}{m*c_{e,E}}\right)^{-1}$$

$$= \frac{(c_{0,Li}-c_{e,Li})}{c_{e,Li}} * \frac{c_{e,E}}{(c_{0,E}-c_{e,E})} \qquad \text{Eq. 6.4}$$

Q: sorption capacity [mmol/g]

XPS analysis

To determine the composition of the sorbent and the oxidation state of the present elements, X-ray photoelectron spectroscopy was conducted at the sorbent prior to the experiment and after the desorption and wash desorption steps of cycle 20. The XPS evaluation refers to the sorbent after the desorption step, unless otherwise stated. The XPS measurements were performed using a K-Alpha+ XPS spectrometer (ThermoFisher Scientific, Brno). The Thermo Avantage software was used for data acquisition and processing. All samples were analysed using a micro-focused, monochromated Al Kα X-ray source (400 µm spot size). The K-Alpha+

charge compensation system was employed during analysis, using electrons of 8 eV energy and low-energy argon ions to prevent any localised charge build-up. The spectra were fitted with one or more Voigt profiles (BE uncertainty: ± 0.2 eV) and Scofield sensitivity factors were applied for quantification (Scofield, 1976). All spectra were referenced to the C 1s peak (C-C, C-H) at 285.0 eV binding energy controlled by means of the well-known photoelectron peaks of metallic Cu, Ag, and Au, respectively.

6.3. Results & interpretation

Bruchsal geothermal brine

As feed solution, the geothermal brine of the geothermal powerplant of Bruchsal was used. Selected elements are listed in Table 6.1, and the complete analysis is given in Table A6.1 or in e.g. Sanjuan et al. (2016). The fluid chemistry is dominated by Na with 40.59 g/L and Ca with 7.39 g/L, respectively (Table 6.1, A6.1). Lithium is present at 163 mg/L, and Pb, As, Ba and Zn with 0.71 mg/L, 3.7 mg/L, 7.1 mg/L and 9.8 mg/L, respectively.

Table 6.1: Composition of the Bruchsal geothermal brine.

Li	Na	Mg	S	K	Ca	Mn	Fe	Zn	As	Sr	Ba	Pb
						mg/L						
163	40591	342	153	3199	7393	23.3	<0.001	9.8	3.7	378	7.1	0.71

Sorbent mass development

Continuous sorbent loss in nearly every cycle and step occurred throughout the experiment (Figure 6.2, Table A6.2). Within the first 15 cycles, sorbent loss occurred relatively linearly, with a strong increase in cycle 20 (last 4 points in Figure 6.2). This results probably from leakage in the filter, resulting in the discharge of bigger particles. After 10 additional cycles, hardly any sorbent was left in the reactor, resulting in the abortion of the experiment. The total sorbent loss over the 20 cycles is approximated at 0.4 g or 48% of the initial mass. The cycles 20–30 are not evaluated due to the undeterminable sorbent loss.

The continuous sorbent loss indicates physical degradation of the sorbent, resulting in particle sizes below the outflow sieve pore size of 1µm. The physical degradation most likely stems from collisions of the particles with each other, the stirrer and the reactor wall. Scanning electron microscopy images by e.g. Xiao et al. (2013) and Herrmann et al. (2025) show that the sorbent particles are agglomerates of particles or crystallites <<500 nm. The mechanical forces probably result in the disintegration of the agglomerates or the breakage of small particles. These particles are then discharged through the outflow sieve. The degradation can probably be reduced by a lower stirring speed, but the suspension of the sorbent has to be assured to

achieve maximum sorption. Furthermore, settling, agglomeration and filter clogging have to be prevented.

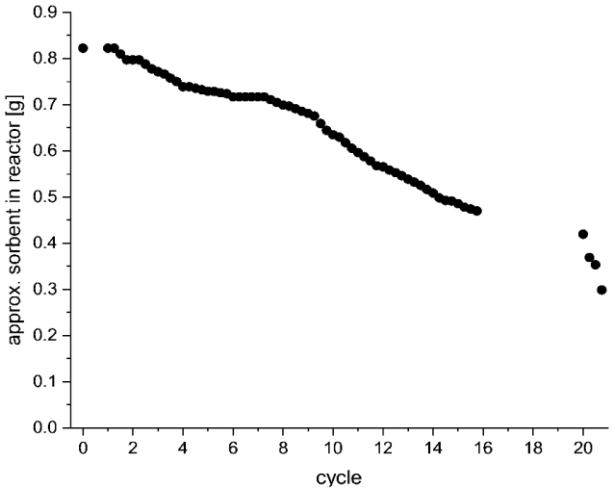

Figure 6.2: Approximated development of sorbent mass in reactor.

Lithium extraction

The total Li sorption is relatively stable in the first six cycles, but decreases in the following cycles (Figure 6.3a). For cycles 2–6, constant desorption occurs as well, followed by a steep decrease in cycles 8–12. Over the cycles 14–20, the decreasing trend continues for sorption and desorption (Figure 6.3a). The outlier in cycle 7 results from an error at the microcontroller in the desorption step of cycle 6, at which brine was pumped into the desorption solution in the reactor. Due to this, the extraction cycle was stopped, the contained solutions pumped out, and the reactor cleaned with ultrapure water. Since the sorbent wasn't properly desorbed, it was still loaded with Li, resulting in lower Li sorption and increased desorption (Figure 6.3a). The cause of the outlier observed in cycle 13 is unknown, as no abnormalities were identified in the log files. Possible explanations include incorrect volumes of the brine or desorption solution or cross-contamination of the desorption solution sample with the wash desorption sample. However, the available data does not allow a definitive attribution of the cause.
In general, Li desorption shows a similar development as Li sorption, but with constantly lower extracted amounts. This difference partially results from Li sorption on the surface of the reactor and other components, as shown in the blank cycles (Table A6.3), resulting in an overestimate of the total sorption. Furthermore, Li weakly bound to the sorbent is removed in the sorption wash step, increasing the difference between total sorption and desorption. Except for the outliers, the decrease in Li sorption and desorption is relatively linear and of similar extent and can be attributed to the sorbent loss (Figure 6.2).

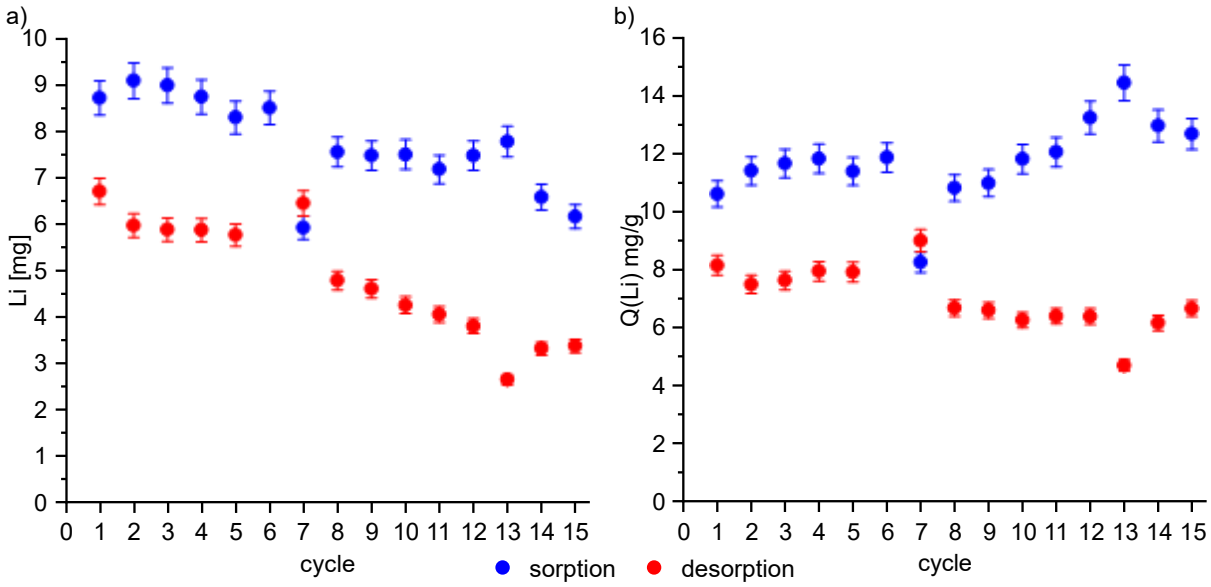

Figure 6.3: Total extraction (a) and sorption capacity (b) of Li

Based on the first cycle, a Li capacity of 10.6 mg/g based on the sorption and 8.17 mg/g based on the desorption is achieved (Table A6.1). This results in a fractional occupancy of 15.8% and 12.2% of the maximum Li capacity of the precursor of 67.0 mg/g (Slunitschek et al., 2025), respectively. From the dissolved Li, 26.7% was extracted based on the sorption and 20.6% on the desorption data. The difference between the values for sorption and desorption results from physisorption to the sorbent and reactor walls, washed away during the washing step and from measurement uncertainty.

Based on the sorption data, Li sorption capacity ranges from 8.27–14.4 mg/g with a mean of 11.7 mg/g. The capacity is relatively constant within the first 9 cycles and increases afterwards until cycle 13, followed by a subsequent decrease to cycle 15 (Figure 6.3b). A reason for the increase cannot be clearly attributed. Based on the desorption data, the mean Li sorption capacity is 7.32 mg/g, ranging from 5.07–9.08 mg/g (Figure 6.3b). Within cycles 1–5 and 8–15, the Li sorption capacities are relatively constant, with slightly lower values for the second group. Excluding the outliers in cycle 7 and 13, the Li sorption capacity ranges from 6.77–8.29 mg/g, with a mean of 7.36 mg/g Li (Figure 6.3b). This shows a relatively constant sorption capacity, indicating a stable Li sorption process.

Extraction of competing elements

Total sorption and desorption of Na, Mg, S, K, Ca and Sr show similar behaviour over all cycles (Figure 6.5). Sorption and desorption are especially high in the first cycle, with 3.9–5.0 times the average value of the cycles 2–20 for sorption and 1.3–3.6 times for desorption (Figure 6.5). For all six elements, total sorption is considerably higher than total desorption, with average sorption of 1.45–339 mg and 0.04–3.59 mg for desorption, excluding the first cycle. Total sorption and desorption fluctuate in a similar pattern, but while total sorption is relatively stable,

total desorption shows a declining trend (Figure 6.5). The similar fluctuations in the sorption and desorption of Na, Mg, S, K, Ca and Sr (Figure 6.5) indicate variations in the experimental setup, e.g. inhomogeneous sorbent distribution in the reactor or sorbent agglomeration, resulting in changes of sorbent-solution interaction. The declining desorption follows the declining amount of sorbent Figure 6.2).

For Na, Mg, S, K, Ca and Sr, the sorption-based sorption capacities show the same curve progression as the total sorption, as shown exemplary for Ca in Figure 6.4. For the desorption-based sorption capacities, the same curve progression is shown as for total desorption (Figure 6.5), but without the decreasing trend and with relatively constant capacities. The constant capacities show that the decreasing total desorption results from the sorbent loss. The sorption-based sorption capacities are significantly higher than desorption-based values (Figure 6.4, A6.1). Furthermore, the relatively constant sorption capacities despite sorbent loss indicate physisorption, as discussed in Slunitschek et al. (2025). The relatively constant sorption capacities over 15 cycles show the stable sorption process and selectivity of the sorbent for these elements.

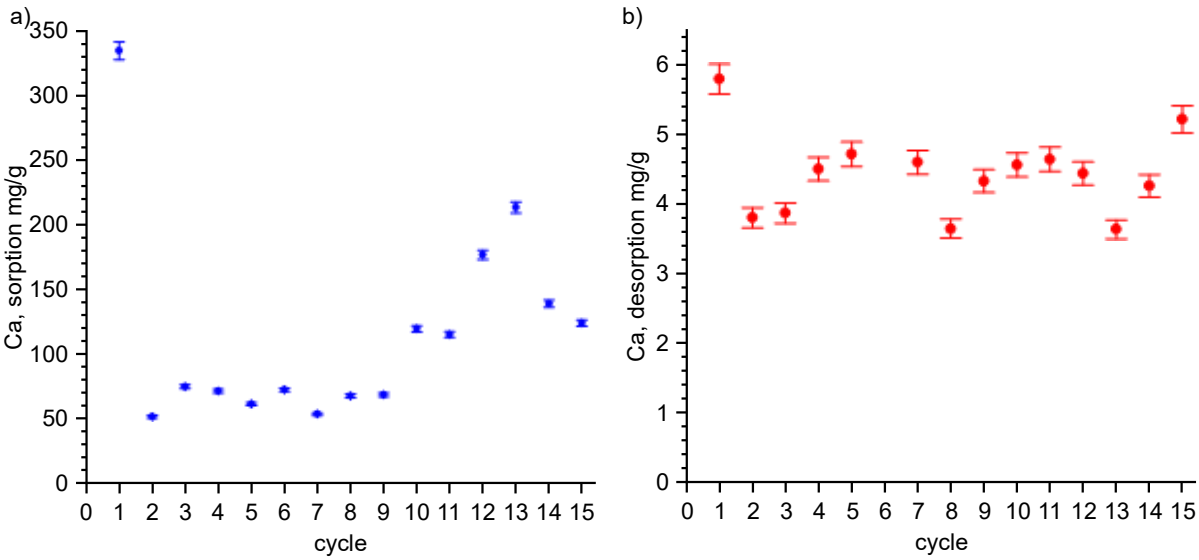

Figure 6.4: Sorption capacity of Ca based on sorption (a) and desorption (b) data. Exemplary for the curve progression of Na, Mg, S, K, Ca, Sr.

The total sorption values of Na, Mg, S, K, Ca and Sr are strongly influenced by interaction of the brine with the reactor walls and other components. This is shown through values being in a similar range as the average values of the blank cycles (horizontal lines in Figure 6.5, Table A6.4). This results in an overestimation of the sorption at the sorbent. Thus, desorption data of Na, Mg, S, K, Ca and Sr are more instructive than sorption data. However, sorbent-based sorption of these elements is distinctively shown in total desorption, with values higher than the average blank. The blank desorption eluate contains increased concentrations of Na, Ca

and K with 14.9 mg/L, 3.54 mg/L and 1.48 mg/L, respectively (Table A6.3, A6.4). Thus, despite the sorption wash step, contaminants are carried over into the desorption solution, e.g. through entrainment of enriched washing solution at particles, reactor and tube surfaces.

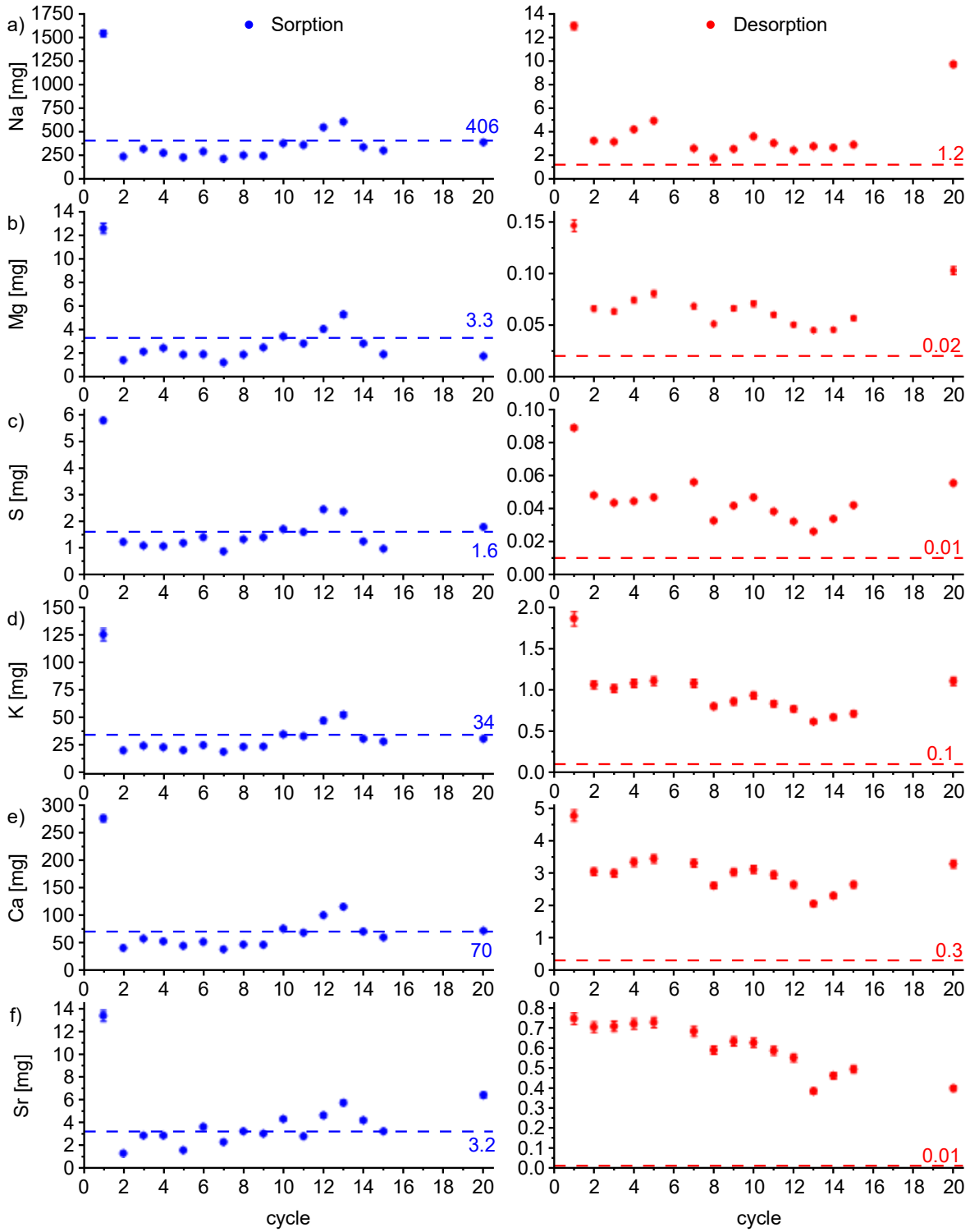

Figure 6.5: Total sorbed and desorbed amount of Na, Mg, S, K, Ca and Sr (a-f). Horizontal line and number give the average blank value.

Zinc, As, Ba and Pb show similarities in the total desorption progression from cycle seven onwards (Figure 6.6). Desorption is strongly increased in cycle seven compared to all other cycles, followed by constant or slightly decreasing total amount until a strong decrease in cycle 13 and increasing values in cycles 14–15 (Figure 6.6). The explanation for the outliers in cycle 7 and 13 is the same as for Li. The total sorption and desorption of Zn, As and Ba and total Pb desorption are significantly higher than the corresponding average blank values (Figure 6.6b–e). This shows distinct sorption by the sorbent.

The total Mn sorption shows a small increase from cycle one to cycle two, from 4.07 to 4.66 mg, followed by constant values of 4.7 mg (Figure 6.6a). This increase could result from incomplete homogeneous distribution of the sorbent inside the reactor. The constant values reflect complete sorption of the dissolved Mn, resulting in concentrations below the detection limit of 0.001 mg/L (Table A6.1). Due to the complete sorption, the sorption capacity increases continuously, reflecting the sorbent loss (Figure A6.2a). The release of Mn during desorption shows a strong initial decrease from 8.33 mg to 5.07 mg over the first three cycles, before slowly decreasing to 4.34 in cycle 20 (Figure 6.6a). The initially higher Mn release probably stems from the dissolution of intermediate synthesis products containing Mn^{3+}, e.g. $LiMnO_2$ or Mn_2O_3, through disproportionation of Mn^{3+} (Gao et al., 2018). The observation of initially decreasing Mn dissolution has been observed in various own experiments (not shown here) and by e.g. Chitrakar et al. (2012), Herrmann et al. (2022), Herrmann et al. (2025). While the amount of sorbent decreases by at minimum 48% and Li desorption by 65% over the 20 cycles, the total Mn dissolution decreases only by 13.7%, from 4.97 mg in cycle four to 4.34 mg in cycle 20 (Figure 6.6a). This indicates acid-induced Mn dissolution in addition to Mn^{3+} disproportionation (Gao et al., 2018; Li et al., 2023), probably due to an increase of the acid-sorbent ratio with increasing cycles. The desorption-based sorption capacity shows a similar curve progression to total desorption, but with a linear increase from cycle 9 onwards (Figure A6.2a). This increase potentially results from the acid-induced desorption.

As shown in Figure 6.6a, Zn sorption and desorption are relatively constant over all 20 cycles, with some minor fluctuations. Total sorption and desorption are in a similar range of 0.90 ± 0.10 mg and 0.72 ± 0.09 mg, respectively. The sorption capacity for both sorption and desorption data show a parallel curve progression (Figure 6.7a, 6.6a). The curves progress in a similar way to the total extraction, but with a continuous increase. This indicates a high selectivity of the sorbent for Zn, as total sorption remains constant while the sorbent mass decreases.

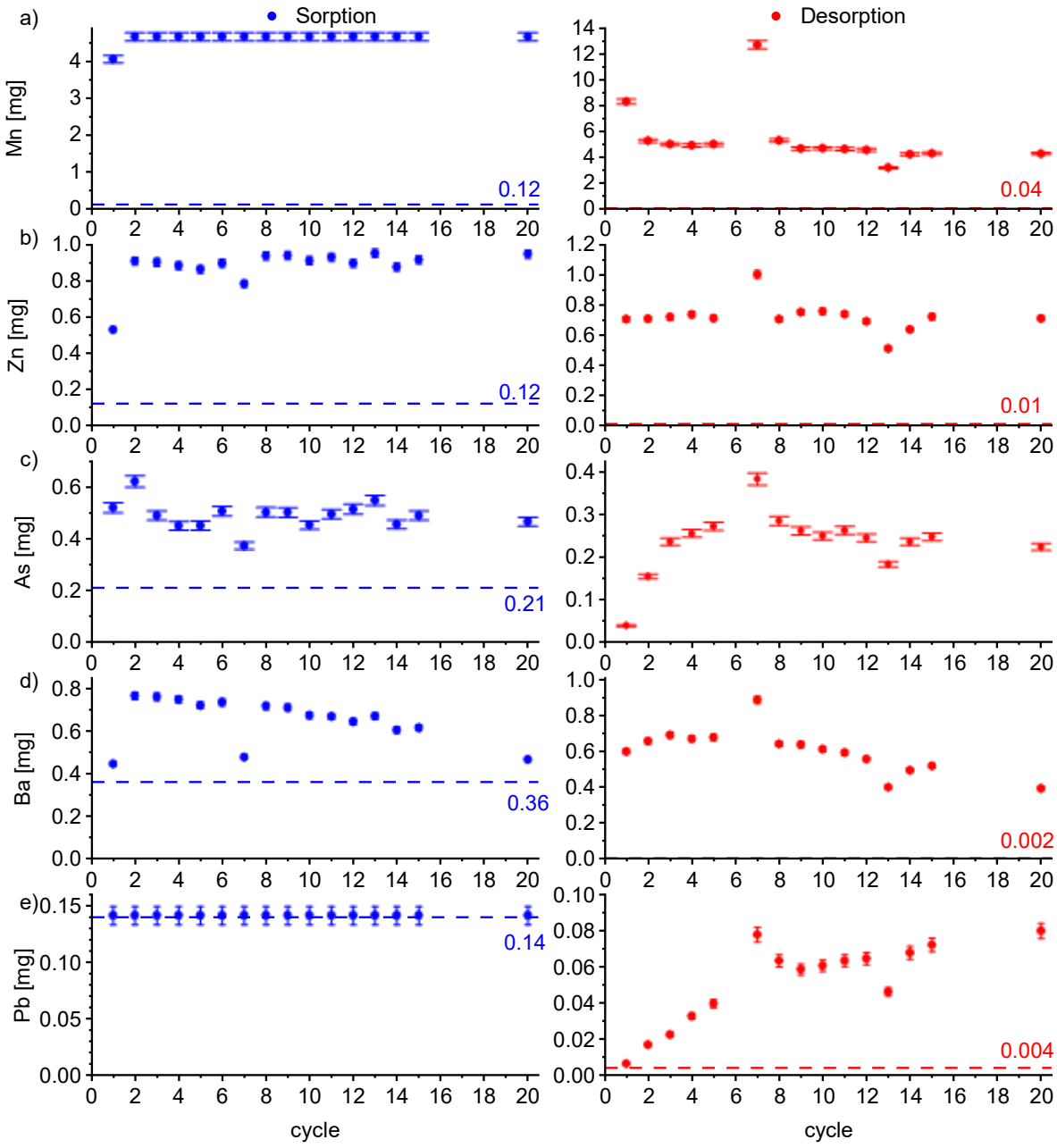

Figure 6.6: Total sorbed and desorbed amount of Mn, Zn, As, Ba and Pb (a-e). Horizontal lines and numbers give the average blank value. No line is given for As because all blank concentrations are below the detection limit of 0.005 mg/L.

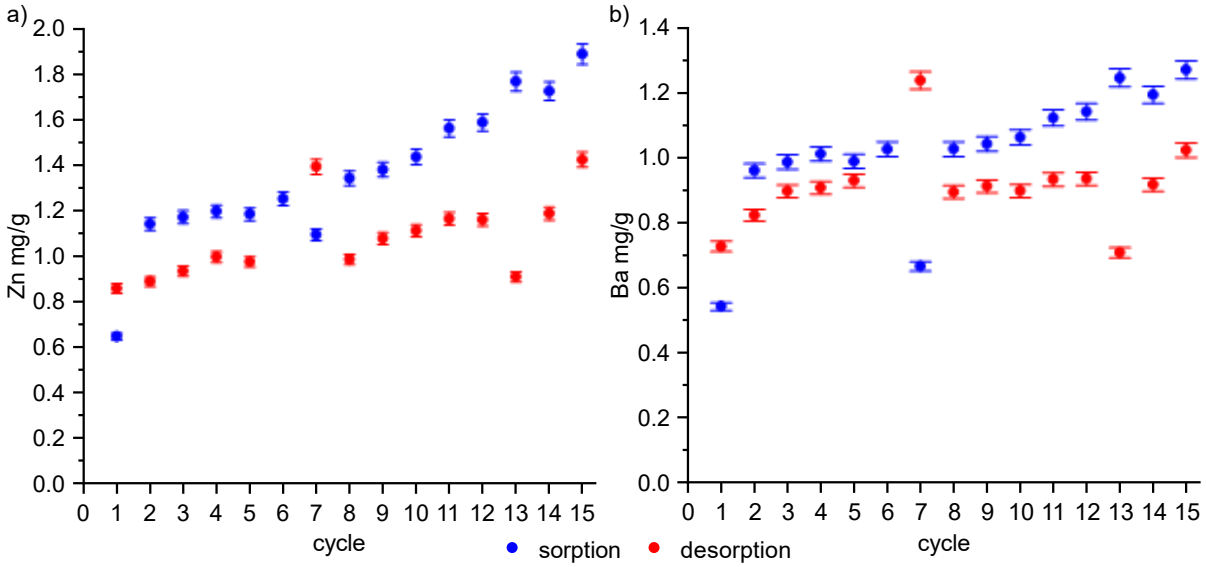

Figure 6.7: Sorption capacity of Zn (a) and Ba (b), based on sorption and desorption data.

While total As sorption is relatively constant, the amount of As released during desorption increases asymptotically until around cycle five, before reaching equilibrium (Figure 6.6c). The As desorption equilibrium at cycles 8–20 is lower than the average As sorption, with 0.24 ± 0.03 mg to 0.49 ± 0.05 mg, respectively. The development of total extraction is shown in the sorption capacity development as well (Figure A6.2b). The asymptotic increase of total desorption followed by constant values at simultaneously higher total sorption indicates accumulation at the sorbent (Figure 6.6c). Thereby, As has to accumulate at the surface, since it cannot enter the tunnels of the sorbent crystal structure (Shen and Clearfield, 1986; Saenko et al., 2007; Slunitschek et al., 2025). In the first five cycles, accumulation of As at the sorbent surface occurs, resulting in the difference between total sorption and desorption. Since the total sorption is relatively constant and the amount of desorbed As increases, the amount of As accumulated per cycle decreases with every cycle (Figure 6.6c). From cycle six onwards, equilibrium is reached, indicating that all binding sites are occupied. In these cycles, As is partially released during desorption, with re-occupation of vacant binding sites during the sorption step. This indicates a finite number of binding sites on the surface of the sorbent.

For Ba, total sorption and desorption show a similar, decreasing trend over all extraction cycles, with similar ranges of 0.45–0.77 mg and 0.39–0.89 mg, respectively (Figure 6.6d). In the first six cycles, total Ba desorption shows an asymptotic increase until equilibrium. The sorption-and desorption-based sorption capacity show a relatively similar curve progressing from cycle 4 onwards (Figure 6.7b, 6.6d). Within the first 5 cycles, accumulation is indicated, as explained for As, followed by a relatively continuous increase from cycle 8 on.

For Pb, constant total sorption is achieved over all cycles (Figure 6.6e), resulting from brine eluate concentrations below the detection limit (0.005 mg/L, Table A6.1). As shown in Figure 6.6e, the average total Pb sorption of the blank cycles equals the total sorption during the

cycles with sorbent. While this shows that Pb can sorb on the surfaces of the test bench, the Pb contained in the desorption solution shows sorbent-based extraction (Figure 6.6e). Total Pb desorption increases asymptotically over all cycles, reaching a final value of 0.08 mg (Figure 6.6e). Whether total Pb desorption has reached equilibrium is unclear, due to the lower sampling resolution after cycle 15. Sorption capacity of the sorption and desorption step show a relatively parallel development, with an asymptotic increase until around cycle 6 (Figure 6.8). This is followed by constant values until cycle 9 and linearly increasing values afterwards. Similarly to Zn, the curve progressions of sorption capacity and total extraction indicate a high affinity of the sorbent for Pb.

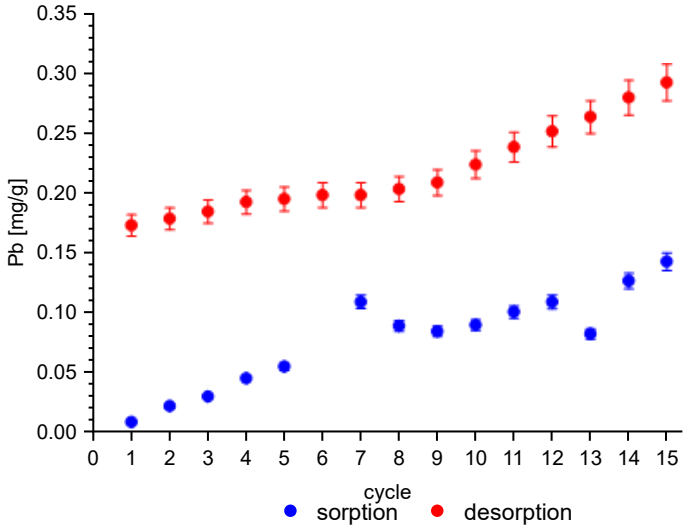

Figure 6.8: Sorption capacity of Pb, based on sorption and desorption data.

Selectivity

Based on the distribution coefficient PK_d, the sorbent shows the highest affinity for Mn with PK_d of 4665 L and for Pb with PK_d of 28 L, assuming complete Pb sorption by the sorbent (Table A6.5). Except for Mn in the first cycle, both elements show constant values over all cycles (Table A6.5), deriving from the eluate concentrations below the detection limit. The PK_d values of Li, Zn and Ba show relatively little spread and are relatively close, with median values of 0.06, 0.17 and 0.18 L, respectively (Figure 6.9, Table A6.5). In comparison, As shows a wider distribution with values ranging from 0.21–1.12 L and a median PK_d of 0.42 L (Figure 6.9). This spread probably results from the low eluate concentrations close to the detection limit (Table A6.1), making it more susceptible to fluctuations. Sodium, Mg, S, K, Ca and Sr all show a similar PK_d distribution and similar median values of 0.007–0.009 L (Figure 6.10, Table A6.5), and thus significantly lower values than Li, Mn, Zn, As, Ba and Pb (Table A6.5, Figure 6.9). Due to the similar PK_d distribution and median values, a distinct order of selectivity of Na, Mg, S, K, Ca and Sr is not determinable.

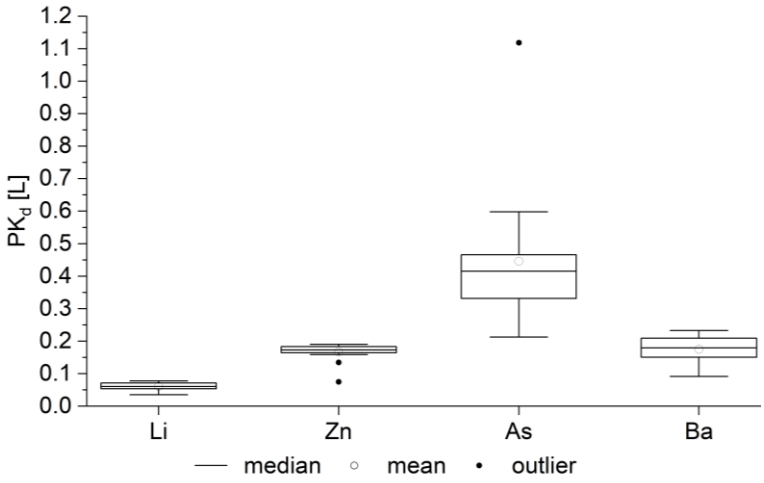

Figure 6.9: Distribution coefficient PK_d of Li, Zn, As and Ba over 20 cycles.

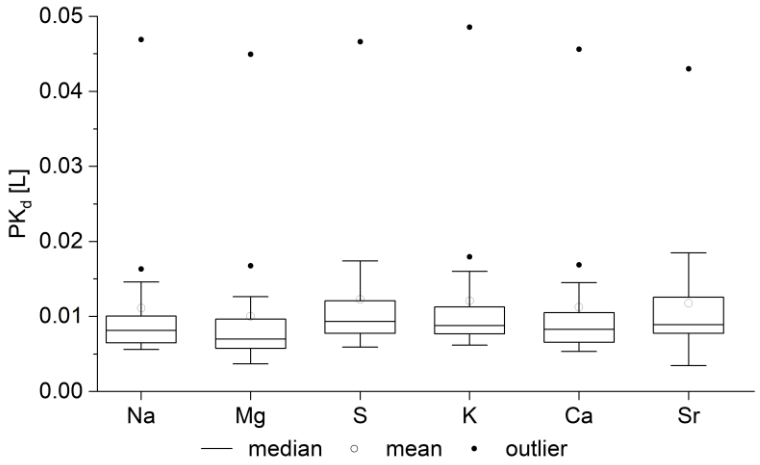

Figure 6.10: Distribution coefficients PK_d of Na, Mg, S, K, Ca and Sr over 20 cycles.

Although the sorbent has a high selectivity for Li (e.g. Reich et al., 2022; Slunitschek et al., 2025), the selectivity for Mn, Pb and As are significantly higher, with average α coefficients of 0.003, 0.002 and 0.15, respectively (Table 6.2). The selectivity of Zn and Ba is similar and preferred over Li, with 0.39 and 0.37, respectively. For Na, K, Ca, Sr and S, the sorbent has lower α coefficients than for Li, with average values of 6.25–8.52 (Table 6.2). For Na, Mg, S, K, Ca and Sr, the similar PK_d distribution and median values (Figure 6.10) support the indication of similar extraction processes, derived from the similar sorption and desorption patterns of these elements (Figure 6.5, A6.1). Based on PK_d and α, the sorbent shows the following order of selectivity: Mn > Pb > As > Zn, Ba > Li > Na, Mg, S, K, Ca, Sr

While the continuous sorbent loss results in a continuous decrease of total Li extraction (Figure 6.3), extraction of Mn, Zn, As and Pb does not decrease (Figure 6.6). Due to the high selectivity of the sorbent for these elements and the relatively low concentration in brine (Table A6.1), even the decreasing amount of sorbent is sufficient for relatively constant extraction. This even

results in increasing sorption capacities for Mn, Zn, Ba, Pb and potentially As (Figure 6.7, 6.8, A6.2).

Table 6.2: Average separation coefficient α of Li over competing elements

Li/Na	Li/Mg	Li/S	Li/K	Li/Ca	Li/Mn	Li/Zn	Li/As	Li/Sr	Li/Ba	Li/Pb
7.20	8.52	6.28	6.55	7.18	0.003	0.39	0.15	7.46	0.37	0.002

XPS-Results

The XPS analysis of the initial sorbent prior to the long-term experiments shows that the material contains Li, Mn, O and C (Figure 6.11, Table A6.6). After 20 extraction cycles, the final sorbent contains Pb, As and S in addition (Figure 6.11c-d; Table A6.6). The detected C are attributed to atmospheric depositions (Chen et al., 2020).

The peak difference of 4.4 eV of Mn 3s is split into two peaks, one at 85.0 eV and the other at 89.4 eV, of the initial sorbent indicates the predominance of Mn^{4+} (Figure 6.11, Junta and Hochella, 1994), which corresponds to the theoretical value of 4+ for Mn in $H_{1.6}Mn_{1.6}O_4$. For the final sorbent, the Mn 3s splitting increases to a higher value, of 4.9 eV (Figure 6.11). This trend indicates a slight decrease of the average Mn oxidation state (Nelson et al., 2000). The decrease of the average oxidation state might indicate an increase of Mn^{3+} concentration in the sorbent, but could as well be just an enrichment of Mn^{3+} at the particle surface in comparison to the bulk (Sato et al., 1997; Amalraj et al., 2013; Ilton et al., 2016). However, the latter is subject to discussion if the observed enrichments are not actually measurement artefacts (Ilton et al., 2016). Within the redox-based Li extraction mechanism, the average oxidation state decreases during Li sorption as Mn^{4+} is reduced to Mn^{3+} and increases during Li desorption due to Mn^{3+} disproportionation (Feng et al., 1992). The observed decrease of Mn oxidation state here is not an observation of the redox mechanism, as the sorbent after desorption is regarded. The observed decrease of oxidation state might be attributable to an Mn^{3+} increase, but the change is too low to determine with certainty.

For both materials, the O 1s peak at 530 eV (Figure 6.11b) is attributed to Mn–O bonds in the crystal framework of the sorbents (Oku et al., 1975; Foord et al., 1984; Marchini et al., 2016; Frankcombe and Liu, 2023), and the peaks at ~531.6 eV are attributed to hydroxide and carbonate bonds (Roychowdhury et al., 2019). The peak at 533.4 eV of the final sorbent is attributed to the C–O bond (Frankcombe and Liu, 2023).

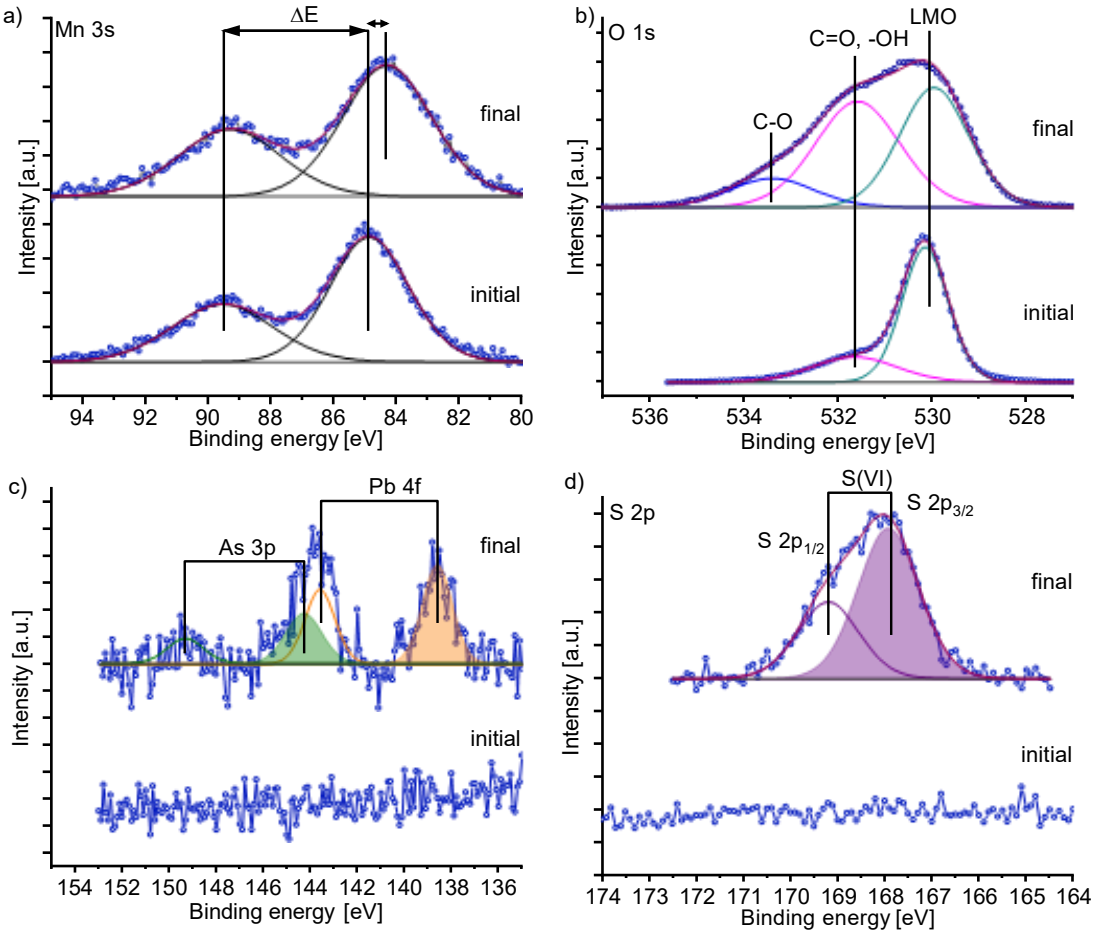

Figure 6.11: XPS spectra of Mn3s (a), As3p and Pb4f (b), S2p (c) and O1s (d) of the sorbent prior to the experiment (initial) and after 20 cycles (final).

After the final desorption, the sorbent spectrum shows a Pb $4f_{7/2}$ peak at 138.5 eV (Figure 6.11c). The Pb $4f_{7/2}$ peak is attributed to Pb–O bonds in inner-sphere bidentate complexes with surface hydroxyl groups (Zhang et al., 2017). On double corner sharing sites, Pb forms surface complexes in the form of M–O–Pb–OH with negatively charged M–O groups, with M–O being the surface hydroxyl group (Zhang et al., 2017). On double edge sharing sites, Pb forms M–O–Pb^{+} inner sphere complexes with M–OH^{2+} sites in addition, but to a negligible extent (Zhang et al., 2017). The adsorption of Pb strongly depends on the pH, as this determines the extent of protonation of surface hydroxyl groups. At a sorbent pH_{pzc} ~ 2.5 (Wang et al., 2009; Slunitschek et al., 2025) and a brine pH ~ 5, deprotonation of surface hydroxyl groups is favoured, resulting in the observed Pb sorption. At pH below the pH_{pzc}, protonation with dissolution of Pb can occur, explaining the presence of Pb in the desorption solution (Figure 6.6, Zhang et al., 2017). Due to the negative electrostatic charge at the sorbent surface at pH > pH_{pzc} (Anderson and Malotky, 1979), Pb and the other cations present in the brine can sorb through outer-sphere physisorption. The Pb binding as M–O–Pb–OH complex leads to hydrolysis of water and liberation of H^{+}, to the same extent as the Pb sorption (Zhang et al., 2017). Thus, the adsorption of Pb results in an acidification of the brine. Depending on the Pb concentration in

a geothermal brine in general, the induced acidification can result in a chemical demand for neutralisation during DLE and thus increased costs.

After the final desorption, the sorbent spectrum contains a weak As 3p doublet with As $3p_{3/2}$ at 143.8 eV and As $3p_{1/2}$ at 149.6 eV (Figure 6.11b, Ajith et al., 2019). This doublet overlaps partially with Pb 4f and can only be qualitatively evaluated and carefully interpreted. This doublet is characteristic of the As–O bond of As^{5+} in As_2O_5 (Ajith et al., 2019). This confirms the adsorption of As on the sorbent as an inner-sphere surface complex with framework O (Manning et al., 2002), discussed in Slunitschek et al. (2025). The observed As–O and Pb–O bonds confirm the accumulation inferred from the aqueous data (Figure 6.6). Both elements are adsorbed in low concentrations of <0.1 atomic-%, as indicated by the noisy spectra (Figure 6.11c, Table A6.6).

The spectrum of the final sorbent shows a S $2p_{3/2}$ peak at 167.9 eV, which is not present in the initial spectrum (Figure 6.11b). The peak is characteristic of S-O bonds of sulphate, but other SO_x species could be possible as well (XPS Database S). Whether or not S is bound to crystal structure O or through chemisorption, precipitation or in the form of secondary phases cannot be determined.

The XPS analysis of the final sorbent after the desorption step shows no Ca peak, whereas the sorbent after the corresponding washing step contains a Ca $2p_{3/2}$ peak at 347.2 eV in trace concentration <0.1 atomic-% (Table A6.6). Due to the low signal, Ca might not have been detected in the measurement of the sorbent after the desorption step. The Ca $2p_{3/2}$ peak is attributed to ionically bound Ca^{2+}, potentially present as carbonate, oxide or hydroxide (Roychowdhury et al., 2019). This is supported by O peaks at ~531.6 eV, attributed to carbonate and hydroxide peaks. Calcium sulphate precipitates from geothermal brines on sorbents have been reported by Reich et al. (2024), but the present Ca $2p_{3/2}$ peak at 347.2 eV does not clearly fit the Ca $2p_{3/2}$ peak of sulphate at 348.0 eV (Christie et al., 1983). Furthermore, Ca is not incorporated into the spinel LMO framework (Nolis et al., 2018).

6.4. Conclusion

The sorbent has a high selectivity and sorption process stability, shown over 15 cycles for all elements. While 15 cycles are too short to deduce the suitability for long-term industrial applications, it gives a good indication and shows the potential. Arsenic and Pb show stable selectivity and accumulation through inner-sphere complexes with framework O at the particle surface is derived. Similarly, Ba accumulation at the sorbent is indicated. Thereby, a limited number of binding sites is indicated, as with As and Pb. The selectivity and the extraction of Na, Mg, S, K, Ca and Sr are relatively constant during cyclic extraction as well, and physisorption as the binding process is indicated

The powdered $Li_{1.6}Mn_{1.6}O_4$ sorbent requires strengthening of its mechanical resistance due to

its susceptibility to mechanical forces. For the application in batch reactors or flow reactors with high forces, a higher mechanical strength is needed. Due to the structure of the particles, separation of crystallites or smaller particles has to be prevented to reduce sorbent loss. Additionally, the batch reactor and stirring design should be optimised for reduction of sorbent degradation.

6.5. Appendix

Table A6.1: Elemental composition of aqueous samples of the 20 cycles. m.u.% is the measurement uncertainty in %.

							sorption						
cycle	Li	Na	Mg	S	K	Ca	Mn	Fe	Zn	As	Sr	Ba	Pb
							mg/L						
pure brine	163	40591	342	153	3199	7393	23.3	<0.001	9.77	3.66	378	7.12	0.71
1	120	32879	279	124	2574	6020	2.97	<0.001	7.10	1.05	311	4.89	<0.005
2	118	39364	335	147	3097	7188	<0.001	<0.001	5.22	0.56	371	3.29	<0.005
3	118	38964	331	148	3076	7105	<0.001	<0.001	5.25	1.20	364	3.32	<0.005
4	119	39171	329	148	3082	7130	<0.001	<0.001	5.34	1.40	363	3.38	<0.005
5	122	39407	332	147	3096	7170	<0.001	<0.001	5.45	1.39	370	3.52	<0.005
6	121	39104	332	146	3073	7134	<0.001	0.24	5.28	1.12	360	3.45	<0.005
7	134	39482	336	149	3103	7201	<0.001	<0.001	5.85	1.77	366	4.73	<0.005
8	125	39301	332	147	3080	7157	<0.001	<0.001	5.07	1.14	362	3.54	<0.005
9	126	39322	329	146	3079	7160	<0.001	<0.001	5.07	1.14	363	3.57	<0.005
10	126	38679	325	145	3024	7014	<0.001	<0.001	5.21	1.38	356	3.75	<0.005
11	127	38761	328	145	3033	7050	<0.001	<0.001	5.12	1.18	364	3.78	<0.005
12	126	37825	322	141	2962	6894	<0.001	<0.001	5.28	1.08	355	3.90	<0.005
13	124	37529	315	141	2936	6818	<0.001	<0.001	5.01	0.92	349	3.77	<0.005
14	130	38874	328	147	3044	7040	<0.001	<0.001	5.39	1.37	357	4.09	<0.005
15	132	39043	332	148	3057	7092	<0.001	<0.001	5.18	1.20	362	4.04	<0.005
20	139	38619	333	144	3044	7035	<0.001	<0.001	5.03	1.32	346	4.78	<0.005
m.u.%	4.24	2.08	3.50	1.25	4.17	2.02	2.38	3.99	2.36	3.61	3.54	2.19	5.21

Table A6.1 continued: Elemental composition of aqueous samples of the 20 cycles. m.u.% is the measurement uncertainty in %.

							desorption						
cycle	Li	Na	Mg	S	K	Ca	Mn	Fe	Zn	As	Sr	Ba	Pb
							mg/L						
pure desorption solution	0.01	<0.3	0.004	0.01	0.13	0.04	<0.001	0.005	0.01	<0.005	0.0004	<0.0002	<0.005
1	83.9	162	1.83	1.11	23.2	59.4	104	1.16	8.85	0.50	9.32	7.49	0.08
2	74.7	41.2	0.83	0.60	13.3	38.0	66.5	0.99	8.88	1.94	8.80	8.21	0.21
3	73.6	39.9	0.79	0.54	12.8	37.4	63.3	0.77	9.03	2.95	8.86	8.64	0.28
4	73.5	53.1	0.93	0.56	13.5	41.7	62.1	1.08	9.23	3.19	9.01	8.39	0.41
5	72.2	62.3	1.01	0.59	13.9	43.0	63.3	0.40	8.92	3.40	9.10	8.47	0.50
7	80.7	33.0	0.86	0.70	13.5	41.3	159	0.69	12.5	4.78	8.54	11.1	0.97
8	59.9	22.9	0.64	0.41	10.1	32.7	66.8	0.28	8.86	3.56	7.38	8.02	0.79
9	57.7	32.5	0.83	0.52	10.8	37.9	59.0	0.18	9.43	3.27	7.93	7.97	0.73
10	53.3	45.4	0.89	0.58	11.7	38.9	59.5	0.44	9.49	3.12	7.84	7.65	0.76
11	50.8	38.6	0.76	0.48	10.5	36.8	58.6	0.18	9.26	3.28	7.35	7.41	0.79
12	47.7	31.1	0.64	0.40	9.69	33.1	57.7	0.14	8.66	3.06	6.91	6.97	0.81
13	33.3	35.2	0.57	0.33	7.76	25.8	40.8	0.06	6.43	2.29	4.85	5.02	0.58
14	41.6	33.8	0.57	0.42	8.44	28.8	53.6	0.08	8.01	2.95	5.80	6.18	0.85
15	42.3	37.0	0.71	0.53	8.98	33.1	54.5	0.07	9.05	3.10	6.21	6.50	0.90
20	29.5	122	1.29	0.69	13.8	41.0	54.3	0.09	8.92	2.80	5.02	4.92	1.00
m.u.%	4.23	2.08	3.78	1.25	4.50	3.72	2.38	3.99	3.99	3.61	3.54	2.19	5.21

Table A6.2: Measured sorbent in step sample over 20 extraction cycles and approximated total sorbent loss. Total sorbent loss per sample (“sorbent loss”) was determined through calculating the ratio of sorbent in sample and sample volume V and multiplying with the step volume. Steps: S = Sorption, WS = Wash sorption, D = Desorption, WD = Wash Desorption. Step volumes: S = 0.2 L, WS = 0.2 L, D = 0.08 L, WD = 0.2 L.

cycle	step	V	mass in sample	sorbent loss	sorbent in reactor	cycle	step	V	mass in sample	sorbent loss	sorbent in reactor
		mL	g	g	g			mL	g	g	g
0					0.822						
1	D	32.5	0.005	0.013	0.810	11	S	42.5	0.002	0.009	0.596
1	WD	42.5	0.003	0.013	0.797	11	WS	32.5	0.001	0.009	0.587
2	D	33.5	0.004	0.009	0.788	11	D	32	0.004	0.010	0.578
2	WD	43	0.002	0.010	0.778	11	WD	42.5	0.002	0.010	0.567
3	S	45	0.001	0.006	0.771	12	S	42.5	0.001	0.002	0.565
3	WS	43	0.001	0.005	0.766	12	WS	42.5	0.001	0.007	0.558
3	D	34	0.004	0.009	0.757	12	D	32.5	0.002	0.005	0.553
3	WD	44	0.002	0.008	0.750	12	WD	42.5	0.001	0.007	0.546
4	S	44	0.002	0.011	0.739	13	S	41.5	0.002	0.007	0.539
4	D	32.5	0.001	0.003	0.735	13	WS	42	0.001	0.007	0.532
4	WD	45	0.001	0.003	0.732	13	D	32	0.003	0.007	0.525
5	S	44	0.001	0.004	0.729	13	WD	42.5	0.002	0.008	0.516
5	WS	42.5	0.000	0.000	0.728	14	S	42.5	0.002	0.008	0.508
5	D	34	0.001	0.003	0.726	14	WS	43	0.002	0.010	0.498
5	WD	42.5	0.000	0.002	0.724	14	D	31.5	0.002	0.006	0.492
6	S	45	0.002	0.007	0.717	14	WD	44	0.000	0.001	0.491
7	D	32.5	0.002	0.006	0.711	15	S	41	0.001	0.005	0.486
7	WD	43	0.001	0.006	0.705	15	WS	42.5	0.002	0.008	0.478
8	S	42	0.001	0.006	0.699	15	D	30	0.002	0.004	0.474
8	WS	42.5	0.001	0.002	0.697	15	WD	42.5	0.001	0.004	0.470
8	D	32.5	0.002	0.005	0.691	20	S	44	0.003	0.013	0.456
8	WD	44	0.001	0.006	0.685	20	WS	44	0.003	0.012	0.445
9	S	42.5	0.001	0.004	0.681	20	D	32.5	0.001	0.002	0.442
9	WS	43	0.001	0.006	0.675	20	WD	32.5	0.002	0.015	0.427
9	D	30	0.006	0.017	0.659						
9	WD	43	0.003	0.015	0.644						
10	S	42	0.002	0.010	0.635						
10	WS	44	0.001	0.005	0.630						
10	D	32	0.005	0.012	0.618						
10	WD	41	0.003	0.012	0.605						

Table A6.3: Chemical analysis of blank cycles of 20 cycle experiment. m.u.% is the measurement uncertainty in %.

						sorption							
	cycle	Li	Na	Mg	S	K	Ca	Mn	Zn	As	Sr	Ba	Pb
						mg/L							
Brine		163	40591	342	153	3199	7393	23.3	9.8	3.66	378	7.12	0.71
Sorption	1	132	33378	281	126	2608	6137	19.2	7.97	2.97	313	5.84	<0.005
Sorption	2	161	40302	339	152	3172	7381	22.9	9.6	3.62	380	7.05	<0.005
Sorption	3	166	41178	348	155	3260	7515	23.5	9.7	3.67	384	7.26	<0.005
Sorption	4	157	39370	334	148	3080	7146	22.6	9.40	3.56	371	6.91	<0.005
Sorption average		154	38557	326	145	3030	7045	22.0	9.17	3.45	362	6.76	<0.005
Wash sorption	1	1.26	332	2.91	1.20	24.4	61.9	0.23	0.11	0.07	3.16	0.06	<0.005
Wash sorption	2	1.19	315	2.74	1.13	23.0	58.7	0.22	0.10	<0.005	3.01	0.06	<0.005
Wash sorption	3	1.51	390	3.44	1.43	29.1	73.6	0.28	0.14	0.06	3.79	0.07	<0.005
Wash sorption	4	1.19	319	2.78	1.21	23.8	59.7	0.22	0.10	<0.005	3.04	0.06	<0.005
Wash sorption average		1.29	339	2.97	1.24	25.1	63.5	0.24	0.11	0.07	3.25	0.06	<0.005
m.u.%		4.23	2.08	3.50	1.25	4.17	2.02	2.38	2.36	3.61	3.54	2.19	5.21
						desorption							
Desorption	1	0.06	12.0	0.19	<0.01	1.32	3.20	0.54	0.11	<0.005	0.14	0.03	<0.005
Desorption	2	0.04	9.6	0.13	<0.01	1.17	2.51	0.43	0.08	<0.005	0.11	0.02	<0.005
Desorption	4	0.08	23.0	0.24	0.10	1.95	4.91	0.41	0.14	<0.005	0.23	0.02	0.05
Desorption average		0.06	14.9	0.19	0.10	1.48	3.54	0.46	0.11	<0.005	0.16	0.02	0.05
Wash desorption	1	0.06	17.0	0.15	0.08	1.26	3.20	0.08	0.03	<0.005	0.16	0.01	<0.005
Wash desorption	2	0.05	13.7	0.13	0.07	1.01	2.68	0.04	0.02	<0.005	0.13	0.00	<0.005
Wash desorption	4	0.05	13.1	0.12	0.06	0.94	2.49	0.04	0.02	<0.005	0.12	0.00	<0.005
Wash desorption average		0.06	14.6	0.13	0.07	1.07	2.79	0.06	0.02	<0.005	0.14	0.01	<0.005
m.u.%		4.23	2.08	3.78	1.25	4.50	3.72	2.38	2.36	3.61	3.54	2.19	5.21

Table A6.4: Comparison of minimum and maximum concentrations in sorption and desorption eluate over the 20 extraction cycles (experiment) and average concentration over the four blank cycles. Min = minimum, max = maximum

		Sorption					Desorption				
		Na	Mg	S	K	Ca	Na	Mg	S	K	Ca
		mg/L					mg/L				
Experiment	Min	32879	279	124	2574	6020	23	0.57	0.33	7.76	25.8
	Max	39482	336	149	3103	7201	122	1.29	0.70	13.9	43.0
Blank	Average	38557	326	145	3030	7045	14.9	0.19	0.10	1.48	3.54

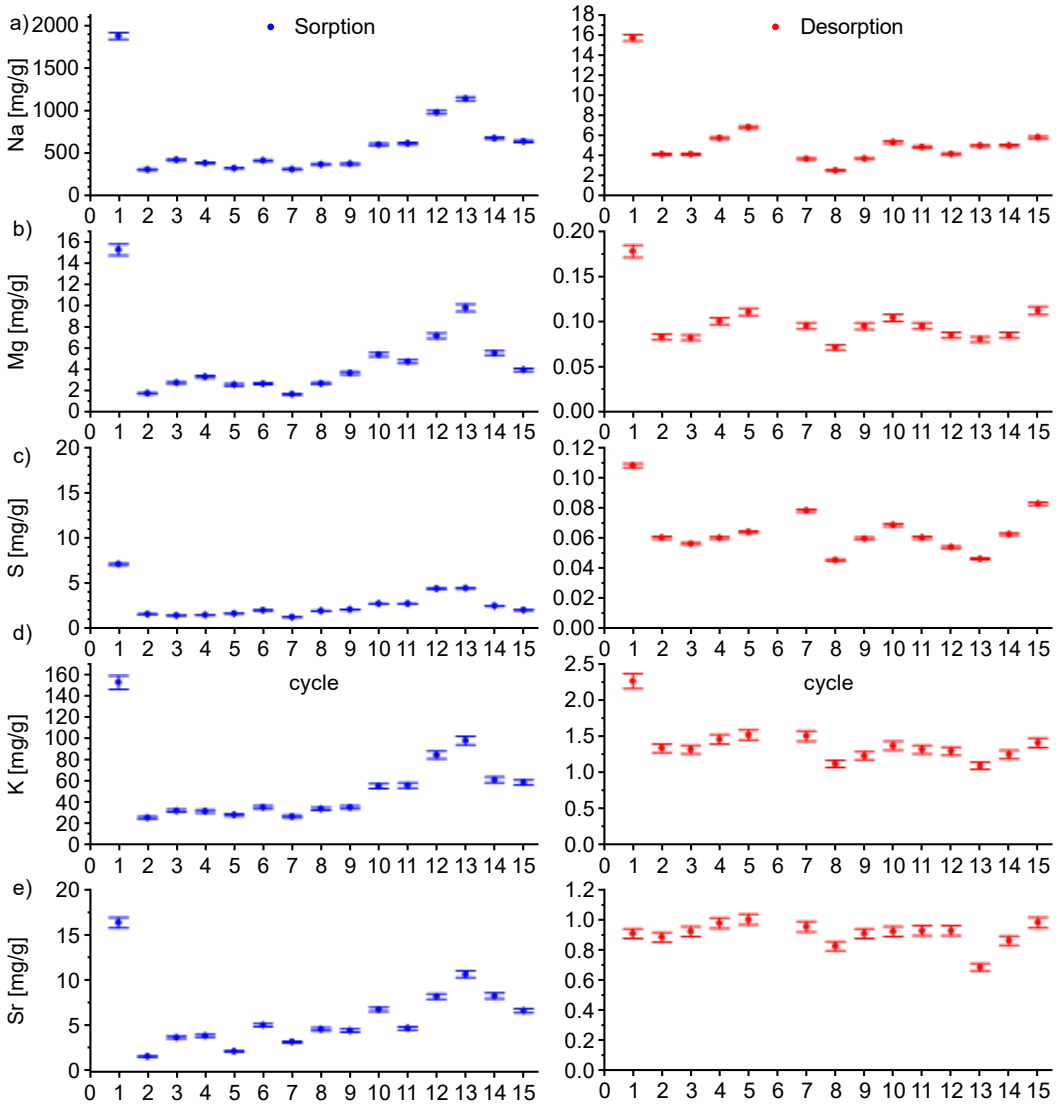

Figure A6.1: Sorption capacity based on sorption and desorption data for Na, Mg, S, K, Sr

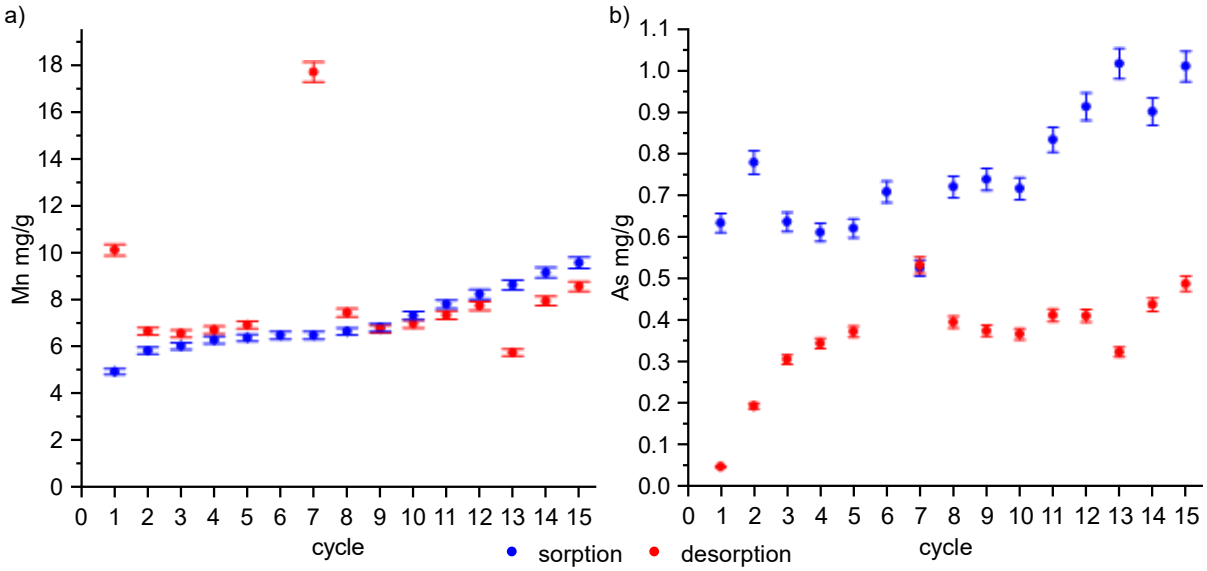

Figure A6.2: Sorption capacity based on sorption and desorption data for Mn (a) and As (b).

Table A6.5: Distribution coefficient PK_d and separation coefficient α over all elements and cycles

Distribution coefficient PK_d [L]												
cycle	Li	Na	Mg	S	K	Ca	Mn	Zn	As	Sr	Ba	Pb
1	0.07	0.047	0.045	0.05	0.05	0.05	1.37	0.08	0.50	0.043	0.09	28.3
2	0.08	0.006	0.004	0.008	0.007	0.006	4665	0.17	1.12	0.003	0.23	28.3
3	0.08	0.008	0.007	0.007	0.008	0.008	4665	0.17	0.41	0.008	0.23	28.3
4	0.07	0.007	0.007	0.007	0.008	0.007	4665	0.17	0.32	0.008	0.22	28.3
5	0.07	0.006	0.006	0.008	0.007	0.006	4665	0.16	0.33	0.004	0.20	28.3
6	0.07	0.008	0.006	0.010	0.008	0.007	4665	0.17	0.45	0.010	0.21	28.3
7	0.04	0.006	0.004	0.006	0.006	0.005	4665	0.13	0.21	0.006	0.10	28.3
8	0.06	0.007	0.006	0.009	0.008	0.007	4665	0.19	0.44	0.009	0.20	28.3
9	0.06	0.006	0.008	0.010	0.008	0.007	4665	0.19	0.44	0.008	0.20	28.3
10	0.06	0.010	0.011	0.012	0.012	0.011	4665	0.18	0.33	0.012	0.18	28.3
11	0.06	0.009	0.009	0.011	0.011	0.010	4665	0.18	0.42	0.008	0.18	28.3
12	0.06	0.015	0.013	0.017	0.016	0.014	4665	0.17	0.48	0.013	0.17	28.3
13	0.06	0.016	0.017	0.017	0.018	0.017	4665	0.19	0.60	0.016	0.18	28.3
14	0.05	0.009	0.009	0.009	0.010	0.010	4665	0.16	0.33	0.012	0.15	28.3
15	0.05	0.008	0.006	0.007	0.009	0.008	4665	0.18	0.41	0.009	0.15	28.3
20	0.04	0.010	0.005	0.012	0.010	0.010	4665	0.19	0.35	0.018	0.10	28.3

Table A6.5 continued: Distribution coefficient PKd and separation coefficient α over all elements and cycles

Separation coefficient α [-]												
cycle	Li/Li	Li/Na	Li/Mg	Li/S	Li/K	Li/Ca	Li/Mn	Li/Zn	Li/As	Li/Sr	Li/Ba	Li/Pb
1	1.00	1.56	1.62	1.57	1.50	1.60	0.05	0.97	0.15	1.70	0.80	0.003
2	1.00	12.4	17.9	9.26	11.7	13.5	0.00002	0.44	0.07	22.4	0.33	0.003
3	1.00	9.12	11.7	10.3	9.48	9.39	0.00002	0.44	0.19	9.71	0.33	0.003
4	1.00	10.1	9.77	10.1	9.65	9.92	0.00002	0.44	0.23	9.33	0.33	0.003
5	1.00	11.4	11.9	8.43	10.2	10.9	0.00001	0.43	0.21	16.0	0.33	0.002
6	1.00	9.29	12.1	7.32	8.57	9.70	0.00002	0.41	0.16	7.04	0.33	0.003
7	1.00	7.91	12.0	7.51	7.18	8.33	0.00001	0.33	0.21	7.11	0.44	0.002
8	1.00	9.19	10.5	6.65	7.80	9.13	0.00001	0.33	0.14	6.79	0.30	0.002
9	1.00	9.23	7.78	6.19	7.64	9.14	0.00001	0.32	0.14	7.14	0.30	0.002
10	1.00	6.05	5.62	5.06	5.16	5.52	0.00001	0.34	0.18	4.95	0.33	0.002
11	1.00	5.99	6.50	5.12	5.15	5.81	0.00001	0.31	0.13	7.36	0.32	0.002
12	1.00	4.07	4.72	3.42	3.72	4.11	0.00001	0.35	0.12	4.57	0.36	0.002
13	1.00	3.84	3.74	3.73	3.49	3.71	0.00001	0.33	0.10	3.82	0.35	0.002
14	1.00	5.73	5.86	5.94	4.97	5.05	0.00001	0.31	0.15	4.30	0.34	0.002
15	1.00	5.88	7.98	7.11	5.00	5.49	0.00001	0.26	0.11	5.24	0.31	0.002
20	1.00	3.47	6.61	2.86	3.48	3.48	0.00001	0.19	0.10	1.92	0.36	0.001

Table A6.6: Main XPS peaks of initial sorbent and after the desorption and desorption wash of cycle 20.

Name	Peak eV	Atomic %	oxidation state/ speciation/bond	comment	source
			Sorbent		
Li1s	54.4	22.4	Li^+	Li in LMO	(Bao et al., 2023)
Mn3s	85.0	*	oxygen bond		(NIST, 2000)
Mn3s	89.4	*	oxygen bond		(NIST, 2000)
O1s	530.2	34.9	oxide oxygen (lattice)		(Frankcombe and Liu, 2023)
O1s	531.7	12.1	hydroxide/carbonate	potentially surface contamination	(Roychowdhury et al., 2019)
C1s	285.0	11.7	C-H & C-C-H		(Chen et al., 2020)
C1s	286.6	1.9	C-O & C-O-H		(Chen et al., 2020)
C1s	288.8	2.2	C=O		(Chen et al., 2020)
			Sorbent after 20 extraction cycles after desorption		
Li1s	53.8	13.31	Li^+	Li in LMO	(Bao et al., 2023)
Mn3s	84.3	*	oxygen bond		(NIST, 2000)
Mn3s	89.2	*	oxygen bond		(NIST, 2000)
O1s	530.0	14.62	oxide oxygen (lattice)		(Frankcombe and Liu, 2023)
O1s	531.6	15.82	hydroxide/carbonate	potentially surface contamination	(Roychowdhury et al., 2019)
C1s	285.0	29.03	C-H & C-C-H		(Chen et al., 2020)
C1s	286.5	6.07	C-O & C-O-H		(Chen et al., 2020)
C1s	288.2	3.84	C=O		(Chen et al., 2020)
$Pb4f_{7/2}$	138.5	0.04	oxide		(Zhang et al., 2017)
$As3p_{3/2}$	143.8	0.08	As5+, As2O5		(Ajith et al., 2019)
$S2p_{3/2}$	167.9	1.40	S^{6+}, sulphate + SO_x	predominantly sulphate, other SOx specie possible	(XPS Database S)

Table A6.6 continued: Main XPS peaks of initial sorbent and after the desorption and desorption wash of cycle 20.

Sorbent after 20 extraction cycles after desorption wash					
Name	Peak eV	Atomic %	oxidation state/ speciation/bond	comment	source
Li1s	53.5	13.9	Li^{+}	Li in LMO	(Bao et al., 2023)
Mn3s	84.2	-	oxygen bond		(NIST, 2000)
Mn3s	89.2	-	oxygen bond		(NIST, 2000)
O1s	529.8	18.6	oxide oxygen (lattice)		(Frankcombe and Liu, 2023)
O1s	531.4	11.2	hydroxide/ carbonate	potentially surface contamination	(Roychowdhury et al., 2019)
O1s	532.9	3.3			
C1s	285.0	25.9	C-C, C-H		(Chen et al., 2020)
C1s	286.7	2.8	C-O		(Chen et al., 2020)
C1s	288.4	2.0	O=C-O-		(Chen et al., 2020)
$Ca2p_{3/2}$	347.2	0.1	Ca^{2+}, carbonate, oxide or hydroxide		(Roychowdhury et al., 2019)
$Pb4f_{7/2}$	138.4	0.02	oxide		(Zhang et al., 2017)
$As3p_{3/2}$	144.6	0.1	As^{5+}, As2O5		(Ajith et al., 2019)
$S2p_{3/2}$	167.8	1.0	S^{6+}, sulphate, SO_x	predominantly sulphate, other SOx specie possible	(XPS Database S)

7. Manuscript

–

Requirements and design of a pilot plant for the on-site investigation of Direct Lithium Extraction (DLE) from pressurised geothermal brines

Klemens Slunitschek [a,b,*], Rebekka Reich[a,b,*], Thomas Hettkamp[c], Elif Kaymakci[d], Kevin Altinger[e], Elisabeth Eiche[a,b], Tobias Kluge[a,b] and Jochen Kolb[a,b]

[a]*Chair of Geochemistry and Economic Geology, Institute of Applied Geosciences, Karlsruhe Institute of Technology, Adenauerring 20b, 76131 Karlsruhe, Germany;*

[b]*Laboratory for Environmental and Raw Materials Analysis (LERA), Institute of Applied Geosciences, Karlsruhe Institute of Technology, Adenauerring 20b, 76131 Karlsruhe, Germany;*

[c]*Bestec GmbH, Bismarckstraße 19, 76870 Kandel, Germany;*

[d]*EnBW Energie Baden-Württemberg AG, Durlacher Allee 93, 76131 Karlsruhe, Germany.*

[e]*Chair of Structural Geology and Tectonics, Institute of Applied Geosciences, Karlsruhe Institute of Technology, Adenauerring 20b, 76131 Karlsruhe, Germany;*

*both authors contributed equally; corresponding authors: Klemens Slunitschek; e-mail: klemens.slunitschek@kit.edu; Rebekka Reich; e-mail: rebekka.reich@kit.edu; postal address: Campus Süd, Adenauerring 20b, Gebäude 50.40, 76131 Karlsruhe, Germany; phone: +49 721 608-43322

Requirements and design of a pilot plant for the on-site investigation of Direct Lithium Extraction (DLE) from pressurized geothermal brines

Lithium is a raw material of major interest for the energy transition that is highly demanded. We identified requirements for pilot plants to investigate DLE sorbents in-situ in pressurized geothermal settings and designed, constructed and tested a pilot plant. The main requirements for the pilot plant are its wide applicability to different brines and sorbents, adaption for batch and flow operation, the prevention of scaling and corrosion, and the possibility to choose between manual and automatic control. Stainless steel was used for all major components and scaling was prevented by keeping elevated pressure and utilizing inert gas in the extraction reactor. A Li extraction test was conducted in the Bruchsal geothermal power plant (Germany), using a Li-Mn-oxide sorbent and compared with a blank, sorbent-free experiment, showing the successful Li extraction through the sorbent. Although cross-contamination of brine into the desorption solution, corrosion and unexplained pressure loss occur, we think these issues can be solved through minor changes to the plant, used components and process design. Despite this, the plant provides the desired capabilities for on-site, in-site, pressurized investigation of DLE in geothermal settings.

Keywords: sorption; ion-exchange; pilot plant; geothermal; pressure

1. Introduction

The demand for raw materials for the green energy transition, like Li, Co and Ni, is expected to increase drastically in the near future.[1] Models on the demand for energy raw materials indicate an increase by factors 2 – 20 to 1.8 – 11 Mt in 2050.[1–3] Recycling, however, cannot cover the demand and is expected to contribute to only 20 – 23% of the cumulative material supply by 2050.[2] Thus, new resources have to be explored and developed. Some of the energy raw materials, especially Li, reach potential economic concentrations in aqueous resources like geothermal brines (e.g. 155 mg/L, Bruchsal, Germany, Table 1), representing a potential deposit.[4] In geothermal power plants, geothermal brine is extracted for the production of heat and/or electricity before reinjection into the subsurface reservoir.[5–7]

Direct Li extraction (DLE) technologies have advanced in the last years, including the development and optimization of direct precipitation, membrane-based processes, electrochemical methods, solvent extraction, sorption and ion exchange (the latter are summarized as sorption in the following).[8] Sorption has been identified as a promising technique well applicable to DLE in operating geothermal power plants.[8–13] Sorbents of nano- to micro-scale particle size are preferentially used in laboratory experiments since sorption processes are strongly dependent on surface properties.[14] Sorption-based batch- or flow-type DLE is conducted by (1) mixing of brine and sorbent for a sorbent-specific time period to

selectively capture Li; (2) recovery of the Li-loaded sorbent by filtration, centrifugation or discharge of brine; and (3) addition of a sorbent-specific desorption solution to (4) produce a Li-rich solution separated from a recycled sorbent that can be reused in the next DLE cycle. As many sorption processes are based on $Li^+ – H^+$ ion exchange, (highly) corrosive acidic desorption solutions (e.g., HCl) are needed. Depending on the operating conditions of the geothermal plant and the physicochemical brine conditions, sorbents should realize fast sorption kinetics, a high Li sorption capacity and selectivity, resist high temperatures and pressures and fulfil high stability and reusability requirements.[8]

Geothermal brine often has a complex chemical composition, a pressure of typically 20 – 50 bar, is highly corrosive (e.g. due to high Cl^- concentration), yields reducing redox conditions and is sensitive to changes in redox conditions, making it challenging for element extraction.[7,15–20] Changes in the physicochemical properties of the brine can cause scales, which may lead to clogging and cementation of pipes, resulting in decreasing heat exchange efficiency.[7,17,19] Since solubility decreases with decreasing temperature for most minerals[21–23], cooling below a critical temperature, typically 60 – 80 °C in the Upper Rhine Valley, Germany, has to be avoided to prevent scaling and guarantee a safe brine reinjection into the subsurface. It is crucial to perform DLE under O_2-free conditions to avoid oxidation and thus formation and precipitation of e.g., Fe(oxy)hydroxide, sulfates (e.g., barite) or calcite-dolomite phases from the brine.[17,20] Consequently, Li extraction has to either be designed and operated under conditions avoiding the formation of scales, or inhibitors need to be added.[20] The first case increases the technical requirements of the extraction facility, while the latter requires the addition of inhibiting chemicals.[7,20] The critical scaling controlling parameters temperature, pressure, redox conditions and pH should not be drastically changed.[8] Depending on the brine chemistry and the sorbent, potentially toxic or radioactive elements (e.g. As or Ra) may sorb or precipitate on the sorbent and thus, accumulate in the product or the sorbent.[7,17,20,24] Therefore, the complex brine chemistry requires a highly selective DLE process.[8] An alternative would be to remove ions that compete with Li and or bear the risk of scale formation or accumulation before Li extraction by special pre-treatment of the brine and re-addition after the extraction, if possible, or disposal.[7,20,25,26]

Some pilot plants for Li extraction from brines and other Li-rich solutions have already been constructed, investigating upscaling of different DLE technologies and their suitability for industrial-scale application.[10,27–36] For example, Yoshziuka et al. published a pilot study with a fixed bed reactor of 60 kg granulated LMO sorbent for the extraction of Li from seawater at a flowrate of 200 L/h.[36] The sorption step of the extraction processes lasted 30 and 150 days and selective Li recovery from seawater is shown. However, in general, few is known about these contraptions, since they are often build by companies and the plant and process design is kept secret. [36]

The company Simbol Materials developed and tested a DLE process with an Al-based sorbent in a geothermal power plant in Salton Sea, USA.[10,37] Maintaining the high ambient temperature of 250 °C is challenging and brine cooling causes scaling.[29,35] Thus, B, Si, Fe, Mn and Zn are removed before the Li extraction process.[37] The French company GeoLith SAS tested their pilot plant and sorbent Li-Capt® with geothermal brine from Cornish Lithium Ltd.'s United Down project and in the geothermal power plant of Bruchsal.[33,38] In this process, the natural pH is increased to 10 before Li extraction, which can hinder reinjection of the brine after the DLE process due to legal issues.[39] The company Lilac Solutions successfully tested a pilot-scale DLE in their Kachi Project in Argentina. They achieved on average 80% Li recovery over 100 cycles, and already reached > 2 000 cycles in a mini-pilot plant.[40] Lilac Solutions DLE technology is tested in a salar, likely under ambient physicochemical conditions, which are significantly different from geothermal brines.

The pilot plant design and construction described in this study realizes a sorbent-based, batch-type DLE under power plant conditions in Bruchsal, Upper Rhine Valley, southern Germany. With minor changes, the reactor can be used as a fixed bed reactor in a flow – through design as well. The pilot plant was installed and implemented into a bypass system at the reinjection pipe of the geothermal power plant of Bruchsal. The Bruchsal geothermal brine is characterized by a production temperature of 120°C, total dissolved solids (TDS) of 120 g/L, pH = 5.1 at 27 °C, 158 mS/cm electrical conductivity and 56 mV redox potential.[41] The brine is dominated by Na^+ and Cl^- at 35.6 g/L and 75.9 g/L, respectively. Lithium is a minor element at 155 mg/L (Table 1). The brine contains up to 1.9 L of dissolved gas per liter brine, consisting of 94.5 vol.-% CO_2, 3.5 vol.-% N_2 and 1.9 vol.-% CH_4.[42] The brine is pumped from the reservoir at 22 ± 2 bar and reinjected at 60 – 80 °C with 18 ± 2 bar at a flow rate of 24 L/s.[42]

Table 1: Chemical composition of the Bruchsal geothermal brine

Li [mg/L]	Na [g/L]	K [g/L]	Mg [mg/L]	Ca [g/L]	Sr [mg/L]	Ba [mg/L]	B [mg/L]	SiO_2 [mg/L]
155	35.6	3.2	347	7.4	354	8.6	35.9	90

Pb [mg/L]	As [mg/L]	Mn [mg/L]	Fe [mg/L]	Zn [mg/L]	SO_4^{2-} [mg/L]	F^- [mg/L]	Cl^- [g/L]	Br^- [mg/L]
3.2	7.8	23.4	44.3	13.6	392	1.6	75.9	310

1.1. Requirements and design realisation

In the scope of the combination of (1) heat and power production in geothermal power plants and (2) direct Li extraction from the produced geothermal brine, the requirements that need to be addressed for a DLE pilot plant are:

- Fast extraction process to recover Li while avoiding long-time surface storage of large brine volumes.
- Implementation at the reinjection side of the geothermal power plant to prevent disturbance of the heat and power production.
- Resistance of all materials and components in direct contact with the brine to high salinity and corrosivity, temperatures of 60 – 80 °C and a pressure of at least 25 bar.
- Applicability for different types and shapes of sorbents.
- Separation of sorption and desorption steps in time and space to minimize cross-contamination
- Possibility for batch and flow operation to study the brine-sorbent interaction and the DLE performance in different extraction setups.
- Addition of a neutralization or buffering solution during experiments to maintain natural pH.
- Adjustable times of every process step to adapt to the kinetic properties of each sorbent.
- Impermeability to gas to avoid gas leakage and air ingress.
- Applicability of different inert gases to prevent the interaction of sorbents with gases.
- Maintaining pressure and temperature.
- Pressure, temperature and pH sensors to monitor the DLE process.
- Full automation and programmability, but also manually controllable to easily adjust operation parameters.
- Installation in a transportable container to allow setup at different test sites.
- The pilot plant must meet safety and environmental regulations.

1.2. Pilot plant construction at the Bruchsal geothermal power plant

The pilot plant is a one-reactor-system (Figure 1), operable as a batch or flow reactor, attached to the bypass at the reinjection pipe of the geothermal power plant by a pressure hose. No pump is needed for brine inflow due to the brine pressure of 18 ± 2 bar, feeding the main component of the pilot plant, a 6 L reactor with a diameter of 150 mm (Figure 3). A carbon

steel (1.0305) body, coated with a 150 – 500 µm thick layer of a Novolac Epoxy Resin to prevent corrosion, was chosen for the reactor (Table A1).[15,16,43]

The fluids enter the reactor from the bottom promoting efficient mixture of fluid and sorbent (Figure 3). To improve mixing efficiency, a distributor plate is fixed at the bottom of the reactor (Figure 3). The distributor plate contains small holes spread over the plate to distribute the inflowing water homogeneously into the reactor, forcing the water to form small eddies and thereby mixing with the sorbent particles. The sorbent is kept within the reactor by two sieves that are welded between two distributor plates at the flanges of the reactor (Figure 3). Here, a 250 µm mesh size was chosen, but other sieves with other sizes are installable and have to be adapted to the particle size. The sealings are made of temperature- and corrosion-resistant PTFE or graphite. The sorbent can be filled into the reactor either through removal of the upper flange of the reactor or the pH probe inlet (Figure 2).

Two separate recirculation loops are attached to the reactor, one for brine and one for the desorption solution (Figure 1, 2), to avoid cross-contamination between the two fluids. Recirculation loops were chosen instead of a stirrer for batch experiments to avoid mechanical degradation of the sorbent upon impact onto the stirrer blades. Circulation ensures constant flow conditions, preventing prolonged, stationary brine storage, which may promote scaling. Cross-contamination is reduced by the two separated loops, each equipped with a centrifugal pump of 28 m^3/h flow rate (Table A1).

To prevent acidification of the brine when using Li^+–H^+ ion exchange sorbents, a buffer feed from a connected reservoir can be pumped into the inflowing or circulating brine by a membrane pump (Table A1, Figure 2). The pH and temperature within the reactor are constantly monitored by a pH probe (Rosemount™ 3300 HT, Emerson Electric Co.) reaching about four cm into the reactor (Figure 1). At the top of the reactor, a pressure sensor and a pressure gauge are installed (Figure 2).

Inert gas is flushed from the top to the bottom of the reactor to discharge the fluid (Figure 2). The gas, here N_2 technical grade, and gas pressure is adjusted to the requirements and each liquid (brine, desorption solution) is discharged through a separate outlet. The Li-depleted brine may either be disposed into a special disposal pond on site, waste containers or reinjected into the reinjection pipe. The desorption solution is either recycled or brought into another reservoir for further processing into a Li-product. Fluid and gas flow are controlled by pneumatic valves (Table A1).

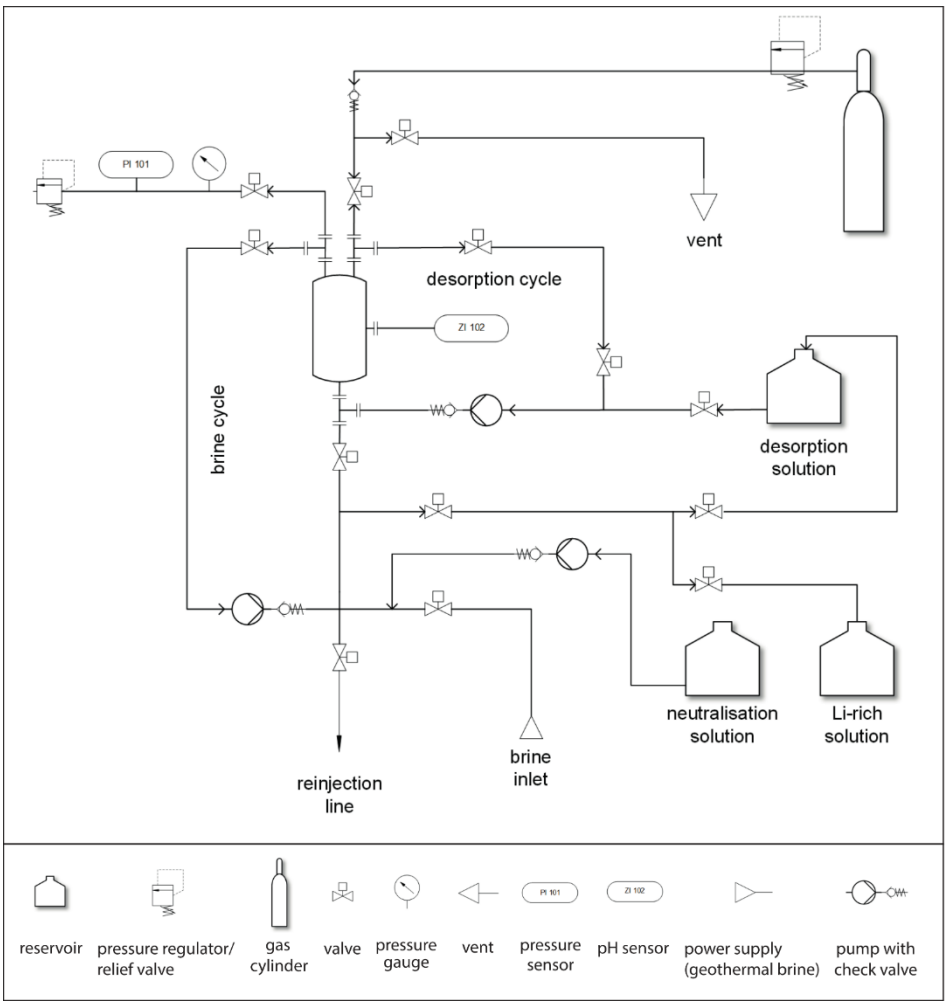

Figure 1: Technical drawing of the pilot plant design

The process automation is based on an SPS Siemens S7-1200. An extraction process sequence determining the action of each component in each process step has been programmed and all relevant parameters, e.g. inflow and circulation time, are adjustable. In order to be able to set up the pilot plant at different sites, it was installed in a standard office container (Table A1).

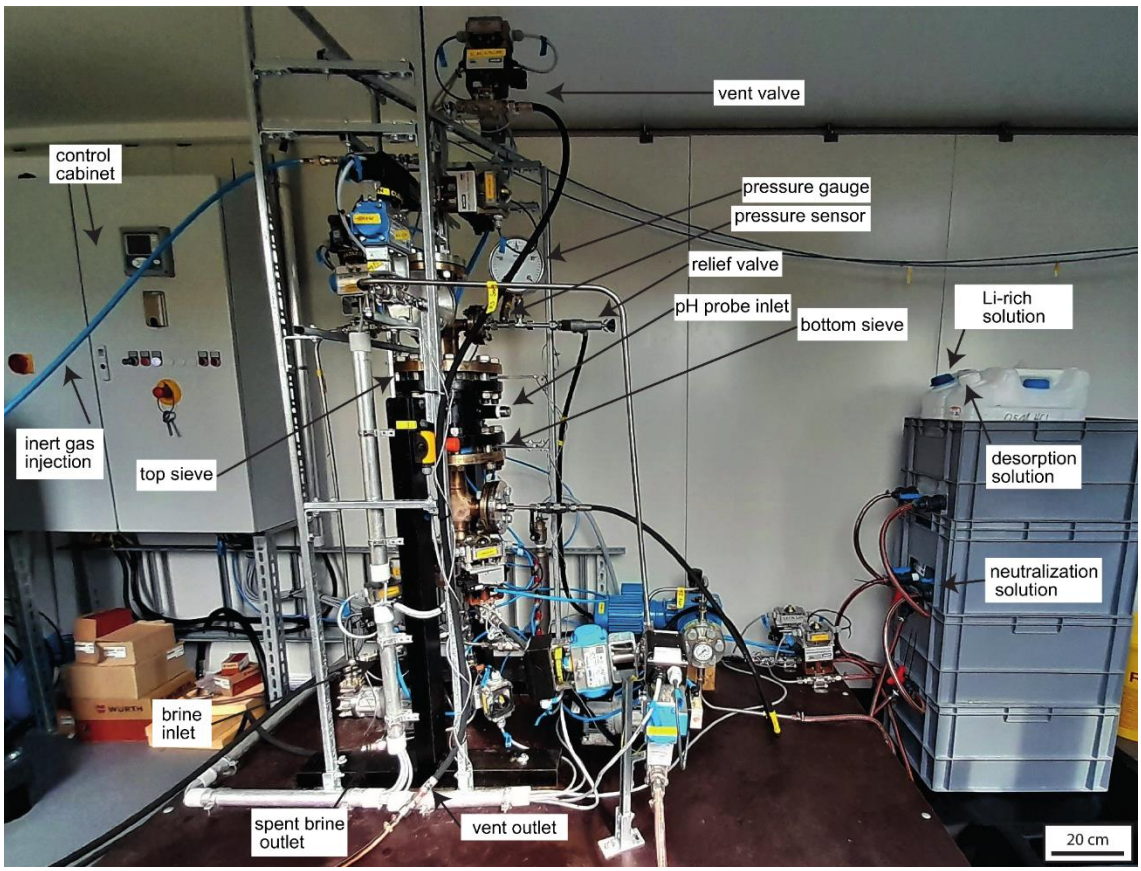

Figure 2: Photograph of the pilot plant. The major components are labelled and marked with arrows. The pilot plant is fixed to a supporting frame, standing within the leakage pan. The sorbent is in the black reactor. Valves, pumps, hoses and pipes are surrounding.

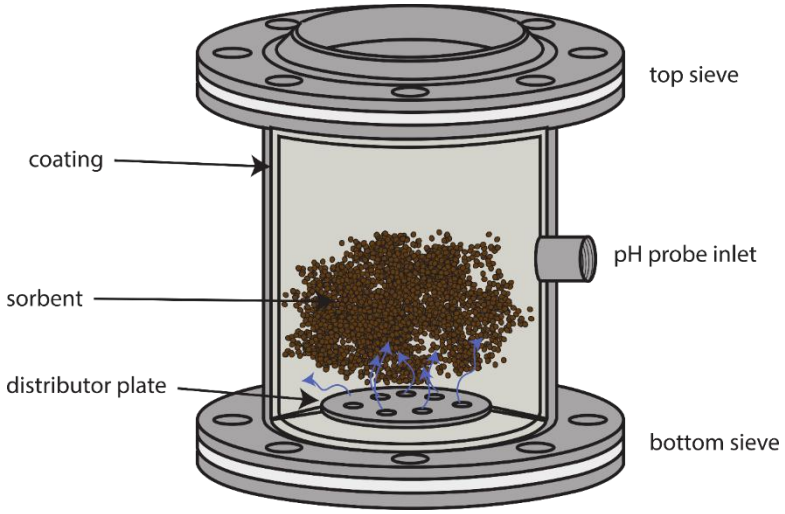

Figure 3: Sketch of the reactor design with distributor plate.

1.3. Plant preparation and functionality tests

After the pilot plant installation at the Bruchsal power plant, commissioning involved a pressure test and volume determination, both using fresh water. For the pressure test, leakage occurred at 33 bar, i.e. approximately 15 bar higher than the operating pressure in the reinjection pipe, proving the pressure stability and leak tightness of the pilot plant at the required 25 bar. For the determination of the reactor volume and attached loops, the corresponding components were filled with water, discharged and the water collected and weighted. A volume of 5.92 ± 0.02 L was determined for the empty reactor with the attached flanges (Table 2, Figure 2). The reactor including the sorption loop comprises a volume of 6.02 ± 0.02 L and including the desorption loop 6.08 ± 0.01 L (Table 2).

Table 2: Results of volume determination of reactor and circulation loops. “st.dev.” = standard deviation

repetition	reactor [L]	reactor + sorption loop [L]	reactor + desorption loop [L]
1	5.94	6.05	6.10
2	5.92	6.04	6.08
3	5.92	6.02	6.08
4	5.88	6.00	6.06
5	5.92	6.00	6.08
6	5.92		
7	5.92		
mean [L]	5.92	6.02	6.08
st. dev. [L]	0.02	0.02	0.01

The functionality of the pilot plant for DLE was tested with an LMO sorbent inside the reactor and without (blank experiment). The blank experiment was conducted in triplicate with 15 min duration of the sorption and desorption step, respectively. For desorption, a 0.5M HCl (pro analysis, Merck) solution was used and all fluids were later analysed using ICP-OES (iCap 7000, Thermo Fisher Scientific) and ICP-MS (iCAP RQ, Thermo Fisher Scientific) in the Laboratory for Environmental and Raw Materials Analysis (LERA), Institute of Applied Geosciences, KIT.

While the pristine desorption solution contains no significant concentrations of ions, the loaded stripping solution contains all elements analysed in the geothermal brine (Table A2). The dominant ions are Na with 543 mg/L, Ca with 112 mg/L and K with 48.4 mg/L, in average over three cycles (Table 3, Table A2), following the composition of the brine. This shows brine cross-contamination, potentially due to incomplete brine discharge, brine filled dead volumes or brine

adhered to surfaces. In order to assess the brine cross-contamination, element ratios with Si for all elements for the brine and loaded desorption solution were calculated, averaged over three cycles. Silica was chosen because it shows only a little concentration change of 3.6% in the brine before and after the sorption step (Table A2). While the alkaline and earth alkaline elements Li, B, Na, Mg, K, Ca, Rb and Sr show similar Si ratios in the brine and desorption solution, V, Cr, Fe, Ni, Cu and Sb show higher ratios, by 636 – 296670% (Table 4, Table A3). In addition, the concentrations of V, Cr, Ni and Cu are also higher in the desorption solution than in the brine (Table 4, Table A2). The enrichment of these elements in the desorption solution is attributed to dissolution from and corrosion of stainless and potentially carbon steel components by the 0.5M HCl desorption solution. The dissolved V may originate from carbon steel and Cr and Ni originate from stainless steels.[44] Also, the brine appears to corrode the components since the concentrations of Ni and Cr are increased in the brine after sorption compared to the pristine brine (Table A2). The corrosion of components by desorption solution and/or brine is supported by the observation of corrosion of carbon steel cutting rings, which were not available from stainless steel, and stainless-steel pipes in the desorption solution loop after approximately two weeks of operation. However, by visual assessment corrosion occurs only at a few places in the plant and to limited extent and is of no concern regarding pilot plant integrity or work safety.

Table 3: Average concentration of selected elements in the desorption solution over three consecutive blank cycles. All elements are listed in Table A2.

Na	Mg	Si	K	Ca	V	Fe	Ni
mg/L	mg/L	mg/L	mg/L	mg/L	mg/L	mg/L	mg/L
543	5.51	0.61	48.4	112	0.002	4.25	7.61

Table 4: Average ratio of selected elements to Si in brine and desorption solution. Ratios for all elements are listed in Table A3.

	V/Si	Cr/Si	Fe/Si	Ni/Si	Cu/Si	Sb/Si
brine mg/L	0.00003	0.001	1.10	0.004	0.001	0.006
desorption mg/L	0.003	0.69	6.99	12.5	0.11	0.18
deviation from brine %	8230	82699	636	296670	19992	3081

1.4. DLE functionality experiment

For the DLE functionality experiment, a Li-Mn-oxide sorbent (LMO) was prepared after Slunitschek et al.[13]. The sorbent is granular with a particle size of 2 – 3 mm and a total amount of 200 g sorbent was synthesized. Around 0.1 L buffering solution of 18.6 wt.-% Na acetate and 4.9 wt.-% acetic acid (pro analysis, Merck) was added to keep the brine at its natural pH

of 5.1.[41] The sorption and desorption time were set to 15 min each, to ensure comparability with the blank experiment. Six extraction cycles were conducted. The first two cycles are excluded from evaluation due to indication of release of residual Li from synthesis (Table A5).

Based on the desorption data, the Li extraction reaches 29%, with a sorption capacity of 1.31 mg/g (Table A5), showing that Li is successfully extracted and the developed plant is suitable to investigate Li extraction. While the sorbent has shown a potential for higher sorption capacities under laboratory conditions[13,45], these results are not comparable with the achieved capacity in this experiment. The predominant reason is the particle size, which is fine powder in most lab experiments, whereas 2 – 3 mm big particles where used here. Additionally, only a step duration of 15 min was used, although fine-grained sorbent powder already requires 24 – 48h to reach equilibrium in laboratory experiments.[45,46] Further reasons for low sorption capacity and Li extraction are the low sorbent – brine ratio and the low pH.[13,45] Since H^+ – Li^+ ion exchange sorbents reach higher sorption capacities at alkaline pH, the low natural brine pH of 5.1 also negatively affects the extraction performance compared to ideal laboratory conditions[45].

During the extraction experiment, sorbent particles got stuck in the 250 µm sieves, and fine grained particles were observed, showing strong physical forces and abrasion of the particles in the high-pressure and high flow regime, negatively influencing the sorbent longevity. A large filter bag containing the sorbent could potentially reduce abrasion through limitation of particle movement inside the reactor. If the filter bag is made of smaller mesh size, it would allow the integration of smaller particles in addition,. Another possibility to decrease the degree of mechanical abrasion may be the fixation of the particles onto carrier structures. If the complete reactor is filled with sorbent particles and used as a flow reactor, particle movement and thus sorbent deterioration is expected to be reduced as well.

Once the reactor is filled with brine and decoupled from the bypass by closing the inlet valve, the pressure drops abruptly by several bars and continuously decreases from ~17 bar to ~8 bar over the remaining time (Figure A1, Table A4). Leakage of the pilot plant is unlikely since the pressure test with N_2 confirmed its leak tightness up to 33 bar, although N_2 has a slightly larger kinetic diameter than CO_2 (3.64 Å vs. 3.30 Å), the main component of the Bruchsal gas phase.[42,47] Another explanation may be cooling of the 60°C hot brine upon contact with the colder reactor and pipes at ~5 – 10°C (experiment conducted in winter, January 2023). The cooling results in an increase in CO_2 solubility in the brine, thereby reducing the gas volume and thus the pressure.[48,48,49] Additionally, gas pockets could form during inflow and influence the pressure development. Regarding the prevention of scales, no scales have been observed over the complete experimental timeframe (6 months), indicating that the prevention through air removal with inert N_2 works.

1.5. Conclusion and improvement of the DLE pilot plant

The constructed pilot plant fulfils the requirements and functionality for investigating sorbent-based DLE in geothermal settings. Some improvements, however, might contribute to better handling and running the pilot plant and strengthen the scientific results.

A reduction of brine cross-contamination into the desorption solution can be achieved by improved removal of entrainment from inner reactor surfaces and particles through e.g. a wash step between sorption and desorption or the structural avoidance of potential fluid traps and dead volumes (e.g. ending pipes like pipe of manometer and pressure sensor). To prevent a strong decrease in pressure during sorption, an initial reactor pressure close to the reinjection line pressure (e.g. ~ 18 bar in Bruchsal) during brine inflow and the installation of a pressure maintenance device may be favourable. To improve process monitoring and exact volume determination, the installation of flowmeters at the in- and outflows is suggested. Currently, the input of sorbent into the reactor is time-consuming and laborious. If a maintenance hatch was integrated into the reactor, the sorbent could be changed more easily. This is strongly recommended in future demonstrations or industrial plants.

2. Acknowledgements

We thank Ralf Wachter for helpful input and discussions regarding the design and construction of the pilot plant. For technical discussions, help and support during the construction and tests on site, we thank Robin Orant and Timo Laub. This research is part of the project “UnLimited”, which is funded by the German Federal Ministry for Economic Affairs and Energy under Grant O3EE4023D.

3. Bibliography

(1) Habib, K.; Hansdóttir, S. T.; Habib, H. Critical metals for electromobility: Global demand scenarios for passenger vehicles, 2015–2050. *Resources, Conservation and Recycling* 2020, *154*, 104603. DOI: 10.1016/j.resconrec.2019.104603.

(2) Xu, C.; Dai, Q.; Gaines, L.; Hu, M.; Tukker, A.; Steubing, B. Future material demand for automotive lithium-based batteries. *Commun Mater* 2020, *1* (1), 1–10. DOI: 10.1038/s43246-020-00095-x.

(3) USGS. *Mineral Commodity Summaries: Lithium*; Mineral Commodity Summaries, 2022.

(4) Schmidt, M. Rohstoffrisikobewertung - Lithium. - DERA Rohstoffinformationen 33, 2017.

(5) Kaya, E.; Zarrouk, S. J.; O'Sullivan, M. J. Reinjection in geothermal fields: A review of worldwide experience. *Renewable and Sustainable Energy Reviews* 2011, *15* (1), 47–68. DOI: 10.1016/j.rser.2010.07.032.

(6) Stober, I.; Bucher, K. *Geothermie*; Springer Berlin Heidelberg, 2012. DOI: 10.1007/978-3-642-24331-8.

(7) Haklıdır Tut, F. S.; Özen Balaban, T. A review of mineral precipitation and effective scale inhibition methods at geothermal power plants in West Anatolia (Turkey). *Geothermics* 2019, *80*, 103–118. DOI: 10.1016/j.geothermics.2019.02.013.

(8) Reich, R.; Slunitschek, K.; Danisi, R. M.; Eiche, E.; Kolb, J. Lithium Extraction Techniques and the Application Potential of Different Sorbents for Lithium Recovery from Brines. *Mineral Processing and Extractive Metallurgy Review* 2022, 1–20. DOI: 10.1080/08827508.2022.2047041.

(9) Safari, S.; Lottermoser, B. G.; Alessi, D. S. Metal oxide sorbents for the sustainable recovery of lithium from unconventional resources. *Applied Materials Today* 2020, *19*, 100638. DOI: 10.1016/j.apmt.2020.100638.

(10) Stringfellow, W. T.; Dobson, P. F. Technology for the Recovery of Lithium from Geothermal Brines. *Energies* 2021, *14* (20), 6805. DOI: 10.3390/en14206805.

(11) Warren, I. *Techno-Economic Analysis of Lithium Extraction from Geothermal Brines*. https://www.nrel.gov/docs/fy21osti/79178.pdf (accessed 2021-07-12).

(12) Ventura, S.; Bhamidi, S.; Hornbostel, M.; Nagar, A. *Selective recovery of Lithium from Geothermal Brines*. Publication number: CEC-500-2020-020; California Energy Commission, 2020.

(13) Slunitschek, K.; Eiche, E.; Kolb, J. Sorption of lithium and competing ions from geothermal brine to lithium manganese oxide sorbent and implication for industrial use. *Separation and Purification Technology* 2025, *378*, 134594. DOI: 10.1016/j.seppur.2025.134594.

(14) Sato, K.; Poojary, D. M.; Clearfield, A.; Kohno, M.; Inoue, Y. The Surface Structure of the Proton-Exchanged Lithium Manganese Oxide Spinels and Their Lithium-Ion Sieve

Properties. *Journal of Solid State Chemistry* 1997, *131* (1), 84–93. DOI: 10.1006/jssc.1997.7348.

(15) Mundhenk, N.; Huttenloch, P.; Sanjuan, B.; Kohl, T.; Steger, H.; Zorn, R. Corrosion and scaling as interrelated phenomena in an operating geothermal power plant. *Corrosion Science* 2013, *70*, 17–28. DOI: 10.1016/j.corsci.2013.01.003.

(16) Mundhenk, N.; Huttenloch, P.; Bäßler, R.; Kohl, T.; Steger, H.; Zorn, R. Electrochemical study of the corrosion of different alloys exposed to deaerated 80°C geothermal brines containing CO2. *Corrosion Science* 2014, *84*, 180–188. DOI: 10.1016/j.corsci.2014.03.027.

(17) Nitschke, F.; Scheiber, J.; Kramar, U.; Neumann, T. Formation of alternating layered Ba-Sr-sulfate and Pb-sulfide scaling in the geothermal plant of Soultz-sous-Forêts. *N. Jb. Miner. Abh.* 2014, *191* (2), 145–156. DOI: 10.1127/0077-7757/2014/0253.

(18) Iberl, P.; Alt, N. S. A.; Schluecker, E. Evaluation of corrosion of materials for application in geothermal systems in Central Europe. *Materials and Corrosion* 2015, *66* (8), 733–755. DOI: 10.1002/maco.201407864.

(19) Boch, R.; Leis, A.; Haslinger, E.; Goldbrunner, J. E.; Mittermayr, F.; Fröschl, H.; Hippler, D.; Dietzel, M. Scale-fragment formation impairing geothermal energy production: interacting H2S corrosion and CaCO3 crystal growth. *Geotherm Energy* 2017, *5* (1), 1–19. DOI: 10.1186/s40517-017-0062-3.

(20) Haas-Nüesch, R.; Heberling, F.; Schild, D.; Rothe, J.; Dardenne, K.; Jähnichen, S.; Eiche, E.; Marquardt, C.; Metz, V.; Schäfer, T. Mineralogical characterization of scalings formed in geothermal sites in the Upper Rhine Graben before and after the application of sulfate inhibitors. *Geothermics* 2018, *71*, 264–273. DOI: 10.1016/j.geothermics.2017.10.006.

(21) Krumgalz, B. S. Temperature Dependence of Mineral Solubility in Water. Part I. Alkaline and Alkaline Earth Chlorides. *Journal of Physical and Chemical Reference Data* 2017, *46* (4). DOI: 10.1063/1.5006028.

(22) Krumgalz, B. S. Temperature Dependence of Mineral Solubility in Water. Part 2. Alkaline and Alkaline Earth Bromides. *Journal of Physical and Chemical Reference Data* 2018, *47* (1). DOI: 10.1063/1.5010290.

(23) Krumgalz, B. S. Temperature Dependence of Mineral Solubility in Water. Part 3. Alkaline and Alkaline Earth Sulfates. *Journal of Physical and Chemical Reference Data* 2018, *47* (2). DOI: 10.1063/1.5031951.

(24) Kölbel, L.; Slunitschek, K.; Kaymakci, E.; Kölbel, T.; Reich, R.; Schneider, J. Lithium recovery from geothermal brines: An investigation into radioactive nuclide uptake on lithium-manganese-oxide (LMO) granules. *Hydrometallurgy* 2024, *224*, 106266. DOI: 10.1016/j.hydromet.2024.106266.

(25) Goldberg, V.; Winter, D.; Nitschke, F.; Held, S.; Groß, F.; Pfeiffle, D.; Uhde, J.; Morata, D.; Koschikowski, J.; Kohl, T. Upscaling Silica Treatment for Metal Extraction Processes in Operating Geothermal Plants. *SSRN Journal* 2023. DOI: 10.2139/ssrn.4359261.

(26) Harvianto, G. R.; Kim, S.-H.; Ju, C.-S. Solvent extraction and stripping of lithium ion from aqueous solution and its application to seawater. *Rare Met.* 2016, *35* (12), 948–953. DOI: 10.1007/s12598-015-0453-1.

(27) Yoshizuka, K. Lithium Recovery from Various Resources Using Ion Exchange. *Journal of Ion Exchange* 2018, *29* (2), 17–24. DOI: 10.5182/jaie.29.17.

(28) Joo, H.; Kim, S.; Kim, S.; Choi, M.; Kim, S.-H.; Yoon, J. Pilot-scale demonstration of an electrochemical system for lithium recovery from the desalination concentrate. *Environ. Sci.: Water Res. Technol.* 2020, *6* (2), 290–295. DOI: 10.1039/c9ew00756c.

(29) Al Radi, M.; Adil Al-Isawi, O.; Abdelghafar, A. A.; Fayez Abu Qiyas, A.; AlMallahi, M.; Khanafer, K.; Assad, M. E. H. Recent progress, economic potential, and environmental benefits of mineral recovery geothermal brine treatment systems. *Arab J Geosci* 2022, *15* (9). DOI: 10.1007/s12517-022-10115-4.

(30) BRGM. *EuGeLi: Lithium extraction from geothermal brines in Europe*. https://www.brgm.fr/en/current-project/eugAeli-lithium-extraction-geothermal-brines-europe (accessed 2022-03-23).

(31) Prairie Lithium. Prairie Lithium Commissions New Direct Lithium Extraction (DLE) Pilot Plant to Further De-Risk Commercial Deployment, 2022. pressurised

(32) Techint. *Tecpetrol developed a state-of-the-art Direct Lithium extraction pilot plant in collaboration with Techint E&C*.

(33) Cornish Lithium. *Pilot Plant for the Extraction of Lithium From Geothermal Waters*:*Basis of Design*. GEO3-REP-002. https://geocubed.co.uk/wp-content/uploads/2021/06/BoD-Rev-2.pdf (accessed 2023-03-21).

(34) Melnikov, S.; Sheldeshov, N.; Zabolotsky, V.; Loza, S.; Achoh, A. Pilot scale complex electrodialysis technology for processing a solution of lithium chloride containing organic solvents. *Separation and Purification Technology* 2017, *189*, 74–81. DOI: 10.1016/j.seppur.2017.07.085.

(35) McKibben, M.; Elders, W.; Raju, A. S. K. Lithium and Other Geothermal Mineral and Energy Resources Beneath the Salton Sea. In *Crisis at the Salton Sea: Research Gaps and Opportunities*; Salton Sea Task Force, Ed.; University of California Riverside, 2021; pp 74–85.

(36) Yoshizuka, K.; Kitajou, A.; Holba, M. Selective recovery of lithium from seawater using a novel MnO2 type adsorbent III-benchmark evaluation. *Ars Separatoria Acta* 2006, *4*, 78–85.

(37) Harrison, S.; Bruton, C.; Jenkins, D.; Dougherty, B.; Houston, J.; Viani, B.; Martin, S.; Mohanta, S.; Sharma, K.; Amine, K. *Technologies for Extracting Valuable Metals and Compounds from Geothermal Fluids.*:*Energy Research and Development Division. Final Project Report. Publication Number: CEC-500-2015-023.*

(38) EnBW. *EnBW and GEOLITH produce lithium in Bruchsal*. https://www.geothermal-lithium.org/en/node/112 (accessed 2023-03-21).

(39) Kölbel, L.; Kölbel, T.; Herrmann, L.; Kaymakci, E.; Ghergut, I.; Poirel, A.; Schneider, J. Lithium extraction from geothermal brines in the Upper Rhine Graben: A case study of potential and current state of the art. *Hydrometallurgy* 2023, *221*, 106131. DOI: 10.1016/j.hydromet.2023.106131.

(40) Lilac Solutions. *Lilac Solutions Celebrates Successful Completion of Kachi Demonstration Plant*. https://lilacsolutions.com/2023/12/lilac-solutions-celebrates-successful-completion-of-kachi-demonstration-plant/ (accessed 2024-01-22).

(41) Sanjuan, B.; Millot, R.; Innocent, C.; Dezayes, C.; Scheiber, J.; Brach, M. Major geochemical characteristics of geothermal brines from the Upper Rhine Graben granitic basement with constraints on temperature and circulation. *Chemical Geology* 2016, *428*, 27–47. DOI: 10.1016/j.chemgeo.2016.02.021.

(42) Fechner, D.; Kondek, M.; Kölbel, T.; Kolb, J. CO2 handling in binary geothermal systems - a modelling approach for different CO2 contents, salinity, pressure, and temperature. In *European Geothermal Congress 2022*; EGEC: Brussels, 2022.

(43) Verma, C.; Olasunkanmi, L. O.; Akpan, E. D.; Quraishi, M. A.; Dagdag, O.; El Gouri, M.; Sherif, E.-S. M.; Ebenso, E. E. Epoxy resins as anticorrosive polymeric materials: A review. *Reactive and Functional Polymers* 2020, *156*, 104741. DOI: 10.1016/j.reactfunctpolym.2020.104741.

(44) Baker, T. N. Processes, microstructure and properties of vanadium microalloyed steels. *Materials Science and Technology* 2009, *25* (9), 1083–1107. DOI: 10.1179/174328409X453253.

(45) Shi, X.; Zhou, D.; Zhang, Z.; Yu, L.; Xu, H.; Chen, B.; Yang, X. Synthesis and properties of Li1.6Mn1.6O4 and its adsorption application. *Hydrometallurgy* 2011, *110* (1-4), 99–106. DOI: 10.1016/j.hydromet.2011.09.004.

(46) Chitrakar, R.; Kanoh, H.; Miyai, Y.; Ooi, K. Recovery of Lithium from Seawater Using Manganese Oxide Adsorbent (H1.6Mn1.6O4) Derived from Li1.6Mn1.6O4. *Ind. Eng. Chem. Res.* 2001, *40* (9), 2054–2058. DOI: 10.1021/ie000911h.

(47) Robeson, L. M.; Smith, Z. P.; Freeman, B. D.; Paul, D. R. Contributions of diffusion and solubility selectivity to the upper bound analysis for glassy gas separation membranes. *Journal of Membrane Science* 2014, *453*, 71–83. DOI: 10.1016/j.memsci.2013.10.066.

(48) Wen, B.; Shi, Z.; Jessen, K.; Hesse, M. A.; Tsotsis, T. T. Convective carbon dioxide dissolution in a closed porous medium at high-pressure real-gas conditions. *Advances in Water Resources* 2021, *154*, 103950. DOI: 10.1016/j.advwatres.2021.103950.

(49) Liu, Y.; Hou, M.; Yang, G.; Han, B. Solubility of CO2 in aqueous solutions of NaCl, KCl, CaCl2 and their mixed salts at different temperatures and pressures. *The Journal of Supercritical Fluids* 2011, *56* (2), 125–129. DOI: 10.1016/j.supflu.2010.12.003.

Appendix

Table A1: List of the used components and material specifications. Material numbers after DIN 10027-2.

component	material/specification	properties/fabric
Bypass	stainless steel DIN 1.4571	DN 80, PN40
Bypass valves	body & ball: stainless steel DIN 1.4408 ball sealing: graphite-filled PTFE	DN 80; PN40
Container	-	6m · 2.4m ·2.6m (l · w · h)
Reactor	body: carbon steel DIN 1.0305 flanges: carbon steel DIN 1.0460	DN150; PN40
Blank flanges	stainless steel ASTM DIN 1.4571	
Reactor coating	TK®-236, Epoxy Novolac basis	150 – 500 µm thickness
Distributor plate	perforated plate: stainless steel ASTM DIN 1.4571 mesh: stainless steel DIN 1.4401	Distributor plate: height: 20 mm, pore size: 12 mm Mesh size: 250 µm
pH probe	high T, scaling and metal resistant, ORP: -1500 to +1500 mV	Rosemount™ 3300 HT
Pressure sensors	Ashcroft: model KXD DIN 1.4571 membrane: DIN 1.4542/1.4548	PN 200
Fluid pressure hose	synthetic rubber with steel wire reinforcement	PN 300-400
Garden hose	plastic/synthetic substance	GARDENA®; PN30
Stabilizing frame	wood	Screen printing plate
Leakage pan	wood and PVC	foil: 1mm thickness; 3mx4m wooden frame: 1.5mx3m
Recirculation pumps	peripheral impeller-type centrifugal pumps; body: stainless steel DIN 1.4581; impeller: SiC-coated DIN 1.4408; shaft Al_2O_3 ceramic; graphite sealing, flange: DIN 1.4404	Speck®, 28 m³/h flow rate; PN50, difference pressure 1.6 bar, suction inlet and pressure outlet 1/2”
Neutralization pump	membrane pump; medium-affected components: Hastelloy C276, membrane: PTFE	LEWA® model: LDB1; 30 L/h; PN 25
Ball valves with pneumatic actuator and magnetic valve	body & ball: stainless steel DIN 1.4408 ball sealing: graphite-filled PTFE	ball valve: PN 40 pneumatic actuator: control pressure 5.5 bar

Table A1 continued: List of the used components and material specifications. Material numbers after DIN 10027-2

component	material/specification	properties/fabric
Steel pipes	stainless steel	external diameter: 12 mm; wall thickness: 4 mm; PN353
Unidirectional valve	stainless steel	PN 400
Inert gas with pressure reducer	nitrogen (N_2) compressed, technical	gas bottle with 50 L, PN 200
Gas pressure hose	PVC fabric hose	PN 310
Fluid reservoirs	Plastic canisters	
Pressurized air	KAESER Typ SXC 3 compressor	
Automation	Siemens® SPS S7-1510	

Table A2: Analysis of commissioning experiment with three extraction cycles without sorbent in the reactor. “mean” refers to the average value over the three cycles. “m.u.%.” is the measurement uncertainty in %.

		sorption							desorption					
sample	unit	brine	buffered brine	c1	c2	c2	mean	m.u. %	0.5M HCl	c1	c2	c3	mean	m.u. %
As	mg/L	7.41	7.18	7.18	7.01	7.26	7.15	2.95	<0.005	0.19	0.15	0.15	0.16	2.95
B	mg/L	33.4	31.9	31.3	30.7	31.2	31.1	2.95	0.01	0.52	0.50	0.52	0.52	2.95
Ba	mg/L	8.76	8.50	8.43	8.46	8.41	8.43	3.43	<0.0001	0.28	0.28	0.29	0.28	3.43
Ca	mg/L	7213	6920	7109	6983	7128	7073	1.49	0.25	115	107	113	112	2.66
Cu	mg/L	0.01	0.01	0.03	0.02	0.01	0.02	1.82	0.0005	0.08	0.06	0.06	0.07	1.82
Fe	mg/L	43.7	42.9	42.6	42.9	42.7	42.7	4.43	0.03	3.44	4.15	5.16	4.25	4.43
K	mg/L	3139	2986	3078	3024	3095	3066	2.68	<0.06	49.9	46.5	48.9	48.4	4.55
Li	mg/L	159	154	153	153	153	153	1.97	0.01	2.54	2.37	2.48	2.47	2.89
Mg	mg/L	345	336	332	334	334	333	1.38	0.01	5.65	5.31	5.57	5.51	4.08
Mn	mg/L	22.6	22.0	21.8	21.9	21.8	21.8	3.88	<0.0005	0.52	0.49	0.51	0.50	4.03
Na	mg/L	34862	34033	34847	34599	35381	34943	2.40	<0.2	554	526	550	543	4.85
Pb	mg/L	3.02	3.06	3.06	3.08	3.14	3.09	2.42	0.0005	0.10	0.09	0.10	0.10	2.42
Rb	mg/L	24.1	23.3	23.0	22.7	23.0	22.9	1.09	<0.00003	0.35	0.33	0.35	0.34	1.09
S	mg/L	109	106	105	104	105	105	1.54	<0.009	1.87	1.77	1.82	1.82	5.53
Si	mg/L	40.4	39.2	38.9	38.7	39.1	38.9	1.13	0.09	0.65	0.59	0.59	0.61	8.88
Sr	mg/L	358	342	340	335	345	340	2.11	<0.0002	5.86	5.50	5.76	5.71	3.17
Zn	mg/L	14.0	13.7	13.6	13.5	13.7	13.6	1.82	0.03	0.25	0.22	0.23	0.23	1.82
V	mg/L	0.001	0.001	0.001	0.001	0.001	0.001	3.13	0.0004	0.001	0.002	0.003	0.002	3.13
Cr	mg/L	$<3*10^{-5}$	0.02	0.03	0.04	0.03	0.03	2.42	0.0005	0.23	0.41	0.61	0.42	2.42
Co	mg/L	0.01	0.70	0.01	0.56	0.58	0.38	1.93	0.0001	0.003	0.01	0.01	0.01	1.93

Table A2 continued: Analysis of commissioning experiment with three extraction cycles without sorbent in the reactor. “mean” refers to the average value over the three cycles. “m.u.%.” is the measurement uncertainty in %.

		sorption							desorption					
sample	unit	brine	buffered brine	c1	c2	c2	mean	m.u. %	0.5M HCl	c1	c2	c3	mean	m.u. %
Ni	mg/L	0.00	0.04	0.05	0.25	0.19	0.16	2.02	0.001	6.97	7.61	8.25	7.61	2.02
Cd	mg/L	0.08	0.07	0.07	0.07	0.07	0.07	1.63	<0.000001	0.001	0.001	0.001	0.001	1.63
Sb	mg/L	0.18	0.18	0.27	0.21	0.21	0.23	1.51	<0.00002	0.16	0.10	0.08	0.11	1.63
Cs	mg/L	11.8	11.7	11.7	11.6	11.9	11.7	2.58	<0.00001	0.19	0.18	0.19	0.19	2.58

Table A3: Element-Si ratio of brine and average loaded desorption solution after desorption step of blank experiment.

	As/Si	B/Si	Ba/Si	Ca/Si	Cu/Si	Fe/Si	K/Si	Li/Si	Mg/Si	Mn/Si	Na/Si	Pb/Si
brine mg/L	0.18	0.80	0.22	182	0.001	1.10	78.8	3.93	8.57	0.56	898	0.08
desorption mg/L	0.27	0.85	0.47	184	0.11	6.99	79.6	4.05	9.06	0.83	893	0.16
deviation from brine %	146	106	216	101	19992	636	101	103	106	148	99	205

	Rb/Si	S/Si	Si/Si	Sr/Si	Zn/Si	V/Si	Cr/Si	Co/Si	Ni/Si	Cd/Si	Sb/Si	Cs/Si
brine mg/L	0.59	2.69	1.0	8.74	0.35	0.00003	0.001	0.01	0.004	0.002	0.01	0.30
desorption mg/L	0.57	2.99	1.0	9.38	0.38	0.003	0.69	0.02	12.5	0.002	0.18	0.31
deviation from brine %	96	111	100	107	109	8230	82699	155	296670	120	3081	101

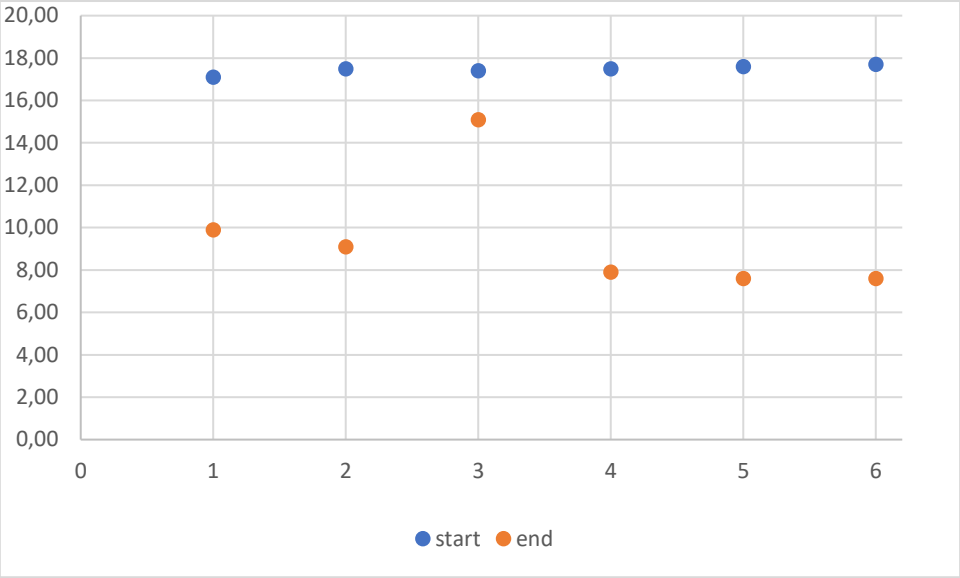

Figure A1: Start and end pressure of DLE functionality experiment

Table A4: Start and end pressure of each extraction cycle of DLE functionality experiment.

cycle	pressure [bar]	
	start	end
1	17.10	9.90
2	17.50	9.10
3	17.40	15.10
4	17.50	7.90
5	17.60	7.60
6	17.70	7.60

Table A5: Lithium concentration (c) in pristine brine and after sorption step and in desorption solution, corresponding sorption capacities (Q) and total Li extraction. “m.u.%” = measurement uncertainty.

	Sorption			Desorption		
cycle	c(Li) mg/L	Q(Li) mg/g	Extraction %	c(Li) mg/L	Q(Li) mg/g	Extraction %
Brine	161					
1	195	-1.02	-21.1	142	4.21	88.9
2	169	-0.25	-5.17	72.9	2.13	45.8
3	158	0.08	1.75	50.7	1.46	31.9
4	152	0.27	5.53	47.6	1.37	29.9
5	152	0.27	5.65	43.9	1.26	27.6
6	150	0.32	6.72	41.0	1.17	25.7
m.u.%	6.08	6.08		6.08	6.08	

8. On-site investigation of DLE performance from pressurised geothermal brine

8.1. Introduction

Laboratory-scale DLE research primarily focuses on basic research, especially the synthesis and description of the sorbent, sorbent immobilisation, sorption and desorption mechanisms, sorbent powder immobilisation and sorbent degradation (e.g. Reich et al., 2022; 2024; Herrmann et al., 2022; Slunitschek et al., 2025). This builds the foundation for the design and development of DLE processes and enables a first estimate of suitability for industrial application. In order to investigate the industrial applicability, process development and integration into a geothermal power plant, upscaled and on-site experiments are required. On-site and in-situ or on-line experiments can account for the differences in geothermal brine composition and condition, e.g. brine pressure, temperature, gas content, etc., not reflected by laboratory experiments. The upscaling allows for investigating hydrodynamic effects and sorbent stability, not or inadequately accounted for in small-scale experiments. Furthermore, upscaled on-line experiments focus on defining solutions for the extraction process and plant designs, rather than the basic mechanisms of the sorbent and sorption process. For the investigation of the DLE performance under conditions close to the ambient geothermal brine conditions, the pilot plant is connected to a bypass of the reinjection line of the geothermal power plant in Bruchsal, Germany. The LMO-based DLE performance is assessed on the extraction of Li and the purity of the desorption solution.

In general, fine LMO powder is used in laboratory-scale research (e.g. Chitrakar et al., 2001; Shi et al., 2011; Herrmann et al., 2022; Slunitschek et al., 2025). However, a small particle size is hardly applicable in high-flow-rate industrial applications, due to, amongst others, clogging of filters, particle agglomeration and high pressure drops in fixed bed reactors (Zhao et al., 2026). To solve this, LMO-containing macro-structures and larger particles can be created through various methodologies. Currently, especially foaming (e.g. Ma et al., 2011; Zhang et al., 2020), electrospinning (e.g. Park et al., 2014; Chung et al., 2017; Cheng et al., 2021; Ding et al., 2022), film casting on membranes (e.g. Zhu et al., 2014; Luo et al., 2022), coating on carrier materials (e.g. Hong et al., 2015; Ryu et al., 2019), composite carrier materials (e.g. Su et al., 2025) and granulation are investigated (Zhao et al., 2026). The currently most promising approach for industrial application is granulated particles (Zhao et al., 2026). For granulation, various materials, e.g. Al_2O_3, chitosan, PVC or PAM are used to create composite particles of LMO and the binder of determined size and porosity (e.g. Park et al., 2012b, 2012a; Xiao et al., 2012; Hong et al., 2013; Xiao et al., 2015; Ryu et al., 2016; Hong et al., 2018; Hong et al., 2019; Ryu et al., 2019). Xiao et al. (2015) created 0.3–0.7 mm-sized LMO granulates with

polyacrylamide, and Xiao et al. (2012) granulated particles of 2.0–3.5 mm diameter. Granulation offers an operationally simple and efficient process, but covering of the particle surface with binder matrix can result in blockage of binding sites, and thus decreased sorption capacity (Zhao et al., 2026). Furthermore, the mechanical strength of the material can be insufficient for industrial flow conditions, limiting the application (Zhao et al., 2026). Another, more unconventional approach of achieving bigger particles is the utilisation of larger MnO_2 particles as a synthesis educt. This approach is followed here. Due to the mesh size of the reactor sieves, LMO particles >250 µm are needed (Chapter 7). At the time of research, only two materials fulfilling this requirement were found on the global market: an electrolytic Mn dioxide with 250-850 µm and a Mn ore with 1–3 mm particle size, both distributed and provided free of charge by TROPAG, Oscar H. Ritter Nachf. GmbH. During synthesis for pre-experiments, the electrolytic MnO_2 disintegrated into fine particles and was therefore disregarded. Thus, the Mn ore was chosen for the experiments in the pilot plant. To fill the reactor (Chapter 7), 5.9 L of sorbent are needed, exceeding the in-house synthesis capacities. Thereby, primarily the hydrothermal synthesis step (Slunitschek et al., 2025) was the limiting factor, with a maximum effective volume of 0.3 L 4M LiOH and 15 g Mn_2O_3. To solve this, efforts were taken to buy $LiMnO_2$ to avoid the hydrothermal synthesis step or outsource the synthesis. However, at the time of research, $LiMnO_2$ was not available in larger quantities on the market. Additionally, no contract manufacturer, university or research facility capable or willing to synthesise the required amounts was found. Thus, synthesis was conducted in-house, resulting in a lower amount of sorbent than originally intended.

8.2. Methodology

Sorbent synthesis

The sorbent $Li_{1.6}Mn_{1.6}O_4$ is synthesised after Slunitschek et al. (2025) with coarse 1–3 mm diameter MnO_2 ore particles (Figure 8.1; NMD 253, TROPAG, Oscar H. Ritter Nachf. GmbH, 80% MnO_2). A total of 346 g of $Li_{1.6}Mn_{1.6}O_4$ is synthesised in two batches for the first calcination, 22 hydrothermal synthesis batches and five batches of the second calcination. The initial desorption of LMO is conducted in 7 batches with 0.5M HCl at a liquid-solid ratio of 50 mL per g LMO for 2 h under stirred conditions (1.25 RPM). Afterwards, the sorbent is washed with 0.05 L/g ultrapure water. Prior to analysis and experiments, the LMO batches are mixed and homogenised.

Figure 8.1: 1–3 mm big MnO_2 ore particles prior to synthesis.

Experiments

In total, five experiments were conducted in the pilot plant with the sorbent (Table A8.1), of which experiments 4 and 5 are evaluated. Experiment 4 is chosen due to its long runtime of 20 consecutive cycles. Experiment 5 is chosen due to 45 extraction cycles and the recycling of the desorption solution. An overview of the setup of all experiments is given in Table A8.1 in the Appendix, and a detailed description of experiments 4 and 5 is given below.

Prior to every experiment, the pilot plant is initialised by replacing all contained air with nitrogen and conducting three background extraction cycles with a sorption and desorption circulation time of one minute without sorbent. Afterwards, the sorbent is placed into the reactor through the pH probe inlet (Chapter 7).

After each of the five experiments, the sorbent is washed with 10 mL/g ultrapure water, dried at 60°C overnight, and a retain sample of ~4 g is taken. Afterwards, the sorbent is desorbed for 24 h with 10 mL/g 0.5M HCl to remove Li and other elements. After a second washing step with 10 mL/g ultrapure water and drying at 60°C overnight, another retain sample of ~1 g is taken.

In experiments 4 and 5, brine is buffered with a 4M acetate solution of pH = 5, containing 229.7 g Na acetate (pro analysis, Merck) and 102.9 mL acetic acid (pro analysis, Merck). The solution is injected into the inflowing brine at a pump rate of 8.3 mL/s, resulting in an overall injection of ~100 mL per 6.02 L total sorption solution volume. For desorption, 6.2 L of 0.5 M HCl is used. For sampling, aliquots of the effluent are collected using a transparent 2 L measuring cup, allowing visual assessment of solid particles in solution

In experiment 4, the extraction process consists of one sorption and desorption step. In both steps, the corresponding solution circulates for 5 min and 20 extraction cycles are conducted. The initial and final amounts of sorbent of experiment 4 are 146 g and 137 g. Thus, 9 g of sorbent is lost, whereby visually the loss is biggest in the first cycles and decreases continuously. In the last cycles, hardly any sorbent is visible in the discharged solutions. Since sorbent loss per cycle cannot be quantified, no sorbent mass correction is done, and the initial sorbent

mass is used for evaluation. Experiment 4 is primarily used for the investigation of the sorption of Li and competing elements and the purity of the desorption solution.

In Experiment 5, 45 extraction cycles are conducted over 5 days. In order to increase Li sorption, the circulation time for the sorption and desorption step is increased to 15 min. Based on the results of experiment 4, the plant is rinsed in a washing step with tap water after each step to increase desorption solution purity. Furthermore, the desorption solution is recycled over all cycles to increase Li concentration in the solution. For this, 22 L of desorption solution are stored in a canister connected to the desorption pump inlet and reactor outlet (Chapter 7). For desorption, 6.2 L of the desorption solution is pumped into the pilot plant, circulated and discharged into the canister after the circulation time, mixing with the remaining solution in the canister. The initial and final amounts of sorbent of experiment 5 are 128 g and 116 g. Thus, 12 g of sorbent are lost during the experiment, whereby visually the loss is biggest in the first cycles and decreases continuously. In the last cycles, hardly any sorbent is visible in the discharged solutions. Since sorbent loss per cycle cannot be quantified, no sorbent mass correction is done, and 116g of sorbent mass is used in the following evaluation. Samples are taken at cycles 1–10, 15–17, 20, 25–27, 30, 35, 39, 40 and 45, with a total sample volume of 3.66 L. Due to a wrong valve position, around 2 L of tap water flowed into the desorption canister before cycle 3, resulting in dilution of around 10%. At the end of the experiment, 17.9 L of the initially 22 L were left. Thus, in addition to sampling, additional desorption solution is lost in the extraction process, most likely as entrainment in the plant. Since this loss cannot be attributed to either specific cycles or moments during the experiment nor quantified per loss event, no volume correction is done. Thus, the starting volume of 22 L is used for evaluation and the calculation of key metrics. Experiment 5 is primarily used for the investigation of recycling of and purity of desorption solution.

In general, primarily the concentration data of the desorption solution is used for evaluation purposes, since the desorption solution will be further processed in an industrial plant. Thus, the absolute concentrations of Li and other elements in the desorption solution are instructive for the downstream processing. In order to determine the sorption by the sorbent alone, background correction is conducted using solution concentrations of the third background extraction cycle. In the case of experiment 5, the duration of the washing step needed to be adapted during the experiment. Therefore, the background extraction cycle prior to the experiment is averaged with one after the experiment and used as a reference.

To determine the extent of brine entrainment and cross-contamination of the desorption solution, element ratios of the uncorrected desorption solution and pristine brine are calculated. For experiment 4, Si is selected as the reference element, due to a nearly constant concentration across all cycles with low fluctuations of 1.3 ± 0.1 mg/L Si (Table A8.3). Furthermore, concentration differs only slightly between spent and pristine brine, with 37.9 ± 0.6 mg/L and

38.5 mg/L, respectively (Table A8.3). Silicon can precipitate under geothermal conditions, resulting in a decrease of the dissolved concentration (van den Heuvel et al., 2016). However. the low concentration change in the spent brine indicates that this effect would only be little, thus permitting the use of element ratios for the estimate of brine entrainment. Additionally, the desorption concentration shows only low fluctuations, with an average of 1.3 ± 0.1 mg/L Si. The element ratios are calculated for all cycles and averaged.

Sulphur is chosen for experiment 5 as a reference in the element ratios, as the concentrations in the spent brine are relatively constant over all cycles and close to the pristine brine, with 106 ± 2.1 mg/L and 110 mg/L, respectively (Table A8.4). Although S might be sorbed and accumulated by the sorbent (Figure 8.2), the accumulation is relatively little (Chapter 6).

An enrichment factor is calculated by normalising the desorption element ratio with the brine element ratio. The enrichment factor allows for the identification of metal enrichment or depletion in the desorption solution relative to the brine. An enrichment factor close to one shows similar element mass ratios in the desorption solution and the brine and indicates brine entrainment as the origin of these elements. Based on these elements, the brine entrainment volume can be estimated. The purity of the desorption solution is calculated as the mass ratio of Li to all contained cations.

For determination of solid chemistry via acid digestion, Mn ore is digested with a $HCl–H_2O_2$ digest after Slunitschek et al. (2025). For synthesis intermediate products, precursor, sorbent and sorbents after experiments, a microwave-assisted protocol (Multiwave 5000 20SVT50, Anton Paar; E38IA043EN-B, Anton Paar) of 2.5 mL 65% HNO3 (suprapur, Merck), 0.5 mL 30%(suprapur, Merck) and 2.5 mL ultrapure water per 0.1g solid is used.

Major and trace elements in all fluid samples are analysed with ICP-OES (iCap 7000, radial mode, Thermo Fisher Scientific) and ICP-MS (iCAP RQ, Thermo Fisher Scientific). The phase identification and attribution of the crystal structure of all solids are carried out with a D8 Discover diffractometer with CuKα radiation (Kα1 λ = 1.54060 Å and Kα2 λ = 1.5444 Å) by Bruker. Measurement is conducted from 2–82° 2θ at 0.02° increments and a measurement time of 0.6 s/step and evaluated with the software Bruker Diffrac.eva 4.1.1 and the database PDF-2, version 2002 (JCPDS-ICDD, 2002).

8.3. Results & interpretation

Synthesis

The educt Mn ore consists of MnO_2 (pyrolusite), $Mn_x^{2+}Mn_{1-x}^{4+}O_{2-2x}(OH)_{2x}$ (nsutite), $(Al_{0.75}Li_{0.25})MnO_2(OH)_2$ (lithiophorite), $K(Mn_7^{4+}Mn^{3+})O_{16}$ (cryptomelane), SiO_2 (quartz) and $Fe_2O_3*H_2O$ (goethite, Figure A8.1). Based on the diffractogram, the ore has an overall

crystallinity of around 46%. The ore is dominated by Mn with 513 mg/g, with elevated concentrations of Al (29.2 mg/g), Fe (24.4 mg/g) and Ba (2.8 mg/g, Table 8.1). Since the HCl–H_2O_2 digest is not able to dissolve Si, the amount of Si in the Mn ore is not determined.

The synthesised precursor is a heterogenous mixture of predominantly $Li_{1.6}Mn_{1.6}O_4$, $LiMnO_2$, Mn_2O_3 and $MnFeO_3$ (bixbyite), Fe_2O_3, and SiO_2, with a crystallinity of 63% (Figure A8.2). With a Li concentration of 56.3 mg/g (Table 8.1), the Li content deviates by 17.4% from the theoretical concentration of 68.1 mg/g. Reasons for the deviation are the incomplete synthesis and presence of the Fe and Si phases. Compared to Mn ore, Al, K, Fe and Ba show lower concentrations but are still present at 0.7–18.9 mg/g (Table 8.1).

After the initial desorption, the sorbent consists of the Li-rich spinel phase $(Li(Li_{0.17}Mn_{0.83})_2O_4$ (database entry PDF 88-0460), Mn_2O_3, $MnFeO_3$, Fe_2O_3, SiO_2, with a crystallinity of around 66% (Figure A8.3). The initial desorption resulted in stripping of only 52.4% of the Li contained in the precursor, explaining the presence of the Li-rich spinel phase. Thus, a Li concentration of 29.5 mg/g remained in the sorbent prior to the first experiment (Table 8.1). At initial desorption, Al, K and Ba were desorbed, resulting in a reduction of the concentration in the sorbent to 10.9 mg/g, 0.3 mg/g and 1.4 mg/g, respectively (Table 8.1). The concentrations of Si and Mn increased slightly, attributable to a relative concentration effect caused by the loss of Li and other elements. The increase in Fe concentration from 18.9 mg/g to 24.1 mg/g probably results from the sorbent heterogeneity and a higher Fe concentration in the digested grains.

The presence of Mn_2O_3 and $LiMnO_2$ in the precursor shows an incomplete transformation of Mn_2O_3 to $LiMnO_2$ in the hydrothermal step and of $LiMnO_2$ to $Li_{1.6}Mn_{1.6}O_4$ in the second calcination. These incomplete reactions most likely stem from the bigger particle size in comparison to the powder used in Slunitschek et al. (2025), requiring longer synthesis step durations. This applies most likely to the incomplete initial desorption as well. After the initial desorption, the sorbent has a Li concentration of 29.5 mg/g (Table 8.1), but after the first three experiments and the accompanying 24 h desorption processes, the remaining Li concentrations decrease to 2.2 mg/g prior to experiment 4 (Table 8.1, A8.2). The Li concentration before experiment 5 is 1.1 mg/g (Table 8.1, A8.2). This supports the interpretation that more time is required to achieve complete desorption.

Table 8.1: Major elements and Li of MnO_2 ore, precursor, initial sorbent and sorbent before experiment 4 and 5. Complete composition in Table A8.2. n.d.: not dissolved.

Material	Li	Al	Si	K	Mn	Fe	Ba
	mg/g	mg/g	mg/g	mg/g	mg/g	mg/g	mg/g
Mn ore	0.03	29.2	n.d.	3.4	513	24.4	2.8
precursor	56.3	13.4	3.0	0.7	505	18.9	1.7
sorbent	29.5	10.9	3.2	0.3	528	24.1	1.4
sorbent experiment 4	2.2	10.3	3.8	1.9	544	15.6	1.8
Sorbent experiment 5	1.1	6.9	2.0	1.3	546	21.3	0.8

Accumulation of competing elements

The initial Li concentration in the sorbent prior to the experiments decreases asymptotically over the course of all experiments (Table 8.1, Figure 8.2a). Lithium is released during the experiments, shown by the lower concentration at the end of an experiment in comparison to the start (Figure 8.2a). Additionally, Li is released during the 24 h desorption treatments, shown by the lower concentration before the following experiment (Figure 8.2a). Over the course of all experiments, the Li concentration is reduced to 0.9 mg/g after the last 24 h desorption after experiment 5 (Figure 8.2a). Thus, no accumulation of Li occurs at the sorbent. For Na, Mg, Al, Si, Ca, Ti, V, Cr, Fe, Co, Cu, Ni, Zn, Sr and Ba, no accumulation is observed either (Table A8.2). For Mn, determination of accumulation is not possible due to the dissolution during desorption (Slunitschek et al., 2025).

The S content of the sorbent is relatively constant over the first four experiments with 1.0 ± 0.01 mg/g, with most variations within the measurement uncertainty (Figure 8.2b, Table A8.2). After experiment 5, the concentration is increased to 1.09 mg/g and 1.13 mg/g after the 24 h desorption (Figure 8.2b). The latter increase is explained by sorbent heterogeneity, measurement uncertainty or relative concentration effect. An accumulation of S at the sorbent is possible, but the sorbent composition data is inconclusive.

The K content of the sorbent increases over the course of the experiments from 0.3 mg/g to 1.6 mg/g (Figure 8.2c). Sorbent concentration increases after experiments 1, 2, 3 and 5. For experiment 4, the starting concentration is particularly high and is probably an outlier. With the exception of experiments 1 and 3, K desorbs during the 24 h desorption, but to a lower extent than the previous increase in the according extraction cycles. This results in a net increase of the K content in the sorbent over all experiments. Although the powdered sorbent of Slunitschek et al., 2025 and Chapter 6 exhibits no strong K sorption, K accumulation and thus sorption is observed here (Figure 8.2c). This could potentially result from the sorption at the K-bearing mineral cryptomelane. While cryptomelane is identified in the XRD analysis of Mn ore, it is not detected in the sorbent, potentially due to a concentration below the detection limit of 3% (Figure A8.1, A8.3).

The As content in the sorbent increases continuously from 0.03 mg/g to 2.9 mg/g over all experiments (Figure 8.2d). The highest increase occurs in experiment 5 with a total accumulation of 2.0 mg/g As or 0.05 mg/g per cycle in average. The high total accumulation in comparison to the other experiments is attributed to the high number of 45 extraction cycles. Experiment 4 confirms the increase in total As accumulation with increasing number of cycles with an overall As accumulation of 0.4 mg/g or 0.02 mg/g per cycle. The different accumulation per cycle of experiment 4 and 5 is attributed to the lower sorption time in the first. During 24 h desorption, As concentration decrease is only negligible (Figure 8.2d). The high As capacity after experiment 2 (Figure 8.2d) is explained by sorbent heterogeneity, as the contents of Na,

Ti, V, Cr, Fe, Cu, Ni, Mo, Pb increase as well while the Mn content decreases (Table A8.3).

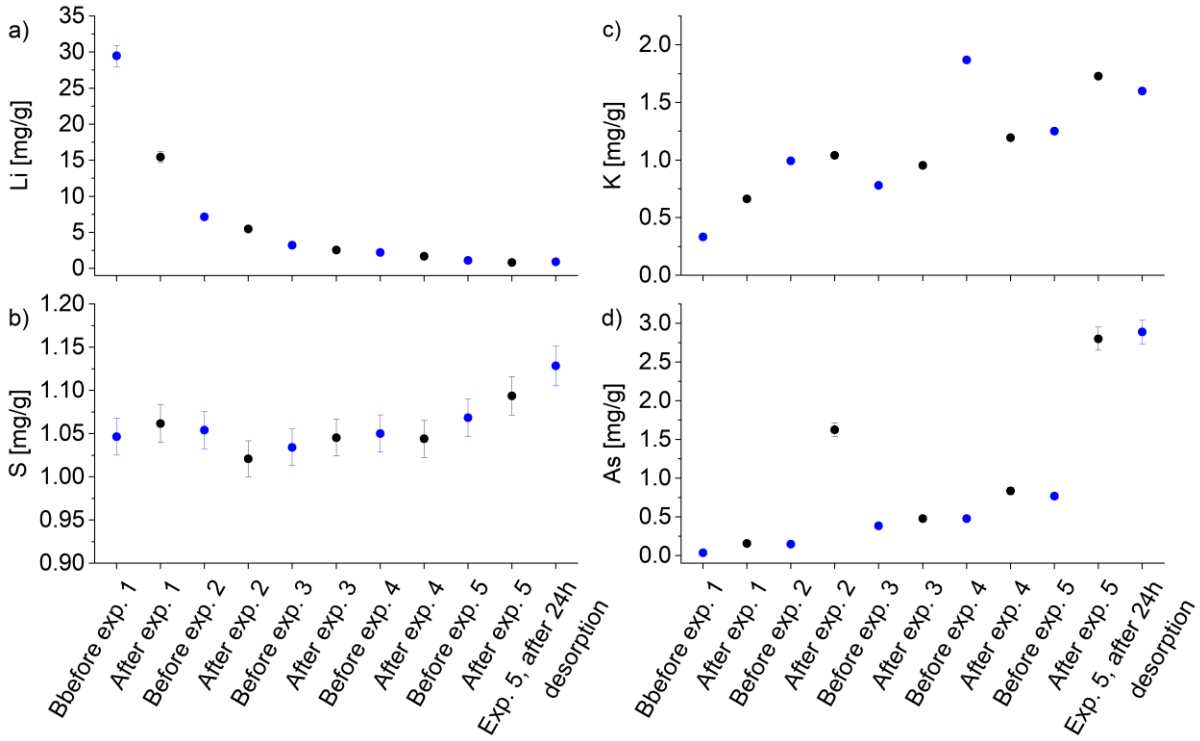

Figure 8.2: Concentration of Li and accumulating elements S, K and As in the sorbent over all experiments. Blue data points highlight the concentration prior to the designated experiment. The concentration before experiment 1 equals the initial sorbent composition. The y-axis of S does not start at 0 for visualisation reasons. “exp.” = experiment.

Molybdenum content in the sorbent increases over all experiments from <0.01 µg/g to 0.1 mg/g, with an outlier of 0.5 mg/g after experiment 2 (Figure 8.3a). The concentration increases continuously without loss during 24 h desorption, except for experiment 4, in which the concentration decreases from 0.024 mg/g to 0.018 mg/g during 24 h desorption (Table A8.2). Similarly to As, the accumulation increases with the number of extraction cycles, thus showing the highest accumulation in experiments 5 and 4. The pristine geothermal brine has a Mo concentration below the detection limit of <0.01 µg/L (experiment 4, Table A8.3), but shows increased concentrations of 0.005–0.01 mg/L in the spent brine of experiment 4 (Table A8.3). The same applies to Ni and Cr as well (Table A8.3). The origin for all three elements, Mo, Ni and Cr, is the corrosion of components of the pilot plant, as stated in Chapter 7.

The Pb concentration increases over all experiments from 0.01 mg/g in the pristine sorbent to 1.1 mg/g after the last 24 h desorption (Figure 8.3b). Similar to Mo, the concentration in the sorbent does not decrease significantly in the 24 h desorption steps, and the accumulation increases with increasing cycles.

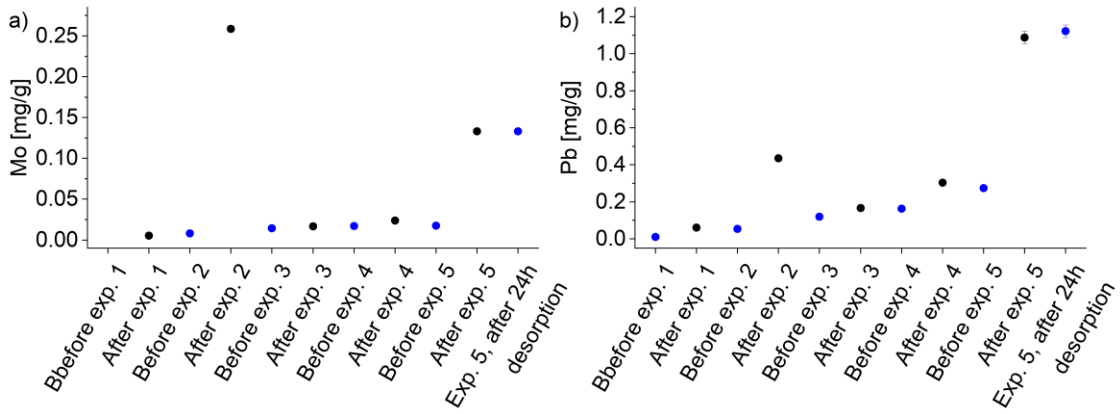

Figure 8.3: Concentration of Mo and Pb in the sorbent over all experiments. Blue data points highlight the concentration prior to the designated experiment. The concentration before experiment 1 equals the initial sorbent composition. “exp.” = experiment.

Sorption and accumulation of elements can potentially occur at the Fe phases contained in the sorbent as well (Figure A8.3). Thus, the sorption and accumulation cannot be attributed to the spinel phase without uncertainty. Nevertheless, since the LMO phase is the dominant phase (Figure A8.3) and Mn is the dominant element with a 26 times higher concentration than Fe, sorption at the spinel phase is most likely. However, this cannot be confirmed from the available data, and further analysis is required.

Recycling of the desorption solution

In order to evaluate the effect of recycling on the concentration of Li and competing elements in the desorption solution, the complete extraction process is regarded and not just the sorbent-related mechanisms. For this purpose, the measured solution concentrations from experiment 5 without blank correction are considered.

The total concentration of the desorption solution, the sum of all measured cations in solution, increases linearly with the number of cycles, with a Pearson correlation coefficient of 1.0 (Figure 8.4a). The average total concentration increase rate, given by linear interpolation of total concentration and cycle number, is 119 mg/L per cycle, with an $R^2 = 1.0$ (Table 8.2).

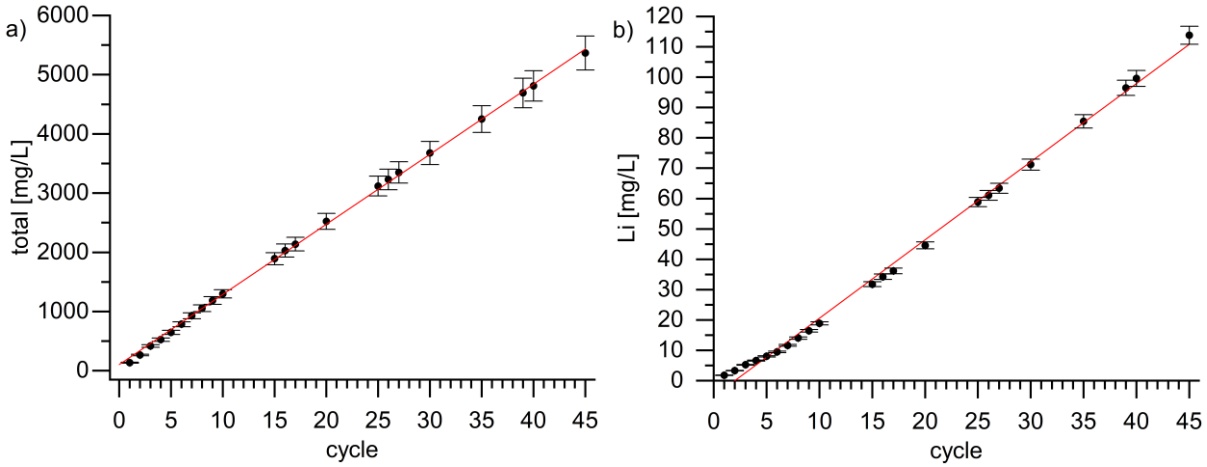

Figure 8.4: Development of total concentration (a) and Li concentration (b) in recycled desorption solution over 45 cycles. Red linear interpolation line for visualisation.

For all elements, the concentration is positively correlated with the number of cycles. The Pearson correlation coefficients of all elements are in the range of 0.98–1.00, except for Cu, Mo and Sb with 0.92, 0.86 and 0.94, respectively (Table 8.2, Figure A8.4). For Cu and Sb, the concentration increases asymptotically over the 45 cycles (Figure A8.4). The concentration of Mo increases asymptotically for the first 7 cycles and then follows a linear trend (Figure A8.4). The concentration of all other remaining elements increases linearly. Although Cu, Mo and Sb do not increase linearly or only partially, a linear slope is still used for calculation of the increase rate. This is justified with the consideration of the average development over all cycles and not a cycle-specific development. Overall, the increase rates vary between 0.001 mg/L per cycle for V and 68.4 mg/L per cycle for Na (Table 8.2).

The desorption solution is dominated by Na, Ca and K, with the highest increase rates per cycle of 68.4 mg/L, 18.1 mg/L and 11.9 mg/L, respectively (Table 8.2). Combined, the three elements account for 82.7% of total concentration increase per cycle. An additional 11.2% stems from combined Mn and Fe, with 8.2 mg/L per cycle and 5.1 mg/L per cycle, respectively (Table 8.2).

The Li concentration increases by 2.6 mg/L per cycle, accounting for 2.2% of the total increase per cycle (Table 8.2). Lithium increases linearly over all cycles, but with a shallower slope in the first five cycles than in cycles 7–45 (Figure 8.4b). The reason for the lower increase is unknown, but could potentially result from a lower Li concentration in the brine.

Table 8.2: Average concentration increase per cycle, based on the slope of linear interpolation of the desorption concentration, including R^2, and Pearson correlation coefficient of concentration and cycle number.

	Li	Na	Mg	Al	Si	S	K	Ca	V	Cr	Mn
increase rate [mg/(L*cycle)]	2.6	68.4	0.8	0.1	0.2	0.3	11.9	18.1	0.001	0.3	8.2
R^2	1.00	1.00	1.00	1.00	1.00	0.96	1.00	1.00	1.00	1.00	1.00
Pearson	1.00	1.00	1.00	1.00	1.00	0.98	1.00	1.00	1.00	1.00	1.00

	Fe	Ni	Cu	Zn	As	Sr	Mo	Sb	Ba	Pb	Total
increase rate [mg/(L*cycle)]	5.1	0.2	0.03	0.4	0.6	1.5	0.01	0.01	0.3	0.2	119
R^2	1.00	1.00	0.85	0.99	1.00	1.00	0.74	0.88	1.00	1.00	1.00
Pearson	1.00	1.00	0.92	1.00	1.00	1.00	0.86	0.94	1.00	1.00	1.00

Origin of impurities

The origin of impurities in the desorption solution is identified through element ratios and enrichment factors. The element ratios in the pristine brine range from $<2*10^{-7}$ for Mo to 932 for Na, and for the average desorption solution from 0.003 for V to 626 for Na (Table A8.3). The enrichment factors range from 0.7 for Na, Mg and Ca to >128,951 for Mo (Table A8.3). In addition to Mo, Cr, Co, and Ni show enrichment factors >100, showing that the desorption solution is highly enriched in these elements, relative to the brine. The high values result from the low concentration of these elements in the brine (Table 8.3, Table A8.3). In addition, Li, Al, V, Mn, Fe, Cu, Zn, As, Sb, Ba and Pb are relatively enriched in the desorption solution, with enrichment factors of 1.8–76.9 Mo (Table 8.3). Element ratios and enrichment factor of S could not be determined, as all desorption solutions show concentrations <0.1 mg/L (Table A8.3).

Table 8.3: Average element ratio of brine and desorption solution and resulting desorption solution enrichment factor of experiment 4. ">" indicates the usage of the detection limit in calculation. n.d.: not determined

	Li/Si	Na/Si	Mg/Si	Al/Si	Si/Si	S/Si	K/Si	Ca/Si	V/Si	Cr/Si	Mn/Si
Brine element ratio	4.0	932	8.6	0.01	1.0	n.d.	82.6	197	0.00004	0.0002	0.6
Desorption element ratio	7.0	626	6.0	0.3	1.0	n.d.	67.9	134	0.003	0.4	17.0
Enrichment factor	1.8	0.7	0.7	54.9	1.0	n.d.	0.8	0.7	76.9	1903	30.0

	Fe/Si	Co/Si	Ni/Si	Cu/Si	Zn/Si	As/Si	Sr/Si	Mo/Si	Sb/Si	Ba/Si	Pb/Si
Brine element ratio	1.1	0.0001	0.0004	0.001	0.4	0.2	10.0	$<2*10^{-7}$	0.01	0.2	0.1
Desorption element ratio	9.6	0.04	0.4	0.04	0.7	1.1	7.7	0.04	0.05	0.6	0.4
Enrichment factor	8.6	271	835	58.2	1.9	5.8	0.8	>128951	9.5	3.0	4.9

Only Na, Mg, K, Ca and Sr have enrichment factors around 1, with values of 0.7–0.8 (Table 8.3), showing similar element ratios in the brine and desorption solution. Furthermore, it indicates that the elements are dominantly introduced into the desorption solution through brine entrainment. However, the deviation of these enrichment factors by 0.2–0.3 from the value of 1 indicates that additional processes are responsible for the transport into the desorption solution, such as sorption at the sorbent (Chapter 5, 6). An average brine entrainment of 23.9 mL (0.024 L) brine per L desorption solution is calculated for these elements, at a range of 22.0–27.0 mL/L. For the 6.2 L desorption volume per cycle, this amounts to a total brine entrainment of 0.15 L. The entrainment results from incomplete brine discharge, brine-filled dead volumes, brine adhered to pilot plant and particle surfaces (see also Chapter 7).

The percentage of each element in the desorption solution originating from brine entrainment is assessed through the brine-correction of the average desorption solution concentration with the average brine entrainment (Table 8.4). The entrainment correction results in negative concentrations for Na, Mg and Ca and an entrainment origin percentage >100%. This originates from the lower enrichment factors compared to the average enrichment factor used to determine the brine entrainment volume (Table 8.4). Correspondingly, K and Sr have low corrected increase rates and high entrainment origin percentages of 89% and 94%, respectively.

Consequently, due to the high entrainment factors, V, Cr, Co, Ni, and Mo have especially low entrainment origin percentages, with 0.0004% to 0.3% (Table 8.4). For V, Cr, Ni and Mo, the dominant source is most likely corrosion of the pilot plant (Chapter 7). Similarly, Cu and Sb originate dominantly from potential pilot plant corrosion, but the entrainment origin percentage is increased in comparison to V, Cr, Ni and Mo, with 1.3% and 7.7%, respectively (Table 8.4). For Fe, brine entrainment is responsible for 8.4%, with the remaining Fe stemming from desorption of previously sorbed Fe, potentially Fe phase dissolution and pilot plant corrosion (Chapter 7). For Li, 41% originates from brine, showing that Li predominantly originates from the sorption process. The high selectivity of the sorbent for Zn, As, Ba and Pb (Slunitschek et al., 2025, Chapter 6) is reflected in the comparatively low entrainment origin percentages of 12–50%. Due to the Si and Al phases in the sorbent, Al and Si could predominantly originate from the sorbent as well. However, this remains uncertain.

Table 8.4: Average of measured desorption concentration, brine entrainment corrected concentration and percentage of element concentration originating from brine entrainment, for experiment 4. n.d.: not determined

	Li	Na	Mg	Al	Si	S	K	Ca	V	Cr	Mn
measured mg/L	8.9	790	7.6	0.4	1.3	<0.1	85.7	168	0.004	0.5	21.4
corrected mg/L	5.2	-67.0	-0.3	0.4	0.3	n.d.	9.8	-12	0.004	0.5	20.9
% entrainment	41	108	104	1.3	73	n.d.	89	107	0.95	0.04	2.4

	Fe	Co	Ni	Cu	Zn	As	Sr	Mo	Sb	Ba	Pb
measured mg/L	12.2	0.1	0.5	0.05	0.9	1.4	9.8	0.1	0.061	0.8	0.49
corrected mg/L	11.2	0.1	0.5	0.05	0.6	1.2	0.6	0.1	0.057	0.6	0.42
% entrainment	8.4	0.3	0.1	1.3	39	12	94	0.0004	7.7	24	15

Purity of desorption solution

The purity of the desorption solution is assessed through the ratio of Li concentration to total concentration. The total concentration of the desorption solution in the DLE process without intermediate wash step is 1110 mg/L, at a desorption solution volume of 6.2 L (Table 8.4). Based on the increase rates in experiment 5, the desorption solution in the DLE process with the intermediate wash step has a total concentration of 119 mg/L, at a desorption solution volume of 22 L (Table 8.2). Normalised to the 6.2 L desorption solution volume of the DLE process without the wash step, this corresponds to a normalised total concentration of 423 mg/L. Thus, the wash step results in a 62 wt.-% reduction in the total concentration of the desorption solution. Similarly to the overall reduction, Na, Mg, K and Ca concentrations are reduced by 69%, 64%, 51% and 62%, respectively (Figure 8.5a). The similarity in reduction of these elements to the overall reduction of 62% supports the brine entrainment origin. Furthermore, it shows that the wash step successfully reduces brine entrainment. In both solutions, Na, K and Ca are the dominant elements, accounting for a combined 94% of the total concentration in the solution without wash step and 83% in the solution with wash step (Figure 8.5, Table 8.2, 8.4). The elements predominantly originating from corrosion, V, Cr, Co, Ni; Cu, Mo and Sb, account for a combined 0.1 wt.-% of all elements in the desorption solution without wash step and for a combined 0.5 wt.-% for the solution with wash step.

The average Li concentration in the desorption solution of the DLE process without intermediate wash step is 8.9 mg/L, corresponding to a purity of 0.8% (Table 8.4). For the DLE process with the intermediate wash step, the average normalised Li concentration in the desorption solution is 9.1 mg/L, at a purity of 2.2%. In comparison to the Li purity of the geothermal brine of 0.3% (

Table A8.4), Li is successfully extracted with a 7-fold increase of purity. However, in comparison to the Li battery grade of >99.5 wt.-%, the maximum desorption solution purity is low. Furthermore, the maximum Li concentration of 9.1 mg/L has to be regarded as low as well, as it represents a dilution of the brine Li concentration by a factor of ~19.

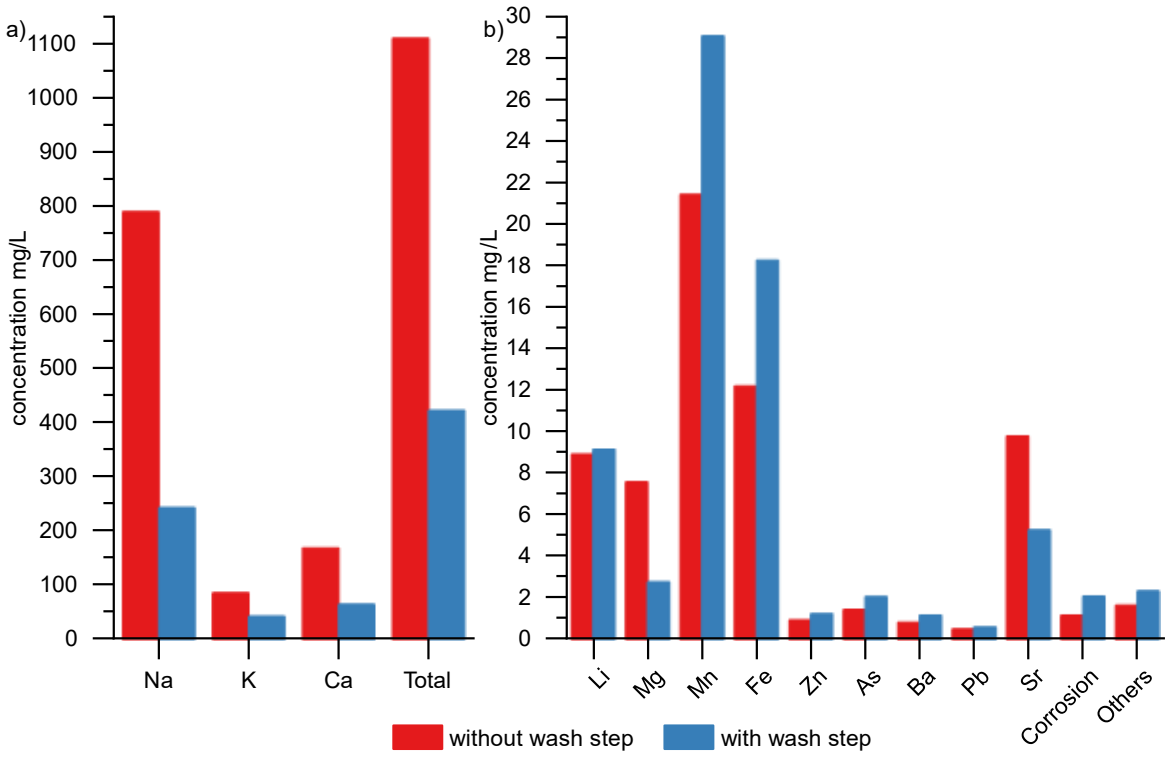

Figure 8.5: Composition of the desorption solution after DLE process without and with intermediate wash step (experiment 4 & 6, respectively). Group corrosion encompasses V, Cr, Co, Ni, Cu, Mo, Sb. Group others encompasses Al, Si, S. Data of experiment 6 normalised by volume.

For the DLE process with wash step, the average brine entrainment is 2.2 mL/L, based on the enrichment factors of Na, Mg and Ca (Table A8.5, A8.6). This corresponds to a normalised brine entrainment volume of 7.8 mL/L. Thus, the wash step reduces the average brine entrainment by 67%, from 23.9 mL/L desorption solution (experiment 4) to 7.8 mL/L. The deviation of 5% points to the 62% reduction in total concentration results from the inaccuracy of the determination of the brine entrainment volume.

Extraction of Lithium

In order to assess the Li extraction performance, the average relative Li extraction, Li sorption capacity and fractional occupancy of the sorbent are calculated for both experiments. In order to regard the whole DLE process in the pilot plant, measured concentrations in the desorption solution without any background corrections are used. To regard the sorption process of the sorbent alone, the parameters are calculated from the entrainment-corrected desorption concentration and increase rate, obtained from experiments 4 and 5, respectively. To calculate

the fractional occupancy of the sorbent, the Li concentration of the precursor of 56.3 mg/g is taken as the reference (Table 8.1). Sorption capacity and fractional occupancy are only calculated for the sorption process.

The Li extraction of the DLE process is similar in both experiments, with 5.9% extraction for experiment 4 and 5.6% for experiment 5 (Table 8.5). The difference is attributed to the higher Li concentration in experiment 5, with 169 mg/L compared to 155 mg/L in experiment 4 (Table A8.3). The sorbent-based extraction accounts for 3.3% and 4.8% extraction, thus contributing 55% and 85% to the Li extraction. The remaining 45% and 15% result from cross-contamination.

The sorption capacities are in a similar range, with 0.2 mg/g and 0.4 mg/g for experiment 4 and 5, respectively (Table 8.5). The difference is attributed to the longer contact time and the slightly higher Li concentration in the brine in experiment 5, with 15 min and 169 mg/L compared to 5 min and 155 mg/L in experiment 4 (Table A8.1, A8.3, A8.4. The sorption capacities correspond to a fractional occupancy of 0.4% and 0.7%, respectively (Table 8.5). Including the starting Li concentration in the sorbent of 2.2 mg/g and 1.1 mg/g (Table 8.1), 4.3% and 1.5% of binding sites are occupied, for experiment 4 and 5, respectively. Thus, 95.7% of the binding sites of the sorbent are unoccupied in experiment 4 and 98.5% in experiment 5. The lower fractional occupancy for experiment 5 despite higher Li sorption capacity results from the lower initial Li concentration in the sorbent.

Table 8.5: Average sorption capacity, Li extraction from brine and fractional occupancy of the DLE and sorption process.

	experiment 4		experiment 5	
	DLE	sorbent	DLE	sorbent
sorption capacity mg/g		0.2		0.4
extraction %	5.9	3.3	5.6	4.8
fractional occupancy %		0.4		0.7

8.4. Conclusion

The operability of the pilot plant is demonstrated by the successful DLE experiments under ambient conditions. Lithium is successfully extracted, and sorbent-based extraction is the dominant source for Li in the desorption solution. However, the sorbent is used inefficiently, and most binding sites remain unoccupied, resulting in a low Li sorption capacity. The low Li sorption performance potentially results from the comparably large sorbent particles. However, the sorbent shows high sorption and selectivity stability for Li and most regarded elements. To achieve higher Li concentrations, recycling of the desorption solution can compensate for low Li extraction performance by progressively enriching Li in the desorption. However, the purity of the desorption solution remains constant, as impurities are enriched progressively as well.

Due to the low Li concentration, the purity of the desorption solution is controlled by the concentration of impurities. In order to increase the purity, the Li concentration needs to increase, e.g. through a higher sorption capacity or more sorbent. Furthermore, in order to make use of the high-selectivity potential of the sorbent, cross-contaminating factors have to be minimised, especially the volume of brine entrainment.

Most of the impurities in the desorption solution are attributable to predominant sources: Na, Mg, S, K, Ca originate from entrainment; intermediate metals V, Cr, Ni, Cu, Mo, Sb and Fe from pilot plant corrosion and Li, Mn, Fe, Zn, As, Ba and Pb from sorption at the sorbent and Fe potentially from sorbent dissolution. The elements originating primarily from corrosion are of low importance for the purity, due to the low amount in solution. However, they can potentially be used to monitor the development of corrosion.

Potentially due to the large particle size, phase transformation of intermediate phases and initial desorption are incomplete. Thus, adaptations to both processes are required. Furthermore, accumulation of K, S, As, Mo and Pb at the sorbent indicates a high selectivity of the sorbent to these elements.

The calculation of element ratios of brine and desorption solution proves to be a valuable and simple tool. Even though the achieved accuracy is reduced, the ratios enable the estimation of brine entrainment volume and element origin well. Given the low requirements of only several analyses of brine and desorption solution and the simple and fast calculation, element ratios are a suitable tool for industrial and scientific application.

8.5. Appendix

Table A8.1: Overview over all conducted experiments in the pilot plant. Experiments 4 and 5 are evaluated in detail in this work. Desorption volume per cycle in experiment 5 is 6.18L.

Experi-ment	Volume		Time		Buffered	Number of cycles	Sorbent mass	
	Sorption	Desorption	Sorption	Desorption			start	end
	L	L	min	min			g	g
1	6.02	6.08	15	15	buffered	6	201	189
2	6.02	6.08	30	30	unbuffered	4	174	166
3	6.02	6.08	30	30	buffered	4	158	153
4	6.02	6.18	5	5	buffered	20	146	137
5	6.02	22	15	15	buffered	45	129	115

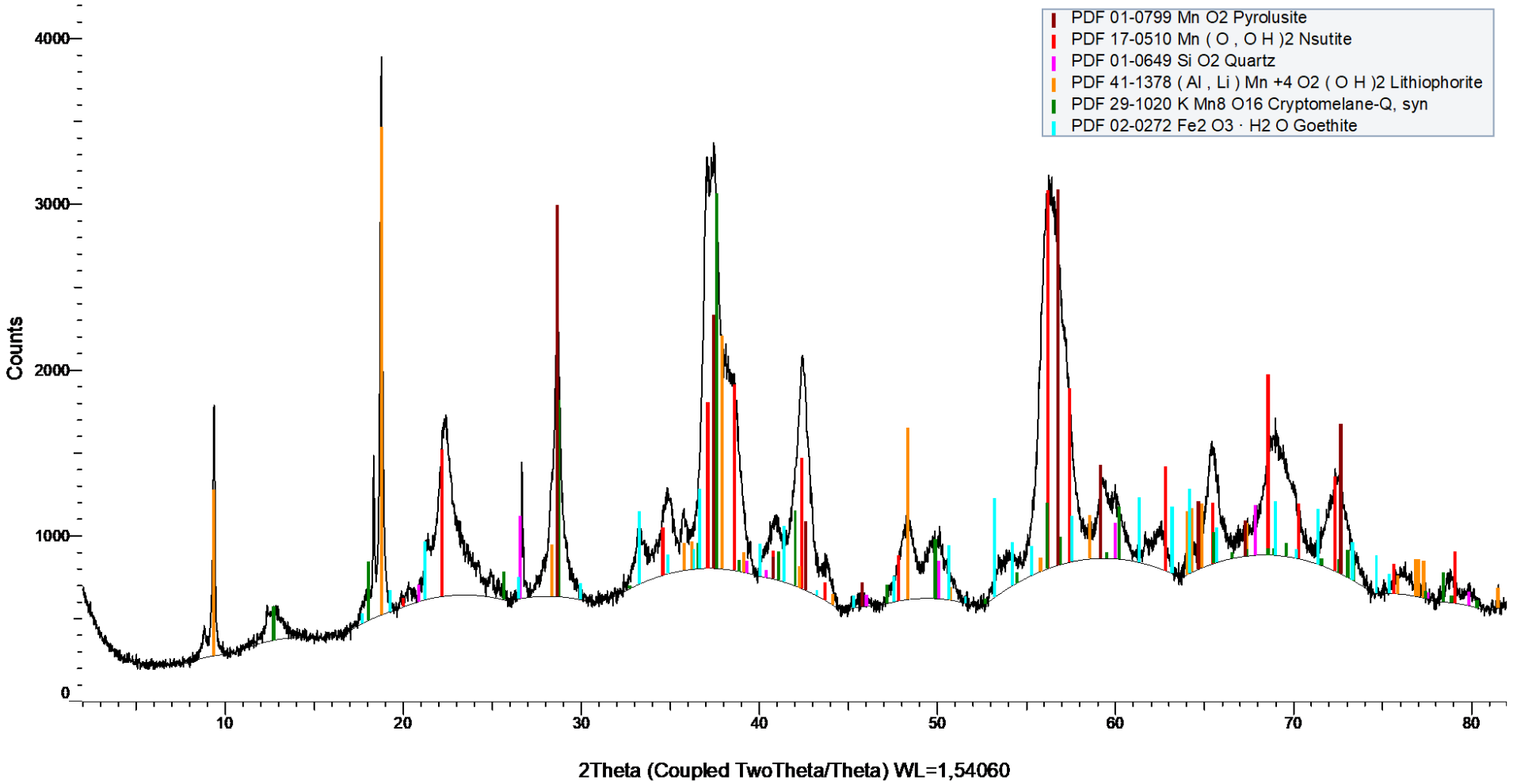

Figure A8.1: Diffractogram of MnO_2 ore prior to synthesis with attributed phases. Narrow black line at the bottom of phase bars represents background.

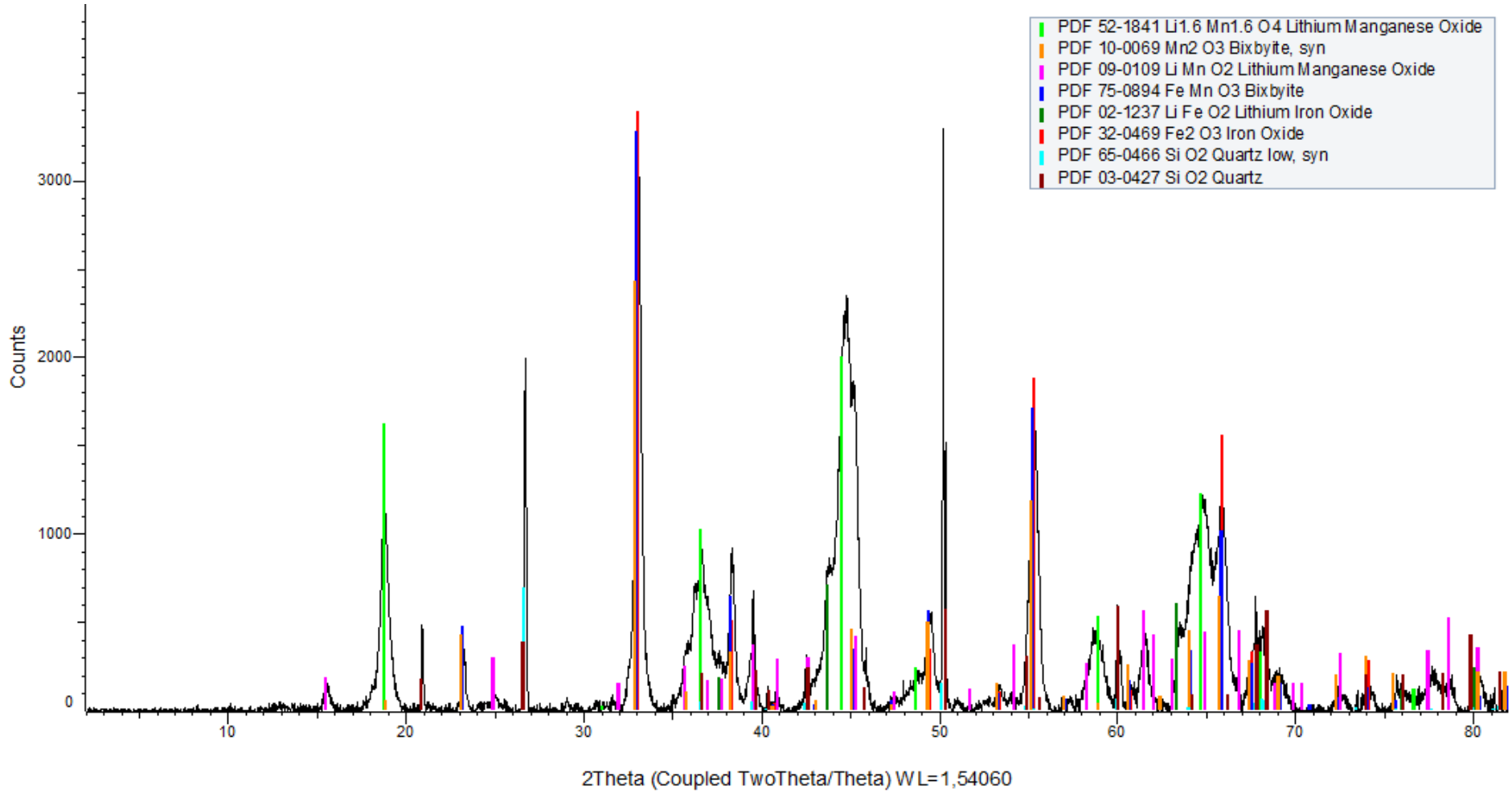

Figure A8.2: Diffractogram of precuros $Li_{1.6}Mn_{1.6}O_4$ with attributed phases. Narrow black line at the bottom of phase bars represents background.

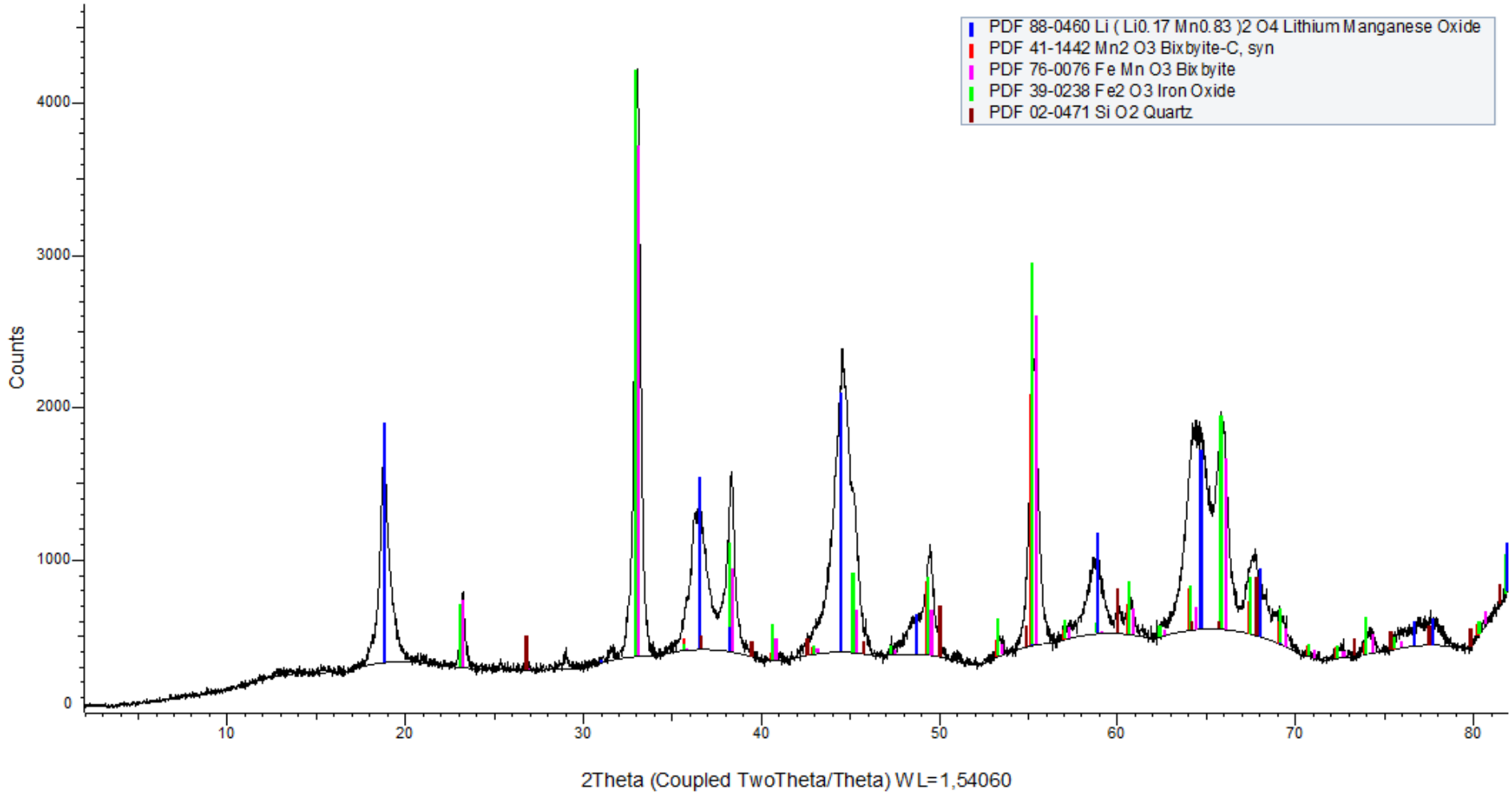

Figure A8.3: Diffractogram of sorbent with attributed phases. Narrow black line at the bottom of phase bars represents background.

Table A8.2: Chemical composition of Mn ore, precursor and sorbent before and after all experiments. “Start” refers to the sorbent after 24 h desorption. “End” refers to the sorbent after the experiment before 24 h desorption. “Ex5 after 24 h des” refers to the sample after the 24 h desorption and consecutive wash. m.u. = measurement uncertainty, n.a. = not analysed, ex = experiment. Values for m.u. are valid for the columns to the left until the next m.u. column.

	Mn ore	m.u.	Precursor	Initial sorbent ex1 start	ex1 end	ex2 start	ex2 end	ex3 start	ex3 end	ex4 start	ex4 end	ex5 start	m.u.	ex5 end	ex5 after 24 h des	m.u.
	mg/L	%					mg/L						%		mg/L	%
							Digest aqueous concentration									
Li	0.06	4.30	113	59.0	31.0	14.1	10.6	6.51	5.09	4.45	3.41	2.21	4.94	1.65	1.81	3.95
Na	0.33	3.19	0.20	0.08	0.18	0.10	0.29	0.12	0.18	0.13	0.21	0.26	4.88	0.35	<0.1	13.7
Mg	1.72	4.81	0.82	0.43	0.40	0.41	0.35	0.46	0.49	0.48	0.31	0.27	1.78	0.27	0.39	4.05
Al	63.1	4.36	26.8	21.8	18.7	20.3	17.8	16.9	16.6	20.4	16.4	13.8	2.34	14.5	14.8	2.34
S	n.a.	n.a.	2.42	2.10	2.13	2.08	1.97	2.09	2.09	2.09	2.11	2.12	2.04	2.19	2.25	2.01
Si	<0.003	0.89	6.04	6.40	5.42	6.36	4.85	3.99	3.58	7.55	3.38	3.87	2.53	3.32	3.87	2.53
K	7.33	7.67	1.45	0.67	1.34	1.96	2.01	1.58	1.91	3.72	2.42	2.49	0.50	3.46	3.19	3.85
Ca	1.08	4.17	1.27	0.91	1.11	0.75	0.79	0.77	0.74	0.64	0.61	0.73	2.61	1.48	0.72	3.47
Ti	n.a.	n.a.	0.72	0.81	0.65	0.77	1.49	0.72	0.66	0.61	0.73	0.69	0.59	0.86	0.70	0.59
V	n.a.	n.a.	0.10	0.12	0.10	0.12	0.20	0.13	0.11	0.11	0.12	0.11	1.58	0.12	0.14	1.58
Cr	n.a.	n.a.	0.07	0.02	0.02	0.03	0.54	0.04	0.03	0.04	0.03	0.03	3.08	0.10	0.08	3.08
Mn	1109	5.50	1009	1056	1112	1116	907	1099	1088	1084	1082	1087	4.97	1101	1109	2.68
Fe	52.7	4.59	37.8	48.2	34.2	48.0	162	40.4	31.2	31.1	41.1	42.4	1.46	41.6	41.2	3.67
Co	n.a.	n.a.	1.37	1.54	1.52	1.56	1.74	1.77	1.86	1.50	1.58	1.42	1.44	1.41	1.26	1.44
Cu	n.a.	n.a.	0.70	0.44	0.46	0.46	0.61	0.35	0.42	0.37	0.35	0.26	0.16	0.30	0.28	0.16
Ni	n.a.	n.a.	0.80	0.76	0.81	0.86	1.43	1.23	1.02	0.67	0.68	0.59	1.49	0.63	0.67	1.49
Zn	1.00	1.22	0.94	0.58	0.60	0.54	0.55	0.48	0.55	0.61	0.51	0.40	3.48	0.44	0.46	1.41
As	0.06	1.09	0.06	0.06	0.31	0.29	3.14	0.77	0.95	0.95	1.68	1.53	5.30	5.61	5.76	1.21
Sr	0.35	4.63	0.22	0.20	0.25	0.21	0.15	0.21	0.18	0.20	0.19	0.16	3.14	0.18	0.17	3.11
Mo	n.a.	n.a.	$<3*10^{-5}$	$<3*10^{-5}$	0.01	0.02	0.50	0.03	0.03	0.03	0.05	0.04	1.49	0.27	0.27	1.49
Pb	n.a.	n.a.	0.02	0.02	0.12	0.11	0.84	0.24	0.33	0.33	0.61	0.55	3.06	2.18	2.24	3.06
Ba	6.03	1.78	3.31	2.76	2.32	3.52	1.57	4.24	2.30	3.52	2.09	1.60	1.60	1.24	1.91	2.32

Table A8.2 continued.: Chemical composition of Mn ore, precursor and sorbent before and after all experiments. “Start” refers to the sorbent after 24 h desorption. “End” refers to the sorbent after the experiment before 24 h desorption. “Ex5 after 24 h des” refers to the sample after the 24 h desorption and consecutive wash. m.u. = measurement uncertainty, n.a. = not analysed, ex = experiment. Values for m.u. are valid for the columns to the left until the next m.u. column.

	Mn ore	m.u.	Precursor	Initial sorbent ex1 start	ex1 end	ex2 start	ex2 end	ex3 start	ex3 end	ex4 start	ex4 end	ex5 start	m.u.	ex5 end	ex5 after 24 h des	m.u.
	mg/g	%					mg/g						%		mg/g	%
							Digest solid concentration									
Li	0.03	4.30	56.3	29.5	15.4	7.14	5.47	3.22	2.55	2.23	1.69	1.11	4.94	0.82	0.91	4.94
Na	0.15	3.19	0.10	0.04	0.09	0.05	0.15	0.06	0.09	0.06	0.10	0.13	4.88	0.17	<0.05	4.88
Mg	0.80	4.81	0.41	0.22	0.20	0.21	0.18	0.23	0.24	0.24	0.15	0.14	1.78	0.14	0.20	1.78
Al	29.2	4.36	13.4	10.9	9.28	10.3	9.23	8.37	8.31	10.3	8.10	6.94	2.34	7.21	7.41	2.34
S	n.a.	n.a.	1.2	1.05	1.06	1.05	1.02	1.03	1.05	1.05	1.04	1.07	2.04	1.09	1.13	2.04
Si	<0.001	0.89	3.02	3.20	2.69	3.23	2.51	1.97	1.79	3.79	1.67	1.95	2.53	1.66	1.94	2.53
K	3.39	7.67	0.72	0.33	0.66	0.99	1.04	0.78	0.96	1.87	1.20	1.25	0.50	1.73	1.60	0.50
Ca	0.50	4.17	0.63	0.46	0.55	0.38	0.41	0.38	0.37	0.32	0.30	0.37	2.61	0.74	0.36	2.61
Ti	n.a.	n.a.	0.36	0.40	0.32	0.39	0.77	0.36	0.33	0.31	0.36	0.35	0.59	0.43	0.35	0.59
V	n.a.	n.a.	0.05	0.06	0.05	0.06	0.10	0.06	0.06	0.05	0.06	0.06	1.58	0.06	0.07	1.58
Cr	n.a.	n.a.	0.03	0.01	0.01	0.02	0.28	0.02	0.02	0.02	0.02	0.02	3.08	0.05	0.04	3.08
Mn	513	5.50	505	528	553	566	469	544	545	544	535	546	4.97	550	556	4.97
Fe	24.4	4.59	18.9	24.1	17.0	24.3	83.6	20.0	15.6	15.6	20.3	21.3	1.46	20.8	20.6	1.46
Co	n.a.	n.a.	0.69	0.77	0.76	0.79	0.90	0.88	0.93	0.75	0.78	0.71	1.44	0.70	0.63	1.44
Cu	n.a.	n.a.	0.35	0.22	0.23	0.23	0.31	0.17	0.21	0.19	0.17	0.13	0.16	0.15	0.14	0.16
Ni	n.a.	n.a.	0.40	0.38	0.40	0.44	0.74	0.61	0.51	0.34	0.33	0.29	1.49	0.32	0.33	1.49
Zn	0.46	1.22	0.47	0.29	0.30	0.27	0.28	0.24	0.28	0.30	0.25	0.20	3.48	0.22	0.23	3.48
As	0.03	1.09	0.03	0.03	0.16	0.15	1.63	0.38	0.47	0.48	0.83	0.77	5.30	2.80	2.89	5.30
Sr	0.16	4.63	0.11	0.10	0.13	0.11	0.08	0.10	0.09	0.10	0.09	0.08	3.14	0.09	0.09	3.14
Mo	n.a.	n.a.	<0.00001	<0.00001	0.01	0.01	0.26	0.01	0.02	0.02	0.02	0.02	1.49	0.13	0.13	1.49
Pb	n.a.	n.a.	0.01	0.01	0.06	0.05	0.44	0.12	0.17	0.16	0.30	0.27	3.06	1.09	1.12	3.06
Ba	2.79	1.78	1.66	1.38	1.16	1.79	0.81	2.10	1.15	1.77	1.03	0.80	1.60	0.62	0.96	1.60

Table A8.3: Sorption and desorption data of experiment 4. “m.u.%”=measurement uncertainty in %.

	Sorption																				
	Li	Na	Mg	Al	Si	S	K	Ca	V	Cr	Mn	Fe	Co	Ni	Cu	Zn	As	Sr	Mo	Sb	Ba	Pb
	mg/L																					
brine	155	35866	331	0.20	38.5	105	3178	7571	0.002	0.01	21.8	42.8	0.01	0.02	0.03	15.1	7.44	386	$<1*10^{-5}$	0.20	8.24	3.02
blank	151	35821	322	<0.0001	37.3	101	3100	7396	0.002	0.04	21.2	41.8	0.01	0.05	0.02	14.6	7.22	379	0.01	0.19	8.03	3.02
1	144	35558	320	0.22	36.9	100	3024	7255	0.002	0.11	20.1	36.2	0.01	0.21	0.03	13.9	5.94	376	0.01	0.18	7.47	2.57
2	146	35406	319	0.36	36.8	100	2975	7133	0.002	0.09	22.3	37.4	0.01	0.49	0.03	14.0	5.94	366	0.01	0.16	7.65	2.66
3	146	35385	324	0.16	37.5	101	3030	7264	0.002	0.06	19.5	34.1	0.13	0.25	0.02	14.0	5.41	370	0.01	0.14	7.55	2.43
4	146	35227	326	0.14	37.5	101	3028	7246	0.002	0.05	19.2	33.4	0.14	0.17	0.01	13.9	5.39	374	0.01	0.14	7.49	2.41
5	146	35088	324	0.13	37.6	101	3020	7233	0.002	0.05	19.3	34.0	0.11	0.15	0.02	14.0	5.47	370	0.01	0.13	7.56	2.45
6	146	35341	326	0.12	37.5	102	3040	7290	0.002	0.04	19.5	34.2	0.08	0.14	0.01	14.1	5.56	373	0.01	0.13	7.56	2.49
7	146	35189	326	0.11	37.5	102	3019	7241	0.002	0.05	19.6	34.6	0.08	0.16	0.01	14.2	5.66	365	0.01	0.13	7.56	2.52
8	145	35397	328	0.11	37.8	102	3032	7287	0.002	0.05	19.6	34.6	0.10	0.15	0.01	14.2	5.55	371	0.01	0.13	7.51	2.50
9	149	35260	332	0.13	38.3	104	3022	7237	0.002	0.05	20.1	35.4	0.14	0.16	0.01	14.5	5.80	369	0.01	0.13	7.73	2.54
10	149	35501	334	0.11	38.5	103	3061	7309	0.002	0.05	20.3	35.8	0.13	0.14	0.01	14.5	5.80	374	0.01	0.13	7.75	2.56
11	151	35156	335	0.38	38.6	103	3028	7257	0.002	0.09	25.9	37.2	0.27	0.21	0.03	14.6	5.73	370	0.01	0.13	7.89	2.69
12	150	35360	331	0.17	38.1	102	3005	7185	0.002	0.05	21.8	39.1	0.17	0.24	0.02	14.6	6.22	362	0.01	0.14	7.93	2.83
13	149	35265	331	0.10	38.4	102	3051	7304	0.002	0.05	20.4	36.2	0.20	0.29	0.01	14.4	5.74	372	0.01	0.12	7.78	2.69
14	151	35511	336	0.10	38.8	104	3077	7352	0.002	0.05	20.5	36.8	0.12	0.18	0.01	14.6	5.83	374	0.01	0.12	7.91	2.70
15	148	35347	332	0.08	38.3	103	3057	7299	0.002	0.05	20.2	36.3	0.14	0.16	0.01	14.5	5.81	372	0.01	0.12	7.72	2.77
16	147	35358	329	0.09	38.0	104	3046	7302	0.002	0.05	20.2	35.9	0.14	0.16	0.01	14.6	5.90	367	0.01	0.13	7.69	2.77
17	143	35485	324	0.09	37.4	102	3056	7316	0.002	0.05	19.8	35.1	0.14	0.15	0.01	14.3	5.74	374	0.01	0.12	7.50	2.78
18	144	35233	326	0.10	37.6	103	3036	7299	0.002	0.05	20.1	35.7	0.11	0.14	0.01	14.4	5.88	371	0.01	0.13	7.58	2.79
19	149	35037	333	0.10	38.4	103	3040	7250	0.003	0.05	20.6	36.7	0.12	0.14	0.01	14.4	5.97	374	0.01	0.13	7.82	2.80
20	153	35062	338	0.09	39.1	105	3033	7274	0.002	0.06	21.1	37.7	0.12	0.15	0.01	14.7	5.99	369	0.01	0.12	8.04	2.83
m.u.%	3.72	1.24	1.83	6.22	2.83	2.96	1.42	3.00	2.58	2.51	2.76	3.06	4.16	3.16	4.51	4.10	3.35	3.03	1.15	3.44	2.03	2.90

Table A8.3 continued: Sorption and desorption data of experiment 4. “m.u.%”=measurement uncertainty in %.

	Desorption																				
	Li	Na	Mg	Al	Si	S	K	Ca	V	Cr	Mn	Fe	Co	Ni	Cu	Zn	As	Sr	Mo	Sb	Ba	Pb
	mg/L																					
HCl	$<7*10^{-4}$	0.48	0.003	0.003	0.004	<0.1	<0.3	0.04	0.001	0.0003	0.0004	<0.002	$1*10^{-5}$	0.0002	$<4*10^{-5}$	0.004	<0.004	0.0002	$<1*10^{-5}$	<0.00001	0.0003	0.0001
Blank	2.30	527	5.06	0.01	0.61	1.42	45.4	107	0.001	0.14	0.41	1.69	0.002	0.26	0.03	0.26	0.16	5.47	0.02	0.10	0.15	0.06
1	8.62	760	7.23	0.65	1.23	<0.1	80.7	161	0.004	0.26	29.8	8.0	0.05	0.43	0.10	0.82	0.67	9.04	0.03	0.09	0.80	0.28
2	7.48	716	6.79	0.50	1.10	<0.1	77.0	151	0.003	0.23	22.7	6.8	0.03	0.34	0.08	0.69	0.72	8.47	0.03	0.07	0.68	0.27
3	9.31	808	7.68	0.44	1.32	<0.1	87.4	171	0.004	0.26	24.4	12.7	0.05	0.36	0.07	1.00	1.40	9.85	0.03	0.08	0.92	0.50
4	9.45	805	7.67	0.38	1.35	<0.1	87.0	171	0.004	0.31	23.4	13.0	0.05	0.37	0.06	1.04	1.57	9.94	0.03	0.07	0.93	0.54
5	9.44	815	7.79	0.32	1.32	<0.1	87.8	174	0.004	0.34	22.5	12.9	0.05	0.39	0.06	1.05	1.61	10.1	0.03	0.07	0.92	0.55
6	9.39	804	7.66	0.34	1.29	<0.1	87.1	171	0.004	0.38	22.6	13.0	0.05	0.40	0.05	1.02	1.61	9.98	0.04	0.07	0.90	0.56
7	9.24	800	7.64	0.34	1.27	<0.1	86.8	170	0.004	0.39	21.8	12.8	0.04	0.40	0.05	1.02	1.62	9.94	0.04	0.06	0.87	0.53
8	9.33	810	7.72	0.33	1.29	<0.1	87.9	172	0.003	0.39	21.6	12.6	0.04	0.41	0.05	1.00	1.61	10.1	0.04	0.06	0.86	0.53
9	9.28	820	7.82	0.33	1.28	<0.1	88.6	174	0.004	0.47	20.9	12.9	0.05	0.45	0.04	1.00	1.60	10.2	0.05	0.06	0.85	0.52
10	9.18	812	7.78	0.33	1.29	<0.1	87.8	173	0.004	0.45	20.7	12.8	0.05	0.44	0.04	0.99	1.58	10.1	0.05	0.06	0.82	0.53
11	8.78	782	7.50	0.34	1.24	<0.1	85.0	166	0.005	0.75	24.2	13.7	0.06	0.62	0.05	0.89	1.40	9.58	0.06	0.06	0.79	0.49
12	6.95	696	6.67	0.27	1.04	<0.1	75.7	147	0.004	0.50	18.2	8.57	0.04	0.44	0.04	0.63	0.96	8.33	0.05	0.04	0.57	0.34
13	8.58	777	7.49	0.30	1.24	<0.1	84.7	166	0.004	0.51	18.7	12.4	0.05	0.46	0.04	0.88	1.42	9.65	0.05	0.05	0.75	0.48
14	9.01	799	7.78	0.30	1.29	<0.1	87.1	171	0.004	0.50	19.4	12.9	0.05	0.46	0.04	0.94	1.53	10.0	0.05	0.05	0.79	0.52
15	9.03	804	7.82	0.34	1.33	<0.1	87.4	173	0.004	0.52	19.2	12.9	0.05	0.47	0.04	0.95	1.53	10.1	0.05	0.05	0.79	0.53
16	9.18	810	7.83	0.35	1.30	<0.1	88.4	174	0.005	0.61	20.1	13.6	0.05	0.54	0.04	0.95	1.54	10.1	0.07	0.06	0.80	0.53
17	9.08	797	7.69	0.36	1.29	<0.1	87.1	171	0.004	0.65	20.0	13.5	0.05	0.55	0.04	0.94	1.55	10.0	0.07	0.05	0.79	0.52
18	9.02	789	7.60	0.32	1.29	<0.1	86.5	170	0.005	0.66	19.9	13.4	0.05	0.55	0.04	0.94	1.56	9.92	0.07	0.05	0.78	0.52
19	8.90	797	7.68	0.33	1.26	<0.1	86.8	171	0.004	0.63	19.2	13.0	0.05	0.54	0.04	0.93	1.50	10.0	0.07	0.05	0.76	0.51
20	8.90	796	7.68	0.33	1.25	<0.1	86.8	171	0.004	0.58	18.9	12.6	0.05	0.51	0.04	0.92	1.48	10.0	0.06	0.06	0.75	0.51
m.u.%	4.08	1.39	5.24	5.69	3.91	2.96	1.05	3.00	3.05	4.17	2.76	3.06	2.04	2.02	3.44	4.10	3.35	3.03	2.96	2.49	2.03	1.37

Table A8.4: Sorption and desorption data of experiment 5. “m.u.%”=measurement uncertainty in %.

	Sorption																					
	Li	Na	Mg	Al	Si	S	K	Ca	Co	V	Cr	Mn	Fe	Ni	Cu	Zn	As	Sr	Mo	Sb	Ba	Pb
	mg/L																					
brine	169	36868	342	<0.0001	37.9	110	3313	7466	0.01	$<1.5*10^{-5}$	$<3*10^{-5}$	22.9	40.8	0.01	0.03	15.1	8.96	356	<4*10-5	0.19	8.73	3.23
blank start	171	36574	345	<0.0001	38.1	111	3282	7445	0.11	$<1.5*10^{-5}$	0.03	23.2	42.0	0.10	0.05	15.0	8.90	358	<0.00004	0.26	8.79	3.22
blank end	167	36546	339	<0.0001	37.3	109	3235	7298	0.02	$<1.5*10^{-5}$	0.03	22.7	40.5	0.06	0.02	14.7	8.71	352	<0.00004	0.11	8.59	3.14
1	159	35988	333	0.43	36.4	107	3187	7279	0.17	$<1.5*10^{-5}$	0.14	20.8	25.8	0.44	0.13	14.4	4.63	349	<0.00004	0.18	7.92	2.27
2	159	35761	333	0.38	36.4	107	3180	7248	0.13	$<1.5*10^{-5}$	0.06	21.2	34.3	0.18	0.10	14.4	6.99	347	<0.00004	0.18	8.10	2.72
3	160	36059	337	0.13	36.6	108	3221	7313	0.13	$<1.5*10^{-5}$	0.09	18.3	26.1	0.50	0.10	14.3	4.53	348	<0.00004	0.14	7.93	2.28
4	150	33636	317	0.39	34.5	103	3000	6875	0.21	$<1.5*10^{-5}$	0.07	17.7	25.7	1.49	0.05	13.4	4.67	328	<0.00004	0.12	7.44	2.16
5	158	35595	330	0.21	36.1	106	3166	7232	0.09	$<1.5*10^{-5}$	0.03	20.6	32.4	0.30	0.04	14.3	6.23	339	<0.00004	0.10	8.09	2.82
6	160	35911	333	0.16	36.6	108	3185	7280	0.02	$<1.5*10^{-5}$	0.02	20.4	32.5	0.08	0.03	14.5	6.25	350	<0.00004	0.11	8.13	2.75
7	158	36206	332	<0.0003	36.5	108	3197	7265	0.17	$<1.5*10^{-5}$	0.08	17.4	26.7	1.02	0.02	13.9	5.07	348	<0.00004	0.10	7.70	2.30
8	156	36354	332	<0.0003	36.3	108	3200	7257	0.12	$<1.5*10^{-5}$	0.06	16.8	26.7	0.44	0.02	13.6	5.09	345	<0.00004	0.10	7.47	2.20
9	157	36323	334	<0.0003	36.3	106	3219	7299	0.11	$<1.5*10^{-5}$	0.06	17.1	26.2	0.31	0.01	13.7	5.02	347	<0.00004	0.10	7.58	2.15
10	152	35736	328	<0.0003	35.6	105	3152	7132	0.12	$<1.5*10^{-5}$	0.07	16.7	26.6	0.33	0.01	13.2	5.06	340	<0.00004	0.10	7.27	2.17
15	154	36080	330	<0.0003	36.0	106	3154	7147	0.12	$<1.5*10^{-5}$	0.10	18.8	32.4	0.19	0.02	13.4	6.56	342	<0.00004	0.12	7.54	2.59
16	153	34744	329	0.09	35.5	106	3072	6961	0.23	$<1.5*10^{-5}$	0.15	17.0	28.6	2.33	0.01	13.2	5.43	337	<0.00004	0.07	7.33	2.22
17	154	35378	329	<0.0003	35.8	106	3110	7040	0.10	$<1.5*10^{-5}$	0.08	19.1	33.0	0.18	0.02	13.5	6.80	339	<0.00004	0.12	7.60	2.63
20	155	35448	333	<0.0003	36.1	108	3142	7102	0.12	$<1.5*10^{-5}$	0.10	17.6	27.4	0.33	0.34	13.4	5.30	341	<0.00004	0.08	7.42	2.25
25	155	36060	332	<0.0003	36.1	108	3204	7234	0.09	$<1.5*10^{-5}$	0.15	17.3	26.5	0.33	0.01	13.3	5.10	343	<0.00004	0.10	7.34	2.10
26	147	34291	318	0.10	34.4	102	3047	6914	0.17	$<1.5*10^{-5}$	0.16	16.7	28.3	1.89	0.01	12.6	5.26	325	<0.00004	0.11	7.05	2.11
27	155	35533	329	<0.0003	36.1	105	3149	7128	0.06	$<1.5*10^{-5}$	0.11	20.0	34.0	0.17	0.02	13.6	6.99	343	<0.00004	0.12	7.72	2.64
30	154	35754	332	<0.0003	35.9	106	3183	7181	0.13	$<1.5*10^{-5}$	0.15	17.4	26.4	0.34	0.01	13.1	5.07	346	<0.00004	0.10	7.31	2.12
35	155	35585	335	<0.0003	36.2	107	3163	7146	0.11	$<1.5*10^{-5}$	0.17	17.8	26.7	0.34	0.01	13.2	5.03	342	<0.00004	0.10	7.35	2.14
39	143	33581	314	<0.0003	33.5	99	2996	6756	0.15	$<1.5*10^{-5}$	0.10	16.3	25.7	1.01	0.01	12.3	5.07	318	<0.00004	0.10	6.87	2.02
40	154	35578	334	<0.0003	35.6	106	3174	7149	0.11	$<1.5*10^{-5}$	0.15	18.4	27.4	0.38	0.01	13.3	5.41	337	<0.00004	0.10	7.40	2.23
45	154	35864	335	0.09	35.8	106	3215	7218	0.05	$<1.5*10^{-5}$	0.18	18.7	27.2	0.34	0.01	13.2	5.36	343	<0.00004	0.11	7.39	2.25
m.u.%	2.60	2.82	4.05	0.51	1.68	0.86	0.99	4.46	2.28	5.30	4.89	4.38	7.02	3.78	4.62	2.75	1.34	4.33	1.41	1.58	3.52	1.42

Table A8.4 continued: Sorption and desorption data of experiment 5. “m.u.%”=measurement uncertainty in %. “Pure HCl” indicates the pristine desorption solution

	Desorption solution																					
	Li	Na	Mg	Al	Si	S	K	Ca	Co	V	Cr	Mn	Fe	Ni	Cu	Zn	As	Sr	Mo	Sb	Ba	Pb
	mg/L																					
pure HCl	0.01	0.68	<0.001	0.003	<0.004	<0.01	<0.4	0.03	$<2*10^{-6}$	0.0003	0.0002	<0.0004	<0.002	0.0001	$<6*10^{-5}$	0.002	<0.004	<0.0001	$<4*10^{-5}$	$<7*10^{-5}$	<0.0001	0.0001
blank start	0.49	115	6.80	0.01	1.97	11.0	11.8	68.1	0.00	0.001	0.13	0.11	1.11	0.15	0.11	0.1	0.12	1.32	0.02	0.13	0.19	0.05
blank end	1.01	195	2.03	0.05	0.28	0.86	17.3	40.4	0.01	0.004	0.75	0.63	4.07	0.35	0.01	0.1	0.13	2.04	0.04	0.02	0.17	0.07
1	1.78	80	0.86	0.28	0.35	1.08	11.3	19.0	0.03	0.003	0.31	12.6	5.67	0.27	0.27	0.3	0.58	1.11	0.02	0.07	0.24	0.16
2	3.34	162	1.74	0.48	0.58	1.11	23.2	37.4	0.05	0.004	0.58	22.4	9.53	0.50	0.46	0.3	0.98	2.22	0.04	0.11	0.44	0.27
3	5.23	255	2.73	0.58	0.89	1.55	36.5	58.7	0.08	0.006	0.84	32.0	15.1	0.72	0.60	0.5	1.75	3.54	0.06	0.15	0.68	0.44
4	6.57	312	4.04	0.78	1.31	3.30	45.1	77.9	0.07	0.007	1.22	40.7	20.6	1.10	1.09	0.6	2.24	4.40	0.09	0.19	0.85	0.57
5	8.03	390	4.89	0.90	1.54	3.62	56.6	95.6	0.09	0.008	1.39	48.3	24.0	1.29	0.88	0.7	2.57	5.45	0.10	0.21	1.01	0.68
6	9.50	481	5.85	1.10	1.76	4.25	69.4	116	0.11	0.009	1.57	54.8	26.8	1.44	29.2	0.8	2.93	6.65	0.11	0.23	1.16	0.76
7	11.6	570	6.79	1.06	2.03	4.53	82.9	137	0.12	0.010	1.75	61.9	31.6	1.57	0.93	1.0	3.50	8.05	0.11	0.25	1.41	0.91
8	14.0	646	7.62	1.42	2.32	4.87	95.7	156	0.14	0.23	5.53	69.4	36.9	5.01	1.30	1.3	4.25	9.55	0.38	0.27	1.73	1.14
9	16.4	722	8.47	1.33	2.59	5.18	109	176	0.23	0.013	2.25	77.5	42.6	1.92	49.9	1.6	5.04	11.0	0.12	0.29	2.04	1.35
10	18.9	785	9.20	1.36	2.83	5.47	120	193	0.18	0.013	2.48	85.0	47.9	2.07	1.08	2.0	5.70	12.4	0.13	0.31	2.37	1.54
15	31.8	1124	13.0	2.03	4.07	6.79	181	283	0.20	0.021	4.28	125	74.4	3.13	1.32	3.8	8.93	20.0	0.16	0.39	4.02	2.50
16	34.2	1208	13.9	2.15	4.32	7.27	195	304	0.33	0.022	4.49	132	79.0	3.32	1.35	4.1	9.28	21.6	0.18	0.40	4.33	2.59
17	36.1	1274	14.7	2.25	4.53	7.52	206	321	0.35	0.022	4.65	137	81.5	3.48	1.38	4.3	9.54	22.9	0.18	0.40	4.53	2.74
20	44.6	1498	17.1	2.65	5.24	8.31	245	379	0.36	0.025	5.45	161	97.1	3.96	1.46	5.4	11.4	27.8	0.19	0.43	5.61	3.23
25	58.8	1824	20.8	3.43	6.56	9.50	306	469	0.42	0.034	7.78	209	128	5.29	1.62	7.5	15.0	35.7	0.25	0.48	7.49	4.28
26	61.0	1888	21.5	3.65	6.83	9.88	317	487	0.56	0.035	8.18	216	132	5.61	1.66	7.9	15.3	36.9	0.27	0.50	7.77	4.38
27	63.4	1960	22.3	3.76	6.97	10.0	329	506	0.58	0.036	8.36	223	136	5.73	1.67	8.1	15.3	37.6	0.27	0.49	8.02	4.39
30	71.2	2144	24.4	4.20	7.62	10.6	362	556	0.59	0.039	9.22	247	150	6.33	1.71	9.3	17.2	42.3	0.28	0.50	9.01	4.96
35	85.4	2458	28.0	4.99	8.77	11.7	419	643	0.67	0.045	11.1	293	178	7.48	1.82	11.3	20.5	50.7	0.32	0.53	10.9	5.85
39	96.5	2704	30.9	5.58	9.70	12.4	462	710	0.80	0.048	12.3	327	199	8.26	1.87	12.8	22.3	56.5	0.36	0.54	12.3	6.48
40	99.6	2772	31.7	5.79	9.93	12.6	474	727	0.88	0.050	12.5	336	204	8.47	1.89	13.2	22.9	58.6	0.36	0.54	12.6	6.55
45	114	3094	35.5	6.24	10.9	13.2	527	810	0.88	0.053	13.8	375	230	9.22	1.92	14.9	25.4	64.7	0.38	0.53	14.3	6.80
m.u.%	2.6	5.6	5.0	2.81	1.7	3.6	3.6	6.5	0.97	0.7	1.4	3.8	7.0	1.3	1.9	1.7	1.5	4.3	1.7	2.1	3.4	2.0

Table A8.5: Element ratio for pristine brine and the desorption increase rate and resultant enrichment factor of experiment 5. For Al, V, Cr and Mo, the detection limit is used for the calculation. Detection limits are given in Table 8.4.

	Li/S	Na/S	Mg/S	Al/S	Si/S	K/S	Ca/S	V/S	Cr/S	Mn/S
brine	1.5	334	3.1	$<9.1*10^{-7}$	0.3	30.0	67.7	$<1*10^{-7}$	$<2*10^{-7}$	0.2
increase rate	9.4	249	2.8	0.5	0.9	43.5	66.1	0.004	1.2	29.9
enrichment factor	6.1	0.8	0.9	>548946	2.6	1.5	1.0	>32104	>4270388	144

	Fe/S	Ni/S	Cu/S	Zn/S	As/S	Sr/S	Mo/S	Sb/S	Ba/S	Pb/S
brine	0.4	$7*10^{-5}$	0.0002	0.1	0.1	3.2	$<3*10^{-7}$	0.002	0.1	0.03
increase rate	18.8	0.8	0.1	1.3	2.1	5.4	0.03	0.04	1.2	0.6
enrichment facto	50.7	10111	489	9.3	26.0	1.7	>72271	22.5	15.1	20.5

Table A8.6: Concentration of Na, Mg and Ca in the brine, corresponding increase rates and estimated entrainment volume per L desorption solution (mL brine per L desorption solution per cycle) and average over the complete 22 L desorption solution for experiment 5, based on Table A8.5.

	Na	Mg	Ca	Average
brine [mg/L]	36868	342	7466	
increase rate [mg/L per cycle]	68.4	0.8	18.1	
entrainment volume [mL/L per cycle]	1.9	2.3	2.4	2.2
Total entrainment for 22L solution [mL per cycle]	40.8	49.9	53.3	48.0

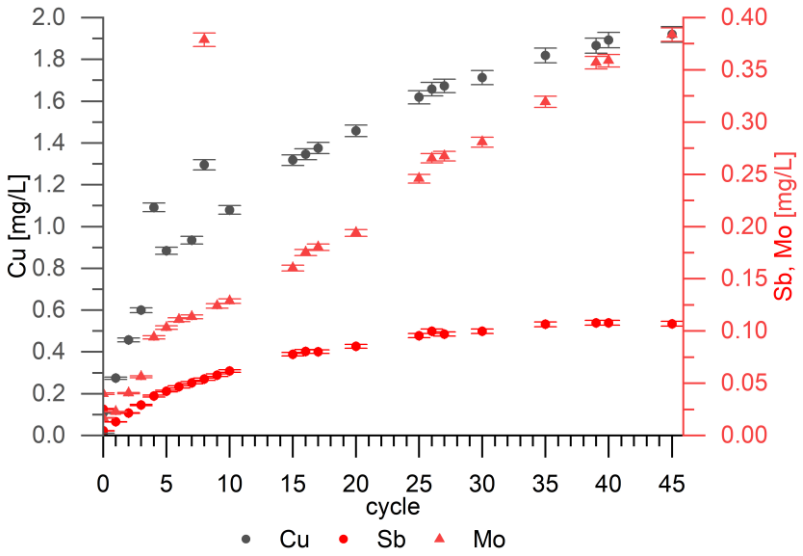

Figure A8.4: Cu (left), Sb and Mo (right) concentration development in recycled desorption solution of experiment 5 over all 45 cycles.

9. Publication

–

Lithium recovery from geothermal brines: An investigation into radioactive nuclide uptake on lithium-manganese-oxide (LMO) granules

Lena Kölbel; Klemens Slunitschek; Elif Kaymakci; Thomas Kölbel; Rebekka Reich; Jochen Schneider.

This work has been published in Hydrometallurgy (224, 106266)

published: February 2024

available online:

https://www.sciencedirect.com/science/article/abs/pii/S0304386X24000069?via%3Dihub

DOI: 10.1016/j.hydromet.2024.106266.

Hydrometallurgy 224 (2024) 106266

Contents lists available at ScienceDirect

Hydrometallurgy

journal homepage: www.elsevier.com/locate/hydromet

Lithium recovery from geothermal brines: An investigation into radioactive nuclide uptake on lithium-manganese-oxide (LMO) granules

Lena Kölbel [a,*], Klemens Slunitschek [b], Elif Kaymakci [c], Thomas Kölbel [c], Rebekka Reich [b], Jochen Schneider [a]

[a] Hydrosion GmbH, Tizianstr. 96, 80638 Munich, Germany
[b] Chair of Geochemistry and Economic Geology, Institute of Applied Geosciences, Karlsruhe Institute of Technology, Karlsruhe, Germany
[c] EnBW Energie Baden-Württemberg AG, Research and Development Department, Durlacher Allee 93, 76131 Karlsruhe, Germany

ARTICLE INFO

Keywords:
Lithium extraction
Geothermal
Sorption
Radium isotopes
210Pb
LMO sorbents

ABSTRACT

Due to the growing demand for lithium, the exploitation of non-conventional lithium sources such as Li-bearing geothermal brines is currently on the rise. These brines contain up to 200 mg L^{-1} of lithium along with a diverse range of other dissolved elements, including naturally occurring radionuclides. In this study, data from a radiochemical monitoring process performed during the pilot plant testing of direct lithium extraction (DLE) at a geothermal site in the Upper Rhine Graben (URG) are presented. The tests were conducted under thermodynamic *p-T* conditions of the geothermal plant ($T = 60$ °C, $p = 18$ bar). The results present an uptake of the long-lived radionuclides ^{226}Ra (^{228}Ra) and ^{210}Pb by the granulated lithium-manganese-oxides (LMO) sorbent employed. Elevated pH values enhance the sorption of nuclides formed in the Th-U decay series, due to the increased negative charge on the LMO surface. The radioactivity uptake on the sorbent was found to be time-dependent. Experiments with a 5-min contact time resulted in relatively low sorption capacities, while extending the sorption time to 30 min significantly increased the accumulation of Ra isotopes and ^{210}Pb on the sorbent surface. During the regeneration phase, the radioactive load on the LMO sorbent could be reduced using 0.5 M HCl. The mass balance analysis of the investigated radionuclides demonstrates desorption percentages ranging from 16% to 100% per extraction cycle.

1. Introduction

Increasing demand for the critical raw material lithium has directed attention towards exploring alternative and non-conventional lithium sources. Among these sources are Li-bearing geothermal brines, which possess the potential to contribute to a secure and domestic supply of lithium (Schmidt, 2023).

The highest geothermal temperature gradients in Germany are found in the Upper Rhine Graben (up to 110 K km^{-1} according to Pribnow and Schellschmidt, 2000). These favorable conditions have led to the establishment of several operating geothermal sites in the region, where the lithium concentrations of the produced geothermal brines are nearly 200 mg L^{-1} (Sanjuan et al., 2016).

In addition to lithium, these brines exhibit high mineralization levels (TDS > 100 g L^{-1}) and contain a diverse range of elements, including naturally occurring radionuclides. The natural decay chains of ^{238}U, ^{232}Th and ^{235}U consist of elements with varying hydrogeochemical properties and multiple isotopes. While in closed systems all daughter nuclides will achieve secular radioactive equilibrium with respect to their parent nuclides (daughter/parent activity ratio becomes unity), deep geothermal brines interact with the adjoining rocks. In consequence of these water-rock interactions, an elemental fractionation occurs resulting in a state of disequilibria (Osmond and Cowart, 1992). Such radioactive disequilibria have been commonly observed in deep geothermal brines in the Upper Rhine Graben (e.g., Eggeling et al., 2013). Here, radium isotopes (^{228}Ra, ^{226}Ra, ^{224}Ra, ^{223}Ra) exhibit activities significantly higher than those of their thorium progenitors (^{232}Th, ^{230}Th, ^{228}Th, ^{227}Th). Additionally, isotopes of lead (including ^{210}Pb with a half-life of 22.3 y) demonstrate comparatively high solubility (Fig. 1; Kölbel et al., 2020).

To extract lithium as a co-product from URG's geothermal brines, DLE technologies seem to be a promising option. Currently, sorption and ion exchange techniques are on the rise. Various inorganic sorbents, including lithium-manganese-oxides (LMO) of the spinel-type, are being

* Corresponding author.
E-mail address: lena.koelbel@hydrosion.de (L. Kölbel).

https://doi.org/10.1016/j.hydromet.2024.106266
Received 8 August 2023; Received in revised form 8 January 2024; Accepted 9 January 2024
Available online 14 January 2024

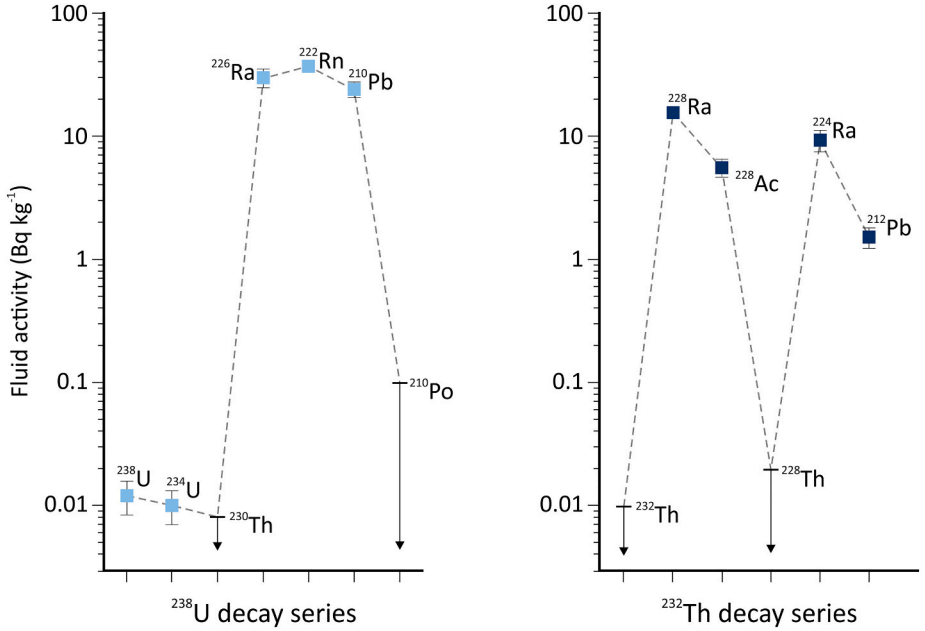

Fig. 1. Uranium and thorium series disequilibria: specific activity of ^{238}U and ^{232}Th and their decay products measured in the Bruchsal brine. Error bars represent uncertainties due to counting statistics (±2σ); ^{230}Th, ^{210}Po, ^{232}Th and ^{228}Th activities are upper limits. Radionuclide movement down the decay chain is from left to right (Kölbel et al., 2020).

used in these processes (Warren, 2021; Reich et al., 2022).

Several studies have investigated the sorption behavior of metals (e.g., Elwakeel and Atia, 2014; Wei et al., 2021; Elwakeel et al., 2021), including their unstable isotopes, on manganese oxides, particularly in the field of water treatment. Nirdosh et al. (1990), for example, studied the adsorption-desorption behavior of ^{226}Ra on hydrated metal oxide systems. Moon et al. (2003) characterized MnO_2 resins (produced by the reductive precipitation of MnO_2 on a macroporous resin substrate) for radium adsorption over wide ranges of pH, contact times and salt concentrations. The investigations of Wang et al. (2007) and Patterer et al. (2018) address the efficient removal of lead ions from aqueous solutions by means of manganese oxide-coated carbon nanotubes and manganese oxides recovered from spent alkaline and Zn/C batteries, respectively.

These studies indicate that the sorption of radium is mainly controlled by a surface charge effect and therefore dependent on the pH value. In an optimal pH range, positively charged alkaline earth species (e.g., Ra^{2+}) can diffuse into the surface layers (Davis and Kent, 1990). Moon et al. (2003) postulates that Ra^{2+} is the predominant Ra species up to a pH of 11, where it begins to hydrolyze to $Ra(OH)^+$ and in the presence of HCO_3^- ions, forms the carbonate species $Ra(HCO_3)^+$ and Ra (CO_3) (aq).

Wang et al. (2007) observed a similar sorption behavior for lead at Mn oxide-coated carbon nanotubes. Here, the negatively charged surface is responsible for enhanced adsorption of positively charged Pb^{2+} and $PbOH^+$ ions through electrostatic interaction and surface complexation at higher pH. In contrast, the adsorption effect is very weak at low pH values due to competition from H_3O^+ (e.g., Han et al., 2006).

In the extraction process of lithium from geothermal brines in the URG, a possible build-up of foreign ions on the metal oxides cannot be ruled out. However, there is a lack of publicly available data addressing the potential accumulation of natural radionuclides on LMO sorbents during lithium extraction from geothermal brines. This gap of information should be minimized, as radioactive uptake could have a negative impact on the sorbent performance, but also requires radiochemical monitoring strategies to observe the radioactive loading of the sorbent in terms of radiation protection.

In this study, we present the first set of results of the radiochemical monitoring developed and conducted in conjunction with the DLE testing at the geothermal site in Bruchsal, located at the eastern main boundary of the URG. For the experiments, a granular lithium-manganese-oxide sorbent was used. The investigations focused on the sorption characteristics of the radionuclides of Th-U decay series, dissolved in the brine under thermodynamic *p-T* conditions of the geothermal facility ($T = 60$ °C, $p = 18$ bar). The extent of radionuclide sorption was determined qualitatively and quantitatively by performing radiochemical analyses of both, the sorption and desorption solution as well as of the LMO sorbent. This resulted in a comprehensive data set that allows the determination of the effect of various factors (pH and contact time). Furthermore, using a mass balancing approach, estimates on sorption kinetics were derived, supporting the assessment of radiochemical effects on direct geothermal lithium production.

Table 1
Parent and daughter nuclides and their half-lives.

Parent nuclide	Half-life ($t_{1/2}$)	Daughter nuclides	Half-life ($t_{1/2}$)
^{226}Ra	1600 y	^{222}Rn	3.83 d
		^{218}Po	3.05 m
		^{214}Pb	26.8 m
		^{214}Bi	19.9 m
		^{214}Po	164 µs
^{210}Pb	22.3 y	^{210}Bi	5.01 d
		^{210}Po	138.4 d
^{228}Ra	5.75 y	^{228}Ac	6.13 h
^{228}Th	1.91 y	^{224}Ra	3.66 d
		^{220}Rn	55.6 s
		^{216}Po	0.15 s
		^{212}Pb	10.64 h
		^{212}Bi	60.6 m
		^{208}Tl	3.05 m
		^{212}Po	0.30 µs

2. Conceptual model

The radiochemical monitoring program relies on the principle of *secular equilibrium*. This specific type of radioactive equilibrium typically occurs when the parent nuclide's half-life is significantly larger

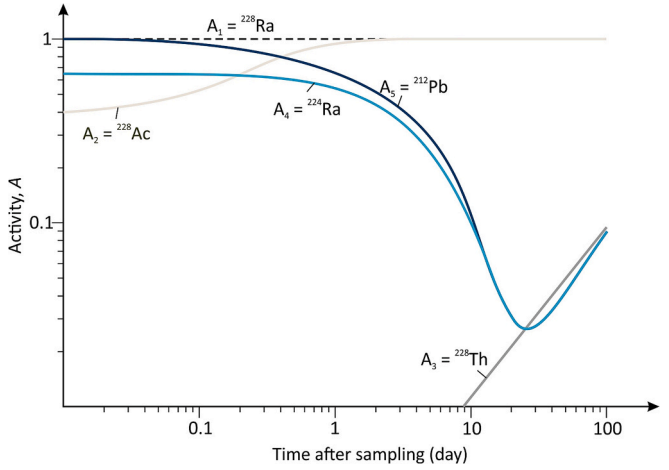

Fig. 2. Several successive transformations within the ^{232}Th decay series for the Bruchsal brine: The dotted lines represent the simulated time-depended evolution over activities of ^{228}Ra and its daughters (^{228}Ra → ^{228}Ac → ^{228}Th → ^{224}Ra → ^{212}Pb). Calculations were performed by means of CAS software (PTC Mathcad).

compared to the daughter's half-life ($t_{1/2}$ (A) > > $t_{1/2}$ (B)). Such conditions are fulfilled by the radionuclides of the natural decay series, where primordial nuclides are remarkable for their long half-lives and are still present in measurable quantities today.

When the radionuclides dissolved in the geothermal brines of the URG are pumped to the surface during geothermal utilization (or lithium recovery), the interaction processes in the reservoir section which are responsible for the observed radioactive fluid disequilibria are interrupted. Consequently, radionuclides from the Th-U series tend to establish a state of radioactive equilibrium. The time required to achieve this radioactive (*secular*) equilibrium depends on the daughter nuclide's half-life. Table 1 shows the information on parent and daughter nuclides and their $t_{1/2}$ values.

Since short-lived radionuclides ($t_{1/2}$ < 10 days) reach secular radioactive equilibrium with their long-lived parent nuclides in a comparatively short time (latest after several tens of days), the relationships have been derived for parent and daughter nuclides is shown in Table 1. Note that the ratio of parent to daughter activity (disintegration) becomes unity in the state of secular equilibrium.

Fig. 2 illustrates the time-dependent evolution using the example of the thorium decay series radionuclides which can be described by a system of coupled differential equations. Their general solution was first provided by Bateman (1910). A radioactive decay chain ($N_1 \rightarrow N_2 \rightarrow \ldots \rightarrow N_i$) with the decay constant λ_i can be described by the following differential equations:

$$\frac{dN_1}{dt} = -\lambda_1 N_1 \tag{1a}$$

$$\frac{dN_i}{dt} = \lambda_{i-1} N_{i-1} - \lambda_i N_i \ (i = 2, \ldots, n) \tag{1b}$$

Assuming zero concentrations of all daughters at time zero

$$N_1(0) \neq 0 \quad \text{and} \quad N_i(0) = 0 \quad \text{when} \quad i > 1 \tag{2}$$

Bateman (1910) expressed the concentration of the *n*th radionuclide time *t* as follows:

$$N_n(t) = \frac{N_1(0)}{\lambda_n} \sum_{i=1}^{n} \lambda_i \alpha_i exp[-\lambda_i t] \tag{3}$$

where the coefficients are calculated by

Table 2
Radionuclides and half-lives of uranium and thorium decay series.

Decay series	Radionuclide	Half-life ($t_{1/2}$) (y)
^{238}U	^{238}U	4.47×10^{9}
	^{234}U	2.46×10^{5}
	^{230}Th	75.4×10^{4}
	^{226}Ra	1600
	^{210}Pb	22.3
^{232}Th	^{232}Th	1.41×10^{10}
	^{228}Ra	5.75
	^{228}Th	1.91

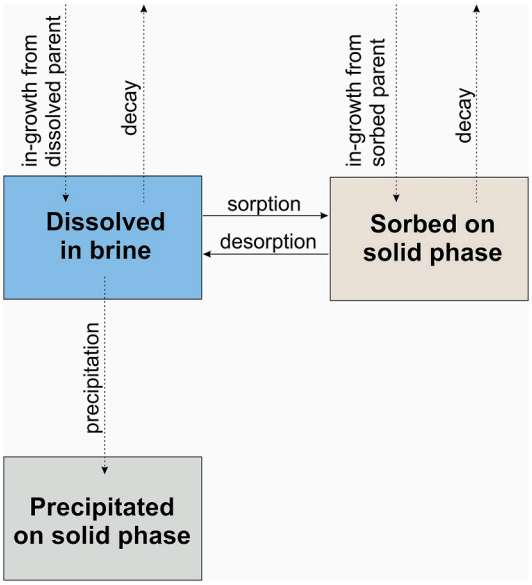

Fig. 3. Transfer of radionuclides between three categories (dissolved, sorbed or precipitated). Reversible and irreversible processes are indicated by arrows with solid and dashed lines. Figure adapted from Ku et al. (1998).

$$\alpha_i = \prod_{j=1}^{n} \frac{\lambda_j}{(\lambda_j - \lambda_i)} \qquad (j \neq i) \tag{4}$$

Based on the principles of radioactive equilibrium conditions discussed above and leveraging the known migration behavior of the natural radionuclides in the Bruchsal system (Kölbel et al., 2020), a radiochemical monitoring program that focused on the long-lived radionuclides listed in Table 2 was designed.

Since the isotopes of uranium and thorium given in Table 2 have comparatively long half-lives but are not dissolved in the Bruchsal brine (Kölbel et al., 2020), the focus of the radiochemical monitoring program was directed towards the long-lived radium isotopes (^{226}Ra: $t_{1/2}$ = 1600 y, ^{228}Ra: $t_{1/2}$ = 5.75 y) as well as the long-lived lead isotope ^{210}Pb ($t_{1/2}$ = 22.3 y).

In the context of lithium extraction experiments, first-order kinetics govern the processes of sorption-desorption (and subordinate precipitation, as observed in different adsorption studies under high pH-values, e.g., Wang et al., 2007) of naturally occurring radionuclides (e.g., Ku et al., 1998).

Surface adsorption of the radioactive radium and lead isotopes has been assumed based on the lithium-ion sieve (LIS) structure of LMO sorbents, which only allows lithium ions to enter the vacancies due to the small ionic radius of Li^+, compared to the other metal ions (e.g., Xu et al., 2016).

Applying the water–rock interaction modeling approach developed by Ku et al. (1992) to the Bruchsal batch experiments, it can be observed

Table 3
Configuration of the Li extraction test series E1 - E4 performed at the Bruchsal site.

Test series	Number of cycles	Contact time (min)	Mass of sorbent at the start of testing (g)	Buffer
E1	6	15	200	CH_3COONa
E2	4	30	174	–
E3	4	30	158	CH_3COONa
E4	20	5	146	CH_3COONa

that radionuclides transported with the geothermal brine may reside in three categories: dissolved in brine, sorbed on solid phase, and precipitated on solid phase (Fig. 3). The respective location of the radionuclides thus determines the activity distribution between the liquid brine before and after extraction step and the solid phase (sorbent).

The sorption capacity can be calculated by the following equation (e.g., Patterer et al., 2018):

$$q_{ads} = \frac{V(\lambda C_0 - \lambda C_{ads})}{m} \quad (5)$$

where q_{ads} is the sorption capacity of the sorbent to adsorb the respective radionuclide (mg g^{-1}), V is the brine volume (L), C_0 is the initial concentration of radionuclide dissolved in the Bruchsal brine (atoms L^{-1}), C_{ads} is the concentration of radionuclide remaining in the brine after sorption (atoms L^{-1}) and m is the weight of LMO sorbent (g). Note that the index notation "*ads*" and "*des*" stand for the adsorption and desorption solutions investigated.

The removal percentage of radionuclides (R%) can be derived by the following relationship (Karapinar et al., 2021):

$$R\% = \frac{\lambda C_0 - \lambda C_{ads}}{\lambda C_0} \bullet 100\% \quad (6)$$

The efficiency of the desorption step expressed as desorption percentage (D%) is formulated as follows:

$$D\% = \frac{\lambda C_{des}}{(\lambda C_0 - \lambda C_{ads})} \bullet 100\% \quad (7)$$

where C_{des} is the release of a given radionuclide into the desorption solution (atoms L^{-1}).

3. Experimental

3.1. Design of Li extraction experiments

Experiments for lithium extraction as a co-product of geothermal exploitation were conducted at the Bruchsal geothermal site on a pilot plant scale. The extraction experiments were carried out in batch mode, using a 6 L reactor installed in the pilot plant. To ensure effective mixing between sorbent and brine or desorption solution, additional recirculation pipelines and pumps were employed for each solution. The DLE unit is connected to the geothermal brine circuit via a bypass system. Approximately 2 m^3/h of the geothermal brine after geothermal utilization was injected at a temperature of 60 °C in the DLE unit. A 200 g sample of LMO sorbent was used in the tests. The sorption (and desorption) process is primarily based on an ion exchange mechanism (Shi et al., 2011):

$$H_{1.6}Mn_{1.6}O_4 + Li^+(aq) \rightleftharpoons Li_{1.6}Mn_{1.6}O_4 + H^+(aq) \quad (8)$$

A total of four test series were performed during a period of three months. An overview of the individual test set-up is given in Table 3. To test the recyclability of the used LMO, the sorbent was reused throughout all series of experiments. However, due to mechanical abrasion and losses during the lithium extraction tests, the original mass of 200 g slightly decreased during the tests.

In the sorption step, the granular LMO sorbent was loosely placed into the reactor before floating with geothermal brine. To prevent acidification of the brine caused by H^+ release during Li sorption (Eq. (8)), a Na acetate buffering solution was added to the inflowing geothermal brine, maintaining the pH in the range of 4 to 5. In the desorption phase, the lithium captured on the LMO granules was extracted using a 0.5 M HCl solution, thereby effectively regenerating the sorbent.

The first test series, E1, included in total of six cycles, each consisting of a sorption and a desorption step with a contact time of 15 min. In experimental series E2 and E3, the contact time was extended to 30 min, with four cycles in each case. The E2 series was performed without buffering to investigate sorption-induced pH changes and the effects on radionuclide sorption. The aim of test series E4 was to significantly increase the number of cycles to gather information on the sorbent's reusability. With a contact time of 5 min each, a total of 20 extraction cycles were completed.

Table 4
Physical parameters and chemical composition of the Bruchsal brine.

Physical parameters		Chemical composition		
Well (location)	GB2	Species (element or ion)	mg L^{-1}	µg L^{-1}
Collection date	25.02.2021	Li	155	
$T_{sampling}$ (°C)	31.7	Na	36,000	
Conductivity at 25 °C (mS cm^{-1})	163.7	K	3200	
pH	5.2	Ca	6900	
Eh (mV)	98	Mg	320	
		Sr	350	
		Ba	5.9	
		HCO_3	351	
		Cl	72,000	
		SO_4	350	
		S_2	< 0.02	
		SiO_2	89	
		Al		0.062
		Sb	0.18	
		As	9.3	
		Pb	3.2	
		B	34	
		Cd		78.3
		Cs	12.3	
		Fe (total)	52.0	
		Cu		20.8
		Mn (total)	24.1	
		U		<0.003
		Th		<0.0004
		DOC	<1	
		TDS	126,000	

(Kölbel et al., 2023).

3.2. Test medium

Table 4 provides a list of the physical parameters and chemical composition of the Bruchsal brine. The in situ Eh–pH conditions are difficult to determine due to the variations in pressure and temperature at reservoir and sampling location at ground level. At the sampling point, pH value was 5.2, while Eh value was 98 mV (with respect to the standard hydrogen electrode). Since pH measurements were taken from unpressurized samples, the effects of degassing (mainly CO_2) must be taken into consideration.

The geothermal brine is characterized by high concentrations of chloride, sodium and other alkali metals and alkaline earth metals, with total dissolved solids (TDS) of 126 g L^{-1}. Sodium (Na = 36,000 mg L^{-1}) and chloride (Cl = 72,000 mg L^{-1}) are the dominant cation and anion, respectively. The content of dissolved lithium is about 155 mg L^{-1}.

Since sorption of foreign ions cannot be ruled out, as shown by various LMO-based laboratory tests (Chitrakar et al., 2000, 2001; Shi et al., 2011; Park et al., 2014), special attention must be paid to

Table 5
Specific activities of ^{238}U, ^{235}U and ^{232}Th decay series radionuclides dissolved in the Bruchsal brine, data result from long-term fluid monitoring.

Decay series	Radionuclide	Specific activity (Bq kg^{-1})	Relative uncertainty (%)	Spectrometry surveys
Uranium series	^{238}U	0.012	59	α
	^{234}U	0.01	66	α
	^{230}Th	< 0.08		α
	^{226}Ra	29.0	8.3	γ
	^{222}Rn	37.8	7.4	γ
	^{210}Pb	15.8	26	γ
	^{210}Po	< 0.1		α
Actinium series	^{235}U	< 0.004		α
	^{227}Ac	< 0.1		α
	^{223}Ra	0.47	60	γ
Thorium series	^{232}Th	< 0.01		α
	^{228}Ra	15.9	5.8	γ
	^{228}Ac	6.1	27	γ
	^{228}Th	< 0.02		α
	^{224}Ra	10.3	7.5	γ
	^{212}Pb	15.7	6.4	γ

(Kölbel et al., 2020); Relative uncertainties are quoted in percentage (± 2σ from counting statistics); α = alpha; γ= gamma.

Table 6
Observed long-lived radionuclides during the radiochemical monitoring and gamma-ray energies and intensities.

Series	Long-lived nuclide of interest	Half-life (y)	Measured nuclide	Gamma-ray energies (E_y) and intensities (I_y)	
				E_y (keV)	I_y (%)
^{238}U series	^{226}Ra	1600	^{226}Ra	186.2	3.6
	^{210}Pb	22.3	^{210}Pb	46.5	4.3
^{232}Th series	^{228}Ra	5.75	^{228}Ac	338.3	11.3
				911.1	25.8
				968.9	15.8

Data for gamma-ray energies (E_y) and intensities (I_y) originate from Condomines et al. (2010).

potentially harmful components when addressing issues related to the purity of the desorption solution, occupational safety, and disposal. Potentially harmful components in the Bruchsal brine include heavy metals such as Pb, As, Cd (cf. Table 4), as well as naturally occurring radionuclides (Table 5).

3.3. Sampling and analytical methods

After each extraction cycle, samples of the sorption and desorption solutions were collected in 1 L wide-necked PET bottles. This enabled cycle-specific mass balancing of the investigated radionuclides. For sorption cycles, liquid samples were acidified to pH 1–2 using 2.5 mL 65% HNO_3 (suprapur).

The liquid samples were analyzed for the above-mentioned long-lived radionuclides (^{226}Ra, ^{228}Ra, ^{210}Pb) by gamma spectrometry. These surveys were carried out using a p-type HPGe coaxial detector of 30% efficiency (with respect to 3″×3″ NaI (Tl) detector). The germanium crystal used had a diameter of 76 mm. The detector was embedded in a 10-cm lead shield to protect against background radiation. A list of the gamma rays used for the determination of activities of isotopes of interest is provided in Table 6. The measurement duration for each analysis ranged between 20 and 24 h.

The activity of ^{226}Ra was directly measured using its gamma-ray energy at 186.2 keV. Any possible interference with ^{235}U (185.7 keV) was found to be negligible due to the low uranium activity in Bruchsal brine (Kölbel et al., 2020). The ^{228}Ra activity was determined by the specific activity of its daughter ^{228}Ac ($t_{1/2}$ = 6.2 h). Here, secular equilibrium was achieved at the latest after a time delay of 60 h between sampling and measurement. Direct assay of ^{210}Pb was performed by measurement of the 46.5 keV photon.

Gamma spectrometry surveys allow simultaneous, non-destructive measurements without any further sample preparation. This is especially important for the gamma spectrometric investigations of the sorbent, as the LMO granules were used several times.

Therefore, a special measurement routine of the sorbent was designed and applied. First, a zero measurement was carried out prior to the start of E1 testing to ensure no radioactive contamination of the solid material. At the end of each DLE test section (E1, E2, E3, E4), gamma spectrometry surveys were performed to analyze the uptake of radionuclides from Th-U series at the sorbent surface. The solid samples were

Table 7
Radionuclide signatures (specific activities A_i) of sorption solutions and related sorption capacities $q_{ads,i}$

Test series	Experimental conditions			Sample code	Specific activity of different radionuclides A_i (Bq L^{-1})*			Sorption capacity of different radionuclides $q_{ads,i}$ (mBq g^{-1})		
	LMO (g)	Time (min)	Na-acetate buffer		^{226}Ra	^{210}Pb	^{228}Ra	^{226}Ra	^{210}Pb	^{228}Ra
E1	200	15	Added	E1-z1-Ads	25 ± 4	7.3 ± 1.8	16 ± 2	118 ± 8	256 ± 5	95 ± 4
				E1-z2-Ads	24 ± 3	7.9 ± 1.8	16 ± 2	140 ± 7	245 ± 5	91 ± 4
				E1-z3-Ads	26 ± 4	11 ± 3	16 ± 2	91 ± 8	150 ± 6	94 ± 4
				E1-z4-Ads	23 ± 3	7.7 ± 1.5	15 ± 2	186 ± 7	267 ± 4	122 ± 4
				E1-z5-Ads	22 ± 3	6.8 ± 1.7	14 ± 2	241 ± 7	306 ± 5	152 ± 4
				E1-z6-Ads	22 ± 3	8.8 ± 1.6	15 ± 2	225 ± 7	246 ± 5	150 ± 4
E2	174	30	Not added	E2-z1-Ads	22 ± 4	10 ± 2	13 ± 2	238 ± 8	204 ± 5	204 ± 4
				E2-z2-Ads	21 ± 3	11 ± 3	14 ± 2	281 ± 7	186 ± 5	176 ± 4
				E2-z3-Ads	25 ± 4	14 ± 3	14 ± 2	145 ± 8	72 ± 6	181 ± 4
				E2-z4-Ads	22 ± 3	13 ± 3	15 ± 2	262 ± 8	112 ± 6	149 ± 4
E3	158	30	Added	E3-z1-Ads	20 ± 4	8.0 ± 2.6	13 ± 2	337 ± 8	300 ± 6	225 ± 4
				E3-z2-Ads	22 ± 4	12 ± 3	14 ± 2	269 ± 8	154 ± 6	192 ± 4
				E3-z3-Ads	20 ± 3	7.9 ± 2.1	13 ± 2	355 ± 7	320 ± 5	237 ± 4
				E3-z4-Ads	20 ± 3	9.6 ± 2.2	14 ± 2	365 ± 7	260 ± 5	203 ± 4
E4	146	5	Added	E4-z1-Ads	26 ± 4	15 ± 2	16 ± 2	122 ± 8	41 ± 5	122 ± 4
				E4-z3-Ads	26 ± 4	12 ± 2	17 ± 2	123 ± 8	164 ± 5	82 ± 4
				E4-z5-Ads	24 ± 3	14 ± 2	16 ± 2	207 ± 7	83 ± 5	124 ± 4
				E4-z7-Ads	26 ± 4	12 ± 2	17 ± 2	126 ± 8	167 ± 5	84 ± 4
				E4-z10-Ads	24 ± 4	13 ± 3	16 ± 2	211 ± 8	127 ± 6	127 ± 4
				E4-z15-Ads	26 ± 4	14 ± 3	17 ± 2	128 ± 8	85 ± 6	85 ± 4
				E4-z20-Ads	25 ± 4	12 ± 3	17 ± 2	173 ± 8	173 ± 6	86 ± 4

*The quoted errors are 1σ-deviations in Bq L^{-1} derived from counting statistics. Values of the sorption capacity are based on Eq. (5).

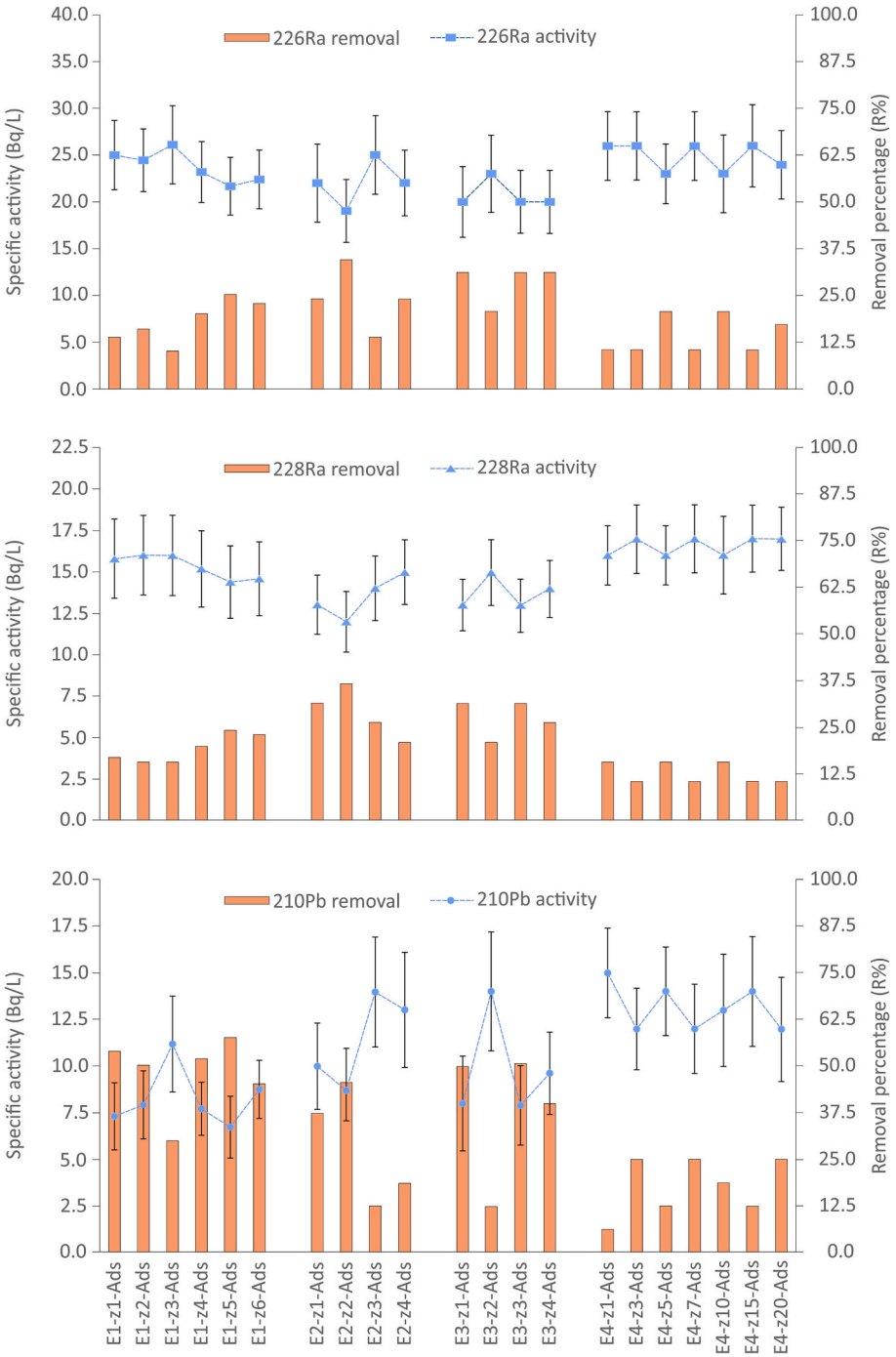

Fig. 4. ^{226}Ra, ^{228}Ra and ^{210}Pb specific activities of the sorption solution (symbols) and their removal percentage (bar chart for data from Table 7). Experimental conditions as listed in Table 7.

washed with distilled water before gamma spectrometric measurements. The solid samples were measured in the wet state and the adsorption capacities were calculated based on these results. The water content of the LMO granules varied between 21 and 24%.

To minimize the impact of foreign ions on the subsequent test series, a 24-h desorption procedure using 0.5 M HCl as desorbing agent was carried out in the laboratory between two test series. Since this regeneration process also affected the radioactive load of the sorbent, specific activities of the radionuclides associated with the LMO sorbent were measured and documented before initiating the next series of tests.

4. Results and discussion

4.1. Sorption studies

4.1.1. Gamma-spectrometric results of sorption solutions

Specific activities in the brine after sorption as well as the sorption capacities of ^{226}Ra, ^{210}Pb and ^{228}Ra determined for each sorption cycle are listed in Table 7.

The specific activities of ^{226}Ra and ^{228}Ra vary between 20 and 26 Bq L^{-1} and 13 and 17 Bq L^{-1}, respectively, across all experiments and extraction cycles. Using Eq. (5) sorption capacities of 91 and 365 mBq g^{-1} for ^{226}Ra and 82 and 237 mBq g^{-1} for ^{228}Ra were calculated.

Table 8
Reference values of the Bruchsal brine, as well as zero measurements of the desorption solution and LMO sorbent.

Object of investigation	Activity units	Nuclide and activity		
		^{226}Ra	^{210}Pb	^{228}Ra
Bruchsal brine	Bq L^{-1}	29 ± 4	16 ± 3	19 ± 2
Desorption solution	Bq L^{-1}	<1.3	<0.9	<1.6
LMO sorbent	mBq g^{-1}	<18	<24	<4.4

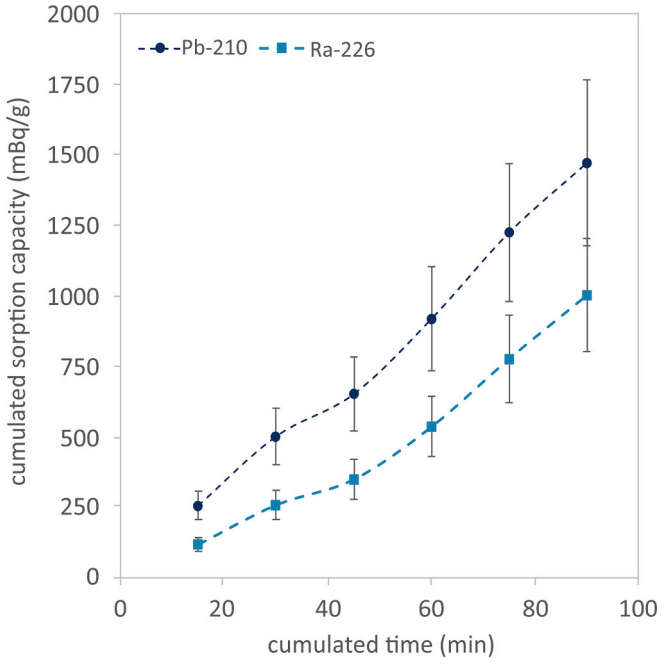

Fig. 5. Cumulative sorption capacity of ^{210}Pb and ^{226}Ra for extraction experiment E1. Cumulative time corresponds to the contact time t = 15 min for six cycles performed (see Table 7).

Estimates of the relative removal percentage R%, depicted in Fig. 4, reveal similar values for the two radium isotopes, attributed to their chemically similar behavior (e.g., Brown et al., 2022). The removal percentage of the two Ra isotopes ranges between 10 and 32%, with an average value of 20%.

The specific ^{210}Pb activities vary between 6.8 and 15 Bq L^{-1}. Regarding the initial brine value of 16 Bq L^{-1} (Table 8), relatively high maximum removal percentages R% of ^{210}Pb were achieved. Especially for the first cycles of the extraction experiment E1, where the sorbent was used for the first time, removal percentages of >50% were observed, resulting in a maximum sorption capacity of 306 mBq g^{-1}.

Fig. 5 compares the sorption capacities of ^{226}Ra and ^{210}Pb cumulated for experiment E1. Notably, ^{210}Pb sorption capacity is significantly higher, suggesting that lead ions may have a higher ability to approach the sorbent surface during adsorption compared to other competing cations (Vajedi and Dehghani, 2019). This higher affinity might be attributed to various factors, such as specific interactions of cations with the sorbent, differences in their ion sizes, charge densities and the type and distribution of the active groups on the sorbent (Chiban et al., 2011). However, to detail the key processes responsible for these observations, further investigations are required.

Karapinar et al. (2021) proposed a positive correlation between the ionic radii of metal ions and their adsorption capacities, indicating that larger ionic radii have a favorable effect on the adsorption process. From this perspective, microporous adsorption of small metal ions might play only a minor role. Since the (Pauling) ion radii of lead (1.20 Å according to Rohrer, 2001) and radium (1.40 Å according to Rohrer, 2001) differ only slightly, other factors may be responsible for the preferential uptake of ^{210}Pb at the LMO sorbent. Potential impact of various factors in the experimental set-up (such as contact time, pH and buffer solution) on the measured results are discussed in the following sections.

Table 9
Evolution of pH during the test series E2 and E3 measured in the sorption solutions.

Test series	Sample code	Solution pH	Sorption capacity (mBq g^{-1})	
			^{226}Ra	^{210}Pb
E2 (without buffer solution)	E2-Brine+N	4.1		
	E2-z1-Ads	2.6	238	204
	E2-z2-Ads	1.9	281	186
	E2-z3-Ads	1.9	145	72
	E2-z4-Ads	1.7	262	112
E3 (with Na acetate buffer)	E3-Brine+N	4.3		
	E3-z1-Ads	4.3	337	300
	E3-z2-Ads	4.2	269	154
	E3-z3-Ads	4.1	355	320
	E3-z4-Ads	4.1	365	260

Contact time 30 min each; Samples "E2-Brine+N" and "E3-Brine+N" are reference samples of the Bruchsal brine, therefore there is no information on the sorption capacity of ^{226}Ra and ^{210}Pb.

4.1.2. *Effect of pH on sorption*

The impact of solution pH on ^{226}Ra and ^{210}Pb sorption capacity of LMO granules was investigated by comparing test series E2 and E3. Both test series were conducted under identical conditions (cf. Table 3), but the liquid in experiment E2 was not buffered. The absence of Na acetate buffer solution led to comparatively low pH values (Table 9) due to the release of protons during the lithium-ion exchange process (cf. Eq. (8)). In the unbuffered experiment E2, the pH value dropped from 4.1 in the brine to 2.6 (cycle 1) and further to 1.7 (cycle 4). In contrast, in the buffered experiment E3, only slight changes (minimum pH = 4.1) in pH value were observed compared to the buffered geothermal brine (maximum pH = 4.3).

The sorption of ^{226}Ra and ^{210}Pb from the Bruchsal brine by LMO was found to be pH-dependent, affecting both the sorbent and the adsorbate characteristics (Fig. 6).

An increase in pH (E2: average pH = 2; E3: average pH = 4) resulted in an increase in the mean sorption capacity from 230 mBq g^{-1} to 330 mBq g^{-1} (^{226}Ra) and 140 mBq g^{-1} to 260 mBq g^{-1} (^{210}Pb), respectively. The related nuclide removal varied from 14% to 31% (^{226}Ra) and 13% to 51% (^{210}Pb).

This sorption characteristic aligns with the study of Nirdosh et al. (1990), where radium removal was found to be highly sensitive to the solution pH. In their experiments with Mn-based metal oxides, the sorption percentage of ^{226}Ra was 100% at pH 10 and 40% at pH 1, despite unfavorable zeta potentials at low pH values.

At pH values above the point of zero charge (PZC), however, a prominently negative surface charge of the sorbent stemming from a considerable amount of surface coverage by hydroxyl groups can be assumed. Although the pH_{PZC} was not determined in this study, a comparison with published literature values reveals pH values in a range of 2.5–7.8. The comparatively high value of 7.8 was determined by Tian et al. (2010), who investigated the adsorption behavior of Li^+ on a nano-lithium-ion screen of hybrid magnesium/lithium manganese oxide. Most other studies found the pH_{PZC} in the range of 3.5 to 4.3 (Nirdosh et al., 1990; Kosmulski, 2009; Seip et al., 2021; Demir et al., 2022), while Wang et al. (2009) reported a much lower PZC of about 2.5.

Thus, at the pH range of 4.1–4.3 tested in the present study, it may be presumed that the sorbent carries a negative surface charge. Consequently, electrostatic attraction takes place between negative surface charge and positive charge of the metal ions (such as Ra^{2+}, Pb^{2+}) leading

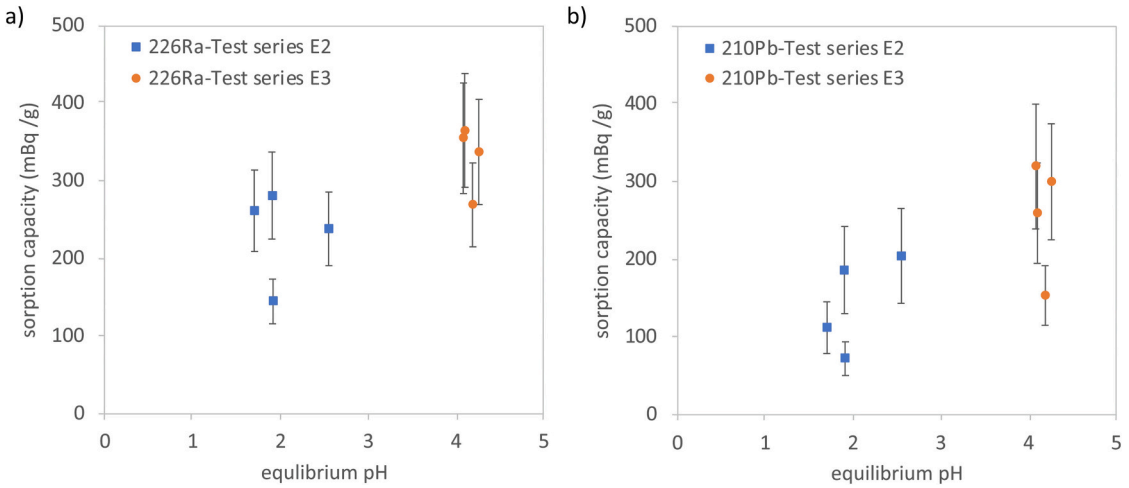

Fig. 6. Sorption capacity of ^{226}Ra (a) and ^{210}Pb (b) as a function of the pH of sorption solution. Test series E2: without Na-acetate buffer; Test series E3: with Na-acetate buffer (30 min contact time each).

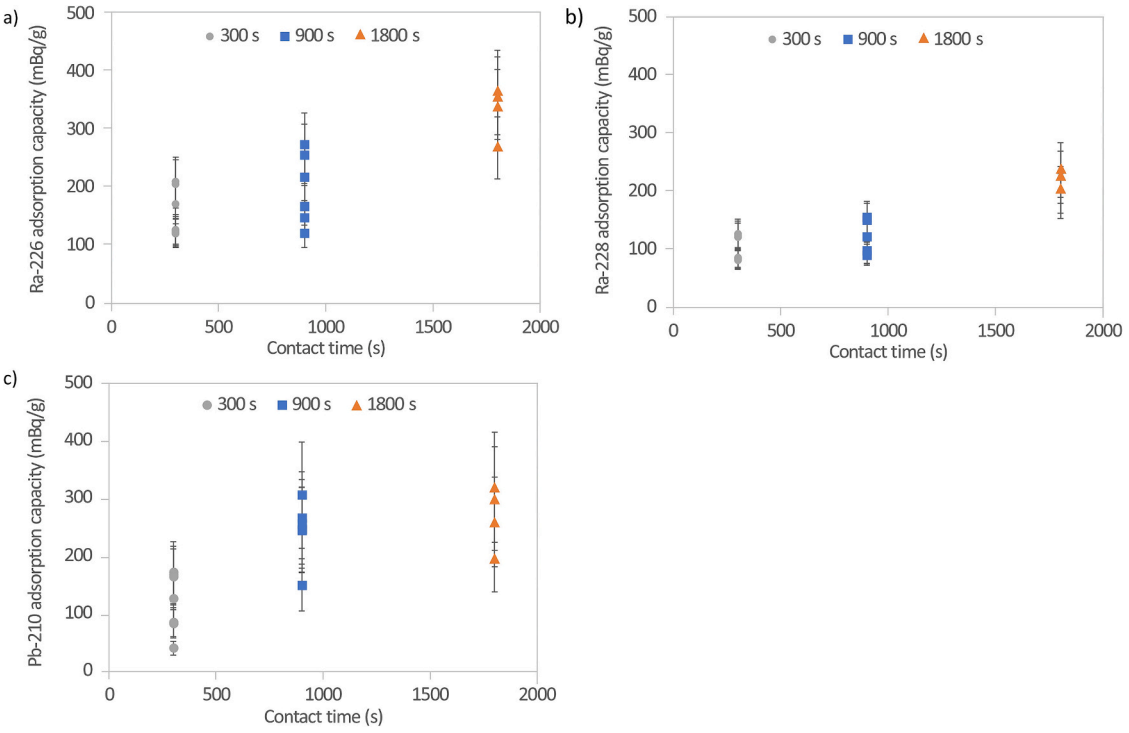

Fig. 7. Time-dependent evolution of the sorption capacity of radium ^{226}Ra (a), ^{228}Ra (b) and lead ^{210}Pb (c).

to an enhancement in the sorption efficiency (Agrawal et al., 2005). A similar phenomenon has been detected for Pb(II) in different adsorption-desorption studies (e.g., McKenzie, 1980; Wang et al., 2007).

4.1.3. Effect of contact time on sorption

The batch experiments E1, E3 and E4 were all carried out under identical conditions, with only the contact times being varied. Fig. 7 shows the sorption capacities of ^{226}Ra (^{228}Ra) and ^{210}Pb as a function of time.

For lead and radium, the lowest sorption capacities were recorded in test series E4 with the shortest reaction time of 5 min (300 s). As the contact time increased, the sorption capacity of the investigated radionuclides also increased. Consequently, the highest values were to be assigned to test series E3 with $t = 30$ min (1800 s).

A comparison between E3 and E4 reveals that the sorption capacities for ^{210}Pb showed only slight improvement despite the longer contact time, while sorption capacities of the Ra isotopes changed only slightly between tests E1 (15 min) and E4 (5 min). However, a significant increase can be seen in E3, where the contact time was 30 min. Here, the sorption capacity has tripled compared to the 5-min experiment.

These results suggest that ^{210}Pb exhibits faster kinetics compared to ^{226}Ra and ^{228}Ra, and that ^{210}Pb reached sorption close to the equilibrium value. It is known that the sorption process consists of two steps: The first step is dispersion through the outer liquid layer around the sorbent, while the second step consists of diffusion into the inner zones together with the pore fluid (Wang et al., 2010). An exact determination of the adsorption behavior cannot be derived from the present dataset. This would require additional equilibrium studies. However, the equilibrium time for ^{210}Pb can be approximately estimated in the order of 15 to 30 min.

Table 10
Estimates on the dimensionless partition coefficient K of ^{226}Ra, ^{228}Ra and ^{210}Pb.

Test series	Sample code	Dimensionless partition coefficient K		
		^{226}Ra	^{228}Ra	^{210}Pb
E1	E1-z1-Ads	0.20	0.20	1.18
	E1-z2-Ads	0.23	0.19	1.02
	E1-z3-Ads	0.15	0.19	0.43
	E1-z4-Ads	0.29	0.25	1.08
	E1-z5-Ads	0.38	0.32	1.37
	E1-z6-Ads	0.34	0.30	0.82
E3	E3-z1-Ads	0.45	0.46	1.00
	E3-z2-Ads	0.32	0.36	0.33
	E3-z3-Ads	0.45	0.46	1.03
	E3-z4-Ads	0.45	0.36	0.67
E4	E4-z1-Ads	0.12	0.19	0.15
	E4-z3-Ads	0.12	0.12	0.33
	E4-z5-Ads	0.21	0.19	0.14
	E4-z7-Ads	0.12	0.12	0.33
	E4-z10-Ads	0.21	0.19	0.23
	E4-z15-Ads	0.12	0.12	0.14
	E4-z20-Ads	0.16	0.12	0.33

Furthermore, the low radionuclide sorption in the 5-min experiment demonstrate that sorption kinetics observed in the field experiment are much slower compared to kinetic studies performed in the laboratory, where Pb(II) could be adsorbed by over 90% in less than five minutes (e.g., Patterer et al., 2018). One possible reason for this observation might be the high concentration of competing ions dissolved in the geothermal brine which leads to a competition among the cations for free adsorption sites at the LMO surface.

4.1.4. Sorbent-brine concentration ratios

Partitioning of isotopes between solid and liquid phases has been described in a variety of ways. Krishnaswami et al. (1982), for example, have defined a dimensionless partition coefficient K, which corresponds to the ratio of adsorbed atoms to dissolved atoms ($\frac{\overline{C}}{C}$):

$$K = \frac{k_1}{k_2 + \lambda} = \frac{\overline{C}}{C} \tag{9}$$

where k_1 is the first-order adsorption rate constant (s^{-1}), k_2 is the first-order desorption rate constant (s^{-1}) and λ is the radioactive decay constant of nuclide (s^{-1}). The partition coefficient K is related to the distribution coefficient K_d of nuclides, expressed in units of volume per mass (mL g^{-1}), as typically determined in the laboratory by adsorption-desorption experiments:

$$K = K_d = \frac{C_d}{C} \tag{10}$$

where C_d is the concentration of the adsorbed radionuclides on solids in atoms per mass and C is concentration of dissolved radionuclides in atoms per fluid volume.

Note that no additional sorption-desorption laboratory experiments were carried out as part of this study. The distribution coefficients were derived from the measured values and are intended to illustrate the relative sorption behavior of the Th-U series radionuclides studied during lithium extraction using LMO under real *T-p* conditions of the geothermal plant system.

A value of $K > 1$ support the tendency of a given radionuclide to be adsorbed onto the LMO granules, while a K value smaller than 1 present the tendency of a given radionuclide to reside in the liquid phase.

Table 10 displays estimates on the dimensionless partition coefficient K of ^{226}Ra, ^{228}Ra and ^{210}Pb. Since the establishment of sorption equilibrium for the investigated Ra and Pb isotopes cannot be proven, the values listed in Table 10 correspond to the recording of the respective actual state of the investigated cycles of the series of experiments. The K values for ^{226}Ra and ^{228}Ra range from 0.12 to 0.46, with the highest values being associated with test series E3 (contact time 30 min) and the lowest with experiment E4 (contact time 5 min).

Table 11
Radionuclide signatures (specific activities A_i) of desorption solution and corresponding desorption percentage (D%).

Test series	Sample code	Measured specific activity A_i (Bq L^{-1})			Desorption percentage (D%)		
		^{226}Ra	^{210}Pb	^{228}Ra	^{226}Ra	^{210}Pb	^{228}Ra
E1	E1-z1-Des	5.6 ± 2.9	3.0 ± 1.5	3.1 ± 0.8	112	35	97
	E1-z2-Des	5.0 ± 2.6	2.3 ± 0.4	2.8 ± 0.7	89	29	93
	E1-z3-Des	3.0 ± 1.9	2.1 ± 1.6	2.1 ± 1.0	77	44	70
	E1-z4-Des	5.4 ± 2.1	4.2 ± 1.5	3.3 ± 0.7	79	51	87
	E1-z5-Des	4.9 ± 1.2	3.5 ± 1.2	3.4 ± 0.7	59	38	74
	E1-z6-Des	4.4 ± 1.2	4.2 ± 2.2	3.2 ± 0.7	58	58	73
E2	E2-z1-Des	3.9 ± 1.0	2.5 ± 0.7	2.2 ± 0.7	56	42	37
	E2-z2-Des	2.0 ± 0.8	0.8 ± 0.7	1.2 ± 0.3	25	16	24
	E2-z3-Des	3.2 ± 1.1	1.9 ± 0.6	2.2 ± 0.4	80	95	44
	E2-z4-Des	3.8 ± 1.1	2.4 ± 0.9	2.1 ± 0.5	54	80	53
E3	E3-z1-Des	6.4 ± 1.4	4.7 ± 1.0	4.1 ± 0.5	71	59	68
	E3-z2-Des	3.6 ± 1.0	2.3 ± 0.7	2.4 ± 0.3	51	58	48
	E3-z3-Des	6.5 ± 1.6	5.2 ± 1.2	4.4 ± 0.6	72	64	73
	E3-z4-Des	8.3 ± 1.8	6.6 ± 1.3	4.6 ± 0.6	92	103	92
E4	E4-z1-Des	2.4 ± 0.4	1.0 ± 0.6	1.8 ± 0.3	80	100	60
	E4-z3-Des	3.0 ± 0.6	2.3 ± 0.4	2.0 ± 0.3	100	58	100
	E4-z5-Des	3.8 ± 0.6	2.2 ± 0.6	2.4 ± 0.4	76	110	80
	E4-z7-Des	2.9 ± 0.6	1.9 ± 0.7	1.9 ± 0.4	97	48	95
	E4-z10-Des	3.4 ± 0.6	2.0 ± 0.9	2.2 ± 0.4	68	67	73
	E4-z15-Des	3.0 ± 0.7	2.1 ± 0.5	1.8 ± 0.3	100	105	90
	E4-z20-Des	3.0 ± 0.6	2.0 ± 0.5	1.8 ± 0.3	75	50	90

0.5 M HCl solution was used for regeneration with 15 min contact time (test series E1), 30 min contact time (E2 and E3) and 5 min contact time (E4), respectively. The quoted errors are 1σ-deviations derived from counting statistics. Values of the desorption percentage are based on Eq. (7).

The dimensionless partition coefficient was also determined for ^{210}Pb from the results listed in Table 7. The resulting K values for ^{210}Pb vary between 0.14 and 1.37, whereby measured values of approximately 1 were achieved for test series E1 and E3 except for a few cycles (e.g., E1-z3-Ads; E3-z2-Ads) which is probably due to uncertainties of measurements. From Eq. (9), k_1/k_2 closely approximates K if $k_2 > \lambda$. In that case, K values around 1 indicates near-equilibrium states. In contrast, the calculated partition coefficients for test series E4 (5-min contact time) are marked by values significantly smaller than 1.

4.2. Desorption

Hydrochloric acid belongs to the group of inorganic acids that can form various types of complexes and, as strong chelating agents, can cause greater desorption of ions from the sorbent into the desorption solution. The regenerability and reusability of LMO sorbents in the removal of Th-U series radionuclides from geothermal brines are

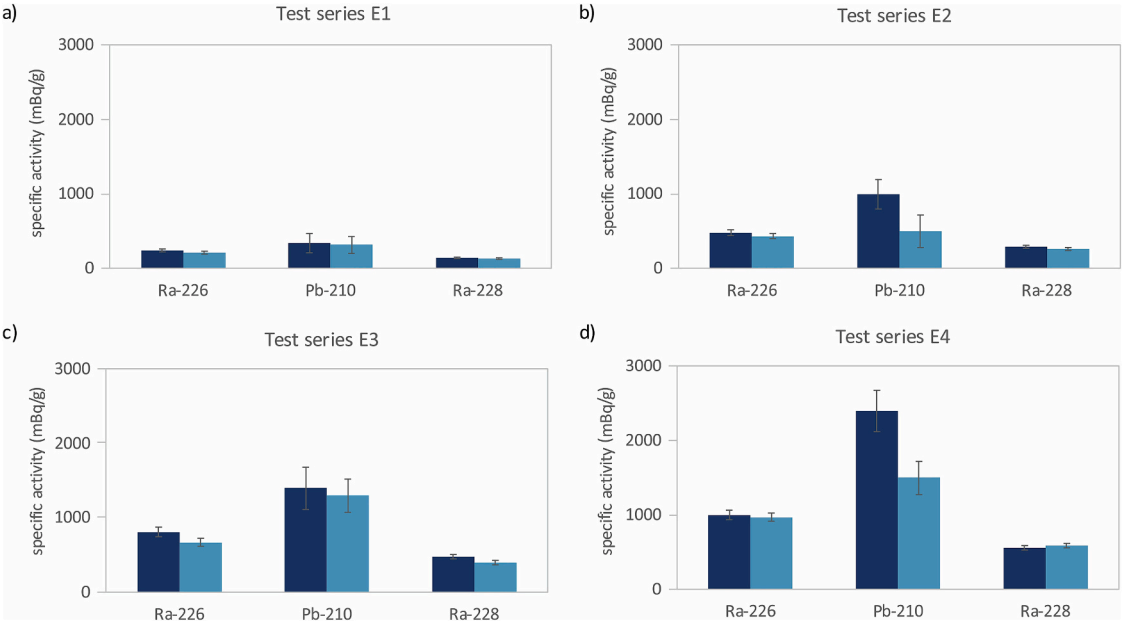

Fig. 8. Evolution of the radioactive loading of the LMO sorbent used for the test series E1 (a), E2 (b), E3 (c) and E4 (d). Measurement carried out after completion of the respective test series in the pilot plant using 0.5 M HCl as desorbing agent (dark blue coloring); Measurement carried out after 24 h desorption in the laboratory using 10 mL 0.5 M HCl/g LMO (light blue coloring). (For interpretation of the references to color in this figure legend, the reader is referred to the web version of this article.)

Table 12
Specific activities of ^{226}Ra, ^{210}Pb und ^{228}Ra measured on the LMO sorbent used.

Test series	Description	Measured specific activities (mBq g^{-1})		
		^{226}Ra	^{210}Pb	^{228}Ra
E1	After on-site testing	240 ± 17	340 ± 129	140 ± 8
	After lab desorption	210 ± 17	320 ± 115	130 ± 8
E2	After on-site testing	480 ± 38	1000 ± 200	290 ± 20
	After lab desorption	432 ± 35	500 ± 220	260 ± 18
E3	After on-site testing	810 ± 65	1400 ± 280	480 ± 34
	After lab desorption	670 ± 54	1300 ± 221	400 ± 28
E4	After on-site testing	1000 ± 60	2400 ± 360	560 ± 28
	After lab desorption	970 ± 58	1500 ± 255	590 ± 30

The quoted errors are 1σ-deviations derived from counting statistics.

important parameters for the assessment of radiation risk during lithium extraction.

The investigations of the desorption solutions per regeneration cycle combined with the results of the sorption solutions investigated, enables the calculation of a mass balance for a given radionuclide.

Specific activities of ^{226}Ra, ^{210}Pb and ^{228}Ra of the desorption solutions, as well as their desorption percentages are listed in Table 11.

Desorption values >100% result from the experimental uncertainties of the measured specific activities of the sorption and desorption solutions, indicating complete desorption.

In general, desorption performance was relatively high for the test series E1 and E3, while it was lowest for experiment E4. The lower absolute desorption in experiment E4 probably results from the low sorption, indicating that the relatively short contact time of 5 min may have affected the LMO loading (unloading). However, E4 shows high desorption percentages up to 100% (Table 11), indicating a highly reversible sorption. Compared to E3, test series E2 shows lower desorption percentages for all regarded radionuclides, especially for ^{226}Ra and ^{228}Ra.

For ^{226}Ra, the specific activities of the desorption solutions vary between 2.0 and 8.3 Bq L^{-1}. Samples with high ^{226}Ra activity also show comparatively high ^{228}Ra activity, with a maximum specific activity of the latter of 4.6 Bq L^{-1}. The maximum ^{210}Pb activity observed is 6.6 Bq L^{-1} in cycle 4 of test series E4, with a mean of about 3 Bq L^{-1}.

The comparatively poor desorption performance for ^{210}Pb indicates its stronger sorptive binding to the surface of the LMO sorbent. This may be influenced by several factors such as the size of the metal ions and their electronegativity (Maleki et al., 2016).

The comparatively lower desorption performance for ^{210}Pb results in total to a higher loading at the sorbent compared to radium, as could be proven by radiochemical investigations of the sorbent (see below).

4.3. Studies on the LMO sorbent

4.3.1. Uptake of ^{226}Ra, ^{228}Ra and ^{210}Pb

The radioactive uptake on the LMO granules as a function of DLE experiments is illustrated in Fig. 8. The corresponding measured values are listed in Table 12. Note that in terms of reusability of the sorbent, a 24-h desorption step was carried out in the laboratory following the test series E1, E2, E3 and E4.

The specific activities of ^{210}Pb, ^{226}Ra and ^{228}Ra steadily increased during the entire test period. The specific activities of ^{210}Pb were found to be around twice as high as those of ^{226}Ra, confirming the results of the analyzed desorption solution, which showed lower efficiency of the desorption steps during the pilot tests.

The 24-h desorption events reduced the radioactive loading of the sorbent with ^{226}Ra and ^{228}Ra by approximately 10%, except for test series E4 in which specific activities of radium stayed constant, where the deviations were in the range of measurement uncertainty. In contrast, the ^{210}Pb loading was reduced by almost 40% in E4 and 50% in E2. Whether this is an expression of a modification in the sorption mechanism or a consequence of the comparatively high measurement uncertainties of Pb (Fig. 8) remains to be further investigated.

The relatively low desorption percentage of 10% of radium is most likely due to the chosen volume/mass ratio of desorbing agent to sorbent (10 mL 0.5 M HCl/g LMO), since higher desorption percentages were achieved at the higher volume/mass ratio at the desorption within the test series (Table 11). Thus, higher volumes of HCl and/or higher concentrated acids would have possibly yielded improved results, as shown in the study by Karapinar et al. (2021). However, since the pilot tests aimed to maximize the recyclability of the sorbent, a gentle process

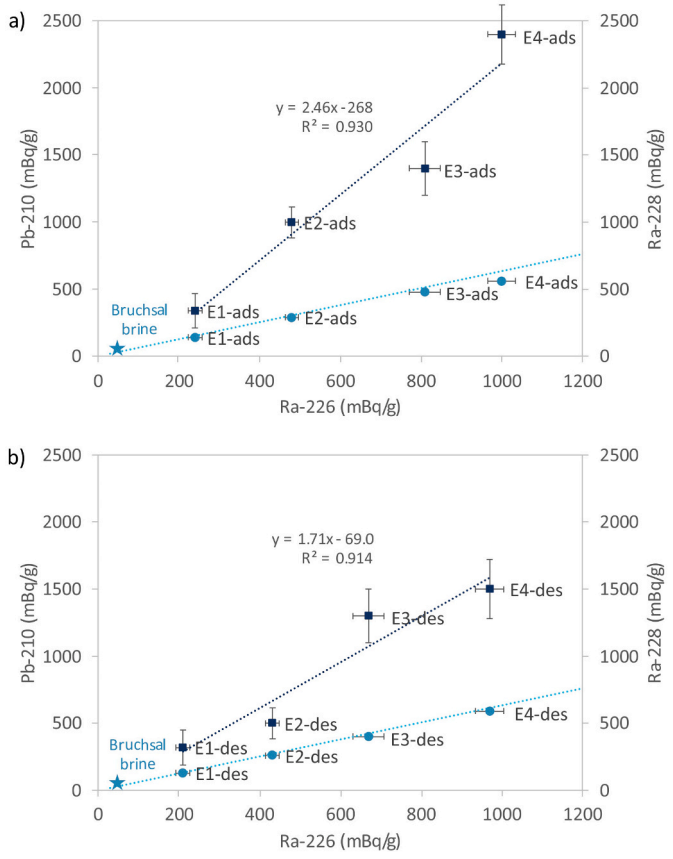

Fig. 9. Accumulation of ^{210}Pb and ^{228}Ra vs. ^{226}Ra on the LMO sorbent after completion of the respective extraction test series (a) and after performing the 24 h desorption in the laboratory (b). Squares: ^{210}Pb/^{226}Ra (dark blue coloring); Circles: ^{228}Ra/^{226}Ra (light blue coloring). (For interpretation of the references to color in this figure legend, the reader is referred to the web version of this article.)

approach was applied.

4.3.2. ^{210}Pb/^{226}Ra and ^{228}Ra/^{226}Ra ratio

Studying the ^{210}Pb/^{226}Ra as well as the ^{228}Ra/^{226}Ra isotope ratio can provide valuable insights into the sorption mechanism of radium and lead during lithium extraction steps. The ^{228}Ra/^{226}Ra ratio establishes a relationship between the decay series of ^{232}Th and ^{238}U. The Bruchsal brine presents a ^{228}Ra/^{226}Ra activity ratio of 0.66 ± 0.07, marked with a star symbol in Fig. 9. The gamma spectrometry surveys of the granulated LMO sorbent show that the ^{228}Ra/^{226}Ra ratio of the sorbent is in line with the observed fluid ratio throughout the series of experiments. Deviations are within the range of measurement uncertainties (Fig. 9a). This positive correlation in specific activities demonstrates that the sorption process equally affects both radium isotopes dissolved in the brine due to their same chemical behavior.

Furthermore, a positive correlation of ^{210}Pb with the long-lived ^{226}Ra is noticeable (R^2 = 93%). With increasing ^{210}Pb loading of the sorbent, the proportion of ^{226}Ra also increases suggesting similar sorption mechanism of the chemically different elements. However, ^{210}Pb seems to have a higher affinity than ^{226}Ra due to the higher removal percentage (Fig. 4) and the lower desorption percentage of ^{210}Pb compared to ^{226}Ra listed in Table 11. The higher desorption of ^{210}Pb in the 24 h desorption may result from the low volume/mass ratio leading to low radium desorption.

Comparable isotopic signatures of ^{210}Pb/^{226}Ra and ^{228}Ra/^{226}Ra, respectively, were observed for the eluates analyzed after 24 h desorption in the laboratory (Fig. 9b) and in the desorption solutions investigated (cf. Table 11).

Assuming that precipitation processes are negligible in the present pH value range, sorption remains the dominating process for nuclide uptake by the LMO sorbent. Since the radioactive loading of the sorbent is significantly reduced by using HCl as desorption agent, sorption seems to be a (at least partially) reversible process.

5. Conclusions

Sorption behavior of Th-U series nuclides dissolved in the geothermal brine at Bruchsal was studied in the framework of on-site tests for lithium extraction. The following findings can be derived from the data set obtained:

- Radioactive isotopes of radium and lead are sorbed by the lithium-manganese-oxide (LMO) sorbent in the DLE tests performed at Bruchsal. The maximum uptake of ^{210}Pb is 60%; uptake of ^{226}Ra and ^{228}Ra is half as high.
- Higher pH values favor the sorption of the Th-U series nuclide probably due to higher negative charge of the LMO surface. Increasing the pH from 2 to 4 leads to an increase of the mean sorption capacity from 230 mBq g^{-1} to 330 mBq g^{-1} (^{226}Ra) and 140 mBq g^{-1} to 260 mBq g^{-1} (^{210}Pb).
- ^{226}Ra sorption capacity is highest for the test series with longest contact time of 30 min while comparably high sorption capacities for ^{210}Pb reached after 15 min.
- The values of the dimensionless distribution coefficient *K* for ^{226}Ra and ^{228}Ra vary between 0.12 and 0.45; *K* for ^{210}Pb vary between 0.14 and 1.37. For DLE experiments with contact times >15 min, the partition coefficient of ^{210}Pb fluctuates around a value of 1 and thus indicates a sorption equilibrium for this isotope.
- The regeneration phase using HCl as the desorbing agent reveals a reduction of the radioactive loading of the LMO sorbent. Desorption percentage of radium isotopes (^{226}Ra, ^{228}Ra) and ^{210}Pb varies between 25 and 100% and 16 to 100%, respectively, resulting in an average uptake in the range of 45–82 mBq g^{-1}: ^{228}Ra = 45 mBq g^{-1}; ^{226}Ra = 60 mBq g^{-1}; ^{210}Pb = 82 mBq g^{-1}.
- Despite this positive desorption performance, radioactive loading of LMO granules increases with each test series conducted. After completion of the last experiment E4, the measured specific activity of ^{226}Ra (^{228}Ra) is about 1000 (560) mBq g^{-1} while the measured specific activity of ^{210}Pb amounts to 2400 mBq g^{-1}.

Further investigations into the specific sorption processes will enable the development of a technical solution for the future reduction or prevention of radionuclide accumulation on Mn-based oxide sorbents. Further research is in progress to determine the sorption processes in more detail.

CRediT authorship contribution statement

Lena Kölbel: Writing – review & editing, Writing – original draft, Visualization, Project administration, Methodology, Investigation, Conceptualization. **Klemens Slunitschek:** Writing – review & editing, Writing – original draft, Investigation. **Elif Kaymakci:** Writing – review & editing, Project administration, Investigation. **Thomas Kölbel:** Writing – review & editing, Visualization, Supervision. **Rebekka Reich:** Writing – review & editing, Investigation. **Jochen Schneider:** Supervision, Resources.

Declaration of competing interest

The authors declare that they have no known competing financial interests or personal relationships that could have appeared to influence the work reported in this paper.

Acknowledgments

We gratefully acknowledge financial support from the Federal Ministry for Economic Affairs and Climate Action (BMWK) within the UnLimited project under grant no. 03EE4023. This study would not have been possible without the great cooperation within the UnLimited team. In addition, we would like to thank the laboratories of EnBW Kernkraft GmbH (Philippsburg) and IAF Radioökologie GmbH (Radeberg) for their expertise and support in carrying out the radiochemical measurements. The authors are also grateful to the staff of GeoB for their support. Careful reviews by anonymous reviewers improved the manuscript significantly.

References

Agrawal, A., Sahu, K.K., Pandey, B.D., 2005. Systematic studies on adsorption of lead on sea nodule residues. J. Colloid Interface Sci. 281 (2005), 291–298. https://doi.org/10.1016/j.jcis.2004.08.103.

Bateman, H., 1910. Solution of a system of differential equations occurring in the theory of radioactive transformations. Proc. Camb. Philos. Soc. 15, 423–427.

Brown, P., Matyskin, A., Ekberg, C., 2022. The aqueous chemistry of radium. Radiochim. Acta 110 (6–9), 505–513. https://doi.org/10.1515/ract-2021-1141.

Chiban, M., Soudani, A., Sinan, F., Persin, M., 2011. Single, binary and multi-component adsorption of some anions and actions on *C. edulis* plant particles. J. Colloids Surf. B. 82, 267–276. https://doi.org/10.1016/j.colsurfb.2010.09.013.

Chitrakar, Ramesh, Kanoh, Hirofumi, Miyai, Yoshitaka, Ooi, Kenta, 2000. A new type of manganese oxide (MnO 2 ·0.5H 2 O) derived from li 1.6 Mn 1.6 O 4 and its Lithium ion-sieve properties. In. Chem. Mater. 12 (10), 3151–3157. https://doi.org/10.1021/cm0000191.

Chitrakar, Ramesh, Kanoh, Hirofumi, Miyai, Yoshitaka, Ooi, Kenta, 2001. Recovery of Lithium from seawater using manganese oxide adsorbent (H1.6Mn1.6O4) derived from Li1.6Mn1.6O4. Ind. Eng. Chem. Res. 40 (9), 2054–2058. https://doi.org/10.1021/ie000911h.

Condomines, M., Rihs, S., Lloret, E., Seidel, J.L., 2010. Determination of the four natural Ra isotopes in thermal waters by gamma-ray spectrometry. Appl. Radiat. Isot. 68, 384–391. https://doi.org/10.1016/j.apradiso.2009.10.056.

Davis, J.A., Kent, D.B., 1990. Surface complexation modeling in aqueous geochemistry (Eds.). In: Hochella, M.F., White, A.F. (Eds.), Mineral–Water Interface Geochemistry, Vol. 23. Mineralogical Society of America, Washington, DC, pp. 177–260 (ISSN: 1943-2666).

Demir, M.M., Toprak, S., Oncel, C., Yilmaz, S., BABA, A., Aksoy Koc, G., 2022. Lithium Extraction from Geothermal Brine Using y-Mno2. In: A Case Study for Tuzla Geothermal Power Plant. https://doi.org/10.2139/ssrn.4239318.

Eggeling, L., Genter, A., Kölbel, T., Münch, W., 2013. Impact of natural radionuclides on geothermal exploitation in the upper Rhine graben. Geothermics 47, 80–88. https://doi.org/10.1016/j.geothermics.2013.03.002.

Elwakeel, K.Z., Atia, A.A., 2014. Uptake of U(VI) from aqueous media by magnetic Schiff's base chitosan composite. J. Clean. Prod. 70, 292–302. https://doi.org/10.1016/j.jclepro.2014.02.017.

Elwakeel, K.Z., Hamza, M.F., Guibal, E., 2021. Effect of agitation mode (mechanical, ultrasound and microwave) on uranium sorption using amine- and dithizone-functionalized magnetic chitosan hybrid materials. Chem. Eng. J. 411, 128553 https://doi.org/10.1016/j.cej.2021.128553.

Han, R.P., Zou, W.H., Zhang, Z.P., Shi, J., Yang, J.J., 2006. Removal of copper(II) and lead(II) from aqueous solution by manganese oxide coated sand I. Characterization and kinetic study. J. Hazard. Mater. 137, 384–395. https://doi.org/10.1016/j.jhazmat.2006.02.021.

Karapinar, H.S., Kilicel, F., Ozel, F., Sarilmaz, A., 2021. Fast and effective removal of Pb (II), cu(II) and Ni(II) ions from aqueous solutions with TiO2 nanofibers: synthesis, adsorption-desorption process and kinetic studies. Int. J. Environ. Anal. Chem. https://doi.org/10.1080/03067319.2021.1931162.

Kölbel, L., Kölbel, T., Maier, U., Sauter, M., Schäfer, T., Wiegand, B., 2020. Study of water-rock interactions in the Bruchsal geothermal system by means of U-Th series radionuclides. Geotherm. Energy 8, 24. https://doi.org/10.1186/s40517-020-00179-4.

Kölbel, L., Kölbel, T., Herrmann, L., Kaymakci, E., Ghergut, I., Poirel, A., Schneider, J., 2023. Lithium extraction from geothermal brines in the upper Rhine graben: a case study of potential and current state of the art. Hydrometallurgy 106131. https://doi.org/10.1016/j.hydromet.2023.106131.

Kosmulski, M., 2009. pH-dependent surface charging and points of zero charge. IV. Update and new approach. J. Colloid Interface Sci. 337 (2), 439–448. https://doi.org/10.1016/j.jcis.2009.04.072.

Krishnaswami, S., Graustein, W.C., Turekian, K.K., Dowd, J.F., 1982. Radium, thorium, and radioactive lead isotopes in groundwaters: applications to the in-situ determination of adsorption-desorption rate constants and retar- dation factors. Water Resour. Res. 18 (6), 1633–1675. https://doi.org/10.1029/WR018i006p01663.

Ku, T.L., Luo, S., Leslie, B.W., Hammond, D.E., 1998. Assessing in-situ radionuclide migration from natural analog studies: response to McKinley and Alexander (1996). Radiochim. Acta 80, 219–223. https://doi.org/10.1524/ract.1998.80.4.219.

Ku, T.-L., Luo, S., Leslie, B.W., Hammond, D.E., 1992. Decay-series disequilibria applied to the study of water-rock interaction and geothermal systems. In: Ivanovich, M., Harmon, R.S. (Eds.), Uranium-Series Disequilibrium: Applications to Earth, Marine, and Environmental Sciences. Clarendon Press, Oxford, pp. 631–668.

Maleki, A., Hayati, B., Najafi, F., Gharibi, F., Joo, S.W., 2016. Heavy metal adsorption from industrial wastewater by PAMAM/TiO2 nanohybrid: preparation, characterization and adsorption studies. J. Mol. Liq. 224 (A), 95–104. https://doi.org/10.1016/j.molliq.2016.09.060.

McKenzie, R.M., 1980. The adsorption of Lead and other heavy metals on oxides of manganese and Iron. Aust. J. Soil. Res. 1980 (18), 61–73. https://doi.org/10.1071/SR9800061.

Moon, D.S, Burnett, W.C., Nour, S., Horwitz, P., Bond, A., 2003. Preconcentration of radium isotopes from natural waters using MnO2 Resin. Applied Radiation and Isotopes 59 (4), 255–262. https://doi.org/10.1016/S0969-8043(03)00193-3.

Nirdosh, I., Trembley, W.B., Johnson, C.R., 1990. Adsorption-desorption studies on the 226Ra-hydrated metal oxide systems. Hydrometallurgy 24 (1990), 237–248. https://doi.org/10.1016/0304-386X(90)90089-K.

Osmond, J.K., Cowart, J.B., 1992. Ground water. In: Ivanovich, M., Harmon, R.S. (Eds.), Uranium-Series Disequilibrium: Applications to Earth, Marine, and Environmental Sciences. Oxford Science Publications, p. 290.

Park, Myoung Jun, Nisola, Grace M., Beltran, Arnel B., Torrejos, Rey Eliseo C., Seo, Jeong Gil, Lee, Seong-Poong, et al., 2014. Recyclable composite nanofiber adsorbent for li+ recovery from seawater desalination retentate. Chem. Eng. J. 254, 73–81. https://doi.org/10.1016/j.cej.2014.05.095.

Patterer, M.S., Medici, F., Peluso, M.A., Sambeth, J.E., 2018. Lead adsorption from aqueous solution using manganese oxides recovered from spent alkaline and Zn/C batteries. Chem. Eng. Trans. 67 (ISBN 978-88-95608-64-8.).

Pribnow, D., Schellschmidt, R., 2000. Thermal tracking of upper crustal fluid flow in the Rhine graben. Geophys. Res. Lett. 27, 1957–1960. https://doi.org/10.1029/2000GL008494.

Reich, R., Slunitschek, K., Danisi, R.M., Eiche, E., Kolb, J., 2022. Lithium extraction techniques and the application potential of different sorbents for Lithium recovery from brines. Miner. Process. Extr. Metall. Rev. 1–20. https://doi.org/10.1080/08827508.2022.2047041.

Rohrer, G.S., 2001. Structure and Bonding in Crystalline Materials. Cambridge University Press, Cambridge. https://doi.org/10.1017/CBO9780511816116.

Sanjuan, B., Millot, R., Innocent, Ch., Dezayes, Ch., Scheiber, J., Brach, M., 2016. Major geochemical characteristics of geothermal brines from the upper Rhine graben granitic basement with constraints on temperature and circulation. Chem. Geol. 428, 27–47. https://doi.org/10.1016/j.chemgeo.2016.02.021.

Schmidt, M., 2023. Rohstoffrisikobewertung – Lithium. DERA Rohstoffinformationen 54, 81.

Seip, A., Safari, S., Pickup, D.M., Chadwick, A.V., Ramos, S., Velasco, C.A., Cerrato, J.M., Alessi, D.S., 2021. Lithium recovery from hydraulic fracturing flowback and produced water using a selective ion exchange sorbent. Chem. Eng. J. 426, 130713 https://doi.org/10.1016/j.cej.2021.130713.

Shi, X., Zhou, D., Zhang, Z., Yu, L., Xu, H., Chen, B., Yang, X., 2011. Synthesis and properties of Li1.6Mn1.6O4 and its adsorption application. Hydrometallurgy 110, 1-4, 99–106. https://doi.org/10.1016/j.hydromet.2011.09.004.

Tian, L., Ma, W., Han, M., 2010. Adsorption behavior of li+ onto nano-lithium ion sieve from hybrid magnesium/lithium manganese oxide. Chem. Eng. J. 156 (1), 134–140. https://doi.org/10.1016/j.cej.2009.10.008.

Vajedi, F., Dehghani, H., 2019. The characterization of TiO2-reduced graphene oxide nanocomposites and their performance in electrochemical determination for removing heavy metals ions of cadmium(II), lead(II) and copper(II). Mater. Sci. Eng. B 2019 (243), 189–198. https://doi.org/10.1016/j.mseb.2019.04.009.

Wang, J., Zheng, S., Shao, Y., Liu, J., Xu, Z., Zhu, D., 2010. Amino-functionalized Fe(3)O(4)@SiO(2) core-shell magnetic nanomaterial as a novel adsorbent for aqueous heavy metals removal. J. Colloid Interface Sci. 349 (1), 293–299. https://doi.org/10.1016/j.jcis.2010.05.010.

Wang, Lu, Meng, Chang Gong, Ma, Wei, 2009. Study on li+ uptake by lithium ion-sieve via the pH technique. Colloids Surf. A: Physicochem. Eng. Asp. 334 (1–3), 34–39. https://doi.org/10.1016/j.colsurfa.2008.09.050.

Wang, S.-G., Gong, W.-X., Liu, X.-W., Yao, Y.-W., Gao, B.-Y., Yue, Q.-Y., 2007. Removal of lead(II) from aqueous solution by adsorption onto manganese oxide-coated carbon nanotubes. Sep. Purif. Technol. 58 (2007), 17–23. https://doi.org/10.1016/j.seppur.2007.07.006.

Warren, I., 2021. Techno-Economic Analysis of Lithium Extraction from Geothermal Brines. National Renewable Energy Laboratory, Golden, CO. NREL/TP-5700-79178.

Wei, Y., Salih, K.A.M., Rabie, K., Elwakeel, K.Z., Zayed, Y.E., Hamza, M.F., Guibal, E., 2021. Development of phosphoryl-functionalized algal-PEI beads for the sorption of Nd(III) and Mo(VI) from aqueous solutions – application for rare earth recovery from acid leachates. Chem. Eng. J. 412, 127399 https://doi.org/10.1016/j.cej.2020.127399.

Xu, X., Chen, Y., Wan, P., Gasem, K., Wang, K., He, T., Adidharma, H., Fan, M., 2016. Extraction of lithium with functionalized lithium ion-sieves. Prog. Mater. Sci. 84, 276–313. https://doi.org/10.1016/j.pmatsci.2016.09.004.

10. Discussion

Requirements for geothermal DLE and sorbent identification

The overall research aim of this thesis is to evaluate the potential of a selected LMO sorbent for DLE from geothermal brines. For this, requirements for geothermal DLE are identified from geothermal brine properties and the process conditions in geothermal power plants of the Upper Rhine Graben (URG). For integration into a geothermal power plant, resistance to high pressure of up to 25 bar, temperatures of 60–80°C and high salinity and corrosivity is required (Chapter 7). Additionally, the extraction process has to be fast to avoid large brine storage, due to the high flow rates of up to 90 L/s (Chapter 7, Stober and Bucher, 2012). To avoid the formation of scales, the technology has to work at the brine pH level of ~5 (Sanjuan et al., 2016; Reich et al., 2022). In order to achieve a relatively pure desorption solution, the technology has to have a high Li selectivity due to the high salinity of the brine (Reich et al., 2022). Furthermore, the technology must enable high Li recovery (Reich et al., 2022).

Spinel LMO sorbents are identified as a promising technology, based on the known fast kinetics and high selectivity for Li and low selectivity for the brine-dominating alkaline and alkaline earth elements (Reich et al., 2022). Furthermore, spinel LMO are functional at the native brine pH, even if sorption capacity is reduced in comparison to basic conditions (Reich et al., 2022). The attributed potential for high Li recovery is based on the LMO sorbents' high Li sorption capacity (Reich et al., 2022) and reported recovery rates ≥80% (e.g. Shi et al., 2011; Zandevakili et al., 2014; Seip et al., 2021).

Thermal stability of the sorbent under the brine temperatures of 60–80°C was assumed, since the sorbent is synthesised at a temperature of ~100–200°C during the hydrothermal step and ~400°C during the calcination (e.g. Chitrakar et al., 2000; Shi et al., 2011). Furthermore, different studies show successful Li extraction at 50°C without deterioration of the sorbent (e.g. Shi et al., 2011, Zhang et al., 2021a). The recent study by Disu et al. (2025) confirms the assumption of stability at elevated temperatures by observing no damage to the sorbent during extraction at 85°C. Furthermore, the study shows an exponential increase of sorption capacity in LMO between temperatures of 50–85°C, reinforcing the suitability of LMO for geothermal DLE.

The resistance of LMO sorbents to the pressure of the brine stream is assumed, as no specific studies on pressure resistance have been found. The assumption is based on the pressure during the hydrothermal synthesis step. Inside the autoclave, a saturation pressure of around 15 bar is created at 200°C (IAPWS, 2007; Shi et al., 2011).

Regarding the effects of high salinity and corrosivity, no detrimental effects on the sorbent have been reported in studies with highly saline brines, like e.g. Chitrakar et al. (2012), Zandevakili et al. (2014) or Zhang et al. (2021b) . Thus, LMO sorbents fulfil all the requirements necessary

for application in geothermal DLE. The biggest disadvantage of the LMO sorbents is the Mn dissolution due to the redox Li sorption process (Reich et al., 2022). Furthermore, reduction of the sorbent through organic molecules and subsequent Mn dissolution can occur. However, this has been primarily reported from application in oilfield brines, containing organic phases (Seip et al., 2021). Aside from the redox sensitivity, potential disadvantages are not related to the extraction process itself, such as challenging large-scale synthesis or acid costs (Reich et al., 2022).

Spinel LMO sorbents encompass various chemical compositions, such as $LiMn_2O_4$ or $Li_{1.33}Mn_{1.67}O_4$, often within the range of $Li_{1+x}Mn_{2-X}O_4$ with $0 \leq x \leq 0.33$, or the Li-rich spinel $Li_{1.6}Mn_{1.6}O_4$ (Wang et al., 2006). The sorbent $Li_{1.6}Mn_{1.6}O_4$ is chosen for the investigations over other LMO sorbents, due to its high Li concentration and the average oxidation state of Mn^{4+}, potentially resulting in lower Mn dissolution. The assessment of the potential of the sorbent for geothermal DLE focuses on Li sorption performance, selectivity and purity of the desorption solution. The Li sorption performance determines the sorbent demand and plant size in industrial DLE, while selectivity and desorption solution purity determine the extent of downstream purification to achieve battery grade.

Assessment of the lithium sorption performance of LMO in Upper Rhine Graben brine

Sorbent synthesis

The Li sorption performance is assessed based on Li sorption capacity and kinetics. These two factors are highly relevant to industrial geothermal DLE, controlling sorbent demand and the duration of extraction cycles, regardless of flow- or batch-reactor setup. The sorption capacity strongly depends on the phase purity of the sorbent material, with regard to the spinel phase and presence of other phases. With MnO_2 powder as the educt, the synthesis produces a precursor material that predominantly consists of the target phase $Li_{1.6}Mn_{1.6}O_4$, showing a high degree of conversion of intermediate phases (Slunitschek et al., 2025). For the granular Mn ore as a starting material, the same synthesis protocol resulted in a less pure precursor material with greater deviations from the ideal composition (Chapter 8). In the granular precursor and sorbent material, synthesis intermediate phases are contained to a greater extent compared to the powder precursor and sorbent material, as shown in the diffractograms in Slunitschek et al. (2025) and Chapter 8. Additionally, phase purity of the granular material is reduced by the non-manganese phases, such as Fe_2O_3 and SiO_2.

The reason for the incomplete transformation of Mn_2O_3 to $LiMnO_2$ in the hydrothermal step is most likely due to Li transport limitation. Diffusion-driven mass transfer is facilitated by large surface areas and small particle diameters (Qiu et al., 2009; Amalraj et al., 2013). Thus, larger particle diameters result in longer diffusion path lengths and reduced mass transfer rates. Since the Mn ore granulates are comparatively large with a 1–3 mm particle diameter,

diffusion-driven processes require more time than for the powder sorbent with a <40 µm diameter. Thus, the incomplete transformation of Mn_2O_3 to $LiMnO_2$ results from an insufficient duration of the hydrothermal step, leading to an incomplete distribution of Li inside the granular particles. The incomplete transformation of $LiMnO_2$ to $Li_{1.6}Mn_{1.6}O_4$ might be due to thermal diffusion limitation and would thus require a longer duration of the second calcination step. An increase in transformation ratio through temperature increase is only possible to a limited extent, as new impurity phases can be formed. For the hydrothermal step, pure-phase $LiMnO_2$ is achieved at 160°C–180°C, while at temperatures ≥200°C the layered Li_2MnO_3 phase is formed (Liu et al., 2008; Fu et al., 2020). The optimal temperature range for the transformation of $LiMnO_2$ to $Li_{1.6}Mn_{1.6}O_4$ through calcination is 400°C–450°C, while an increase of temperature to >500°C results in the formation of Li_2MnO_3 and $LiMn_2O_4$ (Shi et al., 2011; Fu et al., 2020; Disu et al., 2025). Furthermore, heat damage to the crystal structure can occur at temperatures >550°C (Disu et al., 2025).

Similar to the transformation of Mn_2O_3 to $LiMnO_2$, the initial Li desorption of the granular sorbent is limited by Li diffusion. In the initial desorption of the granular sorbent, only 52.4% of the contained Li is desorbed, whereas 97.2% of Li is removed from the powder sorbent (Chapter 8, Slunitschek et al., 2025). During initial desorption, Li desorbs from the outer layers of the particle, resulting in a concentration gradient and Li migration from the inside to the outside (Ammundsen et al., 1999; Huang et al., 2020). The duration of the initial desorption step was insufficient for complete intraparticle Li transfer. Consequently, Li concentration in the granular sorbent decreases continuously over the course of all pilot plant experiments, spanning over 5 months.

The incomplete transformation and heterogeneous composition of the granular precursor and sorbent result in a reduced maximum Li sorption capacity in comparison to the precursor from pure powder MnO_2, with 56.3 mg/g and 67.0 mg/g, respectively (Chapter 8, Slunitschek et al., 2025). However, the deviation is just 8.4%, showing that large precursor and sorbent particles have the potential for a high Li sorption capacity. In order to increase the maximum Li capacity, incomplete transformation can probably be reduced through adaptation of the synthesis process, especially through increasing the duration of synthesis steps. Furthermore, a higher-purity synthesis starting material can be used. Alternatively, the non-manganese phases can be removed by comminution and separation. However, this would result in the loss of the large particle size.

Resistance to high pressure and high temperature is not investigated directly, but a first indication can be derived from the pilot plant experiments. Decreasing continuous sorbent loss occurred over 45 extraction cycles, accumulating to a total loss of ~11% of sorbent weight (experiment 5 in Chapter 8). Thus, 89% of the granular sorbent remained, suggesting a certain degree of stability under the geothermal conditions. In contrast, the continuous loss of the

powdered sorbent over 15 cycles suggests reduced mechanical stability in the applied stirred conditions. Overall, sorbent degradation can result from, amongst others, potentially temperature and pressure stress, hydrodynamic stress, disproportionation during desorption (Reich et al., 2022; Slunitschek et al., 2025), microcracking (Liu et al., 2019; Huang et al., 2020) and splitting of nanoparticle agglomerates (Safari et al., 2020).

Lithium sorption performance

The achieved sorption capacities at 15 min contact time with powder sorbent are in a similar range for the different brines, with 14.6 mg/g from Soultz-sous-Forêts brine (Slunitschek et al., 2025) and 10.6 mg/g from Bruchsal brine (Chapter 6, based on the first cycle; Table 10.2). The deviations result, amongst others, from the higher Li concentration leading to higher sorption capacity, with 175 mg/L in Soultz-sous-Forêts brine and 163 mg/L in Bruchsal brine (Table 10.1, Herrmann et al., 2025). Furthermore, the sorption capacity from Bruchsal brine is decreased due to the higher sorbent mass-brine volume (m/V) ratio, with 2.5 to 4.11 g/L, respectively (Herrmann et al., 2025).

Table 10.1: Composition of all brines used in Slunitschek et al. (2025), Chapter 6 and Chapter 8, respectively. n.a.: not analysed.

	Li	Na	Mg	K	Ca
	mg/L	mg/L	mg/L	mg/L	mg/L
Soultz-sous-Forêts, depleted Slunitschek et al. (2025)	175	32422	131	3337	7013
Bruchsal, depleted Chapter 6	163	40591	342	3199	7393
Bruchsal, on-site Chapter 8	169	36868	342	3313	7466

	Mn	Zn	As	Sr	Ba	Pb
	mg/L	mg/L	mg/L	mg/L	mg/L	mg/L
Soultz-sous-Forêts, depleted Slunitschek et al. (2025)	16.6	2.31	3.23	432	4.41	n.a.
Bruchsal, depleted Chapter 6	23.3	9.77	3.66	378	7.12	0.71
Bruchsal, on-site Chapter 8	22.9	15.1	8.96	356	8.73	3.23

Similar to the sorption capacity, the powder sorbent achieves similar Li extraction and fractional occupancy values from both brines at the same contact time (Table 10.2). Thus, the sorbent shows a similar Li sorption performance in both brines, despite the differences in brine chemistry. The fractional occupancies of 15.6% and 21.8% show that many binding sites are unoccupied and only a fraction of the Li sorption potential is utilised.

While the evaluation of the powder is based on sorption data, the evaluation of the granular sorbent is based on the entrainment-corrected desorption data. This results from the

application point of view of the pilot plant experiments. For the granular sorbent, the parameters are significantly lower, with maximum Li capacities of 0.4 mg/g, fractional occupancies of 0.7% and Li extraction of 4.8% (Table 10.2). Thus, the Li sorption performance of the granular sorbent is significantly lower in comparison to the powdered sorbent. This results predominantly from low usage efficiency of the sorbent, as shown in the low fractional occupancy, and only partly from the higher m/V ratio of 21.4 g/L. Achievement of fractional occupancies of 44–65% has been reported for $Li_{1.6}Mn_{1.6}O_4$ and similar spinel LMO sorbents, corresponding to sorption capacities of up to 30–44 mg/g (Chen et al., 2016; Li et al., 2018; Qian et al., 2019; Herrmann et al., 2025; Slunitschek et al., 2025). This shows a highly efficient usage of the sorbent, which is only achievable under optimal conditions. Thereby, especially the brine pH is of importance, as Li^+-H^+ ion exchange correlates positively with pH (Shi et al., 2011). To use the sorbent so efficiently and achieve such high sorption capacities, a pre-treatment step with base addition of e.g. NaOH could be integrated, as discussed in Reich et al. (2022). However, this could potentially lead to scale formation and needs to be investigated. Furthermore, the resulting lower sorbent demand and thus costs need to balance the base expenses. Further Li sorption influencing factors, e.g. temperature, brine Li concentration, and contact time, are not or only partly changeable, due to the constraints from the geothermal power plant and the brine.

Table 10.2: Lithium sorption capacity , fractional occupancy and Li extraction at 15 min contact time. From the kinetic experiment in Slunitschek et al. (2025), Chapter 6 and 8.

sorbent form & brine	Sorption capacity	Fractional occupancy	Li extraction	Source
	mg/g	%	%	
powder Soultz-sous-Forêts	14.6	21.8	21.0	Slunitschek et al. (2025)
powder Bruchsal	10.6	15.6	20.6	Chapter 6
granular Bruchsal	0.4	0.7	4.8	Chapter 8

Similar to the synthesis, the limited performance of the granular sorbent stems from the large particle diameter and diffusion limitation. Consequently, binding sites within the particle do not participate in the sorption process, as the contact time is too short. This results in low Li sorption and thus low fractional occupancy and low Li sorption capacity. Regarding only the sorbent, this indicates that particle size is the dominant factor for Li sorption performance and the effect of phase purity is relatively low.

Thus, in order to increase the Li sorption performance, diffusion limitation needs to be reduced, e.g. through smaller particles, higher specific surface area or higher temperature. Han et al. (2012) showed that the sorption capacity of 2–3 mm large granulates with a porosity of 90.4%

was just 20.4% of the powder capacity when extracting Li from seawater. Yoshizuka et al. (2006) granulated the spinel sorbent λ-MnO_2 to 1–2 mm large particles and extracted Li from seawater, reaching ~4.7 mg/g, calculated after the data provided in the article. Xiao et al. (2015) achieved a sorption capacity of 4.3 mg/g with a PVC-granulated LMO sorbent of 0.3–0.7 mm and a brine from the Qarhan salt lake, China. Furthermore, Xiao et al. (2012) used LMO granulates of similar size to this study (Chapter 8), with 2.0–3.5 mm diameter, and achieved a sorption capacity of 16.1 mg/g. Compared to powdered sorbents, which achieved Li sorption capacities of e.g. 30.6 mg/g (Slunitschek et al., 2025) or 40.8 mg/g (Chitrakar et al., 2001), the granulated materials have lower capacities. In comparison to the granular, ore-derived sorbent, significantly higher sorption capacities can be achieved with granulated sorbents, albeit not reaching the capacities of powdered sorbents.

In Xiao et al. (2012; 2015), the particles are granulated from powdered sorbent, potentially resulting in higher porosity, higher inner and outer surface area and lower diffusion limitation, facilitating Li sorption. This is in contrast to the granular sorbent from Mn ore, exhibiting a compact particle structure and likely possessing a lower porosity and specific surface area. Intraparticle diffusion is identified as the limiting process in Xiao et al. (2012; 2015).

As shown in Chapter 8 and the literature, an increase in particle size is often accompanied by a strong decrease in sorption capacity. This reduces the significance of powder-based sorption capacity as a metric for industrial application. Thus, powder-based sorption capacities are only to a limited extent suitable for the initial potential evaluation of sorbents for industrial DLE, independent of the brine type.

Lithium sorption kinetics

In Slunitschek et al. (2025), fast Li sorption kinetics are achieved, reaching Li sorption capacities of 12.8 and 14.6 mg/g at contact times of 5 and 15 minutes, respectively. With the granular sorbent, Li sorption capacities of 0.29 and 0.39 mg/g are achieved at comparable Li concentrations and the same contact times (Chapter 8). In this regard, the Li sorption kinetics for the granular sorbent are 37–44 times slower than for the powder sorbent, based on the Li sorption rates for both durations (Table 10.3). As shown in Reich et al. (2022), one advantage of LMO is the fast sorption kinetics, which are confirmed here for the powder sorbent, but slow kinetics are indicated for the granular sorbent. The indicated slow sorption kinetics most likely result from diffusion limitation, as discussed above. Thus, in order to increase the sorption kinetics, an increase in specific surface area, e.g. through increased porosity, or a decrease in particle size is required.

Table 10.3: Lithium sorption capacity Q and average sorption rate in relation to contact time t for the powder and granular sorbent.

Sorbent form & brine	t	Q	Sorption rate	Source
	min	mg/g	mg/(g*min)	
powder	5	12.8	2.55	Slunitschek et al. (2025)
Soultz-sous-Forêts brine	15	14.6	0.97	
granular	5	0.32	0.064	Chapter 8
Bruchsal brine	15	0.68	0.045	

The powdered sorbent possesses a high Li sorption performance, based on its high Li sorption capacity and fast Li sorption kinetics. However, this potential is not retained in the granular material. As particles larger than powder are required for industrial integration, granular LMO materials maintaining the Li sorption performance of $Li_{1.6}Mn_{1.6}O_4$ while minimising diffusion limitations are needed.

Investigation of selectivity and element accumulation

Selectivity

The selectivity of the sorbent determines the co-extraction of other elements contained in the brine and the purity of the desorption solution, amongst other processes. Through the selectivity determination and their type of binding, countermeasures can be identified to prevent co-extraction and increase desorption solution purity.

Similar orders of selectivity are achieved for the Soultz-sous-Forêts and Bruchsal depleted brines, with:

Mn > Zn > As > Ba > **Li** > Sr > Ca > K, Mg > Na (Soultz-sous-Forêts, Slunitschek et al., 2025)

Mn > Pb > As > Zn, Ba > **Li** > Na, Mg, S, K, Ca, Sr (Bruchsal, Chapter 6)

The sorbent shows a higher selectivity for Li than the brine-dominating elements Na, Ca and K (Table 10.1). Although the separation of Li from Mg can be difficult due to the similar ionic radii (Song et al. 2017; Wei et al. 2020), a higher selectivity for Li is achieved here. The low selectivity for Mg enables the application of the sorbent for DLE from Mg-rich brines, which cannot be processed through evaporative mining or other sorbents, such as LiAl–LDH (Safari et al., 2020; Wu et al., 2025) . For both brines, the selectivity for Mn, Zn, As and Ba is higher than for Li, with the highest selectivity for Mn. The switched order for Zn and As from Soultz-sous-Forêts and Bruchsal might result from the higher Zn concentration in the Bruchsal brine (Table 10.1), leading to a higher separation coefficient, with 0.39 in Chapter 6 and 0.09 in Slunitschek et al. (2025). As discussed in Slunitschek et al. (2025) and Chapter 6, the higher selectivity of Mn, Zn, As and Pb stems from inner-sphere binding, as shown for As and Pb by the XPS analysis.

Although an order of selectivity was not determinable for the granular sorbent, due to the strong influence of entrainment and corrosion, the sorption behaviour of the granular sorbent is similar to the powdered sorbent. The enrichment of Li, Fe, Zn, As, Ba and Pb in the pilot plant desorption solution supports the high selectivity of the sorbent for these elements. Furthermore, high selectivity for S, K, As, Mo and Pb is shown through the accumulation at the sorbent, although the behaviour of S, K and Mo remains unclear. The low transport of Na, Mg, K and Ca by sorption into the desorption solution and predominant transport by entrainment supports the low selectivity for these elements.

Accumulation

Accumulation of ions at the sorbent is observed in all studies, where most of the accumulating elements have a higher selectivity than Li (Table 10.4). No relation between accumulation and the differences in composition of depleted Soultz-sous-Forêts, Bruchsal and on-line Bruchsal brine has been determined (Table 10.1). The accumulation of Zn is shown in Slunitschek et al. (2025), while no indications are given in the test-bench and pilot plant experiments. The reason for this is unclear, as Zn occurs in all brines (Table 10.1). The same applies to Ba, for which accumulation is indicated in the laboratory experiments but not in the pilot plant experiments. The accumulation of Pb observed in Kölbel et al. (2024b) is shown and confirmed through XPS analysis in Chapter 6. While the distinct presence of S at the sorbent is shown in Chapter 6, results in Chapter 8 are inconclusive. Since Pb and S have not been regarded in Slunitschek et al. (2025), no statement regarding the accumulation is possible. For Mo, no comparison is possible as it was only analysed in the experiments in Chapter 8. In contrast to the pilot plant experiments, no K binding is shown in Slunitschek et al. (2025) and the test bench experiment. This might result from the sorption of K at K-bearing minerals, e.g. cryptomelane, contained in the Mn ore but not in the MnO2 powder. While accumulation of Ca is only observed in Chapter 6, Herrmann et al. (2025) report indications for Ca surface deposits on LMO sorbents after DLE experiments with Bruchsal geothermal brine as well. In addition, accumulations of Pb, Ba, Sr, Al, Na, K, Mg and Fe from the same brine are reported by Herrmann et al. (2022; 2025). While the accumulations can result from inner- or outer-sphere binding, precipitates from the brine not removed during the washing step cannot be excluded. Reich et al. (2024), for example, observed gypsum crystallites amongst the studied sorbent particles after experiments with geothermal brine, and Nitschke et al. (2014) report the formation of baryte-celestine solid solution scales ($(Ba,Sr)SO_4$) from Soultz-sous-Forêts brine.

Table 10.4: Accumulated elements at the sorbent.

	Accumulation
Slunitschek et al. (2025)	As, Zn, Ba
Chapter 6	Ca, S, As, Ba, Pb
Chapter 8	(S), K, As, Mo, Pb
Kölbel et al. (2024b)	Ra, Pb

The identification of sorbent selectivity, extent of accumulation, and the binding process allows manipulation of the sorbent, aiming to increase selectivity and reduce sorption of competing elements. The selectivity of the sorbent can be influenced by various methodologies, e.g., substitution of Mn in the crystal framework (e.g. Herrmann et al., 2025; Yan et al., 2025). Another approach is coating, in which a layer of a different material is formed on the particle surface, e.g., SiO2, ZrO2, Al oxide, or Ni oxide, acting as a physical barrier (Ohashi and Tai, 2019; Wang et al., 2022; Li et al., 2023).

Due to the charged surface of the sorbent, physisorption and outer-sphere complexes cannot be avoided, such as with Na, K, Ca (Chapter 5). However, through intermediate wash steps, these can be partially or completely removed. For column-flow reactors, plug-flow of the desorption solution can potentially replace the wash step. Thereby, the desorption solution moves through the column with minimal axial mixing, causing physisorbed species to concentrate in the leading fraction of the effluent (Nauman, 2008). This fraction can then be discarded or pumped into the fresh brine stream, if Li is contained in considerable concentrations. In order to avoid inner-sphere complexes, the surface of the sorbent has to be changed, e.g. through the application of a coating. However, inner- and outer-sphere complexes can form on the coated layer as well.

The investigations show that the sorbent has the required high selectivity for Li and only a low selectivity for the brine-dominating elements. Furthermore, a high stability of the sorption processes and the selectivity is shown for the powdered sorbent under laboratory conditions over 15 cycles (Chapter 6) for Li, Na, Mg, S, K, Ca, Sr, Mn, Zn, As, Ba, Pb. The stable selectivity of Li, Mn, Zn, As, Ba and Pb is supported by the on-line experiments through the constant, entrainment-corrected increase rates. Stable selectivity of S and K is indicated through the accumulation at the sorbent, occurring during the on-line experiments. In addition, the accumulation of Mo indicates stable selectivity; however, this was not assessed in the laboratory experiments. Due to the strong impact of brine entrainment, selectivity cannot be assessed for Na, Mg, S, K, Ca and Sr in the on-line experiments. Due to the high selectivity stability for Li and competing elements, the sorbent has a high potential for industrial long-term application in highly saline brines, like those of the Upper Rhine Graben. This is emphasised by the determination of the sorption stability under upscaled in situ conditions.

Purity and origin of impurities

Along with Li concentration, purity is one of the most important properties of the desorption solution. This results from the extent of required downstream purification processing to achieve battery-grade quality. Thus, a minimisation of downstream processing through maximisation of purity in the DLE process is pursued.

The purity of the desorption solution is defined as the ratio of Li concentration to total concentration. Only low purity of the desorption solution was achieved in the pilot plant experiments. The impurity of the desorption solution is dominated by brine entrainment, with plant corrosion and co-extraction by the sorbent as additional sources. The extent of cross-contamination with brine entrainment was successfully reduced through the washing step between sorption and desorption. However, only 2.2% purity of the desorption solution was achieved.

Due to the low amount of sorbent of <150 g, the low sorption capacity of 0.4 mg/g and the comparatively large volume of desorption solution (6.2 L and 22 L), only low Li concentrations in the desorption solution were achieved. While recycling of the desorption solution increased the Li concentration, the concentrations of all other elements increased continuously as well, resulting in a constant Li-impurity ratio. Thus, the high Li concentration relative to the total impurity concentration required to achieve high purity or battery grade could not be achieved. Furthermore, this underscores the need for sufficient sorbent material, especially when conducting research under upscaled conditions.

A high corrosion resistance has been identified as a requirement for the pilot plant, due to the high corrosivity of the brine and the HCl desorption solution (Chapter 8, Mundhenk et al., 2013; Reich et al., 2022). Despite regard for this during the design of the plant through coating of the reactor, using polymer pressure hoses and primarily stainless steel, corrosion still occurs. A reduction of corrosion can be achieved through utilisation of non-metallic components where possible. Furthermore, more noble stainless steel can be used, but this is more expensive.

The investigations identified origins and pathways of contamination of the desorption solution. High purity was not achieved in the experiments, primarily due to the high cross-contamination at low Li concentrations. To thoroughly investigate the effect of different origins on purity, significantly more sorbent is needed.

Comparison with other DLE sorbents

Li-Mn oxide (LMO) and Li-Ti oxide (LTO) ion-exchange sorbents and Li-Al-Layered Double Hydroxide adsorbents (LiAl-LDH) are regarded as the most promising materials for DLE in general, including applications to geothermal brines (Reich et al., 2022; Nikkhah et al., 2024; Wu et al., 2025). However, LMO and LTO have been evaluated at pilot plant scale, but not at

industrial scale (e.g. Yoshizuka et al., 2006; Ventura et al., 2020), while LiAl-LDH have been applied at large-scale mining operations since 1996 in the Salar de Hombre Muerto, Argentina (Vera et al., 2023).

Li-Mn oxide and LTO both exhibit high Li sorption capacities (Reich et al., 2022; Gao et al., 2025; Saleem et al., 2025; Slunitschek et al., 2025). In particular, LTO can achieve Li sorption capacities of up to 78 mg/g, and LTO nanotubes can even reach 160.6 mg/g (Shoghi et al., 2021; Saleem et al., 2025). In comparison, LiAl-LDH exhibits low Li sorption capacities <7 mg/g (Safari et al., 2020). Regarding Li sorption kinetics, the LMO sorbents show faster kinetics than LiAl-LDH and LTO (Reich et al., 2022; Farahbakhsh et al., 2024; Slunitschek et al., 2025; Wu et al., 2025).

The LMO sorbent exhibits low selectivity toward Na, Mg, K and Ca, but shows high selectivity for Mn, Zn, As, Ba, Pb and radionuclides. Lithium Titanium Oxide sorbents also show a high selectivity toward Na, Mg, K and Ca (Reich et al., 2022; Kölbel et al., 2024b; Gao et al., 2025; Wu et al., 2025). In addition, sorption and partial accumulation of the radionuclides ^{226}Ra, ^{228}Ra and ^{210}Pb is reported for LTO sorbents as well (Kölbel et al., 2024a). Based on the sorption of radiogenic ^{210}Pb, sorption of the stable isotope ^{207}Pb can be assumed as well. However, no studies addressing the sorption of Mn, Zn, As or Ba have been found. The selectivity of LiAl-LDH adsorbents is lower in comparison to LMO and LTO sorbents (Reich et al., 2022; Mojid et al., 2025). While no information is available regarding the sorption of Mn, Zn, Ba or Pb, sorption of As is reported by Liu et al. (2006).

Compared to LiAl-LDH, the LMO sorbent shows a higher pH stability. Lithium Aluminum-LDH adsorbents require a minimum brine pH ≥ 6 to prevent deterioration (Saleem et al., 2025), whereas no signs of chemical degradation were observed for the LMO sorbent upon contact with URG brine at pH = 5. Similarly, LTO sorbents also show high pH stability (Gao et al., 2025; Ma et al., 2025). Thus, LMO and LTO sorbents are more suitable for application in low-pH brines. Furthermore, no brine pre-treatment to increase the pH is required, saving costs and chemicals.

Due to the redox-induced dissolution process, LMO sorbents exhibit lower chemical stability than LTO and LiAl-LDH, which may result in a shorter operational lifetime (Gao et al., 2018; Murphy and Haji, 2022; Farahbakhsh et al., 2024; Gao et al., 2025). In addition, LMO and LTO require acidic solutions for desorption, whereas LiCl solution is used for LiAl-LDH, which is typically produced on-site as part of the DLE product stream (Wu et al., 2025). Consequently, operating expenditures are higher for LMO and LTO.

For geothermal DLE applications, both LMO and LTO are promising sorbents due to their high Li sorption capacity and selectivity, but are limited by dissolution and slower kinetics, respectively. In addition, the production of particles suitable for industrial application remains challenging for both sorbents (Gao et al., 2025). In contrast, LiAl-LDH exhibit lower Li sorption

capacity and kinetics, selectivity and narrower pH stability, but offer acid-free desorption. Moreover, established large-scale production capacities and more than two decades of experience in industrial application and process design support the applicability. Although LiAl-LDH typically require brine pre-heating (Reich et al., 2022), this is of limited relevance in the geothermal setting, as elevated brine temperatures are already present. Therefore, LiAl-LDH adsorbents are also promising for the application in geothermal DLE, with the constraint of near-neutral brine conditions.

11. Conclusion

The potential of the LMO sorbent $Li_{1.6}Mn_{1.6}O_4$ for Li extraction from geothermal brines is evaluated based on the Li sorption performance, selectivity and purity of the desorption solution. The fast Li sorption kinetics, high Li sorption capacity, and high Li selectivity make the sorbent suitable for DLE from geothermal brines and other high-flow-rate applications. Therefore, it is important to preserve the high sorption capacity of powdered sorbent in larger particles. While the Mn ore-based sorbent allows for comparably simple production, the inclusion of foreign phases, diffusion limitations, and low sorption capacity currently make it unsuitable for achieving larger sorbent particles for industrial DLE. The stable sorption process over many cycles reflects the sorbent's potential for long-term application. The low selectivity of the sorbent for Na, Mg, K and Mg enable DLE from brines rich in these elements. For brines containing As, Ra, and Pb, preferential sorption and accumulation can reduce the sorbent's suitability. Furthermore, these findings highlight the importance of expanding sorption research to trace elements. To achieve a high-purity desorption solution, high sorbent selectivity, low cross-contamination, and high Li concentrations are required. Through the pilot plant experiments, the sorbent's functionality under ambient brine conditions was proven, and challenges in upscaling were identified. This shows the necessity of evaluating the sorbent in-situ in addition to laboratory experiments.

For further research on the accumulation of elements, the sorption behaviour of competing elements and the influence on Li sorption capacity, studies with mono-ionic solutions, competition experiments with Li and one competing element and brine studies are needed. These studies should always be conducted over several cycles to determine the development of sorption and desorption. To study the accumulation of elements on the sorbent and the development of sorption over time, long-term sorption experiments have to be conducted. In order to prove industrial suitability, experiments should be conducted in-situ and for at least 100 cycles. In addition to the chemical analysis of the experiment eluates and digested sorbents, SEM, XRD and XPS analysis should be conducted to determine the mineralogical phases, type of binding and changes to the sorbent.

Acknowledgments

I deeply thank Prof. Dr Jochen Kolb and Dr Elisabeth Eiche for enabling and supervising my research. Throughout all the years we worked together, you gave me the trust and freedom to develop and shape this research project to my own ideas. For this, I am deeply grateful.
I want to express my biggest gratitude to Prof. Dr Kirsten Drüppel for her support with mineralogical analysis, for answering my countless questions and discussing ideas and for always being open to a little chat. Your criticism and guidance have been of great importance to me.
My deepest respect and gratitude go to Kevin Altinger, without whose support the pilot plant would never have been realised. Additionally, I want to thank him for all the small projects we worked on together and for never getting tired of teaching me mechanical engineering and craft techniques. A major part of this research is based on Ralf Wachter's commitment and determination to create and build the devices and components I came up with. For this, I am deeply thankful.
I deeply thank Janine Wagner, Maya Denker, Chantal Kotschenreuther and Nadine Hüll for analysing countless samples and preparing and conducting experiments; this research would not have been possible without them. Special thanks to Janine Wagner for her organisational efforts and for working through my lengthy experimental descriptions. Furthermore, I want to thank Claudia Mößner, Gesine Preuß, Beate Ötzel and Kristian Nikoloski for their support with analysis and preparation. Furthermore, I want to thank the administrative staff Victoria Weist, Andrea Friedrich and Laura Neira.
Additionally, I want to thank the partners of the UnLimited project, especially Thomas Hettkamp and Elif Kaymakci, as well as the staff of the geothermal power plant in Bruchsal. Furthermore, I want to thank all my co-authors. For the supply of Mn ore and other Mn products and his interest, enthusiasm, and determination to support my work, I want to thank Jens Steenfadt from Tropag Oscar H. Ritter Nachf. GmbH. I thank Dr. Sylvio Indris and Vanessa Troillet for conducting NMR and XPS analyses and discussing the structure of the sorbent.
I also want to thank my PhD colleagues Michèle Jungmann, Rebekka Reich, André Wilhelms, Jonas Bauer and Simon Hector. For their review of this thesis, I want to thank Dr Ole Rabbel, Dr Valentin Goldberg, and Albert Riehm.
Additionally, I want to thank my parents for enabling me to pursue my studies and supporting me. I also want to thank Dr Agnes Slunitschek for her support and absolute trust in me and my abilities. In closing, I would like to thank Maren Zeiß and Verena Urban for their continuous support, patience, and encouragement.

Bibliography

Agemar, Thorsten; Brunken, Jörn; Jodocy, Marco; Schellschmidt, Rüdiger; Schulz, Rüdiger; Stober, Ingrid, (2013): Untergrundtemperaturen in Baden-Württemberg. In *zdgg* 164 (1), pp. 49–62. DOI: 10.1127/1860-1804/2013/0010.

Ajith, Nicy; Bhattacharyya, Kaustava; Ipte, Priyanka R.; Satpati, Ashis K.; Tripathi, Arvind K.; Verma, Rakesh; Swain, Kallola K., (2019): Interaction of arsenic(III) and arsenic(V) on manganese dioxide: XPS and electrochemical investigations. In *Journal of environmental science and health. Part A, Toxic/hazardous substances & environmental engineering* 54 (4), pp. 277–285. DOI: 10.1080/10934529.2018.1544478.

Amalraj, S. Francis; Sharon, Daniel; Talianker, Michael; Julien, Christian M.; Burlaka, Luba; Lavi, Ronit et al., (2013): Study of the nanosized Li2MnO3: Electrochemical behavior, structure, magnetic properties, and vibrational modes. In *Electrochimica Acta* 97, pp. 259–270. DOI: 10.1016/j.electacta.2013.03.029.

Ammundsen, Brett; Jones, Deborah J.; Rozière, Jacques; Burns, Gary R., (1996): Effect of Chemical Extraction of Lithium on the Local Structure of Spinel Lithium Manganese Oxides Determined by X-ray Absorption Spectroscopy. In *Chem. Mater.* 8 (12), pp. 2799–2808. DOI: 10.1021/cm960287s.

Ammundsen, Brett; Islam, M.Saiful; Jones, Deborah J.; Rozière, Jacques, (1999): Local structure and defect chemistry of substituted lithium manganate spinels: X-ray absorption and computer simulation studies. In *Journal of Power Sources* 81-82, pp. 500–504. DOI: 10.1016/S0378-7753(98)00224-9.

Anderson, Marc Arlen; Malotky, Dean Thomas, (1979): The adsorption of protolyzable anions on hydrous oxides at the isoelectric pH. In *Journal of colloid and interface science* 72 (3), pp. 413–427. DOI: 10.1016/0021-9797(79)90343-6.

Anton Paar (Ed.): How to Digest Lithium-Ion Battery Materials for ICP-OES Analysis. E38IA043EN-B.

Bae, Hyuntae; Kim, Youngsik, (2021): Technologies of lithium recycling from waste lithium ion batteries: a review. In *Mater. Adv.* 2 (10), pp. 3234–3250. DOI: 10.1039/D1MA00216C.

Bao, Lu-Ri; Zhang, Jing-Ze; Tang, Wei-Ping; Sun, Shu-Ying, (2023): Synthesis and adsorption properties of metal oxide-coated lithium ion-sieve from salt lake brine. In *Desalination* 546, p. 116196. DOI: 10.1016/j.desal.2022.116196.

Baujard, Clément; Genter, Albert; Cuenot, Nicolas; Mouchot, Justine; Maurer, Vincent; Hehn, Regis et al., (2018): Experience learnt from a successful soft stimulation and operational

feedback after 2 years of geothermal power and heat production in Rittershoffen and Soultz-sous-Forêts plants (Alsace, France). In *GRC Transactions* (42).

Berg, Helena; Göransson, Kenneth; Noläng, Bengt; Thomas, John O., (2000): Electronic structure and stability of Li1 + xMn2 − xO4 spinels. In *J. Mater. Chem.* 10 (6), pp. 1437–1441. DOI: 10.1039/a908746j.

Boch, Ronny; Leis, Albrecht; Haslinger, Edith; Goldbrunner, Johann E.; Mittermayr, Florian; Fröschl, Heinz et al., (2017): Scale-fragment formation impairing geothermal energy production: interacting H2S corrosion and CaCO3 crystal growth. In *Geotherm Energy* 5 (1), pp. 1–19. DOI: 10.1186/s40517-017-0062-3.

Boroumand, Yasaman; Razmjou, Amir, (2024): Adsorption-type aluminium-based direct lithium extraction: The effect of heat, salinity and lithium content. In *Desalination*, p. 117406. DOI: 10.1016/j.desal.2024.117406.

Bundesverband Geothermie, (2024): Oberrheingraben. Edited by Bundesverband Geothermie. Available online at https://www.geothermie.de/bibliothek/lexikon-der-geothermie/o/oberrheingraben, updated on 07.2024, checked on 5/23/2026.

Celestian, Aaron J.; Bourcier, William; Camiré, Christopher L.; Kumar, Jayanthi; Paranthaman, Mariappan Parans, (2026): Mechanism of Lithium Ion Exchange Into Spinel Manganese Oxide. In *J Raman Spectroscopy* 57 (1), pp. 131–139. DOI: 10.1002/jrs.70013.

Cheng, Qian; Zhang, Yuzhe; Zheng, Xudong; Sun, Wen; Li, BoTao; Wang, Dandan; Li, Zhongyu, (2021): High specific surface crown ether modified chitosan nanofiber membrane by low-temperature phase separation for efficient selective adsorption of lithium. In *Separation and Purification Technology* 262, p. 118312. DOI: 10.1016/j.seppur.2021.118312.

Chen, Lifang; Xu, Xin; Song, Jingjing; Zhu, Xuedong; Qi, Zhiwen, (2016): Microwave assisted hydrothermal synthesis of MnO 2 ·0.5H 2 O ion-sieve for lithium ion selective adsorption. In *Separation Sc. & Tech.* 51 (5), pp. 874–882. DOI: 10.1080/01496395.2015.1117100.

Chen, Xiangnan; Wang, Xiaohui; de Fang, (2020): A review on C1s XPS-spectra for some kinds of carbon materials. In *Fullerenes, Nanotubes and Carbon Nanostructures* 28 (12), pp. 1048–1058. DOI: 10.1080/1536383X.2020.1794851.

Chitrakar, Ramesh; Kanoh, Hirofumi; Miyai, Yoshitaka; Ooi, Kenta, (2000): A New Type of Manganese Oxide (MnO 2 ·0.5H 2 O) Derived from Li 1.6 Mn 1.6 O 4 and Its Lithium Ion-Sieve Properties. In *Chem. Mater.* 12 (10), pp. 3151–3157. DOI: 10.1021/cm0000191.

Chitrakar, Ramesh; Kanoh, Hirofumi; Miyai, Yoshitaka; Ooi, Kenta, (2001): Recovery of Lithium from Seawater Using Manganese Oxide Adsorbent (H1.6Mn1.6O4) Derived from Li1.6Mn1.6O4. In *Ind. Eng. Chem. Res.* 40 (9), pp. 2054–2058. DOI: 10.1021/ie000911h.

Chitrakar, Ramesh; Makita, Yoji; Ooi, Kenta; Sonoda, Akinari, (2012): Selective Uptake of Lithium Ion from Brine by H 1.33 Mn 1.67 O 4 and H 1.6 Mn 1.6 O 4. In *Chem. Lett.* 41 (12), pp. 1647–1649. DOI: 10.1246/cl.2012.1647.

Choe, Gogwon; Kim, Hyungsub; Kwon, Jaesub; Jung, Woochul; Park, Kyu-Young; Kim, Yong-Tae, (2024): Re-evaluation of battery-grade lithium purity toward sustainable batteries. In *Nat Commun* 15 (1), p. 1185. DOI: 10.1038/s41467-024-44812-3.

Choi, Jeong-Gil; Do, D. D.; Do, H. D., (2001): Surface Diffusion of Adsorbed Molecules in Porous Media: Monolayer, Multilayer, and Capillary Condensation Regimes. In *Ind. Eng. Chem. Res.* 40 (19), pp. 4005–4031. DOI: 10.1021/ie010195z.

Choubey, Pankaj K.; Kim, Min-seuk; Srivastava, Rajiv R.; Lee, Jae-chun; Lee, Jin-Young, (2016): Advance review on the exploitation of the prominent energy-storage element: Lithium. Part I: From mineral and brine resources. In *Minerals Engineering* 89, pp. 119–137. DOI: 10.1016/j.mineng.2016.01.010.

Christie, A. B.; Lee, J.; Sutherland, I.; Walls, J. M., (1983): An XPS study of ion-induced compositional changes with group II and group IV compounds. In *Applications of Surface Science* 15 (1-4), pp. 224–237. DOI: 10.1016/0378-5963(83)90018-1.

Chung, Wook-Jin; Torrejos, Rey Eliseo C.; Park, Myoung Jun; Vivas, Eleazer L.; Limjuco, Lawrence A.; Lawagon, Chosel P. et al., (2017): Continuous lithium mining from aqueous resources by an adsorbent filter with a 3D polymeric nanofiber network infused with ion sieves. In *Chemical Engineering Journal* 309, pp. 49–62. DOI: 10.1016/j.cej.2016.09.133.

Diallo, Mamadou S.; Kotte, Madhusudhana Rao; Cho, Manki, (2015): Mining Critical Metals and Elements from Seawater: Opportunities and Challenges. In *Environ. Sci. Technol.* 49 (16), pp. 9390–9399. DOI: 10.1021/acs.est.5b00463.

Ding, Kaiyue; Zhu, Guiru; Song, Chenghao; Wang, Qi; Wang, Lin; Wang, Ziqi et al., (2022): Fabrication of polyacrylonitrile-Li1.6Mn1.6O4 composite nanofiber flat-sheet membranes via electrospinning method as effective adsorbents for Li+ recovery from salt-lake brine. In *Separation and Purification Technology* 284, p. 120242. DOI: 10.1016/j.seppur.2021.120242.

Disu, Botelho; Rafati, Roozbeh; Sharifi Haddad, Amin; Muirhead, David, (2025): Maximizing Lithium Adsorption and Selectivity on Manganese-Based Ion Sieves: Effects of Thermal Treatment, Acid Content, and Operating Conditions. In *Ind. Eng. Chem. Res.* 64 (24), pp. 11961–11980. DOI: 10.1021/acs.iecr.5c00735.

Dobson, Patrick; Araya, Naod; Brounce, Maryjo; Busse, Margaret M.; Camarillo, Mary Kay; English, Lauren et al., (2023): Characterizing the Geothermal Lithium Resource at the Salton Sea. A Project Report to the U.S. Department of Energy, Office of Energy Efficiency &

Renewable Energy, Geotherm Technologies Office. Lawrence Berkeley National Laboratory. Available online at https://escholarship.org/uc/item/4x8868mf, checked on 2/5/2024.

Drüppel, Kirsten; Stober, Ingrid; Grimmer, Jens C.; Mertz-Kraus, Regina, (2020): Experimental alteration of granitic rocks: Implications for the evolution of geothermal brines in the Upper Rhine Graben, Germany. In *Geothermics* 88, p. 101903. DOI: 10.1016/j.geothermics.2020.101903.

Dugamin, Elza J. M.; Richard, Antonin; Cathelineau, Michel; Boiron, Marie-Christine; Despinois, Frank; Brisset, Anne, (2021): Groundwater in sedimentary basins as potential lithium resource: a global prospective study. In *Sci Rep* 11 (1), p. 21091. DOI: 10.1038/s41598-021-99912-7.

Eggeling, Lena; Genter, Albert; Kölbel, Thomas; Münch, Wolfram, (2013): Impact of natural radionuclides on geothermal exploitation in the Upper Rhine Graben. In *Geothermics* 47, pp. 80–88. DOI: 10.1016/j.geothermics.2013.03.002.

European Geothermal Congress 2022, (2022). Brussels: EGEC.

Farahbakhsh, Javad; Arshadi, Faezeh; Mofidi, Zahra; Mohseni-Dargah, Masoud; Kök, Cansu; Assefi, Mohammad et al., (2024): Direct lithium extraction: A new paradigm for lithium production and resource utilisation. In *Desalination* 575, p. 117249. DOI: 10.1016/j.desal.2023.117249.

Fatoki, Olukayode; Parupelli, Santosh Kumar; Kaur, Manpreet; Mathew, Alex; Rehmat, Amir; Desai, Salil, (2026): Review of Direct Lithium Extraction Methods: Recent Advances and Outlook. In *Batteries* 12 (4), p. 133. DOI: 10.3390/batteries12040133.

Fechner, Dorothee; Kondek, Milena; Kölbel, Thomas; Kolb, Jochen, (2022): CO2 handling in binary geothermal systems - a modelling approach for different CO2 contents, salinity, pressure, and temperature. In : European Geothermal Congress 2022. Brussels: EGEC.

Feng, Qi; Miyai, Yoshitaka; Kanoh, Hirofumi; Ooi, Kenta, (1992): Lithium+ extraction/insertion with spinel-type lithium manganese oxides. Characterisation of redox-type and ion-exchange-type sites. In *Langmuir* (8), pp. 1861–1867.

Feng, Qi; Miyai, Yoshitaka; Kanoh, Hirofumi; Ooi, Kenta, (1995): Li+ Extraction/Insertion Reactions with LiZn0.5Mn1.5O4 Spinel in the Aqueous Phase. In *Chem. Mater.* (7), pp. 379–384.

Flexer, Victoria; Baspineiro, Celso Fernando; Galli, Claudia Inés, (2018): Lithium recovery from brines: A vital raw material for green energies with a potential environmental impact in its mining and processing. In *The Science of the total environment* 639, pp. 1188–1204. DOI: 10.1016/j.scitotenv.2018.05.223.

Foord, J. S.; Jackman, R. B.; Allen, G. C., (1984): An X-ray photoelectron spectroscopic investigation of the oxidation of manganese. In *Philosophical Magazine A* 49 (5), pp. 657–663. DOI: 10.1080/01418618408233293.

Ford, Robert G.; Scheinost, andreas C.; Sparks, Donald L., (2001): Frontiers in metal sorption/precipitation mechanisms on soil mineral surfaces. In Donald L. Sparks (Ed.): Advances in Agronomy, vol. 74: Academic Press (74), pp. 41–62. Available online at https://www.sciencedirect.com/science/article/pii/S0065211301740308.

Frankcombe, Terry J.; Liu, Yun, (2023): Interpretation of Oxygen 1s X-ray Photoelectron Spectroscopy of ZnO. In *Chem. Mater.* 35 (14), pp. 5468–5474. DOI: 10.1021/acs.chemmater.3c00801.

Frey, Matthis; Bär, Kristian; Stober, Ingrid; Reinecker, John; van der Vaart, Jeroen; Sass, Ingo, (2022): Assessment of deep geothermal research and development in the Upper Rhine Graben. In *Geotherm Energy* 10 (1), pp. 1–67. DOI: 10.1186/s40517-022-00226-2.

Fries, David; Lebouil, Sophie; Maurer, Vincent; Martin, Carine; Baujard, Clément; Ravier, Guillaume et al., (2022): Lithium extraction through pilot scale tests under real geothermal conditions of the Upper Rhine Graben. European Geothermal Congress 2022. Berlin, 2022.

Fu, Yu-Yao; Yang, Xi-yun; Huang, Hai-Qiang; Wang, Yuan-Yuan; Li, Ji-Shen, (2020): Role of process parameters on phase purity of o-LiMnO2 and synthesis of Li1.6Mn1.6O4. In *Chinese Journal of Inorganic Chemistry* 2020 (36/3), pp. 536–546.

Gao, Aolei; Sun, Zhenhua; Li, Shaopeng; Hou, Xinjuan; Li, Huiquan; Wu, Qisheng; Xi, Xinguo, (2018): The mechanism of manganese dissolution on Li1.6Mn1.6O4 ion sieves with HCl. In *Dalton transactions (Cambridge, England : 2003)* 47 (11), pp. 3864–3871. DOI: 10.1039/c8dt00033f.

Gao, Yunyun; Sun, Yanxia; Chen, Li; Tan, Yao; Fan, Rui; Hai, Chunxi; Zhang, Hongjun, (2025): Progress of Research in Titanium-Based Lithium-Ion Sieves for the Extraction of Lithium from Salt Lake Brine. In *ACS omega* 10 (12), pp. 11643–11657. DOI: 10.1021/acsomega.4c08886.

Gerardo, Sheila; Song, Wen, (2025): Lithium recovery from U.S. oil and gas produced waters: resource quality and siting considerations. In *Environ. Sci.: Water Res. Technol.* 11 (3), pp. 536–541. DOI: 10.1039/D4EW00422A.

Hanada, Takafumi; Goto, Masahiro, (2021): Synergistic Deep Eutectic Solvents for Lithium Extraction. In *ACS Sustainable Chem. Eng.* 9 (5), pp. 2152–2160. DOI: 10.1021/acssuschemeng.0c07606.

Han, Yosep; Kim, Hyunjung; Park, Jaikoo, (2012): Millimeter-sized spherical ion-sieve foams with hierarchical pore structure for recovery of lithium from seawater. In *Chemical Engineering Journal* 210, pp. 482–489. DOI: 10.1016/j.cej.2012.09.019.

Herrmann, Laura; Ehrenberg, Helmut; Graczyk-Zajac, Magdalena; Kaymakci, Elif; Kölbel, Thomas; Kölbel, Lena; Tübke, Jens, (2022): Lithium recovery from geothermal brine – an investigation into the desorption of lithium ions using manganese oxide adsorbents. In *Energy Adv.* DOI: 10.1039/D2YA00099G.

Herrmann, Laura; Bohn, Nicole; Pfau, Alisa; Kölbel, Thomas; Ehrenberg, Helmut; Binder, Joachim R.; Jeschull, Fabian, (2025): Synthesis of Lithium Manganese Oxide and Ti-Substituted LMO Sorbents for Lithium Extraction in a Spray-Drying Process. In *ChemSusChem* 18 (13), e202500530. DOI: 10.1002/cssc.202500530.

Hong, Hye-Jin; Park, In-Su; Ryu, Taegong; Ryu, Jungho; Kim, Byoung-Gyu; Chung, Kang-Sup, (2013): Granulation of Li1.33Mn1.67O4 (LMO) through the use of cross-linked chitosan for the effective recovery of Li+ from seawater. In *Chemical Engineering Journal* 234, pp. 16–22. DOI: 10.1016/j.cej.2013.08.060.

Hong, Hye-Jin; Park, In-Su; Ryu, Jungho; Ryu, Taegong; Kim, Byoung-Gyu; Chung, Kang-Sup, (2015): Immobilisation of hydrogen manganese oxide (HMO) on alpha-alumina bead (AAB) to effective recovery of Li+ from seawater. In *Chemical Engineering Journal* 271, pp. 71–78. DOI: 10.1016/j.cej.2015.02.023.

Hong, Hye-Jin; Ryu, Taegong; Park, In-Su; Kim, Mikyung; Shin, Junho; Kim, Byoung-Gyu; Chung, Kang-Sup, (2018): Highly porous and surface-expanded spinel hydrogen manganese oxide (HMO)/Al2O3 composite for effective lithium (Li) recovery from seawater. In *Chemical Engineering Journal* 337, pp. 455–461. DOI: 10.1016/j.cej.2017.12.130.

Hong, Hye-Jin; Park, In-Su; Ryu, Taegong; Kim, Byoung-Gyu; Chung, Kang-Sup, (2019): Macroporous Hydrogen Manganese Oxide/Al 2 O 3 for Effective Lithium Recovery from Seawater: Effects of the Macropores vs Mesopores. Industrial & Engineering Chemistry Research, 58(19), 8342-8348. In *Ind. Eng. Chem. Res.* 58 (19), pp. 8342–8348. DOI: 10.1021/ACS.IECR.9B01613.

Huang, Yimeng; Dong, Yanhao; Li, Sa; Lee, Jinhyuk; Wang, Chao; Zhu, Zhi et al., (2020): Lithium Manganese Spinel Cathodes for Lithium-Ion Batteries. In *Adv. Energy Mater.* 11 (2), p. 2000997. DOI: 10.1002/aenm.202000997.

Hunter, James C., (1981): Preparation of a new crystal form of manganese dioxide: λ-MnO2. In *Journal of Solid State Chemistry* 39 (2), pp. 142–147. DOI: 10.1016/0022-4596(81)90323-6.

Hu, Qili; Ma, Siting; He, Zhihao; Liu, Hengyuan; Pei, Xiangjun, (2024): A revisit on intraparticle diffusion models with analytical solutions: Underlying assumption, application scope and solving method. In *Journal of Water Process Engineering* 60, p. 105241. DOI: 10.1016/j.jwpe.2024.105241.

IAPWS, (2007): Revised Release on the IAPWS Industrial Formulation 1997 for the Thermodynamic Properties of Water and Steam. The International Association for the Properties of Water and Steam. Lucerne, Switzerland (IAPWS R7-97(2012)). Available online at https://iapws.org/documents/release/IF97-Rev?utm_source=chatgpt.com, checked on 6/3/2026.

IEA, (2025): Global Critical Minerals Outlook 2025. Edited by International Energy Association. Available online at https://www.iea.org/reports/global-critical-minerals-outlook-2025, checked on 5/20/2026.

Ilton, Eugene S.; Post, Jeffrey E.; Heaney, Peter J.; Ling, Florence T.; Kerisit, Sebastien N., (2016): XPS determination of Mn oxidation states in Mn (hydr)oxides. In *Applied Surface Science* 366, pp. 475–485. DOI: 10.1016/j.apsusc.2015.12.159.

Informationsportal Tiefe Geothermie: Oberrheingraben. Edited by Informationsportal Tiefe Geothermie. Available online at https://www.tiefegeothermie.de/taxonomy/term/36, checked on 23.05.26.

Jang, Y.; Moorehead, W.Douglas, (2002): Synthesis of the monoclinic and orthorhombic phases of LiMnO2 in oxidizing atmosphere. In *Solid State Ionics* 149 (3-4), pp. 201–207. DOI: 10.1016/S0167-2738(02)00176-5.

JCPDS-ICDD, (2002): PDF-2 Release 2002. Newton Square, Pennsylvania, USA.

Julien, C. M., (2006): Local structure of lithiated manganese oxides. In *Solid State Ionics* 177 (1-2), pp. 11–19. DOI: 10.1016/j.ssi.2005.10.012.

Jungmann, Michèle; Walter, Benjamin F.; Eiche, Elisabeth; Giebel, R. Johannes; Kolb, Jochen, (2024): The Source of Lithium in Connate Fluids: Evidence from the Geothermal Reservoir at Soultz-Sous-Forêts, Upper Rhine Graben, France.

Junta, Jodi L.; Hochella, Michael F., (1994): Manganese (II) oxidation at mineral surfaces: A microscopic and spectroscopic study. In *Geochimica et Cosmochimica Acta* 58 (22), pp. 4985–4999. DOI: 10.1016/0016-7037(94)90226-7.

Khalil, Abdullah; Mohammed, Shabin; Hashaikeh, Raed; Hilal, Nidal, (2022): Lithium recovery from brine: Recent developments and challenges. In *Desalination* 528, p. 115611. DOI: 10.1016/j.desal.2022.115611.

Kiriukhin, Michael Y.; Collins, Kim D., (2002): Dynamic hydration numbers for biologically important ions. In *Biophysical Chemistry* 99 (2), pp. 155–168. DOI: 10.1016/S0301-4622(02)00153-9.

Kölbel, Lena; Kölbel, Thomas; Fechner, Dorothee, (2022): Radiochemical monitoring of geothermal systems: Case study Bruchsal (Upper Rhine Graben). In *Applied Geochemistry* 147, p. 105509. DOI: 10.1016/j.apgeochem.2022.105509.

Kölbel, Lena; Herrmann, Laura; Kölbel, Thomas; Schneider, Jochen, (2024a): Lithium extraction from geothermal brines: Adsorption-desorption studies on 226Ra (228Ra) and 210Pb on lithium-titanium-oxides (LTO). In *Applied Geochemistry* 162, p. 105913. DOI: 10.1016/j.apgeochem.2024.105913.

Kölbel, Lena; Slunitschek, Klemens; Kaymakci, Elif; Kölbel, Thomas; Reich, Rebekka; Schneider, Jochen, (2024b): Lithium recovery from geothermal brines: An investigation into radioactive nuclide uptake on lithium-manganese-oxide (LMO) granules. In *Hydrometallurgy* 224, p. 106266. DOI: 10.1016/j.hydromet.2024.106266.

Kong, Lingchen; Yan, Gangbin; Hu, Kejia; Yu, Yongchang; Conte, Nicole; Mckenzie, Kevin R. et al., (2025): Electro-driven direct lithium extraction from geothermal brines to generate battery-grade lithium hydroxide. In *Nat Commun* 16 (1), p. 806. DOI: 10.1038/s41467-025-56071-x.

Koretsky, C., (2000): The significance of surface complexation reactions in hydrologic systems: a geochemist's perspective. In *Journal of Hydrology* 230 (3-4), pp. 127–171. DOI: 10.1016/S0022-1694(00)00215-8.

Li, Hualun; Pan, Jiahao; Ping, Yitao; Su, Jialun; Fang, Moling; Chen, Tian et al., (2023): Annealed SiO2 Protective Layer on LiMn2O4 for Enhanced Li-Ion Extraction from Brine. In *Nano letters* 23 (22), pp. 10458–10465. DOI: 10.1021/acs.nanolett.3c03136.

Li, Ling; Deshmane, Vishwanath G.; Paranthaman, M. Parans; Bhave, Ramesh; Moyer, Bruce A.; Harrison, Stephen, (2018): Lithium Recovery from Aqueous Resources and Batteries. A Brief Review. In *Johnson Matthey Technology Review* 62 (2), pp. 161–176. DOI: 10.1595/205651317X696676.

Limousin, G.; Gaudet, J.-P.; Charlet, L.; Szenknect, S.; Barthès, V.; Krimissa, M., (2007): Sorption isotherms: A review on physical bases, modeling and measurement. In *Applied Geochemistry* 22 (2), pp. 249–275. DOI: 10.1016/j.apgeochem.2006.09.010.

Liu, Chaofeng; Neale, Zachary G.; Cao, Guozhong, (2016): Understanding electrochemical potentials of cathode materials in rechargeable batteries. In *Materials Today* 19 (2), pp. 109–123. DOI: 10.1016/j.mattod.2015.10.009.

Liu, Qun; Li, Yangxin; Hu, Zheliang; Mao, Dali; Chang, Chengkang; Huang, Fuqiang, (2008): One-step hydrothermal routine for pure-phased orthorhombic LiMnO2 for Li ion battery application. In *Electrochimica Acta* 53 (24), pp. 7298–7302. DOI: 10.1016/j.electacta.2008.04.008.

Liu, Tongchao; Dai, Alvin; Lu, Jun; Yuan, Yifei; Xiao, Yinguo; Yu, Lei et al., (2019): Correlation between manganese dissolution and dynamic phase stability in spinel-based lithium-ion battery. In *Nat Commun* 10 (1), p. 4721. DOI: 10.1038/s41467-019-12626-3.

Liu, Yu Ting; Wang, Ming Kuang; Chen, Tsan Yao; Chiang, Po Neng; Huang, Pan Ming; Lee, Jhy Fu, (2006): Arsenate sorption on lithium/ aluminum layered double hydroxide intercalated by chloride and on gibbsite: sorption isotherms, envelopes, and spectroscopic studies. In *Environ. Sci. Technol.* 40 (24), pp. 7784–7789. DOI: 10.1021/es061530j.

Luo, Hao; Peng, Huawen; Zhao, Qiang, (2022): High flux Mg2+/Li+ nanofiltration membranes prepared by surface modification of polyethylenimine thin film composite membranes. In *Applied Surface Science* 579, p. 152161. DOI: 10.1016/j.apsusc.2021.152161.

Ma, Li-Wen; Chen, Bai-Zhen; Chen, Ya; Shi, Xi-Chang, (2011): Preparation, characterisation and adsorptive properties of foam-type lithium adsorbent. In *Microporous and Mesoporous Materials* 142 (1), pp. 147–153. DOI: 10.1016/j.micromeso.2010.11.028.

Manning, Bruce A.; Fendorf, Scott E.; Bostick, Benjamin; Suarez, Donald L., (2002): Arsenic(III) oxidation and arsenic(V) adsorption reactions on synthetic birnessite. In *Environ. Sci. Technol.* 36 (5), pp. 976–981. DOI: 10.1021/es0110170.

Marchini, Florencia; Rubi, Diego; del Pozo, Maria; Williams, Federcio J.; Calvo, Ernesto J., (2016): Surface Chemistry and Lithium-Ion Exchange in LiMn 2 O 4 for the Electrochemical Selective Extraction of LiCl from Natural Salt Lake Brines. In *J. Phys. Chem. C* 120 (29), pp. 15875–15883. DOI: 10.1021/acs.jpcc.5b11722.

Martin, Gunther; Rentsch, Lars; Höck, Michael; Bertau, Martin, (2017): Lithium market research – global supply, future demand and price development. In *Energy Storage Materials* 6, pp. 171–179. DOI: 10.1016/j.ensm.2016.11.004.

Ma, Tingting; Jin, Zixuan; Jia, Zhiqian; Peng, Wenjuan, (2025): Synthesis of doped titanium-based lithium adsorbents with excellent stability and adsorption performance by solid state reactions. In *Desalination* 594, p. 118300. DOI: 10.1016/j.desal.2024.118300.

Meng, Fei; McNeice, James; Zadeh, Shirin S.; Ghahreman, Ahmad, (2021): Review of Lithium Production and Recovery from Minerals, Brines, and Lithium-Ion Batteries. In *Mineral Processing and Extractive Metallurgy Review* 42 (2), pp. 123–141. DOI: 10.1080/08827508.2019.1668387.

Mojid, Muhammed Rashik; You, Jiahui; Lee, Kyung Jae, (2025): Experimental and reactive transport modeling study of direct lithium extraction From brines with Li/Al-layered double hydroxides. In *Journal of Contaminant Hydrology* 275, p. 104693. DOI: 10.1016/j.jconhyd.2025.104693.

Mundhenk, N.; Huttenloch, P.; Sanjuan, B.; Kohl, T.; Steger, H.; Zorn, R., (2013): Corrosion and scaling as interrelated phenomena in an operating geothermal power plant. In *Corrosion Science* 70, pp. 17–28. DOI: 10.1016/j.corsci.2013.01.003.

Murphy, Olivia; Haji, Maha N., (2022): A review of technologies for direct lithium extraction from low Li+ concentration aqueous solutions. In *Front. Chem. Eng.* 4, Article 1008680. DOI: 10.3389/fceng.2022.1008680.

Nauman, E. Bruce, (2008): Chemical Reactor Design, Optimisation, and Scaleup: Wiley.

Nelson, A. J.; Reynolds, John G.; Roos, Joseph W., (2000): Core-level satellites and outer core-level multiplet splitting in Mn model compounds. In *Journal of Vacuum Science & Technology A: Vacuum, Surfaces, and Films* 18 (4), pp. 1072–1076. DOI: 10.1116/1.582302.

Ngoy, Kitalu Ricin; Lukong, Valantine Takwa; Yoro, Kelvin O.; Makambo, John Beya; Chukwuati, Nonso Christopher; Ibegbulam, Chinedu et al., (2025): Lithium-ion batteries and the future of sustainable energy: A comprehensive review. In *Renewable and Sustainable Energy Reviews* 223, p. 115971. DOI: 10.1016/j.rser.2025.115971.

Nicolaci, Hugo; Young, Paul; Snowdon, Nicholas; Rai, Aditi; Chen, Trina; Zhang, Joy et al., (2023): Global Metals & Mining Direct Lithium Extraction: A potential game changing technology. Edited by Goldman Sachs. Available online at https://www.goldmansachs.com/static-libs/pdf-redirect/prod/index.html?path=/pdfs/insights/pages/gs-research/direct-lithium-extraction/report.pdf&originalQuery=&referrer=https://www.google.com/, checked on 5/21/2026.

Nikkhah, Hasan; Ipekçi, Deniz; Xiang, Wenjun; Stoll, Zachary; Xu, Pei; Li, Baikun et al., (2024): Challenges and opportunities of recovering lithium from seawater, produced water, geothermal brines, and salt lakes using conventional and emerging technologies. In *Chemical Engineering Journal* 498, p. 155349. DOI: 10.1016/j.cej.2024.155349.

NIST, (2000): NIST X-ray Photoelectron Spectroscopy Database (SRD 20), Version 5.0. National Institute of Standards and Technology. Gaithersburg MD. Available online at https://srdata.nist.gov/xps/, checked on 6/1/2025.

Nitschke, Fabian; Scheiber, Julia; Kramar, Utz; Neumann, Thomas, (2014): Formation of alternating layered Ba-Sr-sulfate and Pb-sulfide scaling in the geothermal plant of Soultz-sous-Forêts. In *N. Jb. Miner. Abh.* 191 (2), pp. 145–156. DOI: 10.1127/0077-7757/2014/0253.

Nolis, Gene M.; Adil, Abdullah; Yoo, Hyun Deog; Hu, Linhua; Bayliss, Ryan D.; Lapidus, Saul H. et al., (2018): Electrochemical Reduction of a Spinel-Type Manganese Oxide Cathode in Aqueous Electrolytes with Ca 2+ or Zn 2+. In *J. Phys. Chem. C* 122 (8), pp. 4182–4188. DOI: 10.1021/acs.jpcc.7b12084.

Ohashi, Fumihiko; Tai, Yutaka, (2019): Lithium adsorption from natural brine using surface-modified manganese oxide adsorbents. In *Materials Letters* 251, pp. 214–217. DOI: 10.1016/j.matlet.2019.05.064.

Oku, Masaoki; Hirokawa, Kichinosuke; Ikeda, Shigero, (1975): X-ray photoelectron spectroscopy of manganese—oxygen systems. In *Journal of Electron Spectroscopy and Related Phenomena* 7 (5), pp. 465–473. DOI: 10.1016/0368-2048(75)85010-9.

Ooi, Kenta; Miyai, Yoshitaka; Katoh, Shunsaku; Maeda, Hiroshi; Abe, Mitsuo, (1988): Lithium-ion Insertion/Extraction Reaction with λ-MnO 2 in the Aqueous Phase. In *Chem. Lett.* 17 (6), pp. 989–992. DOI: 10.1246/cl.1988.989.

Ooi, Kenta; Yoshitaka Miyai; Shunsaku Katoh; Hiroshi Maeda; Abe, Mitsuo, (1989): Topotactic lithium(1+) insertion to.lambda.-manganese dioxide in the aqueous phase. In *Langmuir* (5), pp. 150–157.

Park, Jeongeon; Sato, Hideki; Nishihama, Syouhei; Yoshizuka, Kazuharu, (2012a): Lithium Recovery from Geothermal Water by Combined Adsorption Methods. In *Solvent Extraction and Ion Exchange* 30 (4), pp. 398–404. DOI: 10.1080/07366299.2012.687165.

Park, Jeongeon; Sato, Hideki; Nishihama, Syouhei; Yoshizuka, Kazuharu, (2012b): Separation and Recovery of Lithium from Geothermal Water by Sequential Adsorption Process with l-MnO2 and TiO2. In *Ion Exchange Letters* (5), pp. 1–5. Available online at http://iel.vscht.cz/index.html?http&&&iel.vscht.cz/abstracts/1803-4039-05-0001.htm, checked on 11/25/2022.

Park, Myoung Jun; Nisola, Grace M.; Beltran, Arnel B.; Torrejos, Rey Eliseo C.; Seo, Jeong Gil; Lee, Seong-Poong et al., (2014): Recyclable composite nanofiber adsorbent for Li+ recovery from seawater desalination retentate. In *Chemical Engineering Journal* 254, pp. 73–81. DOI: 10.1016/j.cej.2014.05.095.

Persson, Ingmar, (2010): Hydrated metal ions in aqueous solution: How regular are their structures? In *Pure and Applied Chemistry* 82 (10), pp. 1901–1917. DOI: 10.1351/PAC-CON-09-10-22.

Proceedings of the 41st Workshop on Geothermal Reservoir Engineering, (2016). Stanford, CA, USA.

Qian, Fangren; Guo, Min; Qian, Zhiqiang; Li, Quan; Wu, Zhijian; Liu, Zhong, (2019): Highly Lithium Adsorption Capacities of H 1.6 Mn 1.6 O 4 Ion-Sieve by Ordered Array Structure. In *ChemistrySelect* 4 (34), pp. 10157–10163. DOI: 10.1002/slct.201902173.

Qiu, Hui; Lv, Lu; Pan, Bing-cai; Zhang, Qing-jian; Zhang, Wei-ming; Zhang, Quan-xing, (2009): Critical review in adsorption kinetic models. In *J. Zhejiang Univ. Sci. A* 10 (5), pp. 716–724. DOI: 10.1631/jzus.A0820524.

Recepoğlu, Yaşar K.; Kabay, Nalan; Yılmaz-Ipek, İdil; Arda, Müşerref; Yoshizuka, Kazuharu; Nishihama, Syouhei; Yüksel, Mithat, (2017): Equilibrium and Kinetic Studies on Lithium Adsorption from Geothermal Water by λ-MnO 2. In *Solvent Extraction and Ion Exchange* 35 (3), pp. 221–231. DOI: 10.1080/07366299.2017.1319235.

Reich, Rebekka; Slunitschek, Klemens; Danisi, Rosa Micaela; Eiche, Elisabeth; Kolb, Jochen, (2022): Lithium Extraction Techniques and the Application Potential of Different Sorbents for Lithium Recovery from Brines. In *Mineral Processing and Extractive Metallurgy Review*, pp. 1–20. DOI: 10.1080/08827508.2022.2047041.

Reich, Rebekka; Eiche, Elisabeth; Kolb, Jochen, (2024): Delithiation and lithiation of LiFePO4: Implications for direct Li extraction from synthetic solutions and geothermal brines. In *Desalination* 586, p. 117883. DOI: 10.1016/j.desal.2024.117883.

Roychowdhury, Tuhin; Bahr, Stephan; Dietrich, Paul; Meyer, Michael; Thißen, Andreas; Linford, Matthew R., (2019): Calcite (CaCO3), by near-ambient pressure XPS. In *Surface Science Spectra* 26 (1), Article 014025. DOI: 10.1116/1.5109266.

Ryu, Taegong; Haldorai, Yuvaraj; Rengaraj, Arunkumar; Shin, Junho; Hong, Hye-Jin; Lee, Go-Woon et al., (2016): Recovery of Lithium Ions from Seawater Using a Continuous Flow Adsorption Column Packed with Granulated Chitosan–Lithium Manganese Oxide. In *Ind. Eng. Chem. Res.* 55 (26), pp. 7218–7225. DOI: 10.1021/acs.iecr.6b01632.

Ryu, Taegong; Rengaraj, Arunkumar; Haldorai, Yuvaraj; Shin, Junho; Choe, Sang Rak; Lee, Go-Woon et al., (2017): Mechanochemical synthesis of silica-lithium manganese oxide composite for the efficient recovery of lithium ions from seawater. In *Solid State Ionics* 308, pp. 77–83. DOI: 10.1016/j.ssi.2017.05.020.

Ryu, Taegong; Lee, Dong-Hee; Ryu, Jae Chun; Shin, Junho; Chung, Kang-Sup; Kim, Young Ho, (2019): A lithium selective adsorption composite by coating adsorbent on PVC plate using epoxy-silica hybrid binder. In *Hydrometallurgy* 183, pp. 118–124. DOI: 10.1016/j.hydromet.2018.11.011.

Saenko, E. V.; Leont'eva, G. V.; Vol'khin, V. V.; Kolyshkin, A. S., (2007): Variation of the composition and properties of lithium manganese oxide spinel in lithiation-delithiation cycles. In *Russ. J. Inorg. Chem.* 52 (8), pp. 1312–1316. DOI: 10.1134/S0036023607080256.

Safari, Salman; Lottermoser, Bernd G.; Alessi, Daniel S., (2020): Metal oxide sorbents for the sustainable recovery of lithium from unconventional resources. In *Applied Materials Today* 19, p. 100638. DOI: 10.1016/j.apmt.2020.100638.

Saleem, Usman; Wilhelms, Andre; Sottmann, Jonas; Knuutila, Hanna K.; Bandyopadhyay, Sulalit, (2025): Direct lithium extraction (DLE) methods and their potential in Li-ion battery recycling. In *Separation and Purification Technology* 361, p. 131315. DOI: 10.1016/j.seppur.2024.131315.

Sanjuan, B.; Millot, R.; Ásmundsson, R.; Brach, M.; Giroud, N., (2014): Use of two new Na/Li geothermometric relationships for geothermal fluids in volcanic environments. In *Chemical Geology* 389, pp. 60–81. DOI: 10.1016/j.chemgeo.2014.09.011.

Sanjuan, Bernard; Millot, R.; Innocent, Ch.; Dezayes, Chrystel; Scheiber, Julia; Brach, M., (2016): Major geochemical characteristics of geothermal brines from the Upper Rhine Graben granitic basement with constraints on temperature and circulation. In *Chemical Geology* 428, pp. 27–47. DOI: 10.1016/j.chemgeo.2016.02.021.

Sanjuan, Bernard; Gourcerol, Blandine; Millot, Romain; Rettenmaier, Detlev; Jeandel, Elodie; Rombaut, Aurélien, (2022): Lithium-rich geothermal brines in Europe: An up-date about geochemical characteristics and implications for potential Li resources. In *Geothermics* 101, p. 102385. DOI: 10.1016/j.geothermics.2022.102385.

Sato, K.; Poojary, D. M.; Clearfield, A.; Kohno, M.; Inoue, Y., (1997): The Surface Structure of the Proton-Exchanged Lithium Manganese Oxide Spinels and Their Lithium-Ion Sieve Properties. In *Journal of Solid State Chemistry* 131 (1), pp. 84–93. DOI: 10.1006/jssc.1997.7348.

Scofield, J. H., (1976): Hartree-Slater subshell photoionisation cross-sections at 1254 and 1487 eV. In *Journal of Electron Spectroscopy and Related Phenomena* 8 (2), pp. 129–137. DOI: 10.1016/0368-2048(76)80015-1.

Seip, Adam; Safari, Salman; Pickup, David M.; Chadwick, Alan V.; Ramos, Silvia; Velasco, Carmen A. et al., (2021): Lithium recovery from hydraulic fracturing flowback and produced water using a selective ion exchange sorbent. In *Chemical Engineering Journal* 426, p. 130713. DOI: 10.1016/j.cej.2021.130713.

Shen, Xiang-Mu; Clearfield, Abraham, (1986): Phase transitions and ion exchange behavior of electrolytically prepared manganese dioxide. In *Journal of Solid State Chemistry* 64 (3), pp. 270–282. DOI: 10.1016/0022-4596(86)90071-X.

Shi, Xichang; Zhou, Dingfang; Zhang, Zhibing; Yu, Liangliang; Xu, Hui; Chen, Baizhen; Yang, Xiyun, (2011): Synthesis and properties of Li1.6Mn1.6O4 and its adsorption application. In *Hydrometallurgy* 110 (1-4), pp. 99–106. DOI: 10.1016/j.hydromet.2011.09.004.

Shoghi, Ali; Ghasemi, Shahnaz; Askari, Masoud; Khosravi, Arash; Hasan-Zadeh, Atefeh; Alamolhoda, Ali Asghar, (2021): Spinel H4Ti5O12 nanotubes for Li recovery from aqueous solutions: Thermodynamics and kinetics study. In *Journal of Environmental Chemical Engineering* 9 (1), p. 104679. DOI: 10.1016/j.jece.2020.104679.

Slunitschek, Klemens; Eiche, Elisabeth; Kolb, Jochen, (2025): Sorption of lithium and competing ions from geothermal brine to lithium manganese oxide sorbent and implication for industrial use. In *Separation and Purification Technology* (378 (3)), p. 134594. DOI: 10.1016/j.seppur.2025.134594.

Sparks, Donald L. (Ed.), (2001): Advances in Agronomy: Academic Press (74).

Steiger, Katharina; Hilgers, Christoph; Kolb, Jochen (Eds.), (2022): Lithium in Europa. THINK-TANK für industrielle Ressourcenstrategien. Karlsruhe.

Stober, I.; Bucher, K., (2015): Hydraulic and hydrochemical properties of deep sedimentary reservoirs of the Upper Rhine Graben, Europe. In *Geofluids* 15 (3), pp. 464–482. DOI: 10.1111/gfl.12122.

Stober, Ingrid; Bucher, Kurt, (2012): Geothermie: Springer Berlin Heidelberg.

Stringfellow, William T.; Dobson, Patrick F., (2021): Technology for the Recovery of Lithium from Geothermal Brines. In *Energies* 14 (20), p. 6805. DOI: 10.3390/en14206805.

Su, Jialun; Fan, Qiyue; Hu, Xiangting; Sun, Yue; Lin, Jie; Xu, Jiayue et al., (2025): Continuous flow extraction of lithium from brine using silica-coated LMO beads. In *Mater. Adv.* 6 (7), pp. 2202–2210. DOI: 10.1039/D4MA01100G.

Sun, Shu-Ying; Song, Xingfu; Zhang, Qin-Hui; Wang, Jin; Yu, Jian-Guo, (2011): Lithium extraction/insertion process on cubic Li-Mn-O precursors with different Li/Mn ratio and morphology. In *Adsorption* 17 (5), pp. 881–887. DOI: 10.1007/s10450-011-9356-0.

Swain, Basudev, (2017): Recovery and recycling of lithium: A review. In *Separation and Purification Technology* 172, pp. 388–403. DOI: 10.1016/j.seppur.2016.08.031.

Thackeray, M. M.; David, W.I.F.; Bruce, P. G.; Goodenough, J. B., (1983): Lithium insertion into manganese spinels. In *Materials Research Bulletin* 18 (4), pp. 461–472. DOI: 10.1016/0025-5408(83)90138-1.

Thackeray, Michael M., (1997): Manganese oxides for ltihium batteries. In *Progress in Solid State Chemistry* (25), pp. 1–71. DOI: 10.14714/CP27.695.

USGS, (2025): Mineral commodity summaries 2025. Edited by United States Geological Survey.

van den Heuvel, Daniela B.; Gunnlaugsson, Einar; Benning, Liane G., (2016): Passivation of metal surfaces against corrosion by silica scaling. In : Proceedings of the 41st Workshop on Geothermal Reservoir Engineering. Stanford, CA, USA.

Ventura, Susanna; Bhamidi, Srinivas; Hornbostel, Marc; Nagar, Anoop; Perea, Elisabeth, (2016): Selective Recovery of Metals from Geothermal Brines. Final Report DE-EE0006747. SRI International.

Ventura, Susanna; Bhamidi, Srinivas; Hornbostel, Marc; Nagar, Anoop, (2020): Selective recovery of lithium from geothermal brines. California Energy Commission (CEC-500-2020-02). Available online at https://www.energy.ca.gov/sites/default/files/2021-05/CEC-500-2020-020.pdf, checked on 10/24/2021.

Vera, María L.; Torres, Walter R.; Galli, Claudia I.; Chagnes, Alexandre; Flexer, Victoria, (2023): Environmental impact of direct lithium extraction from brines. In *Nat Rev Earth Environ*, pp. 1–17. DOI: 10.1038/s43017-022-00387-5.

Vidal, Jeanne; Genter, Albert, (2018): Overview of naturally permeable fractured reservoirs in the central and southern Upper Rhine Graben: Insights from geothermal wells. In *Geothermics* 74, pp. 57–73. DOI: 10.1016/j.geothermics.2018.02.003.

Wang, L.; Ma, W.; Liu, R.; LI, H.; Meng, C., (2006): Correlation between Li+ adsorption capacity and the preparation conditions of spinel lithium manganese precursor. In *Solid State Ionics* 177 (17-18), pp. 1421–1428. DOI: 10.1016/j.ssi.2006.07.019.

Wang, Lei; Wang, Jin; Wang, Xudong, (2022): Synthesis of zirconium-coated lithium ion sieve with enhanced cycle stability. In *Separation and Purification Technology* 303, p. 121933. DOI: 10.1016/j.seppur.2022.121933.

Wang, Lu; Meng, Chang Gong; Ma, Wei, (2009): Study on Li+ uptake by lithium ion-sieve via the pH technique. In *Colloids and Surfaces A: Physicochemical and Engineering Aspects* 334 (1-3), pp. 34–39. DOI: 10.1016/j.colsurfa.2008.09.050.

Weng, Ding; Duan, Haoyue; Hou, Yacong; Huo, Jing; Chen, Lei; Zhang, Fang; Wang, Jiadao, (2020): Introduction of manganese based lithium-ion Sieve-A review. In *Progress in Solid State Chemistry* 30 (2), pp. 139–152. DOI: 10.1016/j.pnsc.2020.01.017.

Wu, Fangshuai; Shivakumar, Karthik R.; Konhauser, Kurt O.; Alessi, Daniel S., (2025): Lithium resources and novel strategies for their extraction and purification. In *npj Mater. Sustain.* 3 (1), p. 30. DOI: 10.1038/s44296-025-00069-5.

Xiao, Guoping; Tong, Kefeng; Zhou, Longsheng; Xiao, Jiali; Sun, Shuying; Li, Ping; Yu, Jianguo, (2012): Adsorption and Desorption Behavior of Lithium Ion in Spherical PVC–MnO 2 Ion Sieve. In *Ind. Eng. Chem. Res.* 51 (33), pp. 10921–10929. DOI: 10.1021/ie300087s.

Xiao, Jia-Li; Sun, Shu-Ying; Wang, Jin; Li, Ping; Yu, Jian-Guo, (2013): Synthesis and Adsorption Properties of Li1.6Mn1.6O4 Spinel. In *Ind. Eng. Chem. Res.* 52 (34), pp. 11967–11973. DOI: 10.1021/ie400691d.

Xiao, Jia-Li; Sun, Shu-Ying; Song, Xingfu; Li, Ping; Yu, Jian-Guo, (2015): Lithium ion recovery from brine using granulated polyacrylamide–MnO 2 ion-sieve. In *Chemical Engineering Journal* 279, pp. 659–666. DOI: 10.1016/j.cej.2015.05.075.

XPS Database S: Basic XPS information section - Sulfur. Edited by B. Vincent Crist. The XPS Library, 2021-2025. Available online at https://xpsdatabase.net/sulfur-s-z16-sulfur-compounds/?v=5f02f0889301, checked on 10/28/2025.

Xu, Xin; Chen, Yongmei; Wan, Pingyu; Gasem, Khaled; Wang, Kaiying; He, Ting et al., (2016): Extraction of lithium with functionalized lithium ion-sieves. In *Progress in Materials Science* 84, pp. 276–313. DOI: 10.1016/j.pmatsci.2016.09.004.

Yang, Fan; Chen, Sichong; Shi, Chentao; Xue, Feng; Zhang, Xiaoxian; Ju, Shengui; Xing, Weihong, (2018): A Facile Synthesis of Hexagonal Spinel λ-MnO2 Ion-Sieves for Highly Selective Li+ Adsorption. In *Processes* 6 (5), p. 59. DOI: 10.3390/pr6050059.

Yang, Xiaojing; Kanoh, Hirofumi; Tang, Weiping; Ooi, Kenta, (2000): Synthesis of Li1.33Mn1.67O4 spinels with different morphologies and their ion adsorptivities after delithiation. In *J. Mater. Chem.* 10 (8), pp. 1903–1909. DOI: 10.1039/b000219o.

Yan, Shuxuan; Pei, Shaozhen; Li, Xiaodong; Luo, Zhongyan; Chen, Xiangping; Szlachta, Małgorzata; Xu, Junhua, (2025): Structural Insights Into Aluminum-Doped Manganese Dioxides as Promising Materials for Direct Lithium Extraction: Modeling and Mechanism Study. In *Adv Materials Inter* 12 (11), Article 2400912. DOI: 10.1002/admi.202400912.

Yoshizuka, Kazuharu; Fukui, Kenji; Inoue, Katsutoshi, (2002): Selective recovery of Lithium from seawater using a novel MnO2 type adsorbent. In *Ars Separatoria Acta* (1), pp. 79–86.

Yoshizuka, Kazuharu; Kitajou, Ayuko; Holba, Marek, (2006): Selective recovery of lithium from seawater using a novel MnO2 type adsorbent III-benchmark evaluation. In *Ars Separatoria Acta* 4, pp. 78–85.

Zandevakili, S.; Ranjbar, M.; Ehteshamzadeh, M., (2014): Recovery of lithium from Urmia Lake by a nanostructure MnO 2 ion sieve. In *Hydrometallurgy* 149, pp. 148–152. DOI: 10.1016/j.hydromet.2014.08.004.

Zhang, Guotai; Zhang, Jingze; Zeng, Jinbo; Sun, Yanxia; Shen, Yue; Li, Xiang et al., (2021a): Improved structural stability and adsorption capacity of adsorbent material Li1.6Mn1.6O4 via facile surface fluorination. In *Colloids and Surfaces A: Physicochemical and Engineering Aspects* 629, p. 127465. DOI: 10.1016/j.colsurfa.2021.127465.

Zhang, Guotai; Zhang, Jingze; Zhou, Yuan; Qi, Guicai; Zeng, Jinbo; Sun, Yanxia et al., (2021b): Practical synthesis of manganese oxide MnO2·0.5H2O for an advanced and applicable lithium ion-sieve. In *Journal of Solid State Chemistry* 293, p. 121768. DOI: 10.1016/j.jssc.2020.121768.

Zhang, Haipeng; Wu, Anbang; Fu, Heyun; Zhang, Ling; Liu, Hui; Zheng, Shourong et al., (2017): Efficient removal of Pb(ii) ions using manganese oxides: the role of crystal structure. In *RSC Adv.* 7 (65), pp. 41228–41240. DOI: 10.1039/C7RA05955H.

Zhang, Shengmiao; Zhou, Pan; Zhu, Wenxiao; Zhu, Yun, (2020): Macroporous Lithium Adsorbent Monolith Prepared via High Internal Phase Emulsion Technique. In *ACS Appl. Polym. Mater.* 2 (7), pp. 2563–2570. DOI: 10.1021/acsapm.0c00197.

Zhao, Qianqian; Yao, Tingting; Liu, Yucheng; Zheng, Xiaoqiang; Yang, Ping, (2026): Multidimensional regulation of the cycling stability of lithium manganese oxides: A review. In *Desalination and Water Treatment* 325, p. 101591. DOI: 10.1016/j.dwt.2025.101591.

Zhu, Guiru; Wang, Pan; Qi, Pengfei; Gao, Congjie, (2014): Adsorption and desorption properties of Li+ on PVC-H1.6Mn1.6O4 lithium ion-sieve membrane. In *Chemical Engineering Journal* 235, pp. 340–348. DOI: 10.1016/j.cej.2013.09.068.